Università degli Studi del Piemonte Orientale
"Amedeo Avogadro"

Dipartimento di Medicina Traslazionale

Dottorato di Ricerca in "Food, Health & Longevity"
XXXV Ciclo

PROTEOMIC ANALYSIS TO INVESTIGATE NEW THERAPUTIC APPROACHES, BIOMARKERS AND PATHOLOGICAL MECHANISMS IN DIFFERENT DISEASES

SSD BIO/10

Dottoranda: **Virginia Vita Vanella**

Tutor: **Dr. Marcello Manfredi**

Coordinatore: **Prof.ssa Antonia Follenzi**

ENGLISH SUMMARY OF THE THESIS

In the present Ph.D. thesis, proteomic, peptidomic and metabolomic analysis were performed to investigate various biological aspects of cancer, viral infection, and metabolic diseases. All the studies were carried out through an untargeted approach using a high-resolution mass spectrometry coupled with liquid or gas chromatography. The first study focused on cancer vaccine-based immunotherapies. Our findings demonstrated that salmonella infection of STSs/bone sarcoma primary human cells induces the release of immunogenic peptides in the extracellular medium. These peptides showed an HLA-binding ability in silico and a capability to induce an antitumor immune response in vitro. In the second study, we employed an untargeted proteomic discovery approach to identify potential MPM biomarkers in serum and pleural effusion. Two candidate biomarkers were confirmed on a bigger cohort of patients by ELISA: Gelsolin for serum and Lumican for pleural effusion. They showed diagnostic, prognostic and histological subtypes discrimination capabilities. The third study of the thesis mainly focused on cancer patients affected by COVID-19 disease. A proteomic analysis was performed to identify immuno-metabolic pathways that intersect Sars-Cov-2 infection and cancer. The emerging proteomic profile of Sars-Cov-2 and cancer patients showed alterations in the modulation of pathways and proteins associated with immunodeficiency, susceptibility to viral infection and inflammatory modulation. These results suggest that the concomitant presence of cancer condition and viral infection may increase the inflammatory state of patients, contributing to extra pulmonary inflammatory complications and fragility in cancer patients. The fourth study focused on the investigation – via proteomic approach - of the host circulating exosome's response to Sars-CoV-2 infection. Our findings showed that circulating exosomes are strongly involved in the processes associated with SARS-CoV-2 infection. The proteomic analysis of plasma exosomes identified several molecules involved in immune response, inflammation, activation of coagulation and complement pathways. Another remarkable result is the presence of several potential biomarkers that are well correlated with the severity of the disease. The last part of the thesis reports a metaproteomics and metabolomics analysis of the gut microbiota in pediatric obese children before and after six and twelve months of Mediterranean Diet (MD) intervention. Our results showed that MD induces in pediatric obese patients the modulation of several bacterial species linked to a general improvement of intestinal dysbiosis, inflammation and metabolic syndrome induced by high-fat diets. In addition, MD also impacted the production and use of gut and circulating SCFAs, suggesting an indirect contribution of bacteria-produced SCFAs to obesity.

ITALIAN SUMMARY OF THE THESIS

Nel presente lavoro di ricerca, sono state eseguite diverse analisi di proteomica, metabolomica e peptidomica basate sulla cromatografia liquida o gassosa e spettrometria di massa per studiare vari aspetti biologici della ricerca sul cancro, sulle infezioni virali e sulle malattie metaboliche. Il primo studio riporta una nuova strategia di vaccinazione immunoterapeutica basata su peptidi immunogenici. I nostri risultati hanno dimostrato che l'infezione da salmonella di cellule umane primarie di sarcoma induce il rilascio di peptidi immunogenici nel mezzo extracellulare. Questi peptidi hanno mostrato una forte capacità di legare gli HLA in silico e di indurre una risposta immunitaria antitumorale in vitro. Il secondo studio riporta l'identificazione, mediante un approccio proteomico *untargeted*, di nuovi biomarcatori del plasma e del versamento pleurico per la diagnosi precoce di mesotelioma pleurico maligno (MPM). Due potenziali biomarcatori sono stati confermati mediante ELISA su una coorte più ampia di pazienti: Gelsolina per il siero e il Lumican per il versamento pleurico. Questi due biomarcatori hanno mostrato un'elevata capacità diagnostica, prognostica e di individuazione del sottotipo istologico. Il terzo studio si focalizza principalmente sui pazienti oncologici affetti da COVID-19. È stata eseguita un'analisi proteomica al fine di identificare i meccanismi biochimici e le vie immunologiche che caratterizzano la condizione patologica dei pazienti con infezione da SARS-CoV-2 e cancro. Il profilo proteomico ha mostrato alterazioni nella modulazione dei pathway e di proteine associate all'immunodeficienza, ad una maggiore suscettibilità ad infezioni virali e alla risposta infiammatoria. Questi risultati suggeriscono che la presenza concomitante di una patologia tumorale e di un'infezione virale può aumentare lo stato infiammatorio dei pazienti, contribuendo alle complicazioni infiammatorie extrapolmonari e alla fragilità dei pazienti oncologici. Il quarto studio descrive la risposta degli esosomi circolanti dell'ospite all'infezione da SARS-CoV-2. I nostri risultati hanno dimostrato che gli esosomi circolanti sono fortemente coinvolti nei processi associati all'infezione da SARS-CoV-2. L'analisi proteomica degli esosomi plasmatici ha identificato diverse molecole coinvolte nella risposta immunitaria, nell'infiammazione, nell'attivazione della coagulazione e nelle vie del complemento. Un altro risultato notevole è la presenza di diversi potenziali biomarcatori correlati con la gravità della malattia. L'ultima parte della tesi riporta un'analisi metaproteomica e metabolomica del microbiota intestinale in bambini pediatrici obesi prima e dopo sei e dodici mesi di Dieta Mediterranea (MD). I nostri risultati hanno mostrato che la MD induce nei pazienti pediatrici obesi la modulazione di diverse specie batteriche legate a un miglioramento generale della disbiosi intestinale, dell'infiammazione e della sindrome metabolica indotta da diete ricche di grassi.

1 INDEX

2 INTRODUCTION AND AIMS OF THE THESIS

Today mass spectrometry (MS) is emerging as a powerful strategy for the identification, characterization, and quantification of thousands of molecules in a biological sample or system. In particular, MS-based proteomic and metabolomic applications have received considerable attention during last years [1]. In system biology, large-scale analysis of metabolites and proteins is essential to understand the response of cellular systems [2,3]. While proteomics is the large-scale study of the entire complement of proteins in a biological system and their changes under different conditions, from physiological states to pathological variations [4], metabolomics aims at the comprehensive and quantitative analysis of a large variety of metabolites in biological samples. A detailed comprehension of the participating proteins and metabolic substrates provides an understanding of the biochemical processes and cellular functions essential to health and/or disease: this information is also necessary to advance translational studies, especially those related to personalized medicine [5]. Proteomics and metabolomics can be used to discover potential biomarkers for the screening and diagnosis of diseases and metabolic disorders, for the understanding of drug responses and molecular pathogenesis, and for the identification of new therapeutic targets. In addition, improvements in both liquid chromatography (LC) and mass spectrometry (MS) instrumentation have also allowed the study and quantification of native peptides [6]. Peptidomics is the comprehensive study of all peptides in a biological sample and system. Peptidomic analysis employs many proteomics methods but with a different target. Since peptides play complex regulatory roles in many biological processes, peptidomic is today employed in several applications, from food to clinical application [7].

In the present Ph.D. thesis, proteomic, metabolomic and peptidomic analysis were performed to explore disease disorders, especially in the context of identifying new therapeutic approaches, exploring biochemical mechanisms and discovering diagnostic/prognostic biomarkers. In particular, five different studies in which the right combination of proteomic, metabolomic and/or peptidomic allowed the in-depth study of protein and biological alterations under different disease conditions will be presented. In light of this, the thesis is divided in three main chapters based on the investigated disease:

- **Cancer**
    - Identification of new immunogenic peptides as potential anticancer vaccines for **sarcoma cancer**.
    - Identification and large cohort validation of novel diagnostic biomarkers for **Malignant Pleural Mesothelioma (MPM).**
    - Investigation of PBMC proteomic alterations in **cancer patients with COVID-19.**

- **Viral infection**
    - Investigation of exosome composition alterations upon **SARS-CoV-2 infection.**

- **Metabolic diseases**
    - Study the impact of MD intervention on the gut microbiota of **pediatric obese patients.**

In the first main chapter, MS-based proteomic and peptidomic technologies were used to investigate several biological aspects in cancer research. The first part stems from an AIRC funded project (Universal Cancer Vaccine: UniCanVax), in which the proposal is a novel immunotherapeutic vaccination strategy based on immunogenic peptides that are naturally released by cancer cells and that could be used as universal vaccines. This project was carried out in collaboration with Prof. Maria Rescigno's group from Humanitas Research Center of Rozzano. The **aim** of this project was **to identify novel immunogenic peptides that could be used as a universal sarcoma vaccine treatment**. Through LC-MS/MS techniques, peptides extracted from the conditioned medium of soft tissue sarcoma (STS)/ sarcoma cells treated with salmonella infection were identified and quantified.

The second study on cancer reports the discovery of new sera and pleural effusions biomarkers of MPM. The **aim** of this project was the **identification and a large-cohort validation of new biomarkers for the early diagnosis of MPM**. Plasma and pleural effusions from patients and controls were analyzed through LC-MS/MS to identify marker proteins that were then validated using ELISA.

The third part of the first chapter is mainly focused on cancer patients affected by COVID-19 disease. An untargeted proteomic analysis of PBMC samples was performed to elucidate the mechanism and immunological pathways that intersect patients with infection and cancer. In particular, the **objective was to investigate the interference between the immunosuppressive and anti-**

inflammatory action of growing tumors and the immune metabolic scenario induced by SARS-CoV-2 infection, as well as to identify new therapeutic strategies for the management of patients with cancer affected by COVID-19.

In the second chapter of the thesis the host circulating exosomes' response to SARS-CoV-2 infection will be presented. The knowledge of the host response to the novel coronavirus SARS-CoV-2 was still limited at the time of the research (beginning of 2020). The **aim** of this study was **to investigate** by proteomic analysis the **alterations of exosome composition upon SARS-CoV-2 infection** and the potential use of plasma exosomes as biomarkers of the disease severity. MS-based proteomic analysis was employed for the characterization of plasma-derived exosomes from COVID-19 patients and healthy controls.

The last chapter of the thesis is focused on metaproteomic and metabolomic approaches to study gut microbiota alterations in pediatric obese patients subjected to a dietary intervention with Mediterranean Diet (MD). Although the study of intestinal microbiome is still challenging, today, thanks to recent developments of metaproteomics and metabolomics, the gut microbiome characterization is possible. The **aim of the project was to investigate the impact of MD intervention on the gut microbiota of pediatric obese patients**. The dietary intervention was based on educational training using gamification, while untargeted metaproteomics and metabolomics were employed to study any alterations of the gut microbiota and plasma after six and twelve months of diet.

3 CANCER

3.1 MASS SPECTROMETRY BASED PROTEOMICS - APPLICATIONS TO CANCER RESEARCH

Cancer is the second leading cause of death and poses a major problem to healthcare systems worldwide [8]. The most diagnosed cancers are breast, lung, and prostate cancers, while the most common causes of cancer death are caused by lung, liver, and stomach cancers. Currently, clinical practices are being improved by research on early detection methods, appropriate classification of risk groups and treatment efficacies. The early detection of cancer is crucial for its ultimate control and prevention [9]. The ability to effectively cure and treat cancer is directly dependent on the ability to detect them at their earliest stages [10]. Advances in conventional diagnostic strategies, such as mammography and Prostate-Specific Antigen (PSA) testing, have provided some improvement in the detection of disease. [11,12] However, they still do not reach the sensitivity and specificity that are needed to reliably detect early-stage disease. In many cases, cancer is diagnosed and treated when cancer cells have already invaded surrounding tissues and, in this case, most conventional therapeutics are limited in their success. [13] On the other hand, detecting cancers when they are at their earliest stages means that current or future treatment strategies will have a higher probability of truly curing the disease. In this scenario, biomarkers represent an important tool for cancer detection and monitoring, and the emerging field of clinical proteomics is especially well suited to the discovery and implementation of these biomarkers. [14] Considering that proteins are biomolecules that directly carry out most biological processes, they are ideal predictors of disease progression. Body fluids, such as serum, are protein-rich information reservoir that contains traces of what the blood has encountered during its circulation through the body [15]. Mass spectrometry-based proteomic analysis is a key method for the rapid detection of cancer-specific biomarkers. Moreover, specific protein profiles may be prognostic, thus helping with proper treatment recommendations. [16] MS-based proteomic techniques are also widely employed for the full understanding of complex molecular pathways related to cancerogenesis. Several studies have shown the great potential of clinical proteomics in the characterization of many diseases and its achievements in the oncological field [17].

Additionally, proteins and peptides are the active targets of most cancer therapeutics, including the growing field of immunotherapies. Cancer immunotherapy is a type of cancer treatment that aims to boost T cell-mediated immune response in order to target and eliminate cancer cells. After many years of disappointing results, immunotherapy has become a clinically validated treatment for a variety of human malignancies [18]. In addition, therapeutic cancer vaccines against tumor-related epitopes that directly stimulate T cells have been clinically effective and are currently available [19]. Cancer cells express several antigens, including self-antigens derived from tumor tissues, as well as mutation-derived antigens (i.e., neoantigens), that can be processed and presented as HLA binding peptides (HLAp), leading to their recognition as “non-self” by the host immune system [20]. Currently, mass spectrometry based immunopeptidomics is the only unbiased methodology to interrogate the repertoire of naturally presented HLAp in tissues. Of note, mass spectrometry has been successful in identifying neoantigens on cancer cell lines and in melanoma tissues [21].

The present chapter reports the application of MS-based proteomic and peptidomic technologies with diagnostic, prognostic or therapeutic purposes in oncology research, particularly for soft tissue sarcoma (STS)/sarcoma, mesothelioma and cancer patients affected by SARS-CoV-2.

3.2 IDENTIFICATION OF NEW IMMUNOGENIC PEPTIDES AS POTENTIAL ANTICANCER VACCINES FOR STSS/SARCOMA CANCER

3.2.1 Background and Rationale

Sarcomas account for over 20% of all pediatric solid malignant cancers and about 1% of adults' worldwide. The over seventy known sarcoma sub-types dramatically differ for origin, aggressiveness, response to therapy and intratumor heterogeneity [22]. High grade sarcomas can be highly heterogeneous histologically, with a single tumor containing areas of different histologic grade, necrotic regions, and a variable inflammatory cell infiltrate. These patients as well as the patients with locally advanced disease are often treated with the combination of a perioperative treatment (neoadjuvant or adjuvant), chemotherapy and/or radiotherapy, to improve the long-term outcome and to reduce the risk of relapse [23]. In the last years, immunotherapy has emerged as an attractive approach to refractory cancers. In sarcoma, the role of immunotherapeutic agents is still under evaluation but new strategies to enhance immunogenicity and therapeutic strategies are strongly needed. Most cancer cells down-regulate gap junctions (GJ) resulting in loss of communication with their surrounding microenvironment [24,25]. A previous clinical study documented that the infection of tumor cells with *Salmonella Typhimurium* induces the up regulation of connexin 43 (Cx43), a ubiquitous protein that forms GJ [26]. Cx43 allows the transfer of antigens between tumor cells and dendritic cells (DC) enabling them to induce an efficient anti-tumor response both in human melanoma cells in vitro and in a mouse model of melanoma in vivo [27]. Most important, the increased proteasome activity induced by Salmonella infection on human, murine, and canine tumor cells results in the secretion of non-conventional ER-stress-response-derived immunogenic peptides (ERstrePs) in the extracellular space through Cx43-hemichannels. Mass spectrometry analysis on the supernatant of Salmonella-infected human melanoma cells revealed 12 peptides that were selectively released upon infection and that are capable to bind HLA-2 and HLA-3 molecules directly on dendritic cells and to prime human cytotoxic CD8+ T cells from PBMCs of healthy donors. As a result, healthy-donor CD8+ T cells recognize and kill human melanoma cells in vitro and when xenotransplanted in vivo [26]. These peptides released by cancer cells are not presented by healthy cells and are highly immunogenic and trigger an efficient anti-tumor response in a clinical trial on dogs affected by osteosarcoma and high-grade sarcoma [28]. Based on these considerations, the aim of the present study was the identification of novel

immunogenic peptides released by soft tissue sarcoma (STS)/ sarcoma patients-derived primary tumor cells to formulate a possible vaccine. Peptides were extracted from the medium of STSs/sarcoma cells treated with Salmonella infection and were analyzed with LC-MS.

3.2.2 Materials and Methods

3.2.2.1 Patients

In total, 23 patients (mean age 59 years, range 25–88 years) with a histological diagnosis of primary or recurrent soft tissue or bone sarcoma of any histotype (with the exception of well-differentiated liposarcoma), grade and site were included in the study. Their characteristics are summarized in **Table 3.1**.

Table 3.1: *patients with STSs/sarcoma enrolled in the study*

Patient Code	Gender	Age	Type	Site	Grading	Stage	chemio	radio	Status (Alive/Dead)
HsSa5									
HsSa6	F	47	Myxoid liposarcoma	Upper leg	2		1	0	A
HsSa9	F	44	Other sarcoma	Upper leg	3		0	0	A
HsSa13	F	30	chondrosarcoma	Sternum	1		0	0	A
HsSa14	F	72	Undifferentiated pleomorphic sarcoma	Leg	3	distant metastasis	0	0	A
HsSa15	F	78	Fibrosarcomatous DFSP	Other	3	distant metastasis	0	0	A
HsSa16	F		Dedifferentiated liposarcoma	Retroperitoneum	3		0	0	A
HsSA17	F	74	Myxofibrosarcoma	Buttock	3		0	0	A
HsSA18	F	69	Solitary fibrous tumour	Paravertebral - thoracolumbar	2		0	0	D
HsSA19	M	69	Dedifferentiated liposarcoma	Retroperitoneum	3		0	0	D
HsSA22	F	31	Osteosarcoma	Lower leg	3		0	0	A
HsSA25									
HsSA28	F	51	Myxofibrosarcoma	Upper leg	3		1	1	A
HsSA29	M	67	Dedifferentiated liposarcoma	Upper leg	2		0	1	A
HsSA30	F	88	Giant cell tumour of soft tissue	Upper leg			0	0	A
HsSA31	F	78	Undifferentiated round cell sarcoma	Hand	3		1	0	A
HsSA32	F	76	Dedifferentiated liposarcoma	Retroperitoneum	3		0	0	A
HsSA33	F		Dedifferentiated liposarcoma	Retroperitoneum	3		0	0	A
HsSA35	F	25	Phyllodes tumor	Breast	3		1	0	A
HsSA37	M	74	Undifferentiated pleomorphic sarcoma	Upper leg	3		0	1	A
HsSA40	F	82	Undifferentiated pleomorphic sarcoma	Upper leg	3	distant metastasis	0	0	D
HsSA42	F	80	Dedifferentiated liposarcoma	Upper leg	3		0	0	
HsSA43	F	49	Synovial sarcoma	Abdominal wall			1	1	A

The patients were diagnosed, treated, and follow up at the Humanitas Research Hospital Rozzano, Milan, Italy. Some of the patients included in the study received a systemic chemotherapeutic treatment, with or without radiotherapy, including locally advanced disease for neoadjuvant treatment, non-resectable local recurrence, synchronous or metachronous metastatic disease. The study was approved by the Ethics Committee of Humanitas Clinical and Research Center.

3.2.2.2 Sample preparation

Primary human STS and bone sarcoma cells, obtained from dissociation of human tumor specimens, were left untreated or infected with an attenuated vaccine strain of Salmonella enterica serovar Typhi (Ty21a). This in vitro part was performed by our collaborator from Humanitas University.

Briefly, single bacterial colonies were grown overnight and restarted the next day to reach an absorbance at 600 nm of 0.6, corresponding to 0.6 x 10^{9} colony-forming units (CFUs)/mL. Primary human sarcoma cells (2 x 10^{6} cells/mL) were incubated with the bacteria for 90 min, in tubes, at a cell-to-bacteria ratio of 1:50, in the appropriate medium containing L-glutamine without antibiotics. Then, the cells were washed and incubated in medium supplemented with gentamicin (50 mg/mL), for 18 hours to kill extracellular bacteria. Cell viability was tested by Annexin/PI staining (BD). During incubation, immunogenic peptides are released - via Cx43 hemichannels - by cancer cells in the extracellular space. At the end of incubation, the supernatants were collected. Successively, supernatants were filtered through a 0.22 µm filter to get rid of any remaining potentially live bacteria and concentrated through the use of chromabond SPE C18 devices (Macherey-Nagel). Once eluted with 80% CH_3CN in 0.1% Formic Acid (FA) solution, samples were dried by speed vacuum, solved in water, and sonicated with Bioruptor 30'' ON + 30'' OFF (2 cycles). Next, low and high molecular weight fractions were separated with Amicon Ultra-0.5 mL 10 kDa centrifugal filter (Millipore, Billerica, MA, USA). Low molecular peptides were concentrated in a centrifuge vacuum concentrator and then acquired by nano-scale liquid chromatographic mass spectrometry.

3.2.2.3 Mass spectrometry analysis

2 µl of each sample were loaded on EASY nano-LC 1200 system (Thermo Scientific, Milano, Italy) coupled to a 5600+ TripleTOF system (AB Sciex, Concord, Canada). Peptides separation was achieved on Acclaim PepMap C18 2µm 75µm x 150mm column with a linear gradient from 97% solvent A (100% water, 0.1% formic acid) to 45% solvent B (80% acetonitrile, 0.1% formic acid) over 2 hours at a constant flow rate of 0.3 ml/min. MS data were acquired using a mass range of 100–1600 Da (TOF scan with an accumulation time of 0.25 s), followed by a MS/MS product ion scan from 400 to 1250 Da (accumulation time of 5.0 ms) with the abundance threshold set at 30 cps (40 candidate ions can be monitored during every cycle). The ion source parameters in electrospray positive mode were set as follows: curtain gas (N2) at 30 psig, nebulizer gas (GAS1) at 25 psig, ion spray floating voltage (ISFV) at 2700 V, source temperature at 90 °C and declustering potential at 85V. Two technical replicates were conducted on the LC-MS/MS part of the analysis.

3.2.2.4 Mass spectrometry data processing

Mass spectra were analyzed using MaxQuant software (version 1.5.2.8). Search parameters were set to an initial precursor ion tolerance of 10 ppm and MS/MS tolerance at 20 ppm. Enzyme specificity was set to unspecific and methionine oxidation was set as variable modification**.** The

spectra were searched using the Andromeda search engine in MaxQuant against the Uniprot_Human_2018 sequence database. Label free analysis was carried out, including a 'match between runs' option imposing the following parameters: quantification based on extracted ion chromatograms with minimum ratio count of 1, peptide and protein false discovery rates (FDRs) were set to 0.01 and the minimum required peptide length was set to 7 amino acids. The reversed sequences of the target database were used as decoy database. Comparative analyses were performed using the Perseus software (version 1.5.1.6). Missing values were replaced by random numbers drawn from a normal distribution by the function 'imputation' (width 0.3, down shift 1.8, separately for each column). Peptides were also analyzed using Protein Pilot software v. 4.2 (AB SCIEX, Concord, Canada) and Mascot v. 2.4 (Matrix Science Inc., Boston, USA). No enzyme was specified for both software and oxidized methionine was used as variable modification. The Uniprot_Human_2018 sequence database was used, and a target-decoy database search was performed. False Discovery Rate (FDR) was fixed at 1%. For mascot an assay tolerance of 50 ppm was specified for peptide mass tolerance, and 0.1 Da for MS/MS tolerance. The peptide charges to be detected were set to 2 +, 3 +, and 4 +, and the assay was set on monoisotopic mass. Only peptides with ions score cut-off greater than 20 were considered. Comparative analyses were performed using MarkerView 1.2. (ABSCIEX, Concord, Canada). For all the statistical analysis a t-test analysis was performed imposing a p-value of 0.05 and a fold change greater than 1.3. Net-MHCpan4.1 tool was applied to *in silico* predict the affinity of the peptides for major histocompatibility complex (MHC) class I molecules.

3.2.2.5 Antigen specific-CD8+ T cells expansion from healthy donor PBMCs

Total PBMCs isolated from healthy donors were loaded with either supernatant derived from 2 x 10^6 sarcoma cells treated with Salmonella, or 20 mM Mart-126-35 (Iba Lifesciences) or CMV peptides (pp65, JPT Peptide Technologies) in rotation at 37 °C for 90 minutes. Cells were then plated in complete medium in 24-well plates (2 x 10^6 cells per well) in a final volume of 2 ml. Starting from day 3, every 2-3 days we added recombinant IL-2 (Proleukin, Novartis) at a final concentration of 20 U/mL. Cells were restimulated every 10 days; expanded lymphocytes were enriched in CD8+ T cells by magnetic column separation (Miltenyi Biotec) and stimulated with irradiated (10 Gy) PBMCs that were pulsed with either Mart-1 or CMV peptides-mix, or supernatant from sarcoma cells infected with Salmonella. To pulse, PBMC were incubated for 90 minutes at 37°C in RPMI supplemented with the selected stimulus.

3.2.3 Results and Discussion

3.2.3.1 Isolation and identification of immunogenic peptides derived from the supernatant of Salmonella-treated and -untreated human STS/sarcoma cells

The experimental workflow followed for the identification of immunogenic peptides from supernatants of salmonella treated and untreated human STS/sarcoma cells is summarized in **Figure 3.1**. To isolate peptides present in the supernatant, a combination of SPE and centrifugal filtration method was applied. LC-MS/MS analysis of extracted peptides was performed on a TripleTOF5600+ mass spectrometer with a Nano Spray III ion source coupled to an EASY nano-LC 1200 system. Each sample was analyzed in duplicate. To increase the number of identified peptides, the generated peak lists were searched with three different database search engines: Mascot, Protein Pilot and MaxQuant with 1% FDR.

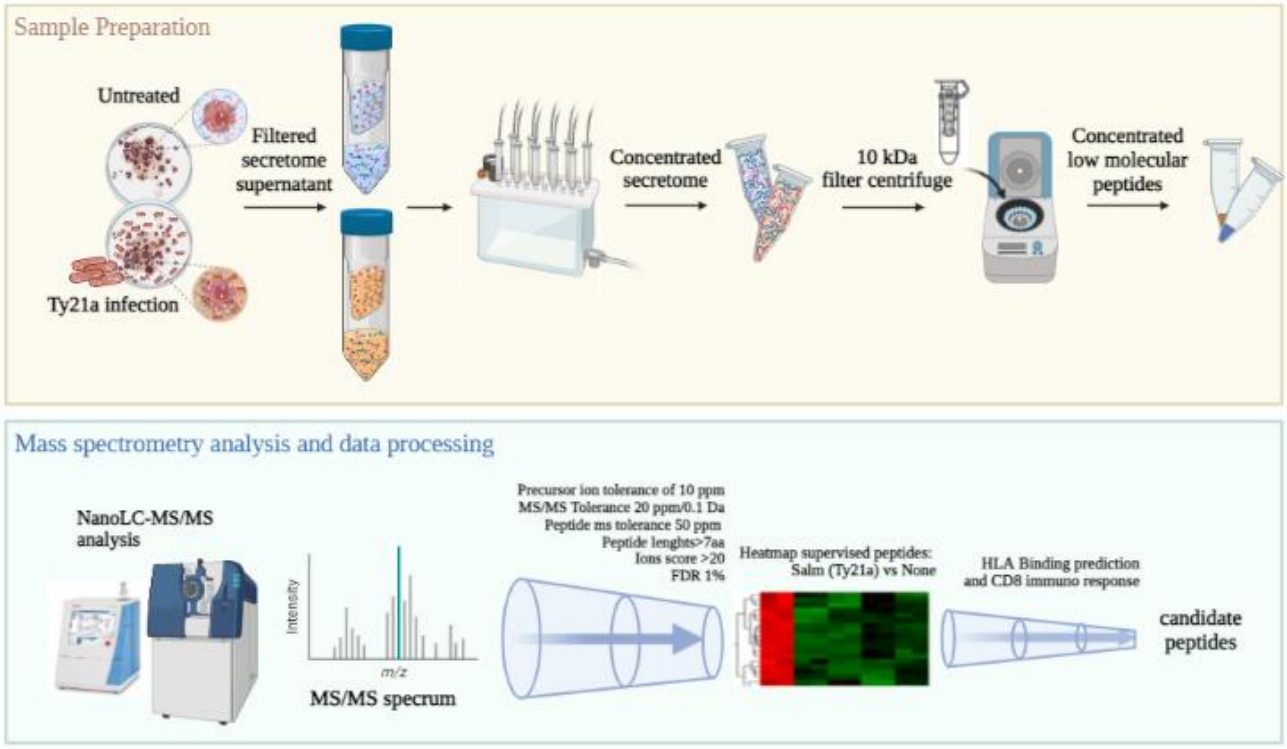

Figure 3.1: *experimental workflow to identify peptides released by human STSs/sarcoma cells upon Salmonella infection*.

A total of 2755 different peptides corresponding to 783 unique proteins were identified in the conditioned medium. Consistent with the finding that Salmonella infection fosters the secretion of peptides [26], we detected a larger number of peptides in the secretome of the Salmonella-infected primary cell line than in the non-infected cell line. Among the thousands of peptides detected, 637

were overexpressed in salmonella infected cell line secretome, of which 73 were shared between at least 2 or more patients. The complete list of the overexpressed peptides and their correspondent parent proteins is shown in **table 3.2**.

Table 3.2: *list of the overexpressed peptides and their correspondent parent proteins.*

PEPTIDE	PROTEIN	PROTEIN NAME
pep1	G3P_HUMAN	Glyceraldehyde-3-phosphate dehydrogenase
pep2	HMGN2_HUMAN	Non-histone chromosomal protein HMG-17
pep3	HMGN2_HUMAN	Non-histone chromosomal protein HMG-17
pep4	MARE1_HUMAN	Microtubule-associated protein RP/EB family member 1
pep5	G3P_HUMAN	Glyceraldehyde-3-phosphate dehydrogenase (GAPDH)
pep6	ROA2_HUMAN	Heterogeneous nuclear ribonucleoproteins A2/B1
pep7	PDIA1_HUMAN	Protein disulfide-isomerase (PDI)
pep8	EF1B_HUMAN	Elongation factor 1-beta (EF-1-beta)
pep9	VIME_HUMAN	Vimentin
pep10	RS19_HUMAN	40S ribosomal protein S19
pep11	VIME_HUMAN	Vimentin
pep12	ACTB_HUMAN	Actin, cytoplasmic 1 (Beta-actin)
pep13	SH3L3_HUMAN	SH3 domain-binding glutamic acid-rich-like protein 3
pep14	SERPH_HUMAN	Serpin H1
pep15	PLEC_HUMAN	Plectin
pep16	TYB4_HUMAN	Thymosin beta-4
pep17	TYB4_HUMAN	Thymosin beta-4
pep18	EF1A1_HUMAN	Elongation factor 1-alpha 1 (EF-1-alpha-1)
pep19	SNRPA_HUMAN	U1 small nuclear ribonucleoprotein A
pep20	LMNA_HUMAN	Prelamin-A/C
pep21	ROA2_HUMAN	Heterogeneous nuclear ribonucleoproteins A2/B1
pep22	HMGA1_HUMAN	High mobility group protein HMG-I/HMG-Y
pep23	HMGA1_HUMAN	High mobility group protein HMG-I/HMG-Y
pep24	VIME_HUMAN	Vimentin
pep25	TBB6_HUMAN	Tubulin beta-6 chain
pep26	H2A1_HUMAN	Histone H2A type 1
pep27	NPM_HUMAN	Nucleophosmin
pep28	H2A2A_HUMAN	Histone H2A type 2-A
pep29	G3P_HUMAN	Glyceraldehyde-3-phosphate dehydrogenase
pep30	HSPB1_HUMAN	Heat shock protein beta-1
pep31	GSTP1_HUMAN	Glutathione S-transferase P
pep32	MIF_HUMAN	Macrophage migration inhibitory factor
pep33	PPIA_HUMAN	Peptidyl-prolyl cis-trans isomerase A
pep34	PTBP1_HUMAN	Polypyrimidine tract-binding protein 1
pep35	PARK7_HUMAN	Parkinson disease protein 7

pep36	NUDC_HUMAN	Nuclear migration protein nudC
pep37	EF1B_HUMAN	Elongation factor 1-beta
pep38	CALR_HUMAN	Calreticulin
pep39	MIF_HUMAN	Macrophage migration inhibitory factor
pep40	G3P_HUMAN	Glyceraldehyde-3-phosphate dehydrogenase
pep41	SC61B_HUMAN	Protein transport protein Sec61 subunit beta
pep42	MIF_HUMAN	Macrophage migration inhibitory factor
pep43	VIME_HUMAN	Vimentin
pep44	PTBP1_HUMAN	Polypyrimidine tract-binding protein 1
pep45	PGK1_HUMAN	Phosphoglycerate kinase 1
pep46	PGK1_HUMAN	Phosphoglycerate kinase 1
pep47	TSP1_HUMAN	Thrombospondin-1 (Glycoprotein G)
pep48	YBOX1_HUMAN	Y-box-binding protein 1
pep49	CPNS1_HUMAN	Calpain small subunit 1
pep50	TBX20_HUMAN	T-box transcription factor TBX20
pep51	NUCB1_HUMAN	Nucleobindin-1
pep52	GDN_HUMAN	Glia-derived nexin
pep53	GDN_HUMAN	Glia-derived nexin
pep54	SH3L3_HUMAN	SH3 domain-binding glutamic acid-rich-like protein 3
pep55	HS90A_HUMAN	Heat shock protein HSP 90-alpha
pep56	IF5AL_HUMAN	Eukaryotic translation initiation factor 5A-1-like
pep57	G3P_HUMAN	Glyceraldehyde-3-phosphate dehydrogenase
pep58	COF1_HUMAN	Cofilin-1
pep59	MARE1_HUMAN	Microtubule-associated protein RP/EB family member 1
pep60	GDN_HUMAN	Glia-derived nexin
pep61	GDN_HUMAN	Glia-derived nexin
pep62	LYOX_HUMAN	Protein-lysine 6-oxidase
pep63	VIME_HUMAN	Vimentin
pep64	CSRP1_HUMAN	Cysteine and glycine-rich protein 1
pep65	LYOX_HUMAN	Protein-lysine 6-oxidase
pep66	VIME_HUMAN	Vimentin
pep67	ACTB_HUMAN	Actin, cytoplasmic 1
pep68	HMGN2_HUMAN	Non-histone chromosomal protein HMG-17
pep69	HMGN2_HUMAN	Non-histone chromosomal protein HMG-17
pep70	IF4H_HUMAN	Eukaryotic translation initiation factor 4H
pep71	ROA2_HUMAN	Heterogeneous nuclear ribonucleoproteins A2/B1
pep72	HMGN2_HUMAN	Non-histone chromosomal protein HMG-17
pep73	SNRPA_HUMAN	U1 small nuclear ribonucleoprotein A

3.2.3.2 Validation of peptides released by human sarcoma cells upon Salmonella infection

To predict the affinity of the peptides for major histocompatibility complex (MHC) class I molecules, in silico prediction tool Net-MHCpan4.1 was used. [29] As further selection criteria, we considered HLA-binding prediction for the most frequent HLA supertype representatives, namely, HLA-A*02:01, -A*03:01, -B*07:02, -B*14:02, -B*40:01, and -B*58:01 and a final list of 26 candidate peptides was selected. To assess the immunogenicity of the 26 selected peptides, our research partner evaluated their ability to induce CD8 T cell responses from 7 healthy donor PBMCs. Among the 24 peptides tested, 12 elicited a cytotoxic response in at least three of seven donors. Of these, 10 peptides were confirmed as immunogenic and could be used as an anticancer vaccine.

3.2.4 Conclusions

Previous findings showed that Salmonella infection of mouse melanoma cells promoted the secretion of neo-antigens in the extracellular space through GJ hemichannels and that were efficacy both in preclinical models and in a therapeutic clinical trial on dogs affected with osteosarcoma, high-grade sarcoma, or metastatic melanoma. In the present research, we found that the same stimulus induces the release of immunogenic peptides in the extracellular medium of STSs/bone sarcoma primary human cells. Identified peptides were not patient specific but were shared among several subjects. They were selected for their overrepresentation in Salmonella treated cell secretomes, for their HLA-binding ability in silico and for their capability to induce an immune response in vitro. These preliminary results showed that they can be considered as a ‘‘signature’’ of antigens that could be used as a universal sarcoma vaccine treatment. If successful, the use of universal peptides will have tremendous translational relevance because providing immediate benefit to metastatic sarcoma patients.

3.3 Gelsolin and Lumican Proteins as Biomarkers of Malignant Pleural Mesothelioma

3.3.1 Background and Rationale

MPM is a highly aggressive malignancy which is linked to asbestos exposure in more than 80% of the cases [30,31]. The diagnosis and treatment of mesothelioma is still challenging. The treatment is based on surgery, chemotherapy, and radiation; however, the estimated median survival remains around 13–15 months after the diagnosis [32]. MPM is divided into three main histological subtypes: the epithelioid that is the most common, which is characterized by the highest median survival, the sarcomatous which is the most aggressive and has the lowest survival, and the biphasic type which contains both cell types [33].

Although several trials are focusing on the development and testing of new therapies for MPM [34–36], the early diagnosis of disease could help improving the overall survival and prognosis of the patients. Today, in fact, the only available instruments for large screening for asbestos-exposed subjects are based on imaging tests, which are costly and expose patients to high doses of radiation [37], while invasive procedures are required for definitive histological and bio-molecular diagnosis of mesothelioma. For this reason, several studies investigated the presence of potential biomarkers for the non-invasive diagnosis in biofluids such as pleural effusion and plasma [38,39]. But although numerous candidate biomarkers have been proposed [40–44], only the soluble mesothelin-related protein (SMRP), which is released by tumour cells into pleural fluid and serum, has been approved by FDA as serum diagnostic biomarker. However, this marker showed a high specificity for the disease, but a low sensitivity, thus limiting its potential diagnostic use [45,46]. In addition, it has been also demonstrated that SMRP is usually not elevated on MPM tumours with sarcomatous and biphasic histology [47–49]. Another circulating protein proposed as biomarkers is Fibulin-3, although a lower specificity in pleural effusion has been reported [50]. A proteomic approach performed on a panel of 13-protein biomarker through SOMAscan technology was able to detect MPM, respect healthy control subjects, with a sensitivity and specificity of 93% and 91%, respectively [51]. In a more recent study, Cerciello et al. proposed an additional diagnostic approach based on a six-peptide signature by targeted proteomics in serum. This signature was able to discriminate patients with MPM from asbestos-exposed donors with a specificity of 0.706, but with a higher sensitivity (61%) when compared to SMRP [52]. Despite several studies proposed numerous potential biomarkers, the discovery of additional markers is needed, especially to improve the

diagnostic sensitivity. In addition, current biomarkers are not able to distinguish between MPM subtypes, which could have a positive impact on the clinical management of patients.

In the present study, a mass spectrometry-based proteomics approach was used to identify new potential sera and pleural effusion markers for the diagnosis of MPM, to differentiate the three histological subtypes and to discriminate MPM from lung adenocarcinoma (AdC) and pulmonary hyperplasia. The potential markers were then validated on a larger cohort of patients.

3.3.2 Materials and Methods

3.3.2.1 Study subjects

The initial discovery set consisted of serum samples from 34 (14 epithelioid, 10 sarcomatous, 10 biphasic) MPM patients, 6 lung AdC patients, 8 pulmonary hyperplasia patients, and 20 healthy controls, and pleural effusion samples from 46 (15 epithelioid, 16 sarcomatous, 15 biphasic) MPM patients, 15 lung AdC patients and 12 pulmonary hyperplasia patients. The demographic and clinical data of the study population recruited for the discovery phase are reported in **Table 3.3.**

Table 3.3: *demographic and clinical characteristics of the subjects included in the discovery study.*

Variable	**Serum**				**Pleural Effusion**		
	MPM (n=34)	**Lung AdC (n=6)**	**Pulmonary hyperplasia (n=8)**	**Healthy (n=20)**	**MPM (n=46)**	**Lung AdC (n=15)**	**Pulmonary hyperplasia (n=12)**
Gender (n°)							
Male	29	4	5	12	38	11	7
Female	5	2	3	8	8	4	5
Age Mean (years)							
Mean±SD	73.35 ±7.65	69.83 ±11.09	68.75 ±10.85	66.8 ±4.13	73.60 ±7.45	68.66 ±12.42	73.08 ±12.38
Histological type (n°)							
Epithelioid	14				15		
Biphasic	10				15		
Sarcomatous	10				16		
Stage (n°)							
I	3				3		
II	0				0		
III	4				7		
IV	2				3		
Unknown	25				33		
Asbestos Exposure (n°)							
Yes	16	1	2		18	0	2
No	0	5	1		0	0	1

Unknown	18	0	5		28	15	9
Mean Survival Time(months)	15	15	17		10	14	42

The validation set consisted of 116 serum samples and 121 pleural effusion samples divide as follow: 12 subjects with lung AdC, 24 subjects with only pulmonary hyperplasia, 77 MPM (23 biphasic, 19 sarcomatous, 35 epithelioid) patients and 10 healthy volunteers were used for the validation of GELS in sera, while 13 subjects with lung AdC, 25 subjects with only pulmonary hyperplasia and 92 MPM (24 biphasic, 14 sarcomatous, 54 epithelioid) patients were included in the validation study of LUM in pleural effusions. Demographical and main characteristics of the validation study patients are reported in **table 3.4**. MPM diagnosis was histologically confirmed, and all patients were enrolled at the time of diagnosis, before beginning any therapeutic treatment. All the patients were recruited from Northern Italy (Casale Monferrato and Alessandria) between 2003 and 2019. The study was approved by the Ethical Committee of Novara Hospital.

Table 3.4: *demographic and Clinical characteristics of the subjects included in the validation study of GELS and LUM*

Variable	**Serum GSN**				**Pleural Effusion LUM**		
	MPM (n=77)	**Lung AdC (n=9)**	**Pulmonary hyperplasia (n=20)**	**Healthy (n=10)**	**MPM (n=90)**	**Lung AdC (n=10)**	**Pulmonary hyperplasia (n=21)**
Gender (n°)							
Male	57	7	12	5	63	8	16
Female	20	2	8	5	27	2	5
Age Mean (years)							
Mean±SD	72.07 ±9.50	72.55 ±10.35	67.85 ±10.06	45.3 ±11.45	70 ±10.61	72.2 ±9.04	71.8 ±10.19
Histological type (n°)							
Epithelioid	35				54		
Biphasic	23				22		
Sarcomatous	19				14		
Stage (n°)							
I	3				1		
II	1				0		
III	6				4		
IV	2				2		
Unknown	55				83		
Asbestos Exposure (n°)							
Yes	16	1	3		12	1	4
No	0	0	1		0	0	0
Unknown	61	8	16		78	9	17

Mean Survival Time(months)	15	28	36		38	39	22

3.3.2.2 Specimens

Blood and pleural effusion samples were collected at the "Santi Antonio e Biagio e Cesare Arrigo" hospital of Alessandria. At the time of enrollment, venous blood samples were collected in vacutainer tubes without anticoagulant, clotted at room temperature for 30 min, and then centrifuged 3000 rpm for 15 min to yield serum. Next, serum samples were immediately transferred to 1.5 ml sterile centrifuge tubes and stored at −80 °C for further analyses. Pleural fluids were drained using thoracic thoracentesis, processed by centrifugation and stored at −80 °C until use.

3.3.2.3 Sample preparation procedure for serum and pleural effusion proteome

6 µL of serum and 40 µL of pleural effusions were depleted of high-abundance proteins using the Seppro IgY14 spin column kit (Sigma-Aldrich Inc., St. Louis, MO, USA) according to the manufacturer's procedure. The method was used to bind human serum HSA, IgG, fibrinogen, transferrin, IgA, IgM, haptoglobin, alpha 2-macroglobulin, alpha 1-acid glycoprotein, alpha 1-antitrypsin, Apo A-I HDL, Apo A-II HDL, complement C3 and LDL (ApoB) in order to increase low-abundance protein identification. The samples were transferred into an Amicon Ultra-0.5 mL 3 kDa centrifugal filter (Millipore, Billerica, MA, USA) to collect high molecular weight proteins. The samples were then subjected to denaturation with TFE, to reduction with DTT 200 mM, to alkylation with IAM 200mM and to complete protein digestion with 1 µg of Trypsin (Sigma-Aldrich Inc., St. Louis, MO, USA). Next, peptides were desalted on the Discovery® DSC-18 solid phase extraction (SPE) 96-well plate (25 mg/well) (Sigma-Aldrich Inc., St.Louis, MO, USA). More specifically, the SPE plate was preconditioned with 1 mL of acetonitrile and 2 mL of water. After loading the sample, the SPE was washed with 1 mL of water. The adsorbed peptides were eluted with 800 µL of acetonitrile:water (80:20), vacuum-evaporated and, lastly, reconstituted in mobile phase (0.1 % formic acid in water) for successive analysis.

3.3.2.4 LC-MS/MS analysis

Samples were analyzed in two phases: a data-dependent acquisition (DDA) followed by data-independent analysis (DIA) on the same sample using the same gradient conditions. All samples were analyzed with a micro-LC Eksigent Technologies (Eksigent, Dublin, USA) system interfaced with a 5600+ TripleTOF system (AB Sciex, Concord, Canada) equipped with DuoSpray Ion Source and CDS

(Calibrant Delivery System). Peptides were separated using Halo C18 column (0.5×100 mm, 2.7 µm; Eksigent Technologies Dublin, USA). The reverse phase LC solvents include solvent A (99.9% water +0.1% formic acid) and solvent B (99.9% acetonitrile +0.1% formic acid). A 30 min gradient was used at a flow rate of 15 µL/min with an increasing concentration of solvent B from 2% to 40%. For DDA acquisition, experiments were set to obtain a high-resolution TOF-MS scan over a mass range of 100–1500 m/z, followed by an MS/MS product ion scan from 200 to 1250 Da (accumulation time of 5.0 ms) with the abundance threshold set at 30 cps (35 candidate ions can be monitored during every cycle). The ion source parameters in electrospray positive mode were set as follows: curtain gas (N2) at 25 psig, nebulizer gas GAS1 at 25 psig, and GAS2 at 20 psig, ion spray voltage floating (ISVF) at 5000 V, source temperature at 450 °C and declustering potential at 25 V. Using the same conditions as described above, a SWATH acquisition using DIA was carried out for the label-free quantification process. The mass spectrometer was operated so that a 50-ms survey scan (TOF-MS) was performed and subsequent MS/MS experiments were performed on all precursors. These MS/MS experiments were carried out in a cyclical manner using an accumulation time of 40 ms per 25-Da swath (36 swaths in total) for a total cycle time of 1.5408 s. The ions were fragmented for each MS/MS experiment in the collision cell using the rolling collision energy. The MS data were acquired with Analyst TF 1.7 (AB SCIEX, Concord, Canada). Peptides (and proteins) were identified using DDA followed by database search, while the quantification was obtained by integrating the area under the chromatographic peak for each ion fragment of identified peptides by using the DIA file.

3.3.2.5 Protein Database Search

The DDA files were searched against the UniProt Swiss-Prot reviewed database containing human proteins (version 01.02.2018, containing 42,271 sequence entries) using Protein Pilot software v. 4.2 (SCIEX, Concord, Canada) and Mascot v. 2.4 (Matrix Science Inc., Boston, USA). Samples were input in the Protein Pilot software with the following parameters: cysteine alkylation, digestion by trypsin, no special factors and False Discovery Rate (FDR) at 1%. For Mascot search, we selected Trypsin as digestion enzyme with 2 missed cleavages, set the instrument to ESI-QUAD-TOF and specified the following modifications for the assay: carbamidomethyl cysteine as fixed modification and oxidized methionine as variable modification. [53,54]. An assay tolerance of 50 ppm was specified for peptide mass tolerance, and 0.1 Da for MS/MS tolerance. The charges of the peptides to search for were set to 2 +, 3 + and 4 +, and the search was set on monoisotopic. A target-decoy

database search was performed, and FDR was fixed at 1%. SwathXtend was employed to build an integrated assay library with the DDA acquisitions to use as the ion library file for all SWATH analysis and quantification.

3.3.2.6 Protein Quantification

Quantification was performed by integrating the extracted ion chromatogram of all the unique ions for a given peptide. Spectral alignment of the SWATH samples (DIA run) was carried out with PeakView 2.2 (ABSCIEX, Concord, Canada) using the spectral library generated above and the following parameters: 6 peptides per protein, 6 transitions per peptide, XIC extraction window of 5 min and a width of 15 ppm. Shared peptides were excluded as well as peptides with modifications. Peptides with FDR lower than 1.0% were exported in MarkerView 1.2 (ABSCIEX, Concord, Canada) for the t-test.

3.3.2.7 ELISA assay

The concentration of serum GELS and pleural LUM were measured using commercially available sandwich-type ELISA kits (FN-test, Wuhan Fine Biotech Co., Ltd., Wuhan, Hubei, China) according to manufacturer's instructions. Briefly, serum and pleural effusion samples were, respectively, diluted 1:200 (GELS) and 1:20 (LUM) using 10 mM PBS, pH 7.1. 100 µL of blanks, diluted standards and samples were added to 96-well strip plates pre-coated with an anti-GELS or -LUM specific antibody and incubated for 90 min at 37˚C. Then, wells were washed twice, anti-GELS or -LUM biotin-conjugated specific antibody added, and incubated for 1 h at 37˚C. Successively, plates were washed again, the streptavidin conjugated horseradish peroxidase (HRP) added, and incubated for 30 min at 37˚C. Next, the plates were washed, the (3,3', 5,5; -tetramethylbenzidine) substrate (TMB) added and incubated for 10 min at 37˚C in the dark. The enzyme-substrate reaction was stopped by adding a sulfuric acid solution and the O.D absorbance was measured spectrophotometrically at a wavelength of 450 nm. GELS and LUM sample concentrations (ng/ml) were determined by comparing the optical density (OD) of the samples to GELS and LUM standard curves, respectively.

3.3.2.8 Bioinformatic and statistic software

Statistical analysis and related graphical representations were done using GraphPad Prism v. 8 and MetaboAnalyst software (www.metaboanalyst.org). Pathway analysis was carried out using Ingenuity Pathways Analysis (IPA) software (Qiagen, Redwood City, CA, USA). Differentially

expressed proteins were used as input and only data pathways with p values<0.05 were examined further.

3.3.3 Results

In this study, the proteomic profiles of sera and pleural effusions from patients with MPM, AdC, pulmonary hyperplasia, and healthy controls were obtained to identify candidate biomarkers for the early diagnosis of MPM and to further characterize the pathways involved in the pathology. Potential markers were then validated in order to confirm the role of these proteins as biomarkers. **Figure 3.2** shows the experimental workflow of the research. For the discovery phase, untargeted proteomics was performed on pleural effusions from 45 MPM patients (15 epithelioid, 15 sarcomatous, 15 biphasic), 15 patients with lung AdC, and from 15 patients with lung hyperplasia. Serum discovery was performed on 34 MPM patients (14 epithelioid, 10 sarcomatous, 10 biphasic) 6 lung AdC patients, 8 patients with lung hyperplasia, and 20 healthy controls.

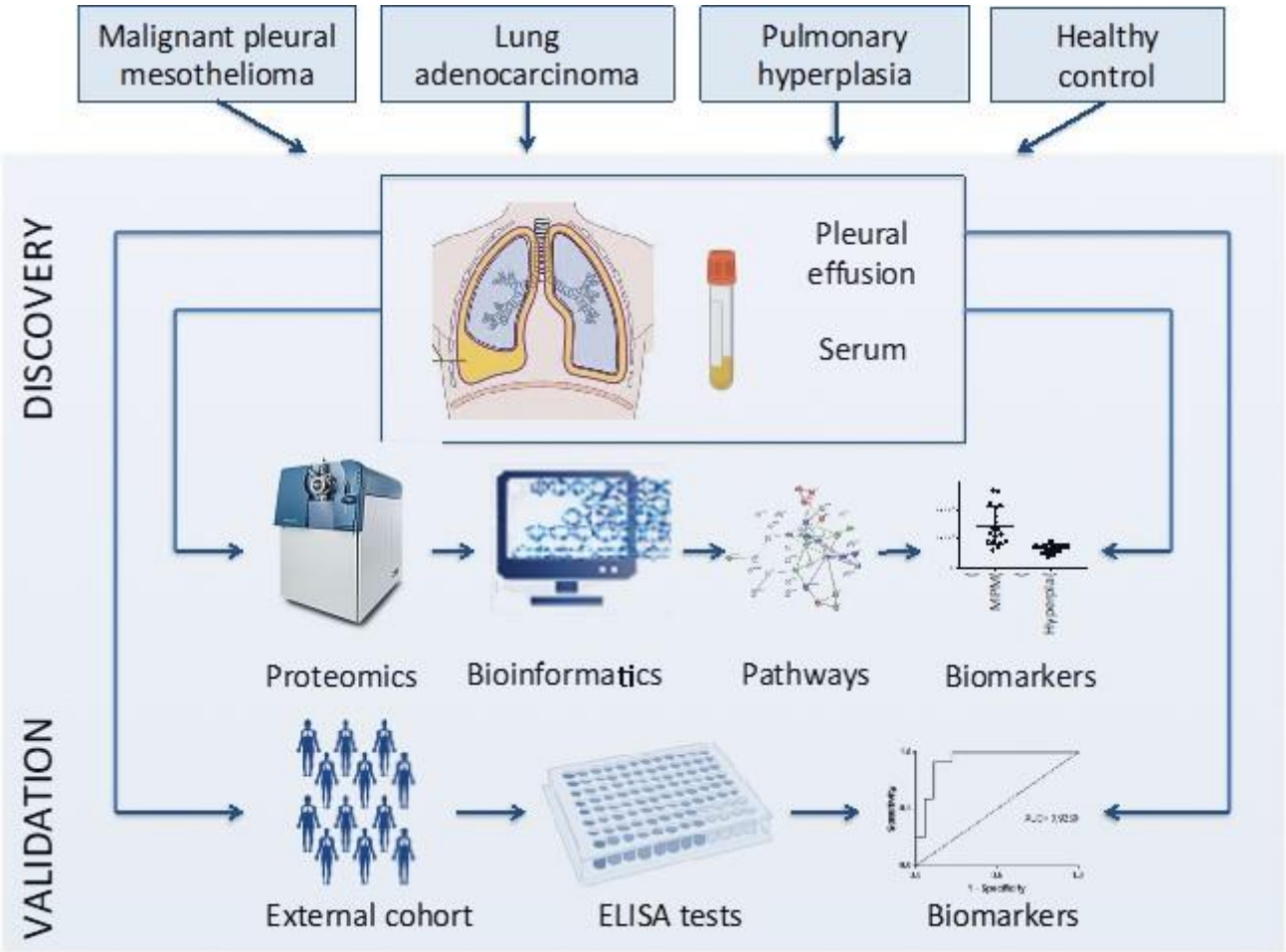

Figure 3.2: *experimental workflow of the study. An untargeted proteomic approach performed on serum and pleural effusion from patients with malignant pleural mesothelioma (MPM), lung adenocarcinoma, pulmonary hyperplasia, and healthy subjects, was used to identify potential biomarkers and the main biological pathways involved in MPM. Then, a validation phase allowed the confirmation of some proteins as potential diagnostic biomarkers of MPM.*

Serum and pleural effusion samples were all depleted from the high-abundant proteins, digested, and then analyzed with SWATH-MS to obtain a proteomic signature of each patient's group. Candidate biomarkers, found in the discovery study, were verified via ELISA in a larger cohort of patients: 12 lung AdC, 24 pulmonary hyperplasia, 77 MPM (23 biphasic, 19 sarcomatous, 35 epithelioid) patients and 10 healthy volunteers were enrolled in the validation study of sera GELS, while 13 lung AdC, 25 pulmonary hyperplasia and 92 MPM (24 biphasic, 14 sarcomatous, 54 epithelioid) patients were included in the validation study of LUM in pleural effusions.

3.3.3.1 Serum proteomic profiling and candidate markers of MPM

To investigate the differential expression of proteins in serum and to identify potential biomarkers for the diagnosis of MPM, a label-free quantification analysis was performed. A total of 445 proteins were identified: among these, 387 proteins were quantified with a peptide confidence cut-off of 99%. Protein abundances were analyzed using multivariate statistical analysis in order to assess the overall differences between MPM patients, pulmonary hyperplasia-affected patients, AdC patients, and healthy subjects.

The score plot representation of supervised partial least square discriminant analysis (PLS-DA) reported in **Figure 3.3A** shows a clear separation of healthy subjects (green dots) from MPM patients (red dots), suggesting the presence of a specific proteomic signature associated to MPM disease.

In addition, the variable importance in projection (VIP) scores plot shows the 15 most significant proteins contributing to the group discrimination observed in the PLS-DA model analysis (**Figure 3.3B**). Proteomic differences between the two groups of samples were mostly due to Alpha-1 antitrypsin (A1AT_HUMAN), Hemopexin (HEMO_HUMAN), Leucine-rich alpha-2-glycoprotein (A2GL_HUMAN), Alpha-1-acid glycoprotein 1 (A1AG1_HUMAN), haptoglobin (HPT_HUMAN), and C-reactive protein (CRP_HUMAN). In addition, the hierarchical clustering heatmap reported in **figure 3.3C** clearly shows the presence of two well-distinct clusters related to MPM and healthy subjects.

On the other hand, the PLS-DA and VIP scores plot of modulated proteins from MPM patients compared to pulmonary hyperplasia-affected patients and MPM patients compared to AdC patients show a less, but also significant, separation between samples (**Supplementary figures 3.1)**.

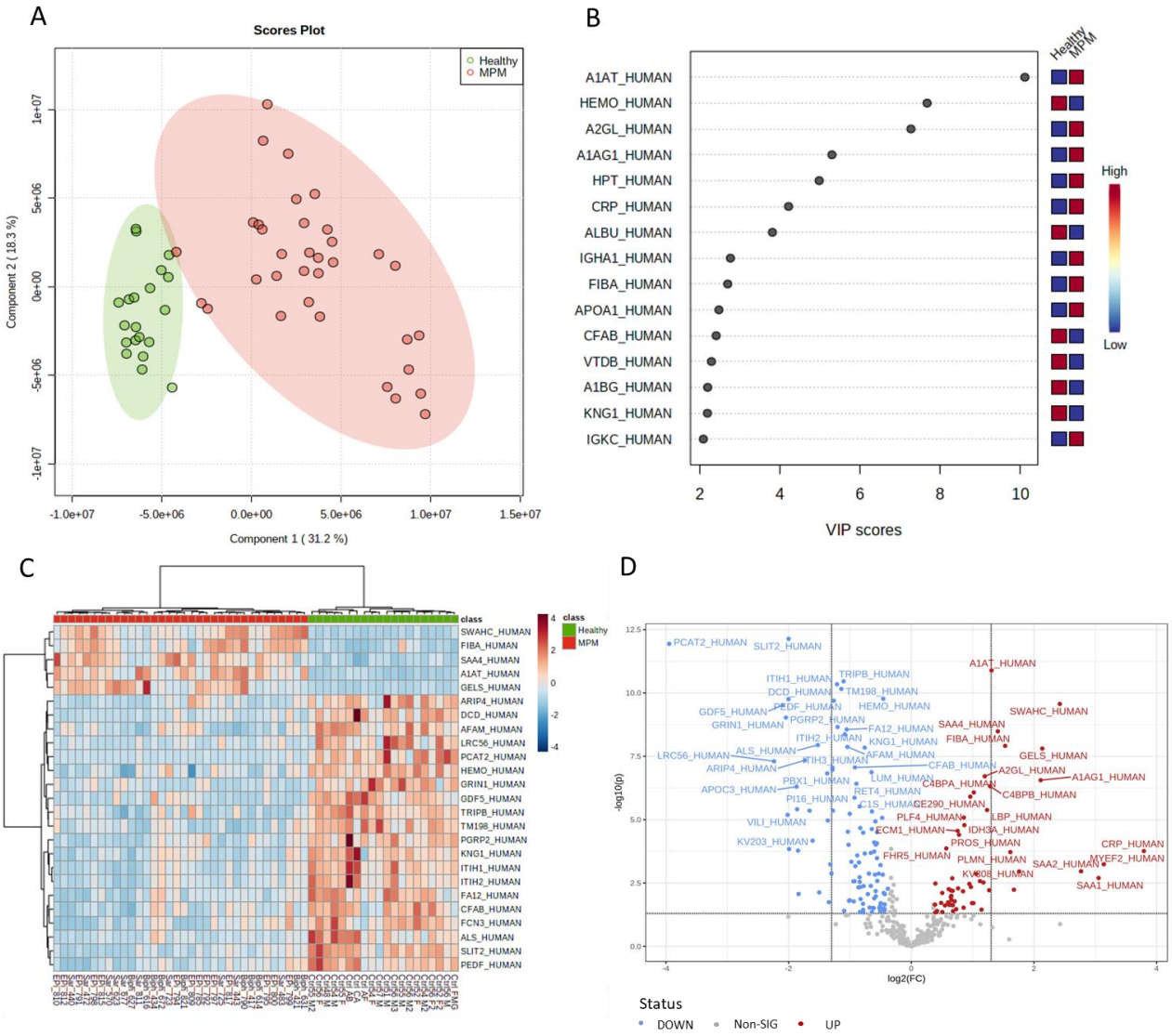

Figure 3.3: proteomic signature associated with MPM disease in serum. (A) Partial least square discriminant analysis (PLS-DA) of MPM patients (red dots) and healthy subjects (green dots), the two groups are well separated. (B) Variable importance in projection (VIP) score plot of the top 15 proteins that differed in MPM patients vs healthy controls. Colored boxes indicate the most predictive or discriminative features in each group (red, high; blue, low). (C) Hierarchical heat map of quantified proteins (MPM patients in red and healthy subjects in green). (D) Volcano plot of modulated serum proteins in MPM: a total of 123 proteins were modulated in MPM patients compared to healthy subjects ((p-value < 0.05 and fold change > 1.3).

Next, we performed a univariate analysis of quantified proteins using the relative abundance of the proteins quantified in all the samples. The volcano plot highlighted the presence of several modulated proteins in MPM patients compared to healthy subjects (**Figure 3.3D**): 58 proteins were

significantly upregulated, while 107 proteins were downregulated (FC > 1.3; p-value ≤ 0.05). In MPM patients, C-reactive protein (13.8-fold), Myelin expression factor 2 (8.8-fold), Gelsolin (4.4-fold), Alpha-1-acid glycoprotein 1 (4.3-fold), Alpha-1 antitrypsin (2.5-fold) serum amyloid A-4 protein (2.4-fold) were up-regulated, while Lysophosphatidylcholine acyltransferase 2 (15-fold), Inter-alpha-trypsin inhibitor heavy chain H1 (2.3-fold), Thyroid receptor-interacting protein 11 (2.1-fold), N-acetylmuramoyl-L-alanine amidase (2.3-fold) were down-regulated. The complete list of modulated proteins is reported in **Supplementary table 3.1**.

The comparison of MPM patients with lung AdC and hyperplasia-affected patients showed a smaller number of modulated proteins respect with the healthy subjects, as reported by the volcano plot and the heat map of log fold changes (**Supplementary figure 3.2)**. 12 and 5 proteins were upregulated and down regulated, respectively, in MPM patients compared to pulmonary hyperplasia-affected patients, while 10 and 22 proteins were up- and down- regulated in MPM compared to AdC patients (FC > 1.3; p-value ≤ 0.05). Interestingly, Inhibitor of growth protein 2 was 2-fold up-regulated in MPM patients compared to both hyperplasia-affected patients and healthy subjects, whereas Thyroxine-binding globulin, complement factor B and Complement component C9 were down-regulated in MPM patients compared to AdC patients and healthy subjects. The modulated proteins with the log (fold change) are reported in **Supplementary figure 3.4.**

3.3.3.2 Circulating Inflammatory and Immune Response proteins are strongly modulated in MPM patients

Ingenuity pathway analysis (IPA) was employed to identify the main pathways and molecular functions associated with modulated proteins in MPM. The differentially expressed proteins of each comparative analysis were analysed. Interestingly, the pathway analysis of the modulated proteins in MPM patients compared to healthy subjects showed a predicted activation of *Acute Phase Response Signaling*, *Coagulation System, Production of Nitric Oxide and Reactive Oxygen Species in Macrophages* and *LPS/IL-1 Mediated Inhibition of RXR Function,* together with a predicted inhibition of *LXR/RXR Activation*, *Complement System, Intrinsic Prothrombin Activation Pathway,* and *IL-8 Signaling* (**Figure 3.4A**). The chord diagram in **Figure 3.4B** reports the top 15 pathways, and their associated proteins, involved in MPM disease.

In contrast, *LXR/RXR Activation* pathway is predicted activated in MPM compared to AdC and the *Coagulation system* is significantly predicted inactivated in MPM compared to Hyperplasia (**Supplementary figure 3.3**). Intriguingly, diseases and disorders analysis identified several proteins

associated with the inflammatory response in MPM compared to healthy subjects (**Figure 3.4C**) such as FA12, PLF4, PEDF, LYAM1, LBP, TBA1C, CRP, PLMN, ADIPO, VCAM1, SAA1, PROS, FINC, ECM1, KNG1, A2AP, BST1, CD14, S10A9, CD44, LYSC, SLIT2, VTNC, GELS, APOE, C163A, FETUA, PGRP2, and LUM, while physiological system development and function bioinformatic elaboration highlighted the involvement of humoral immune response and immune cell trafficking (**Figure 3.4D**).

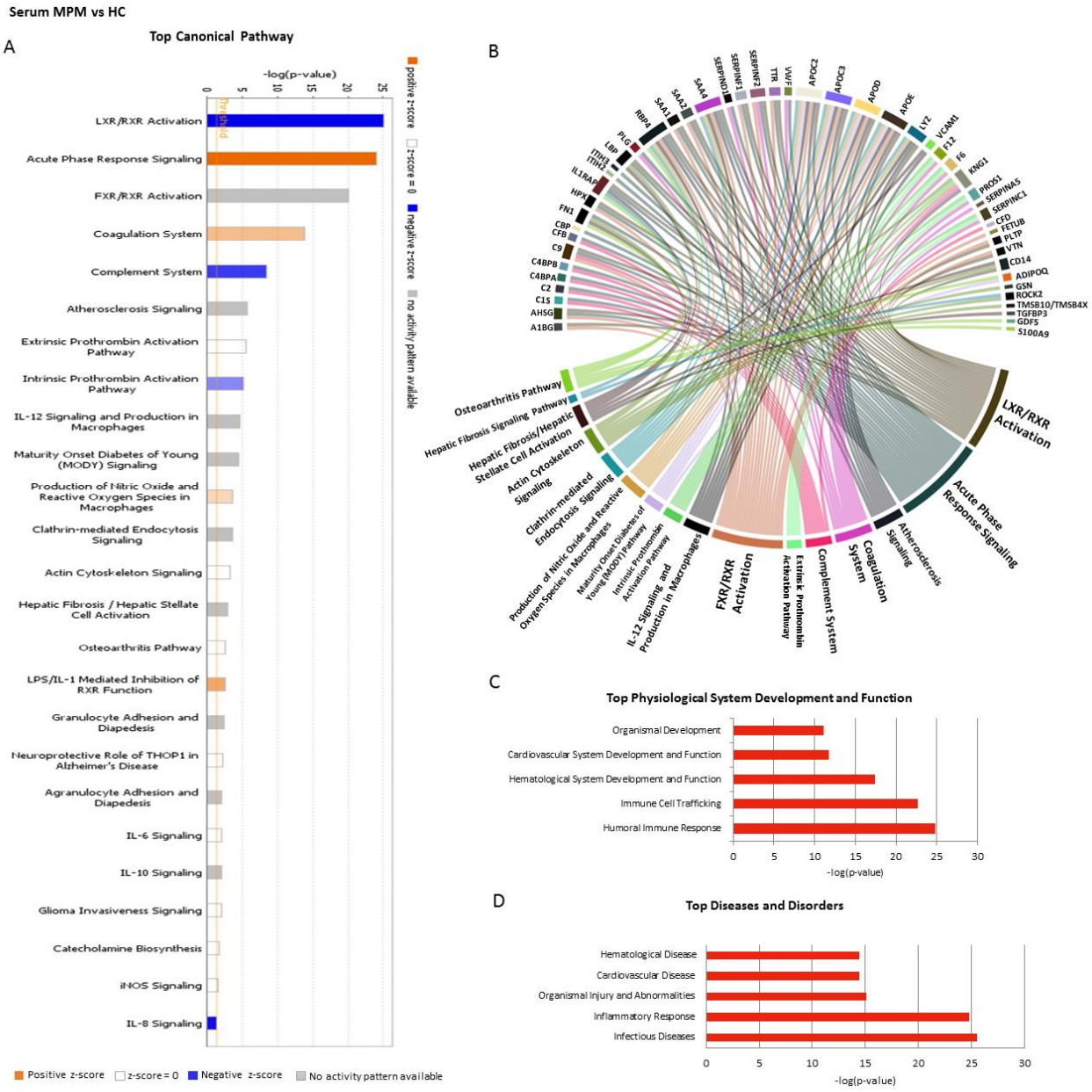

Figure 3.4: *pathways and biological functions in MPM. IPA core analysis of the 123 dysregulated proteins between MPM and healthy control. (A) Significant top 20 canonical pathways that were enriched in the dysregulated proteins. The orange and blue-coloured bars indicate predicted pathway activation, or predicted inhibition, respectively (z-score).*

White bars are those with a z-score at or very close to 0. Grey bars indicate pathways where no prediction can currently be made. (B) Chord diagram showing the most enriched pathway with their differentially expressed proteins. (C) Top molecular and cellular functions (C) and diseases and disorders (D). The higher the -log(p-value) the more involved the functions are.

3.3.3.3 Pleural effusion proteome and biomarkers of MPM

Pleural effusions were analyzed using a label-free quantitation approach in order to investigate the differences between the proteome of MPM, pulmonary hyperplasia and AdC-affected patients.
Three pools obtained from five samples for each group were analyzed. A total of 139 proteins were quantified. Of these proteins, 14 were differentially modulated in MPM compared to hyperplasia-affected patients (10 up- and 4 down- regulated), while 27 were differentially expressed in MPM compared to AdC patients (10 up- and 17 down- regulated), fold change > 1.3 and p-value ≤ 0.05 (**Figure 3.5A-C**). The score plot representation of the PLS-DA shows a separation of MPM patients (red dots) from both lung AdC (violet dots) and from pulmonary hyperplasia (blue dots) (**Figure 3.5B-D**).

3.3.3.4 Acute Phase and Immune Response pathways in MPM pleural effusion

Signalling pathways and disease/functions annotation associated to modulated proteins in pleural effusion were investigated using a bioinformatic approach. **Figure 3.6A** reports canonical pathways enriched in the pleural effusion proteome of MPM patients compared to pulmonary hyperplasia.
The top most enriched canonical pathways included *Haematopoiesis from Pluripotent Stem Cells, Primary Immunodeficiency Signalling, Communication between Innate and Adaptive Immune Cells, Extrinsic and Intrinsic Prothrombin Activation Pathway.*
Diseases and disorders analysis highlighted the involvement of proteins associated to different pathologies such as metabolic, gastrointestinal and endocrine system disorders (**Figure 3.6B**), while physiological system development and function elaboration identified several proteins associated with the Immune Cell Trafficking, Humoral Immune Response, Organismal Functions, Tissue Morphology, Hematological System Development and Function (**Figure 3.6C**).
Bioinformatic analysis performed on the comparison between MPM and AdC indicated that pleural effusion proteins were mainly involved in Acute Phase Response Signaling, Complement System, Coagulation System, Iron homeostasis signaling pathway, LXR/RXR Activation, FXR/RXR Activation, Hepatic Fibrosis / Hepatic Stellate Cell Activation, Systemic Lupus Erythematosus Signaling, GP6 Signaling Pathway and IL-6 Signaling (**Figure 3.6D**).

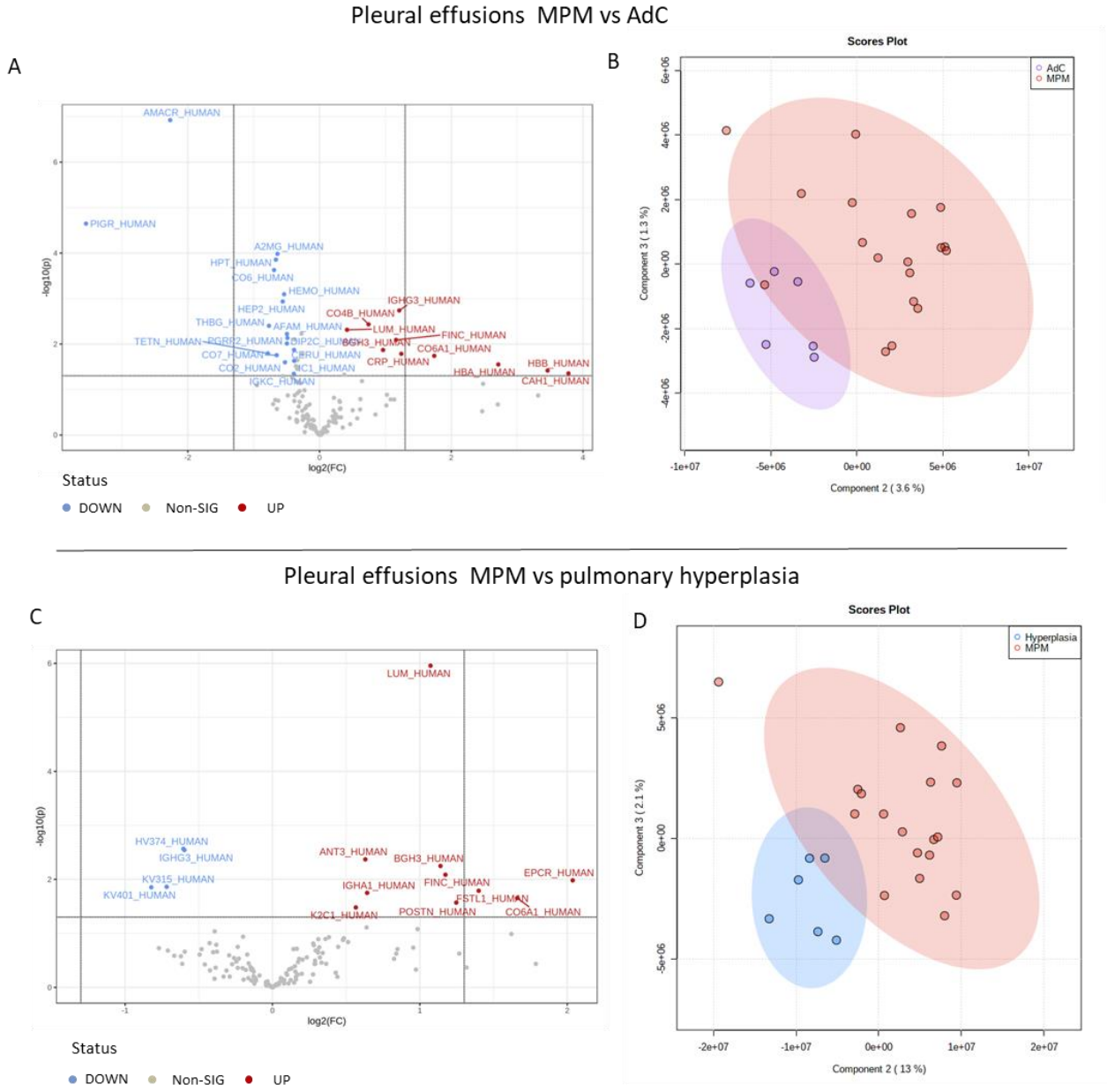

Figure 3.5: *proteomic analysis of pleural effusions. (A-C) Volcano plots of quantified proteins: a total of 27 proteins were modulated in MPM patients compared to lung AdC patients, while 14 proteins were modulated in MPM compared to pulmonary hyperplasia (p-value < 0.05 and fold change > 1.3). (B-D) Partial least square discriminant analysis (PLS-DA) of MPM patients (red dots), AdC patients (violet dots) and pulmonary hyperplasia (blue dots).*

The "Disease and Disorder" elaboration highlighted that several modulated proteins were related to Connective Tissue Disorders, and Inflammatory Response (**Figure 3.6E**). Furthermore, the bioinformatic analysis also showed an involvement of proteins associated with Tissue Morphology,

Organismal Development, Vascular System Development and Function, Visual System Development and Function and Humoral Immune Response (**Figure 3.6F**).

Figure 3.6: *pathways and biological functions in enriched in pleural effusions. (A-B) Canonical Pathway analysis. The orange and blue-coloured bars indicate predicted pathway activation, or predicted inhibition, respectively (z-score). White bars are those with a z-score at or very close to 0. Grey bars indicate pathways where no prediction can currently be made. Top molecular and cellular functions (C) and diseases and disorders (D). The higher the -log(p-value) the more involved the functions are.*

3.3.3.5 Gelsolin and Lumican proteins as biomarkers of MPM

Potential biomarkers identified in the discovery phase were further validated on a larger cohort of patients. Among modulated proteins the following proteins were selected for the validation as biomarker: LUM, FINC, and FIBB for pleural effusion validation assay, while FINC, GELS and VDBP for serum validation assay. Interestingly, GELS resulted significantly overexpressed in serum of MPM compared not only to healthy subjects, but also to lung AdC and pulmonary hyperplasia. Similarly, LUM levels were higher in pleural effusion of MPM patients compared to both lung AdC and pulmonary hyperplasia. While the validation of FINC, FIBB, and VDBP did not confirm the mass spectrometry results, the expression of GELS and LUM in the validation cohort confirmed the potential role of these proteins as novel cancer-derived biomarkers in serum and pleural effusion. The validation cohort for serum GELS included 12 lung AdC, 24 pulmonary hyperplasia, 77 MPM (23 biphasic, 19 sarcomatous, 35 epithelioid) patients and 10 healthy volunteers, while 13 lung AdC, 25 pulmonary hyperplasia and 92 MPM (24 biphasic, 14 sarcomatous, 54 epithelioid) patients were included in the validation study of LUM in pleural effusions. The validation of these two proteins was performed using commercial ELISA kits.

Box plots of both GELS and LUM serum concentrations and relative ROC curves are shown in **Figures 3.7**. The diagnostic power of these putative biomarkers was also evaluated by the ROC curve. Intriguingly, the AUC value for GELS in MPM versus healthy subjects was 1 with 100% specificity and 100% sensitivity. In MPM versus AdC, the AUC value was 0.961 with 91.7% specificity and 93.5% sensitivity, while in MPM compared to pulmonary hyperplasia the AUC value was 0.961 with 83.3% specificity and 97.4% sensitivity. Thus, serum GELS turned out to have a high diagnostic value for discriminating MPM patients from healthy subjects, lung AdC and pulmonary hyperplasia patients (**Figure 3.7A-C-D-E**). Then, we investigated also the discriminative power of LUM in pleural effusion. LUM showed an AUC value of 0.903 with a 100% of sensitivity and 69.2% of specificity in MPM compared to AdC, while it shows an AUC value of 0.786 with a sensitivity of 67.4% and a specificity of 76% in MPM vs pulmonary hyperplasia (**Figure 3.7F-H-I**). These results showed that the discriminative power of GELS in serum is higher than that of LUM in pleural effusion. Another striking result is the direct correlation of the abundance of LUM and GELS with the disease's aggressiveness. In particular, sarcomatous and biphasic MPM displayed higher levels of GELS in serum and LUM in pleural effusions than epithelioid MPM (**Figure 3.7B-C**).

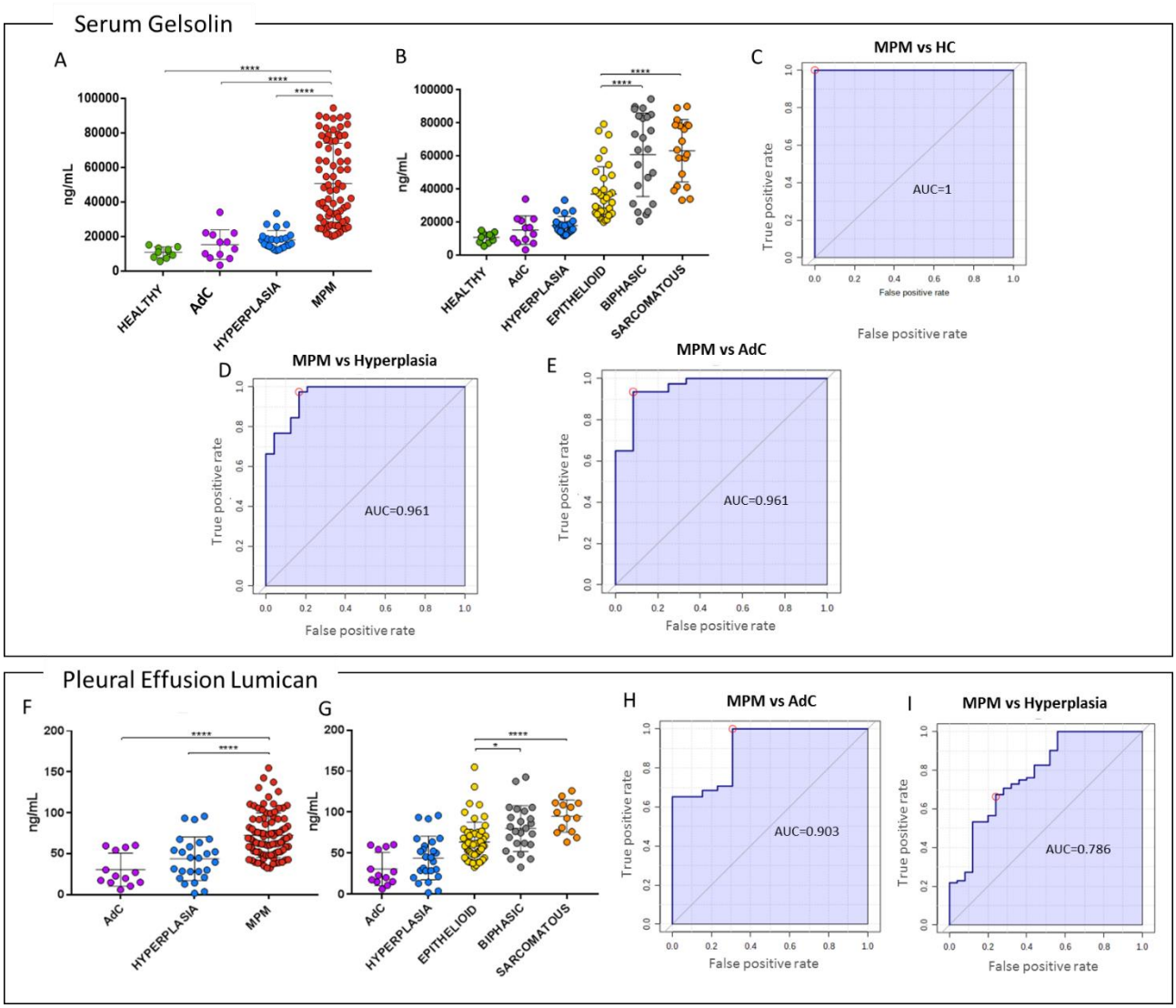

Figure 3.7: *diagnostic power of gelsolin and lumican biomarkers. Boxplots and ROC curves of the two validated biomarkers in serum and pleural effusions using ELISA assay. (A) Serum gelsolin showed significant differences between MPM and the other three groups (AdC, hyperplasia and healthy subjects); gelsolin was also found at higher levels in patients with sarcomatous and biphasic MPM compared to those with epithelioid MPM (B). Discrimination between MPM and healthy subjects with an AUC of 1 (C), MPM and hyperplasia with an AUC of 0.961 (D), and MPM and lung AdC with an AUC of 0.961 (E). Lumican levels in pleural effusion showed significant differences between MPM and both hyperplasia and lung AdC (F). Lumican was also found at higher levels in patients with sarcomatous and biphasic MPM compared to those with epithelioid MPM (G). Discrimination between MPM and lung AdC with an AUC of 0.903 (H), and MPM and hyperplasia with an AUC of 0.786 (I).*

3.3.3.6 *Gelsolin and Lumican proteins as biomarkers of MPM*

Furthermore, GELS and LUM levels were also associated to the prognosis of MPM by performing a survival analysis. The X-tile software was used to identify the optimal cut-off values of high and low GELS/LUM expression groups, and Kaplan-Meier method was used to calculate the survival curve.

Figure 3.8A shows the Kaplan-Meier curve for LUM using 69 ng/mL as cut-off value, while **figure 3.8B** shows a Kaplan-Meier curve for GELS levels using $2.7x10^4$ng/mL as cut-off value. Kaplan–Meier survival curves were significantly different between the two groups (P= 0.041 for LUM and P=0.039 for GELS). The mean survival length for patients with low GELS levels was 24 months, whereas the mean survival length for patients with higher GELS concentrations was significantly reduced at 11 months. Regarding LUM, patients with low abundance of this protein survived on average for 24 months, while patients with higher levels survived on average for 14 months. In both cases, high LUM and GELS levels were significantly associated with poorer survival times, confirming LUM and GELS as markers for poor MPM prognosis.

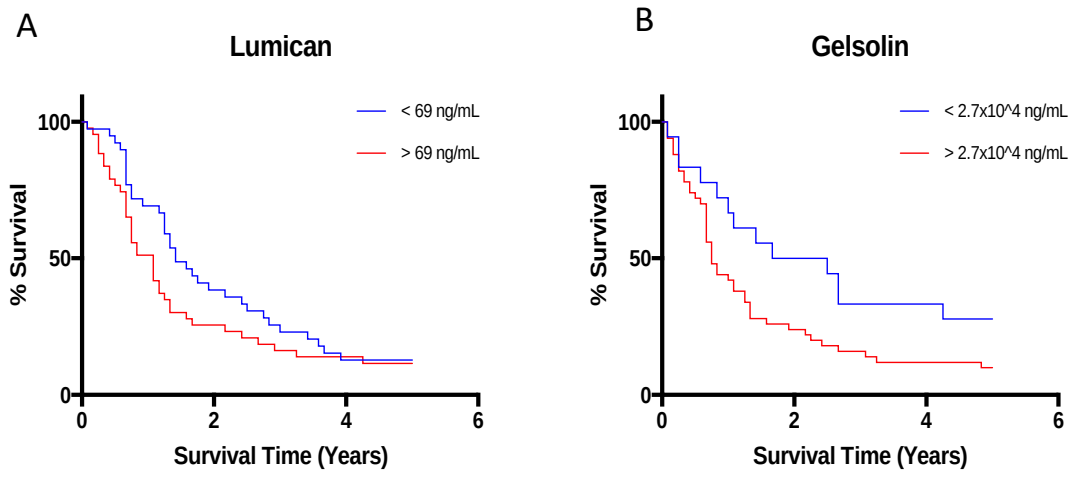

Figure 3.8*: Kaplan–Meier survival graphs for patients with MPM and survival prediction. (A) Kaplan-Meier survival curves for low and high levels of LUM in MPM effusions and (B) for low and high levels of GELS in MPM sera. The mean survival time for the high LUM group and the high GELS group was, respectively, 11 and 14 months compared to 24 months for both the low levels LUM group and the low levels GELS group. These differences were statistically significant (P= 0.041 for LUM and P=0.039 for GELS).*

3.3.4 Discussion

Malignant pleural mesothelioma is a rare and aggressive cancer mainly caused by the exposure to asbestos, with limited treatment options and devastating prognosis. Histologically, MPM is classified into three main different subtypes: epithelioid, sarcomatous, and biphasic, the latter two being the most aggressive. The diagnosis of MPM is often difficult not only because it occurs at advanced stages, but also because the disease presents nonspecific symptoms that don't allow distinguishing

MPM from adenocarcinoma or other benign lung diseases. Since pleural biopsy remains the only standard diagnostic method for MPM, there is a critical need for a specific non-invasive biomarker-based screening test to potentially diagnose mesothelioma at an early stage and thus to improve the overall survival of patients. In the present research we employed an untargeted proteomic discovery approach to identify potential biomarkers that were then validated on a bigger cohort of patients. Two biomarker candidates were confirmed by ELISA, which showed that GELS could be a good serum diagnostic biomarker of MPM, while LUM may be a potential diagnostic biomarker of MPM in pleural effusions. GELS levels were able to distinguish MPM not only from healthy subjects (AUC = 1), but also from AdC and pulmonary hyperplasia reporting an AUC of 0.961 for both groups. In addition, GELS expression increased with cancer aggressiveness: the concentration of GELS was higher in the more aggressive histological subtypes (sarcomatous and biphasic) compared to the epithelioid one. Several studies have reported the association between GELS dysregulation and cancer. GELS is an actin-binding protein expressed both in extracellular fluids and in the cytoplasm of many human cells, where it plays an important role in the morphology and motility of cells[55]. Apart from its role in sequestering actin in extracellular compartments, the extracellular form, called plasma GELS (pGSN), has been implicated in a variety of physiological and pathological processes such as epigenetic processes, signal transduction, transcriptional regulation, apoptosis, modulation of the inflammatory response, and pathogenesis of diseases[56]. Interestingly, the pathway analysis supported the involvement of GELS in the inflammatory response, suggesting a role of GELS in the chronic inflammation that influences and supports tumor growth[57]. Increased Gsn expression was reported in the pulmonary epithelium where researcher shown that it is necessary for the development of pulmonary inflammation and fibrosis[58]. Several studies have revealed the dual roles of GELS as a tumour enhancer or tumour suppressor. The cytoplasmatic content of GELS was found down-regulated in certain types of cancer including glioblastoma, colorectal, bladder, gastric and non-small-cell lung cancers[59–62]. In addition, Wen-Xiang Li et al. showed that an overexpression of GELS reduces the proliferation and invasion of colon cancer cells in vitro[63]. On the contrary, several studies have found that GELS is upregulated in a subset of pancreatic, hepatocellular, and gynaecologic cancers and acts as an oncogene. Increased expression of total plasma GELS has been associated with poor prognosis, poor survival and chemoresistance of patients with ovarian, cervical, and prostate cancer[64–66]. In hepatocellular cancer, GELS may promote cancer progression by regulating epithelial-mesenchymal transition (EMT)[67]. Increased expression of GELS probably facilitates tumor cell motility and enhances its capability and

probability to invade adjacent tissues and metastasis to remote organ sites[68]. Consistent with these findings, our study showed, for the first time, the dysregulation of GELS in the plasma of MPM patients and its correlation with the disease's aggressiveness. Our data suggest that plasma GELS is a promising biomarker for the detection and histological classification of MPM.

The validation of LUM expression in pleural effusions also confirms the potential use of this molecule as MPM biomarkers. Our findings reported an overexpression of lumican in pleural effusion fluid of MPM patients compared to pulmonary hyperplasia and AdC patients with an AUC, respectively, of 0.786 and 0.903. LUM is a secreted member of small leucine rich proteoglycans (SLRP) and it is involved in cellular processes associated with tumorigeneses, such as EMT, cellular proliferation, migration, invasion, and adhesion. In the tumor microenvironment, LUM has been associated with signaling, which can result in either pro-tumorigenic or anti-tumorigenic effects [69]. Its pro-tumorigenic effects are mainly observed in gastric, liver, and bladder cancers, which is associated with poor clinical prognosis [70–72]. Conversely, in melanoma, pancreatic cancer, lung cancer, and breast cancer LUM demonstrates anti-tumorigenic effects, which are associated with better clinical outcomes [73–76]. Cappellesso et al. observed a lower expression of lumican in the lung adenocarcinoma tissue compared to adjacent stromal matrix. In contrast, the pleural effusion fluid had higher levels of LUM which was probably secreted from the stromal fibroblast that were overexpressing LUM. Higher stromal tissue expression of lumican was associated with enhanced invasion, residual tumor, and lower survival [77]. Consistently, our study showed an overexpression of lumican in sarcomatous and biphasic subtypes, which are associated with worse clinical and prognostic outcomes of the cancer than epithelioid one. This suggest that LUM overexpression in pleural effusion fluid may be associated with the worse prognosis and poorer response rate to treatment of sarcomatous and biphasic compared to epithelioid subtype.

Bioinformatics analysis of modulated serum proteins in serum highlighted the involvement of inflammation and immune response in MPM patients. Acute *Phase Response Signaling* and *Coagulation System* were shown to be the main predicted activated pathway in MPM compared to healthy subject with a z-score, respectively, of 1.61 and 0.63. The acute phase response (APR) is a systemic unspecific immune-mediated response that is activated by inflammation, infection, disease and tissue damage due to malignancies, burn injuries or trauma. These stressors may cause the release of mediators including IL-1, IL-6, and TNF-α which stimulate the release of specific circulating proteins [78] such as C-reactive protein, serum amyloid A, ceruloplasmin, haptoglobin, α1-acid glycoprotein, and α-2-macroglobulin [79]. Different studies reported high levels of CRP in

blood and pleural effusion of patients with malignant mesothelioma (MM) compared to healthy subjects [80,81] and its association with short survival [82]. In our study, CRP level was significantly higher in the MPM group (13,8-fold) than in the healthy groups and this is probably correlated with the inflammatory disorders that characterize the development and progression of MPM. In addition, our data reported an increase of other proteins that are positively correlated with APR such as SAA1 (8.3-fold), SAA2 (6.8-fold), SAA4 (2.6-fold), HPT (2.2-fold) and A1AG1 (4,3-FOLD). Proteins known to be negatively correlated with the APR [83], including serum albumin and fetuin A were decreased in MPM patients.

As reported previously, our findings also showed a predicted activation of coagulation system in MPM patients compared to healthy subjects. In this regard, cancer patients show several coagulation abnormalities that are correlated with an increased tendency of these patients to both thrombotic and hemorrhagic complications. It has been reported that patients with cancer may have an increased of blood procoagulant factors or a direct release of procoagulant tissue factor by the cancer cells. Tissue factor complexes with coagulation factors activate the coagulation cascade A [84,85]. Excessive release of procoagulant factors will lead to thromboembolic events (TEE). Derrick Nguyen et al. showed that the rate of TEE in mesothelioma patients is much higher (of 27.7%) than in healthy subjects [86]. In our study, high serum levels of fibrinogen alpha chain (FIBA) were detected in MPM patients compared to healthy subjects. On the other hand, there were no significant intergroup differences in blood coagulation factor levels among patients with MPM and patients with hyperplasia.

Moreover, canonical pathway analysis revealed a predicted inactivation of the complement system in MPM compared to healthy. The complement is a constituent of innate immunity, and its functions include clearance of pathogens and maintenance of homeostasis. The complement proteins are mostly released by the liver, but both tumor and stromal cells also have the ability to produce complement factors. Thus, their presence in the tumor microenvironment is both due to the contribution of the systemic compartment and the local production by the cancer cells. Recent studies revealed that depending on the cancer type, complement can have a pro or anti-tumoral role in the context of certain cancers [87]. In order to clarify the current role of complement in human cancers, Margot Revel et al. classified human cancers in four different groups based on the prognostic impact of the overexpression of complement genes. Interestingly, mesothelioma belongs to the protective complement groups: high expression of complement genes is associated with a favourable prognosis. In our study, the inactivation of complement system is associated to a

downregulation of complement C1s subcomponent, complement C2, complement C9, complement factor B and complement factor D, while C4b-binding protein alpha chain and beta chain, that act as inhibitors of the complement system, are significantly up-regulated in serum of MPM compared to healthy subjects. Our results thus support the involvement of circulating complement proteins, suggesting a more general inhibition of the pathway in the disease.

The top pathways involved in MPM also included the Liver X Receptors/Retinoid X Receptors (LXR/RXR) activation pathway, which has important functions in cholesterol transport, lipid and glucose metabolism, and in the modulation of inflammatory responses, which are essential biological processes for tumour development. In our study, LXR/RXR activation pathway was inhibited in MPM compared to healthy subjects and activated in MPM compared to hyperplasia. There are accumulating evidences that support the involvement of LXRs in a variety of malignancies. A down-regulation of the LXR activation pathway was also observed in prostate cancer [88] and in colon adenocarcinoma [89]. Surprisingly, the involvement of this pathway in malignant pleural mesothelioma has not been previously reported. Twenty-two proteins involved in LXR/RxR activation pathway were differentially expressed. Among the most differentially expressed proteins in this pathway were Lipopolysaccharide-binding protein (LBP), SAA1, SAA2, SAA4, Phospholipid transfer protein (PLTP), hemopexin (HEMO), Interleukin-1 receptor accessory protein (IL1RAP).

Finally, the modulation of several serum proteins involved in the activation of the Production of Nitric Oxide and Reactive Oxygen Species in Macrophages pathway were identified. Intriguingly, this modulation may be associated to the accumulation of reactive oxygen species (ROS) and reactive nitrogen species (RNS), which are produced by alveolar macrophages during asbestos-mediated carcinogenesis. In mesothelioma there is approximately 20 to 40 years latency between the time of asbestos exposure and clinical diagnosis, during which chronic asbestos exposure creates a persistent inflammatory response. The activation of inflammatory cell, especially alveolar macrophages, implicates the release of ROS and RNS. Macrophage-mediated ROS/RNS production and inflammatory cytokines release can potentially lead to MPM carcinogenesis pathway [90].

In conclusion, in the present research two new potential biomarkers, namely gelsolin and lumican, for the diagnosis of MPM were proposed. These proteins were identified using an untargeted proteomic approach performed on serum and pleural effusion samples, and then validated through ELISA using an extended cohort of patients including lung adenocarcinoma patients, healthy subjects and patients with lung hyperplasia.

ELISA validation confirmed the potential use of lumican and gelsolin as MPM biomarkers in pleural effusion and serum, respectively. In addition, their abundance was also higher in patients with sarcomatous and biphasic subtypes compared to the epithelioid one, suggesting their potential use for the detection of the histological subtype. Moreover, high lumican and gelsolin levels were significantly associated with poorer survival times, confirming LUM and GELS as markers for poor MPM prognosis. Finally, the bioinformatic analysis highlighted the overall involvement of proteins related to the inflammatory and immune response in MPM patients.

3.3.5 Supplementary Data

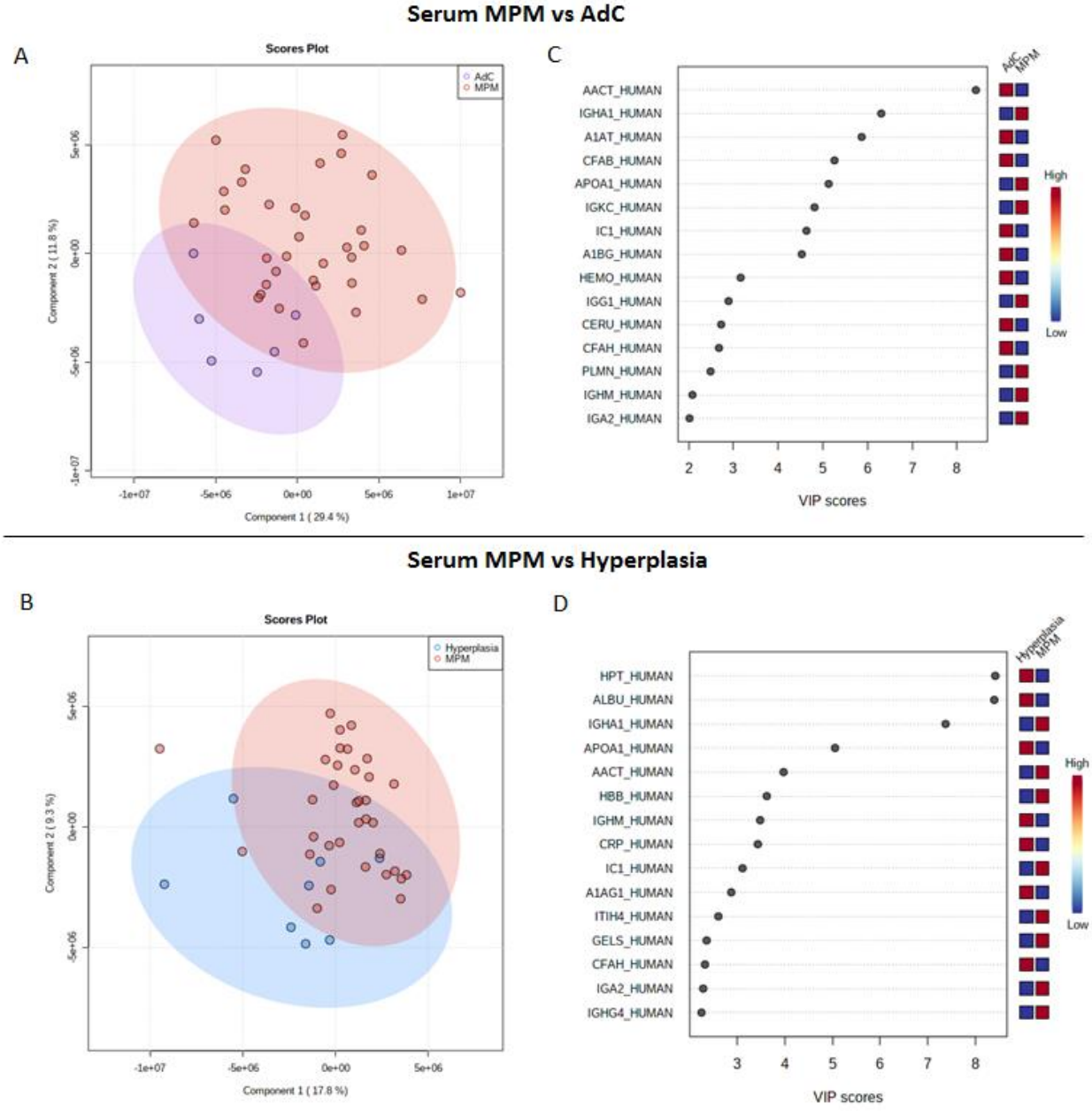

Supplementary figure 3.1: *multivariate analysis. Partial least square discriminant analysis (PLS-DA) of MPM patients (red dots) vs AdC patients (violet dots) (A) and MPM patients vs Hyperplasia patients (blue dots) (B). The three groups are well separated. Variable Importance in Projection (VIP) score plot of the top 15 proteins that differed in MPM patients vs AdC patients (C) and in MPM patients vs Hyperplasia patients (D). Colored boxes indicate the most predictive or discriminative features in each group (red, high; blue, low).*

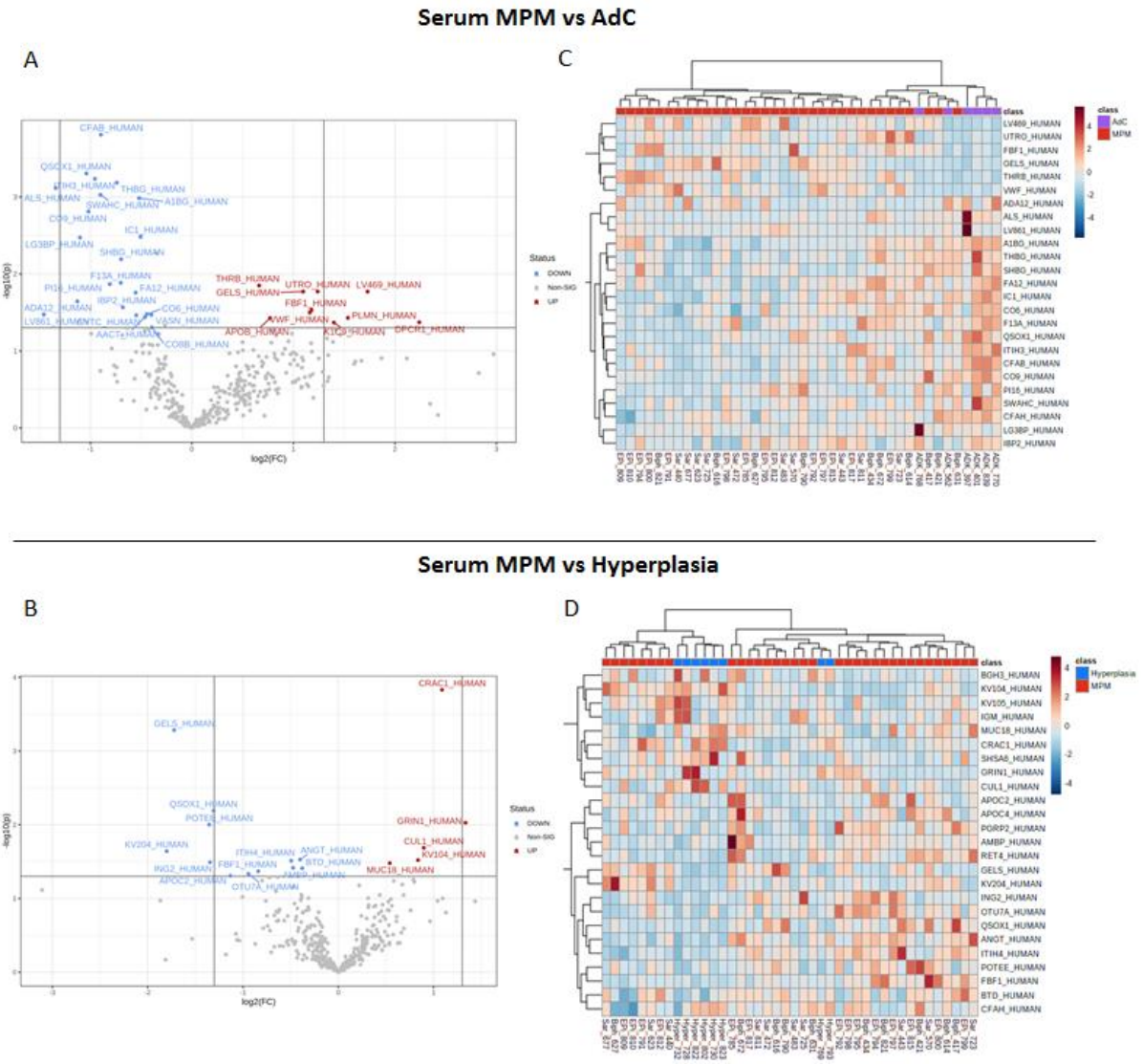

Supplementary figure 3.2: *modulated serum proteins in malignant pleural mesothelioma (MPM). Volcano plots of quantified proteins: a total of 22 proteins were modulated in MPM patients compared to lung adenocarcinoma (AdC) patients (A) and 11 proteins were significantly regulated in MPM compared to hyperplasia-affected patients (B) (p-value < 0.05 and fold change > 1.3). Hierarchical heat maps of quantified proteins with MPM patients in red, AdC patients in violet (C) and hyperplasia-affected patients in blue (D).*

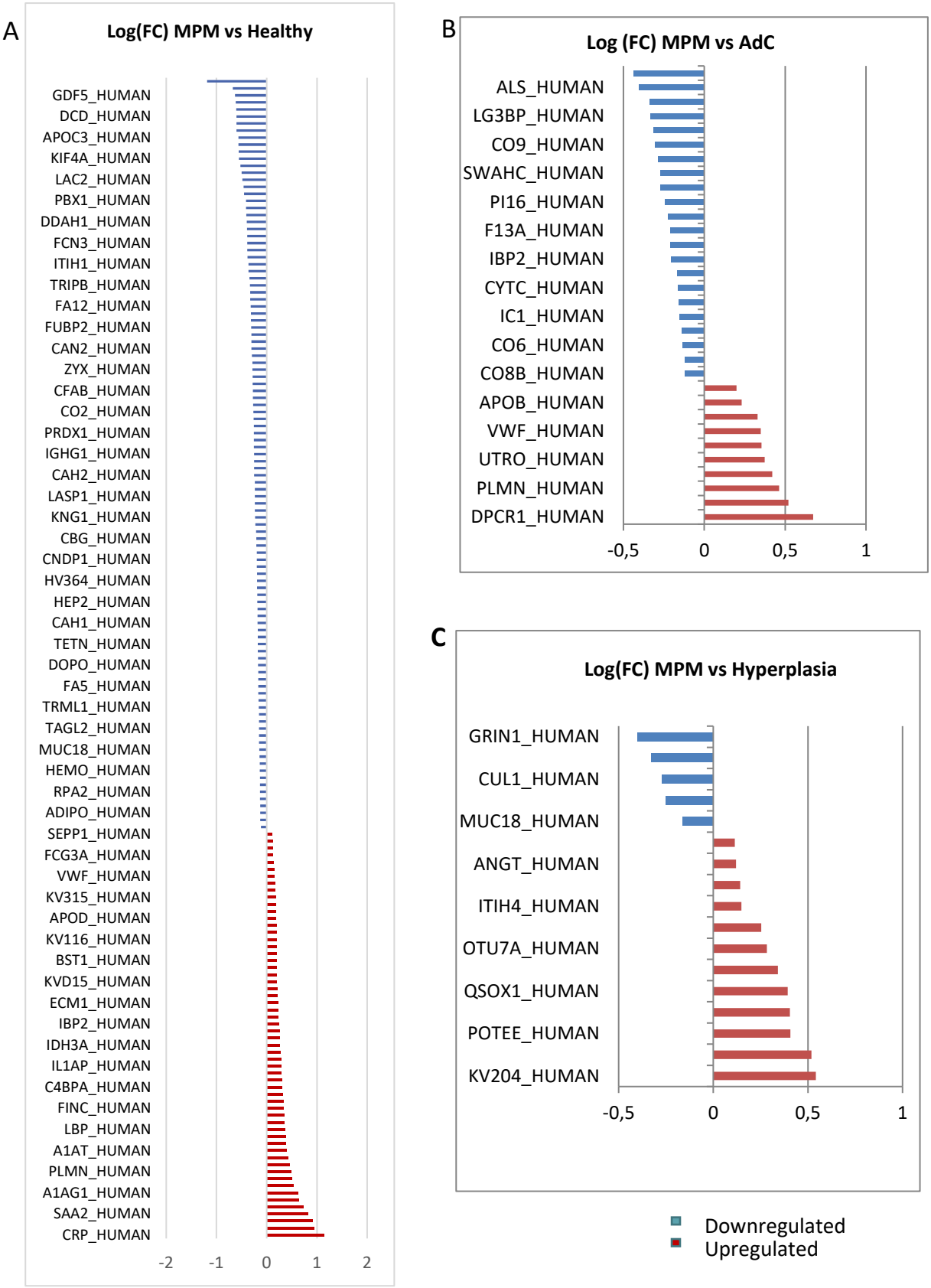

Figure 3.3: *upregulated and downregulated proteins in MPM patients compared to healthy subjects(A); Upregulated and downregulated proteins in MPM patients compared to AdC (B); (C) Upregulated and downregulated proteins in MPM patients compared to pulmonary hyperplasia affected patients (C) (Log FC ≥0.176 or Log FC ≤0.13; p-value<0.05).*

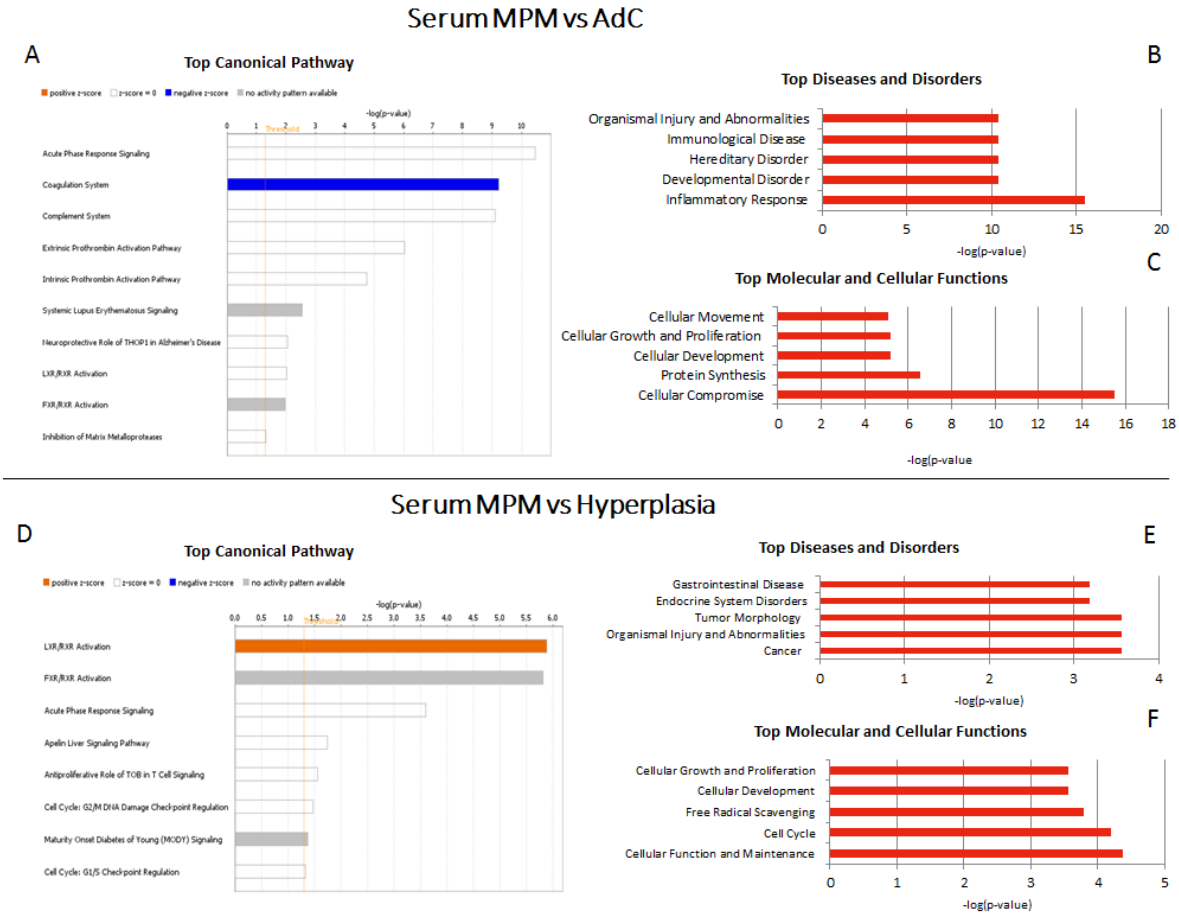

Supplementary figure 3.4: *IPA core analysis. The significant top canonical pathways that were enriched in the serum dysregulated proteins of MPM vs AdC patient group (A) and of MPM vs hyperplasia-affected patient group. The orange and blue-coloured bars indicate predicted pathway activation, or predicted inhibition, respectively (z-score). White bars are those with a z-score at or very close to 0. Grey bars indicate pathways where no prediction can currently be made. B. A chord diagram showing the most enriched pathway with their differentially expressed proteins. C.*

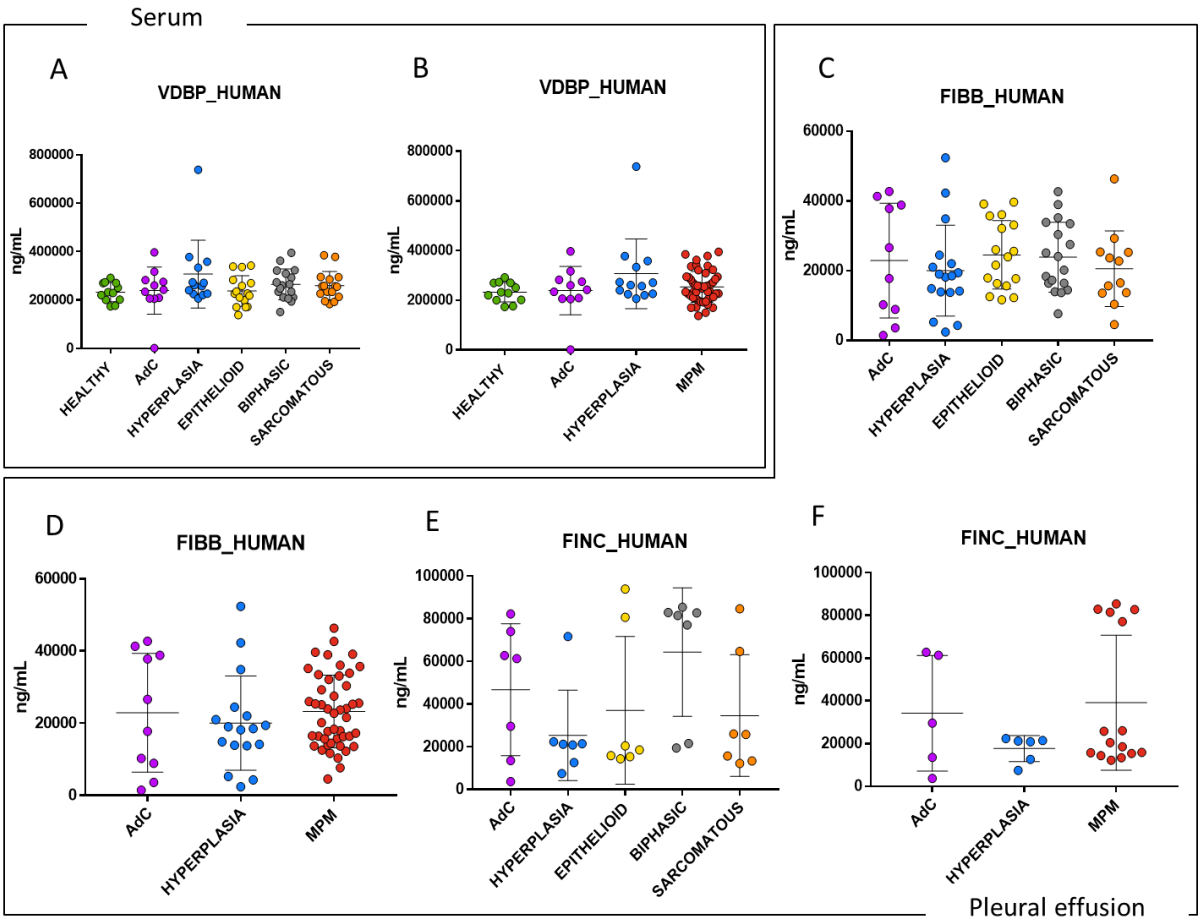

Supplementary Figure 3.5: *Boxplot of biomarkers validated with ELISA assay that did not confirm mass spectrometry results: VDBP (A,B), FINC (C,D), FIBB (E,F).*

Supplementary table 3.1: *list of modulated proteins*

Protein name	Fold change	p-value
CRP_HUMAN	13,85025152	0,00017
MYEF2_HUMAN	8,806223664	0,00057
SAA1_HUMAN	8,300649805	0,002
SAA2_HUMAN	6,807573326	0,00109
SWAHC_HUMAN	5,35812367	2,72E-10
GELS_HUMAN	4,392904989	1,56E-08
A1AG1_HUMAN	4,314601926	2,77E-07
KV308_HUMAN	3,380908317	0,00111
HV5X1_HUMAN	3,188365975	0,00582
PLMN_HUMAN	3,062302959	0,00019
FIBA_HUMAN	2,887455743	1,22E-08
SAA4_HUMAN	2,658701274	3,27E-09
A1AT_HUMAN	2,474351002	1,29E-11
C4BPB_HUMAN	2,435492614	4,81E-07
LV310_HUMAN	2,409926482	0,00609

LBP_HUMAN	2,353117491	4,16E-06
A2GL_HUMAN	2,293805408	1,94E-07
HPT_HUMAN	2,257274447	0,00301
FINC_HUMAN	2,210705714	0,03564
ING2_HUMAN	2,172421718	0,00266
S10A9_HUMAN	2,081783083	0,00138
C4BPA_HUMAN	2,025804842	8,41E-07
LV657_HUMAN	2,016044041	0,01972
LV321_HUMAN	1,984841667	0,01963
IL1AP_HUMAN	1,960405849	0,00452
CE290_HUMAN	1,946576224	1,24E-06
K2C6B_HUMAN	1,927426116	0,00341
IDH3A_HUMAN	1,820117161	1,64E-05
PLF4_HUMAN	1,810375987	8,25E-06
LV147_HUMAN	1,804685759	0,02974
IBP2_HUMAN	1,793450501	0,00669
PROS_HUMAN	1,713452476	3,95E-05
NUP93_HUMAN	1,69576833	0,00514
ECM1_HUMAN	1,687599586	2,77E-05
LV319_HUMAN	1,660406957	0,03405
IGJ_HUMAN	1,631721307	0,01663
KVD15_HUMAN	1,602823309	0,04053
C163A_HUMAN	1,597303789	0,02388
APOA1_HUMAN	1,595210799	0,00642
BST1_HUMAN	1,587929378	0,00206
ICAM2_HUMAN	1,578703401	0,02315
KV133_HUMAN	1,573022796	0,01484
KV116_HUMAN	1,571745444	0,01009
PAP1L_HUMAN	1,564867987	0,00623
KV303_HUMAN	1,562408869	0,01135
APOD_HUMAN	1,536128919	0,02322
NEBL_HUMAN	1,53211904	0,02098
APOE_HUMAN	1,526196873	0,00553
KV315_HUMAN	1,515031594	0,01841
FHR5_HUMAN	1,484376326	0,00014
HV551_HUMAN	1,4618971	0,02433
VWF_HUMAN	1,41843466	0,04431
LYSC_HUMAN	1,418109833	0,00782
FCGBP_HUMAN	1,400049292	0,01932
FCG3A_HUMAN	1,336863253	0,04014
C1RL_HUMAN	1,312170666	0,00332
FUBP1_HUMAN	1,312112996	0,04569
SEPP1_HUMAN	1,307959361	0,02256
CD14_HUMAN	0,766554326	0,00531
ANT3_HUMAN	0,741063971	0,00869

ADIPO_HUMAN	0,74029546	0,02209
TYB4_HUMAN	0,739525327	0,03432
FUBP3_HUMAN	0,737146065	0,03947
RPA2_HUMAN	0,733348806	0,0321
LYAM1_HUMAN	0,73278503	0,00792
IBP3_HUMAN	0,732025194	0,00775
HEMO_HUMAN	0,728079533	1,69E-10
VASN_HUMAN	0,72350724	0,00148
BTD_HUMAN	0,719423037	8,44E-06
MUC18_HUMAN	0,708254232	0,02
CO9_HUMAN	0,706478473	0,01977
TTHY_HUMAN	0,705681605	0,00062
TAGL2_HUMAN	0,703910725	0,04103
LV469_HUMAN	0,702416646	0,02603
LV861_HUMAN	0,70055172	0,02824
TRML1_HUMAN	0,697575286	0,03144
KV224_HUMAN	0,691062663	0,00134
UBR1_HUMAN	0,68042522	0,00261
FA5_HUMAN	0,679216466	3,10E-05
HV307_HUMAN	0,67857786	0,00033
A1BG_HUMAN	0,676992749	8,53E-05
DOPO_HUMAN	0,669552785	0,01057
KAIN_HUMAN	0,669170297	9,70E-05
PHLD_HUMAN	0,668228734	0,00658
TETN_HUMAN	0,665766758	1,17E-05
FETUA_HUMAN	0,665610428	1,18E-05
VTNC_HUMAN	0,662553859	0,00149
CAH1_HUMAN	0,657899212	0,01268
THBG_HUMAN	0,657706407	7,92E-05
HGFA_HUMAN	0,657222633	0,00018
HEP2_HUMAN	0,653110526	0,03066
ALBU_HUMAN	0,648838749	0,03049
CHLE_HUMAN	0,640763752	4,73E-06
HV364_HUMAN	0,640716819	0,0437
AKAP9_HUMAN	0,63965227	2,35E-05
LUM_HUMAN	0,637376712	1,34E-07
CNDP1_HUMAN	0,632768568	0,00021
IPSP_HUMAN	0,632175377	0,00414
SH3L3_HUMAN	0,623515552	0,02932
CBG_HUMAN	0,619291128	0,00135
DSRAD_HUMAN	0,611939619	0,00869
POTEE_HUMAN	0,590910707	0,00022
KNG1_HUMAN	0,590318594	1,44E-08
BGH3_HUMAN	0,583276552	0,00417
PLTP_HUMAN	0,58137846	0,04599

LASP1_HUMAN	0,58005579	3,25E-05
HV226_HUMAN	0,579837055	0,03584
SRRM1_HUMAN	0,578972118	0,02091
CAH2_HUMAN	0,563494075	0,01354
SRGN_HUMAN	0,56173496	0,00455
ROCK2_HUMAN	0,561424587	2,13E-05
IGHG1_HUMAN	0,559605021	0,04421
APOC2_HUMAN	0,557970344	0,00285
C1S_HUMAN	0,55776526	3,01E-06
PRDX1_HUMAN	0,557403282	0,00187
KV305_HUMAN	0,553067434	0,00049
CFAD_HUMAN	0,54995706	0,00466
CO2_HUMAN	0,54247832	0,00026
RET4_HUMAN	0,537514884	3,82E-07
FETUB_HUMAN	0,531150585	0,00068
CFAB_HUMAN	0,528353258	8,67E-08
PI16_HUMAN	0,526093278	1,36E-06
FXL22_HUMAN	0,525201261	0,00268
ZYX_HUMAN	0,521729968	0,01685
VCAM1_HUMAN	0,519221963	0,00272
CD44_HUMAN	0,507828252	0,00046
CAN2_HUMAN	0,49847632	5,86E-06
TBA1C_HUMAN	0,498428436	0,01505
PCDC1_HUMAN	0,494316104	0,01594
FUBP2_HUMAN	0,491880752	9,78E-05
OTU7A_HUMAN	0,487777111	2,99E-05
AFAM_HUMAN	0,485357894	1,35E-08
FA12_HUMAN	0,481222484	2,76E-09
ITIH2_HUMAN	0,471625275	4,29E-09
AIPL1_HUMAN	0,467984798	0,03943
TRIPB_HUMAN	0,465027228	3,46E-11
TM198_HUMAN	0,453364099	6,93E-11
PGRP2_HUMAN	0,434662432	2,20E-09
ITIH1_HUMAN	0,431583159	4,53E-11
PEDF_HUMAN	0,416045879	2,01E-10
A2AP_HUMAN	0,412165657	4,40E-06
FCN3_HUMAN	0,410262648	8,79E-08
ITIH3_HUMAN	0,409773674	1,08E-07
IQCC_HUMAN	0,405298871	0,00134
DDAH1_HUMAN	0,400250824	0,00058
SHBG_HUMAN	0,393635685	0,01804
SYF1_HUMAN	0,389104927	1,08E-05
PBX1_HUMAN	0,386433445	1,50E-07
CENP1_HUMAN	0,353155535	0,00741
ALS_HUMAN	0,347584944	1,14E-08

LAC2_HUMAN	0,327626393	6,78E-05
FCN2_HUMAN	0,316440737	4,42E-06
ARIP4_HUMAN	0,300134779	4,55E-08
KIF4A_HUMAN	0,279607061	0,00857
CNNM4_HUMAN	0,277863138	0,00017
GP1BA_HUMAN	0,274986399	3,87E-06
APOC3_HUMAN	0,2732603	4,99E-07
KV203_HUMAN	0,251189769	0,00014
SLIT2_HUMAN	0,249758846	7,30E-13
DCD_HUMAN	0,249429276	1,75E-10
VILI_HUMAN	0,247046148	6,48E-06
GRIN1_HUMAN	0,242307949	9,38E-10
GDF5_HUMAN	0,233523271	3,04E-10
LRC56_HUMAN	0,211883054	4,95E-08
PCAT2_HUMAN	0,064749288	1,15E-12

3.4 PBMCs Proteomic Alterations in Cancer Patients with COVID-19

3.4.1 Background and rationale

Pathophysiological changes and metabolic disorders, which establish a subclinical syndrome of "homeostatic frailty," are common among the elderly population and are associated with greater susceptibility to infection [91] and cancer [92]. These changes determine immune-senescence and an imbalance between activation and resolution mechanisms of inflammation [e.g., high levels of inflammatory mediators such as interleukin IL-6, tumor necrosis factor-α, and C-reactive protein], that is an immunological scenario typical of the elderly [93]. As a consequence, failure to resolve the inflammatory process undermines metabolic and immune pathways [91]. Of relevance, an overwhelming inflammation is observed in COVID-19 patients, possibly resulting from loss of homeostatic robustness, which is clinically mitigated by treatment with either monoclonal antibody against IL-6 (tocilizumab) [94] and/or with corticosteroids [95]. Aging and various comorbidities associated with COVID-19 severity (i.e., diabetes, cancer, hypertension, cardiovascular disease) are characterized by inflammatory and metabolic disorders, which may represent indicators of homeostatic frailty and immune dysregulation [96]. However, the net immunometabolic contribution that these comorbidities add to COVID-19 disease is still poorly understood. Cancer progression is known to establish immunosuppression, often associated with production of anti-inflammatory and immunosuppressive cytokines (i.e., IL-10, TGFβ) by alternative/M2 activated myeloid cells, macrophages in particular [97,98]. Noteworthy, cancer and COVID-19 exploit distinct patterns of macrophage activation, that promote disease progression in their most severe forms [96]. While an alternative/M2 activation state of macrophages is generally associated with cancer progression, the most severe forms of COVID-19 are supported by a macrophage activation syndrome, which generates a storm of M1-related cytokines [96]. Of relevance, the functional M1 vs M2 dichotomy of macrophage polarization mutually modulates in response to polarizing cytokines Th1 (i.e., IFNγ) and Th2 (i.e., IL-4) respectively [97], whose imbalance is associated with higher COVID-19 risk mortality [99]. Since the M1 and M2 polarization states are metabolically distinct [100] and cancel each other out [101], we investigated whether the immunosuppressive and anti-inflammatory action of growing tumors could interfere with the immune metabolic scenario induced by SARS-CoV-2 infection. In this study we have undertaken proteomic approaches to elucidate the mechanism and immunological pathways that intersect SARS-CoV-2 infection and

cancer and to identify new therapeutic strategies for the management of patients with cancer affected by COVID-19.

3.4.2 Materials and Methods

3.4.2.1 Patients

The analyses were carried out on blood samples collected at the Humanitas Research Hospital. Thirty-four patients were enrolled in the present study: 19 SARS-CoV-2 patients (12 males and 7 females, mean age 67.44 years, ± 15.74), 8 SARS-CoV-2/Cancer Patients (SARS-CoV2/CP) (5 males and 3 females, mean age 72.25 years, ± 12.91), 7 cancer patients (CP) (5 males and 2 females, mean age 70.47 years, ± 13.72). Out of the 19 SARS-CoV-2 patients enrolled, 10 were severe and 9 were mild, while among SARS-CoV-2/CP patients, 2 were severe and 6 mild. Seven healthy subjects were selected as control population. Demographical characteristics of patients involved in the study are reported in **table 3.5**.

Table 3.5: *demographical characteristics of patients infected with SARS-CoV-2, with and without oncological disease, involved in the study.*

Characteristic		**SARS-CoV-2**	**SARS-CoV-2/CP**	**CP**	**HC**
Gender					
	Male	12	5	5	4
	Female	7	3	2	3
Age Mean					
	Mean ± SD	67.44 ± 15.74	72.25 ± 12.91	70.47 ± 13.72	66.8 ± 10.13

3.4.2.2 PBMCs Isolation

Blood samples were collected in heparin and diluted 1:2 with PBS 1X. Subsequently, peripheral blood mononuclear cells (PBMCs) were obtained using a density gradient stratification. Briefly, diluted whole blood samples was carefully layered onto Histopaque-1077 Ficoll (Sigma- Aldrich) and then centrifuged at 1,800 rpm for 30 min at room temperature without brake. After centrifugation, PBMCs were collected at the interface and transferred into a new collection tube.

3.4.2.3 Proteomic analysis

PBMCs were washed twice with PBS 1X by centrifugation at 1,200 rpm for 5 min and lysed using 200 µL of RIPA buffer (50mM Tris HCl pH 7.2, 0.05%SDS) and sonication. Cold acetone was used for protein precipitation followed by resuspension in 100 mM NH4HCO3. Protein content was measured by Bradford Protein Assay (Sigma-Aldrich, St. Louis, MO). Fifty micrograms (50 µg) of proteins were subjected to reduction with DTT, alkylation with iodoacetamide and tryptic digestion at 37 ◦C overnight. Peptides were then desalted on the Discovery® DSC-18 solid phase extraction (SPE) 96-well plate (25 mg/well) (Sigma-Aldrich Inc., St. Louis, MO, USA) and then analyzed by label-free LC–MS/MS, performed by using a micro-LC system (Eksigent Technologies, Dublin, USA) interfaced with a 5600+ TripleTOF mass spectrometer (Sciex, Concord, Canada). Samples were subjected first to data-dependent acquisition (DDA) analysis to generate the MS spectral library, and then to cyclic data independent analysis (DIA) using one technical replicates of each sample. The MS data were acquired and processed as reported from paragraph 3.3.2.4 to 3.3.2.6.

3.4.2.4 Statistical Analysis

Statistical analysis of proteomic data was performed using MarkerView software (Sciex, Concord, Canada) and MetaboAnalyst software (www.metaboanalyst.org). Proteins were considered up- and downregulated using fold change >1.3 or <0.769 and p-value < 0.05. The significance of the difference was also analyzed by non-parametric tests using the Prism v.8 software package (GraphPad Software, San Diego, CA, USA), with statistical significance taken at $p < 0.05$. Bioinformatics analysis of proteomic data was performed using Ingenuity Pathways Analysis (IPA) software (Qiagen, Redwood City, CA, USA).

3.4.3 Results and Discussion

To elucidate the mutual influence between SARS-CoV-2 infection and cancer, we analyzed the global proteome profile of PBMCs samples collected from healthy subjects (n = 7), CP (n = 7), SARS-CoV-2 (n = 19) and SARS-CoV-2/CP (n = 8), with mild or severe symptoms. A total of 869 proteins were quantified in all PBMCs samples. 264 proteins were differentially expressed in the comparison between SARS-CoV-2/CP and CP (**Fig. 3.9a and suppl. Table 3.2**), while 20 proteins were differentially expressed in SARS-CoV-2/CP vs SARS-CoV-2 patients (fold change > 1.3, p-value ≤0.05) (**Fig. 3.9e and suppl. Table 3.3**).

PLS-DA models were built for both the comparisons and they showed a good separation between the two groups of patients (**Fig. 3.9b and g**). The variable importance measured in PLS-DA were reported in figures 1c and h, which list the top 15 important features identified by PLS-DA analysis. The color boxes indicate the relative concentrations of the corresponding proteins in each group under study. The proteomic clustering results are showed in the form of heat maps (**Fig. 3.9d and i**). The figures report the top 25 regulated proteins (t-test) of the two comparisons.

Canonical pathway analysis was used to identify the main pathways associated with SARS-CoV-2 infection in oncological patients (**Figure 3.9e and l**). EIF2 signaling resulted the most significant modulated pathway, predicted inactivated, in SARS-CoV-2/CP vs CP (**Figure 3.9e**). This inactivation could be related to the first host defense mechanism against viral infection. In fact, double strand RNAs and viral proteins accumulations induce a cellular stress and lead to the activation of two eIF2α kinases, PERK and PRK [102,103]. As result, the phosphorylation of eIF2α induces a global inhibition of host translational machinery which does not affect virus replication, but rather favor viral protein production. This could explain the decreased concentration of non-phosphorylated IF2A (fold-change 0.55) in SARS-CoV-2/cancer patients compared to cancer patients (**Fig. 3.10a**). Noteworthy, the eIF2α kinase PERK mediates proteasomal degradation of p53 independently of translational control [104], suggesting that SARS-CoV-2 infection may in perspective favor the onset of DNA damage, increasing the susceptibility to oncological diseases.

The mechanism used by SARS-CoV-2 to avoid the suppression of viral mRNA translation and to ensure continuous viral protein production is not clear yet [105]. In our study, 31 modulated proteins were associated to the EIF2 signaling pathway, of which IF2A, ACTB, HNRNPA1, RPL15, RPL23, RPL23A, RPL26L1, RPL29, RPL3, RPL30, RPL31, RPL34, RPL4, RPL8, RPS21, RPS4X, RPS5, RPS6, RPS9, RPL19, RPL32, RPL27, RPS17, RPS20 were down-regulated, while IF2A, EIF3D, HSPA5, RPL24, RPL27A, and RPS3 were up-regulated (**Suppl. Table 3.2**).

Moreover, a significant decrease in ribosomal protein L26 like 1 (RPL26L1) level was associated with disease severity (**Fig. 3.10b**). RPL26L1 was identified by affinity proteomics analysis in the interactome between host proteins and both Zika virus [106] and SARS-CoV-2 virus [107], while GRB2 was reported as cellular target of SARS-CoV-2 encoded microRNAs [108].

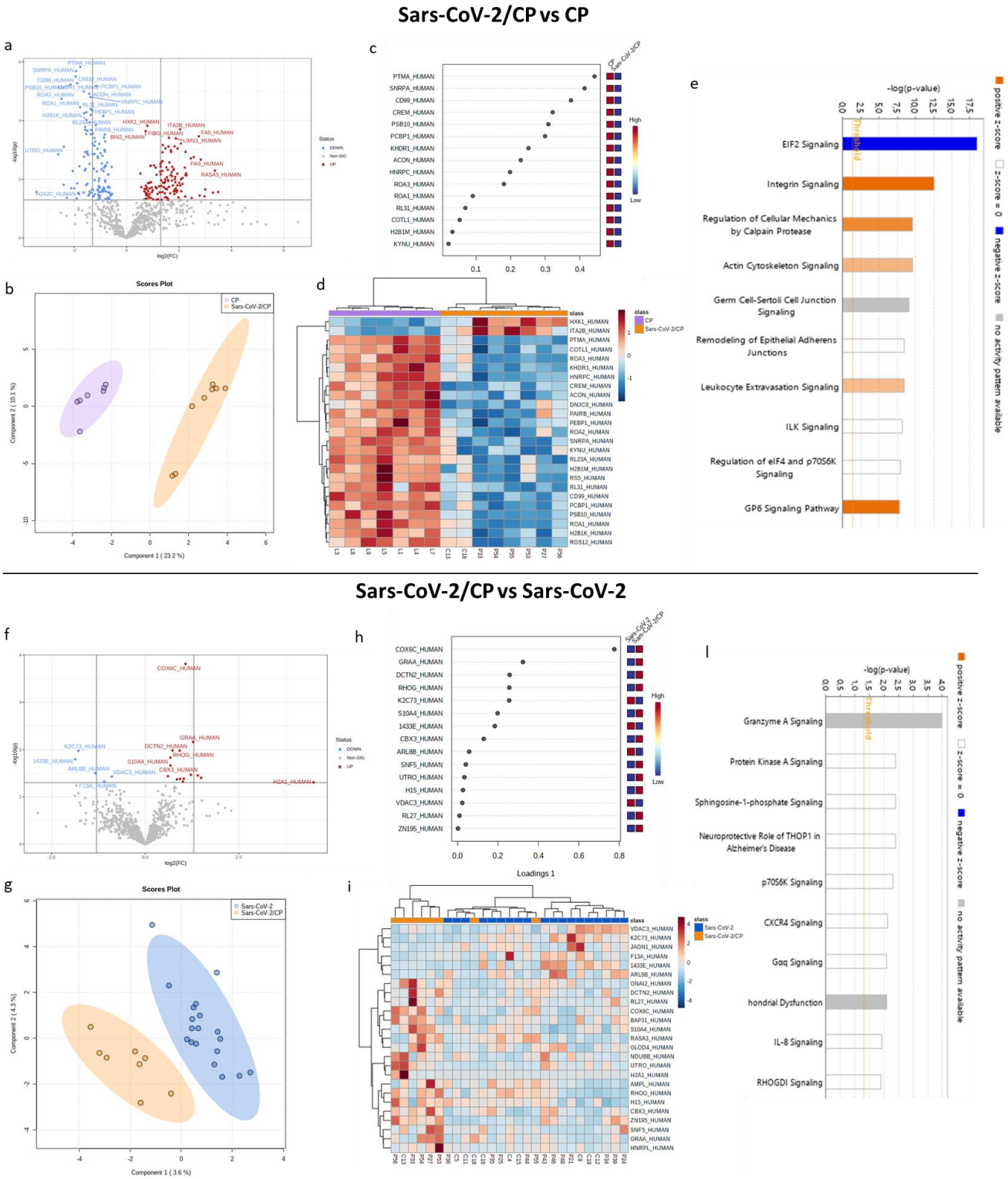

Figure 3.9: *proteomic characterization of PBMCs. Comparison of cancer patients with and without COVID-19: (a) volcano plot reporting the modulation of 264 proteins (FC > 1.3 and p-value < 0.05); (b) partial least square discriminant analysis of the PBMCs proteomic profiles showing the presence of two separate groups of patients and the most important discriminating variables for each group (c). Colored boxes indicate the most predictive or discriminative features in each group (red, high; blue, low). (d)The hierarchical heat maps of quantified proteins, highlighting the two clusters of samples, with cancer COVID-19 patients in orange and cancer patients in purple. e) Bar-plot presenting the top canonical pathway analysis of significantly altered PBMCs proteins regulated in the comparison SARS-Cov-2/cancer and CP. Panels (f) to (l) report the volcano plot, the heatmap, partial least square analysis and canonical pathway analysis in SARS-CoV-2/CP versus SARS-CoV-2 patients.*

Pathway analysis also revealed a predicted alteration of the Integrin Signaling and the Leucocyte Extravasation Signaling pathway in the comparison of *SARS-CoV-2/CP vs CP* (**Fig. 3.9e**), suggesting a dominant influence of SARS-CoV-2 infection on this inflammatory trait [109–111]. Among proteins involved in Integrin Signaling pathway (**Figure 3.10c-e**), our data show reduced levels of both beta (β)-actin (ACTB), required for embryonic development and cell recruitment [112] and Ras-related C3 botulinum toxin substrate 2 (RAC2), whose activation was linked to infantile-onset combined immunodeficiency and susceptibility to viral infections [113].

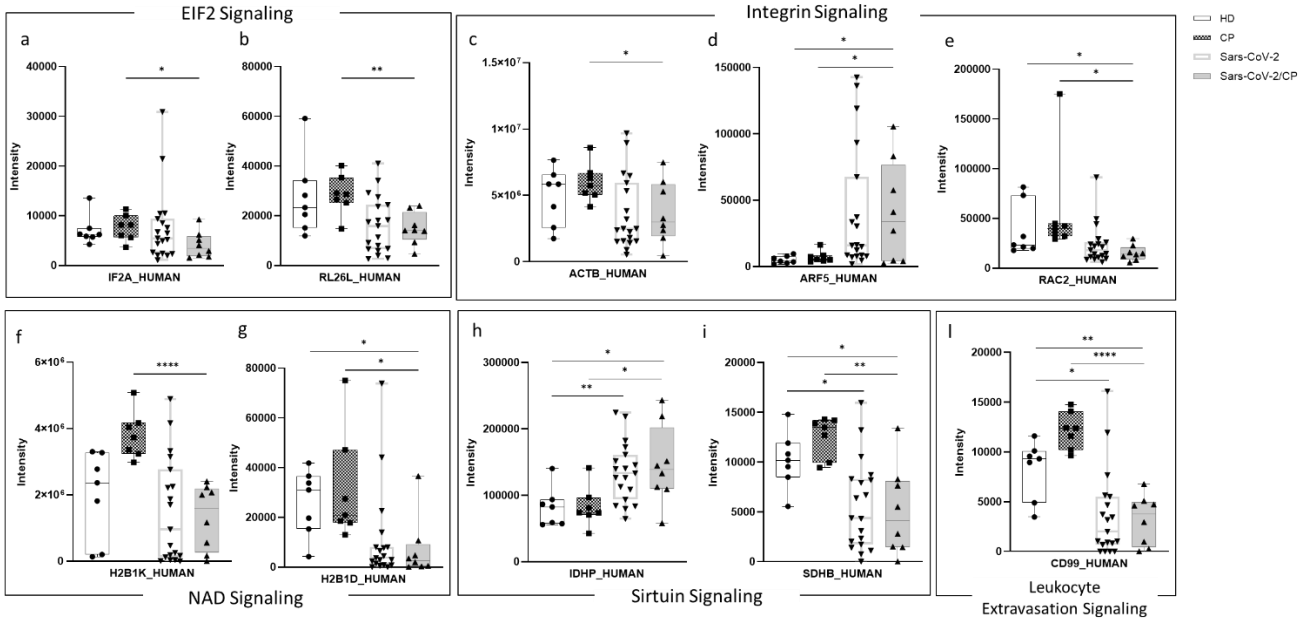

Figure 3.10: *box-plot plot of proteins involved in the main modulated pathways in cancer patients with COVID-19. Integrin Signaling pathway: Actin (a), ADP-ribosylation factor 5 (b), Ras-related C3 botulinum toxin substrate 2 (c); EIF2 Signaling: Growth factor receptor-bound protein 2 (d), 60S ribosomal protein L26-like 1 (e); NAD Signaling: Histone H2B type 1-K, H2B K (f), Histone H2B type 1-D (g); Sirtuin Signaling: Isocitrate dehydrogenase [NADP], mitochondrial (h), Succinate dehydrogenase [ubiquinone] iron-sulfur subunit, mitochondrial (i); Leucocyte extravagation signaling: CD99 antigen (j). (* p-value < 0.05; ** p-value < 0.01; *** p-value < 0.001; **** p-value < 0.0001).*

RAC2 is a plasma membrane-associated small GTPase belonging to the Rho family, together with RAC1 and RAC3 [114]. While RAC1 and RAC2 share a redundant role in later stages of T-cell development, RAC1 has been reported to be down-regulated in COVID-19 patients with mild symptoms compared to healthy subject [115]. Interestingly, activating mutation of RAC2 causes infantile-onset combined immunodeficiency and susceptibility to viral infections [113]. In contrast, increased levels of ADP-ribosylation factor 5 (ARF5) were observed in SARS-CoV-2/CP, as compared to CP (**Figure 3.10d**). ARF5 is a member of the human ARF gene family, which is involved in cell proliferation, motility and differentiation by regulating cellular traffic as well as cancer cell survival,

migration and invasion [116]. Noteworthy, NAD-dependent ADP-ribosylation is emerging as an important regulator of innate immunity, through modulation of IFN type I and II activity, that is targeted by some viruses to counteract host antiviral mechanisms [117,118]. In SARS-CoV-2/CP the expression of ARF5 resulted 7.9-fold higher, as compared to CP, while in contrast ACTB expression resulted 1.6-fold down-regulated (**Fig. 3.10c, d**). We then compared the canonical pathways' significance (-log[p-value]) and prediction (z-score) obtained from all the proteomic-bioinformatic analysis to investigate the main pathways responsible of the immunometabolic changes describing the mutual influence between SARS-CoV-2 and cancer. (**Fig. 3.11**)

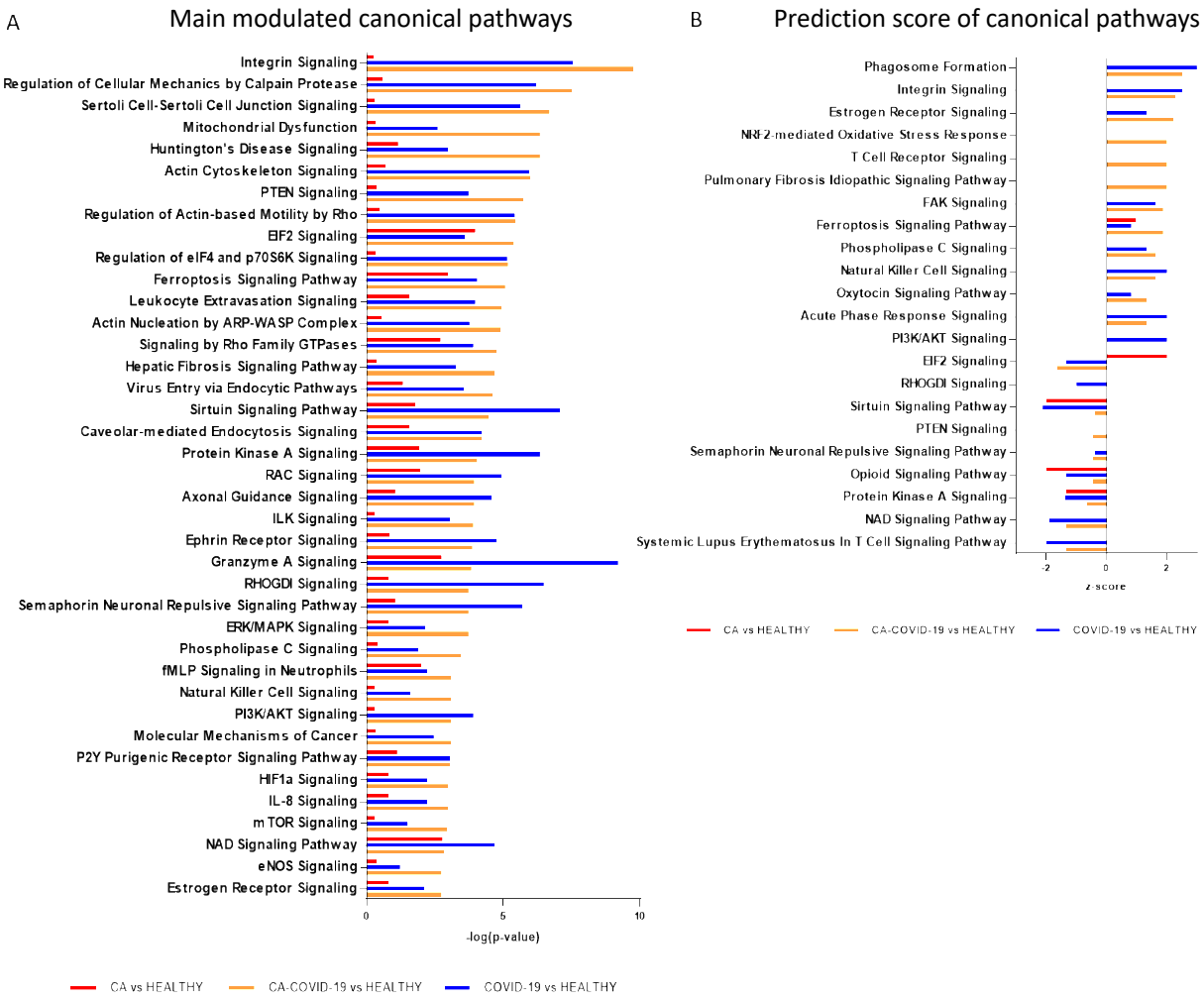

Figure 3.11: *canonical pathway analysis. (a) Bar-plot presenting the main modulated canonical pathways (-log(p-value)) related to PBMCs proteins in SARS-CoV-2/CP (yellow bar), SARS-CoV-2 (blue bar) and CP (red bar) compared to healthy subjects and their prediction score (b). Positive z-score indicates a predicted activation, while negative z-score indicates a predicted inhibition*

Interestingly, the analysis reported a reduced modulation of NAD Signaling and Sirtuin Signaling Pathway in SARS-CoV-2/CP compared to SARS-CoV-2, suggesting a regulatory action of cancer over the influence of SARS-CoV-2 on NAD metabolism (**Fig. 3.11**). It has been postulated that cancer may enhance NAMPT/NAD^+, promoting anti-inflammatory effect against COVID-19 inflammation[96]. . Sirtuin-1 (SIRT1), a NAD-dependent protein deacetylase, plays regulatory roles in different cellular processes such as chromatin structure, gene transcription, metabolism, circadian rhythm, and inflammation [119]. In response to microbial moieties or inflammatory cytokines (i.e., IFNγ) cells increase NAMPT expression and the consequent NAD-dependent activation of SIRT1 deacetylase, thus limiting inflammation and restoring tissue homeostasis [120]. Our data indicate that the predicted inactivation of Sirtuin Signaling pathway can be also related to EIF2a signaling inactivation, whose alteration may result in slower post-stress translation recovery. In this regard, Ghosh et al. [121] demonstrated that SIRT1 regulates EIF2a phosphorylation through the interaction with two mediators of its dephosphorylation, GADD34 and CReP, suggesting a role for SIRT1 in maintaining the steady-state level of phospho-eIF2a.

Intriguingly, the analysis also reported a predicted activation of Estrogen Receptors Signaling (ERs) in both SARS-CoV-2/CP (z-score=2.23) and SARS-CoV-2 patients (z-score=1.34) compared to healthy (Fig. 3b) Different studies have already supported that estrogen and ERs may be related to SARS-CoV-2 infection [122].

Researchers have shown that ERs have a function in regulating cells and pathways in the innate and adaptive immune systems [123]. Both estrogen and ERs contribute to the activation and proliferation of T-lymphocytes and lead to high expression of IFNγ [124]. Interestingly, experimental studies in male and female mice infected with SARS-CoV2 showed that ovariectomy or treatment with estrogen receptor antagonist in female mice increased death rate, which indicates estrogen receptors play a protective effect in mice infected with SARS-CoV-2 [125]. On the other hand, the phosphatidyl-inositol-3-kinase (PI3K)/AKT signaling pathway is significantly over-expressed in SARS-CoV-2 patients compared to healthy. The PI3K/AKT signaling pathway regulates different aspects of cell survival such as protein synthesis, apoptosis inhibition, and cell proliferation. In recent years the link between this cellular pathway and blood clot generation has been reported in several studies. Recently, Pelzl et al. studied the activation status of platelets and PI3/AKT signaling in COVID-19 patients [126]. Interestingly, the results of this study showed that PI3K/AKT phosphorylation is significantly associated with platelet activation in severe COVID-19 patients suggesting that the

inhibition of PI3K/AKT phosphorylation could be a promising strategy to prevent onset of thrombosis in patients with severe COVID-19. Moreover, our data showed a more significance modulation of HIF1α Signaling in SARS-CoV-2/CP vs healthy than SARS-CoV-2 vs healthy. COVID-19 can induce hypoxemia and an overexpression of hypoxia-inducible factor-1α (HIF-1α)[127] which may be involved in the genesis, angiogenesis, invasion and metastasis of lung cancer[128].

3.4.3.1 Conclusions

Despite cancer patients are generally considered more susceptible to SARS-CoV-2 infection [129], the mechanisms that drive their predisposition towards severe forms of COVID-19 have not been deciphered yet. Since metabolic disorders are associated with homeostatic frailty, that predispose to the onset of infection and cancer [91,92] we have carried out a proteomic analysis to identify immuno-metabolic pathways that intersect SARS-CoV-2 infection and cancer.

The emerging proteomic profile of SARS-CoV-2 and cancer patients show alterations in the modulation of pathways and proteins associated with immunodeficiency, susceptibility to viral infection and inflammatory modulation. The alterations observed in this preliminary analysis suggest also that the NAD pathways may represent a fragile metabolic node in both COVID-19 and cancer patients, which undergoes further deterioration in SARS-CoV-2/cancer patients.

In conclusion, this proteome-profiling study, together with additional data coming from metabolomic, lipidomic and flow cytometric analysis (not presented here), could offer a great opportunity to explore the interdependence between COVID-19 and cancer. The better understanding of the interference mechanisms elicited by viral infections and tumors coexistence may provide not only an overview of the balance of benefits and risks when planning normally routine cancer treatments, but also new therapeutic targets for the treatment of patients with cancer affected by COVID-19.

3.4.4 Supplementary Data

Supplementary Table 3.2: *list of modulated protein in SARS-CoV-2/CP vs CP (FC>1.3, p-value<0.05).*

Protein Name	P-value	Fold Change
RAB7A_HUMAN	0,02704	1,052886239
RASA3_HUMAN	0,00508	1,014559683
S10A9_HUMAN	0,02854	0,991753121
SET_HUMAN	0,02209	0,904025369
RAB6B_HUMAN	0,0384	0,895451389
FAS_HUMAN	0,00214	0,851851911

CATG_HUMAN	0,03601	0,838678828
FA5_HUMAN	0,00034	0,829981102
ITB3_HUMAN	0,00175	0,770982726
ARF5_HUMAN	0,04313	0,748687892
ML12B_HUMAN	0,00194	0,738167018
FIBB_HUMAN	0,00741	0,688902908
GLOD4_HUMAN	0,00629	0,683195557
PDLI1_HUMAN	0,00116	0,67765214
URP2_HUMAN	0,00726	0,67739476
PGH1_HUMAN	0,03844	0,672986946
PRPS3_HUMAN	0,00401	0,669571588
1A11_HUMAN	0,00899	0,643468329
CD177_HUMAN	0,01443	0,643466276
GP1BA_HUMAN	0,0256	0,62854069
MYO1G_HUMAN	0,01003	0,625702249
ITA6_HUMAN	0,0006	0,624676352
CALD1_HUMAN	0,01618	0,616862356
ITA2B_HUMAN	2,00E-04	0,615751204
ELNE_HUMAN	0,04995	0,610951346
TGFB1_HUMAN	0,01319	0,606689322
ELOB_HUMAN	0,04135	0,594004373
GLU2B_HUMAN	0,00089	0,585609028
MMRN1_HUMAN	0,01613	0,584135817
GRP2_HUMAN	0,00644	0,582987371
AMPL_HUMAN	0,02382	0,581222728
ZN195_HUMAN	0,0246	0,577877199
HEM2_HUMAN	0,02737	0,575533384
LIMS1_HUMAN	0,00041	0,566453595
ETFA_HUMAN	0,02039	0,565232165
JAM3_HUMAN	0,0126	0,56160607
HPSE_HUMAN	0,00835	0,558907534
GDIA_HUMAN	0,02487	0,557671606
HSPB1_HUMAN	0,01001	0,555735652
OXSR1_HUMAN	0,02443	0,553415653
SC31A_HUMAN	0,02317	0,550497166
CD36_HUMAN	0,00076	0,55014748
TBA4A_HUMAN	0,03187	0,549847409
COPA_HUMAN	0,00451	0,542516933
UBE2N_HUMAN	0,02597	0,541902151
MX1_HUMAN	0,00484	0,539038466
LSM7_HUMAN	0,01617	0,532211244
ANX11_HUMAN	0,00376	0,524313869
RL24_HUMAN	0,00784	0,522720059
G3P_HUMAN	0,01101	0,522630465
CYFP1_HUMAN	0,0058	0,518314236
CBX3_HUMAN	0,00118	0,511488727
ARPC5_HUMAN	0,00103	0,50832478
ENDD1_HUMAN	0,00723	0,505665826
GPDM_HUMAN	0,02998	0,501948882
PPIB_HUMAN	0,00267	0,492713482
CAVN2_HUMAN	0,01826	0,489624175
FIBG_HUMAN	0,00039	0,4869748
RB27B_HUMAN	0,01815	0,486307909
ILK_HUMAN	0,00077	0,481818281
CAN1_HUMAN	0,0114	0,479045765
CATD_HUMAN	0,04998	0,476877509
ILF3_HUMAN	0,01048	0,475618885
DCTN2_HUMAN	0,00478	0,474542632
RL27A_HUMAN	0,04411	0,471974943

TBB1_HUMAN	0,00853	0,465164667
ALBU_HUMAN	0,022	0,464660147
TFR1_HUMAN	0,02069	0,458757007
ITB1_HUMAN	0,00393	0,457816332
GRAA_HUMAN	0,0408	0,45702265
GELS_HUMAN	0,00089	0,447191763
EIF3D_HUMAN	0,02077	0,44574565
PDC10_HUMAN	0,01202	0,444198772
TYPH_HUMAN	0,00993	0,443226281
CAND2_HUMAN	0,04111	0,442349318
KPCB_HUMAN	0,03015	0,440136701
CXCL7_HUMAN	0,01357	0,432961869
HNRPD_HUMAN	0,01847	0,425179188
TCPG_HUMAN	0,01289	0,416430686
SORCN_HUMAN	0,00068	0,415747485
NDUA4_HUMAN	0,0024	0,413176987
SYUA_HUMAN	0,0012	0,412767235
RS13_HUMAN	0,02716	0,412129502
TLN1_HUMAN	0,00517	0,410085976
AKCL2_HUMAN	0,04962	0,404273961
NDKB_HUMAN	0,01684	0,398639092
IPYR_HUMAN	0,0026	0,398340847
NONO_HUMAN	0,01082	0,397455544
6PGD_HUMAN	0,00678	0,392282036
RAP1B_HUMAN	0,00367	0,391250961
VINC_HUMAN	0,00301	0,3881077
ACTN1_HUMAN	0,0055	0,385947424
PDIA1_HUMAN	0,02824	0,385686132
ECHA_HUMAN	0,02778	0,37944155
CBR1_HUMAN	0,0172	0,375284073
CASP3_HUMAN	0,0481	0,363399085
TPM1_HUMAN	0,03164	0,356024838
ATP5I_HUMAN	0,0198	0,348108745
UGPA_HUMAN	0,04883	0,345629009
GRP78_HUMAN	0,00702	0,344926335
FIBA_HUMAN	0,01993	0,339040714
STOM_HUMAN	0,004	0,335844887
RS3_HUMAN	0,0183	0,334107731
TSP1_HUMAN	0,00334	0,315928539
NASP_HUMAN	0,04861	0,306719832
TCPH_HUMAN	0,02354	0,301723637
ACTZ_HUMAN	0,02739	0,291810238
EF1A3_HUMAN	0,01917	0,289999985
MYL6_HUMAN	0,04347	0,281836339
ALDOA_HUMAN	0,01244	0,279737023
FCERG_HUMAN	0,01265	0,279270606
SRC_HUMAN	0,00343	0,279187969
TPM4_HUMAN	0,00347	0,273306551
NTF2_HUMAN	0,01312	0,266717209
DECR_HUMAN	0,03113	0,265821443
COX6C_HUMAN	0,02059	0,265135794
PGM1_HUMAN	0,0431	0,261871468
HNRPU_HUMAN	0,03701	0,253052051
PLEK_HUMAN	0,01349	0,247475697
IDHP_HUMAN	0,02547	0,247193439
1433Z_HUMAN	0,03581	0,244642484
HXK1_HUMAN	1,50E-04	0,238990503
H4_HUMAN	0,03076	0,233840755
NNTM_HUMAN	0,01903	0,233296864

CISY_HUMAN	0,02185	0,231086102
RSU1_HUMAN	0,04498	0,23095947
ZYX_HUMAN	0,0345	0,225685465
PDIA4_HUMAN	0,01644	0,221157465
ACTN4_HUMAN	0,02903	0,220554264
BIN2_HUMAN	0,00023	0,219930887
TERA_HUMAN	0,02116	0,207769091
F13A_HUMAN	0,04759	0,206664982
GSTO1_HUMAN	0,02546	0,204686532
PDIA3_HUMAN	0,01851	0,168996239
TPM3_HUMAN	0,00635	0,159500865
CAP1_HUMAN	0,03113	-0,165756909
RS6_HUMAN	0,03201	-0,167928839
PLEC_HUMAN	0,00382	-0,170389279
MIC19_HUMAN	0,03626	-0,182737023
RANG_HUMAN	0,03299	-0,184018559
TCPE_HUMAN	0,02832	-0,195509103
TCPD_HUMAN	0,01952	-0,195556638
RL4_HUMAN	0,04552	-0,197294673
MGST3_HUMAN	0,0177	-0,205196036
VIME_HUMAN	0,0477	-0,206712327
LSP1_HUMAN	0,00692	-0,209396447
ACTB_HUMAN	0,04482	-0,210804972
HNRH3_HUMAN	0,00683	-0,211498725
HXK3_HUMAN	0,02755	-0,212672153
HP1B3_HUMAN	0,04175	-0,212898056
SF3B6_HUMAN	0,01845	-0,213519807
EF1A1_HUMAN	0,04533	-0,21633873
PTN6_HUMAN	0,00268	-0,221189224
RL8_HUMAN	0,02574	-0,239299902
ENOG_HUMAN	0,00332	-0,239962712
CALM1_HUMAN	0,00361	-0,241154637
HNRL2_HUMAN	0,04713	-0,241971951
NHRF1_HUMAN	0,01207	-0,244910941
RS4X_HUMAN	0,00051	-0,245446781
AN32A_HUMAN	0,0109	-0,246660495
TALDO_HUMAN	0,00113	-0,247285246
ICAL_HUMAN	0,0003	-0,248531426
DPYL2_HUMAN	0,0036	-0,248550263
SH3L3_HUMAN	0,001	-0,253861171
RS21_HUMAN	0,0214	-0,254902825
HMGA1_HUMAN	0,00407	-0,25899856
RBMX_HUMAN	0,00038	-0,259143562
FYB1_HUMAN	0,01899	-0,263230054
UE2NL_HUMAN	0,00525	-0,264503278
CAZA1_HUMAN	0,02605	-0,266088809
IF2A_HUMAN	0,02538	-0,266274666
ROA2_HUMAN	6,94E-05	-0,26788545
SRP14_HUMAN	0,00159	-0,276051845
NUDC_HUMAN	0,02272	-0,278325971
K2C73_HUMAN	0,02463	-0,280259499
RL26L_HUMAN	0,00288	-0,282960326
SSBP_HUMAN	0,00462	-0,287688171
1433F_HUMAN	0,02697	-0,295670186
HNRPM_HUMAN	0,00129	-0,29856186
AHNK_HUMAN	0,03676	-0,304187772
PSIP1_HUMAN	0,04409	-0,30931089
STX7_HUMAN	0,01888	-0,309413595
LBR_HUMAN	0,00062	-0,312467063

CHM1B_HUMAN	0,04267	-0,313097743
H2B1B_HUMAN	0,00943	-0,3148353
NUCKS_HUMAN	0,01862	-0,31739422
CD14_HUMAN	0,02706	-0,318475597
ENOA_HUMAN	0,01714	-0,318832541
ROA0_HUMAN	0,01158	-0,323450334
PRAF3_HUMAN	0,033	-0,324613682
RL23_HUMAN	0,02216	-0,326108213
TYB10_HUMAN	0,03618	-0,327497741
PA2G4_HUMAN	0,00189	-0,327698773
CPNE1_HUMAN	0,04972	-0,329415766
IGHG3_HUMAN	0,02312	-0,334164556
H1X_HUMAN	0,00091	-0,334208037
SEPT7_HUMAN	0,00171	-0,334622104
RL3_HUMAN	0,0054	-0,341682508
PCBP1_HUMAN	6,61E-06	-0,347916075
PAIRB_HUMAN	1,40E-04	-0,35373383
APEX1_HUMAN	0,00053	-0,360285243
TMA7_HUMAN	0,0325	-0,365384597
RBM39_HUMAN	0,01073	-0,368218303
LEUK_HUMAN	0,00138	-0,36859064
GLRX1_HUMAN	0,00072	-0,369371884
ALDR_HUMAN	0,0004	-0,369831088
LMNA_HUMAN	0,0044	-0,375158254
EVL_HUMAN	0,03798	-0,378555335
CY24B_HUMAN	0,02287	-0,382944407
RBM8A_HUMAN	0,00027	-0,389206925
HMGN4_HUMAN	0,00062	-0,389956747
COTL1_HUMAN	4,55E-05	-0,391923638
SDHB_HUMAN	0,00142	-0,394625753
TES_HUMAN	0,02235	-0,39676227
DNJC8_HUMAN	0,00021	-0,407454588
IF5A1_HUMAN	0,00029	-0,409187864
RL29_HUMAN	0,0282	-0,410084515
PEBP1_HUMAN	6,40E-05	-0,41080161
RL31_HUMAN	4,07E-05	-0,412123169
HNRPC_HUMAN	1,58E-05	-0,413448918
RL23A_HUMAN	1,20E-04	-0,423238528
SEPT2_HUMAN	0,00297	-0,427001906
PRKDC_HUMAN	0,03265	-0,428859973
ACON_HUMAN	1,22E-05	-0,430139719
JAGN1_HUMAN	0,02548	-0,432879555
CD44_HUMAN	0,03608	-0,438391054
SARNP_HUMAN	0,00149	-0,440429696
RL15_HUMAN	0,01403	-0,448072998
DPYL5_HUMAN	0,00022	-0,44883726
H2AX_HUMAN	0,00135	-0,450443898
RL34_HUMAN	0,00115	-0,45230952
H2B1K_HUMAN	9,52E-05	-0,458780797
H2B1M_HUMAN	5,22E-05	-0,461223912
PABP3_HUMAN	0,00029	-0,462659718
CYBP_HUMAN	0,01569	-0,463317701
NUDT5_HUMAN	0,00443	-0,473684381
RGS12_HUMAN	2,10E-04	-0,473692349
RS5_HUMAN	1,60E-04	-0,475221454
CAPG_HUMAN	0,00118	-0,4774619
RBM3_HUMAN	0,00497	-0,479584191
KYNU_HUMAN	5,62E-05	-0,487031508
GIMA4_HUMAN	0,0017	-0,488550068

KHDR1_HUMAN	1,01E-05	-0,490975524
H2B3B_HUMAN	0,02824	-0,491918709
ROA1_HUMAN	3,51E-05	-0,532796076
PTMA_HUMAN	1,78E-06	-0,535862824
CD5_HUMAN	0,00361	-0,540379605
H2B2F_HUMAN	0,03171	-0,548985366
H2B2E_HUMAN	0,02895	-0,556978994
HMGN2_HUMAN	0,01381	-0,566580349
CREM_HUMAN	5,36E-06	-0,567808919
RAC2_HUMAN	0,04407	-0,572843444
SNRPA_HUMAN	2,07E-06	-0,58111308
CD99_HUMAN	3,21E-06	-0,584871572
CYC_HUMAN	0,02039	-0,600883926
RL30_HUMAN	0,00524	-0,617672678
H2B1D_HUMAN	0,01999	-0,637724123
PSB10_HUMAN	6,32E-06	-0,648373968
NFKB1_HUMAN	0,04317	-0,686337875
SPTCS_HUMAN	0,01531	-0,722532328
RS9_HUMAN	0,00078	-0,725168945
ROA3_HUMAN	1,83E-05	-0,750747903
UTRO_HUMAN	0,00141	-0,786560827
H2A2C_HUMAN	0,02713	-1,035164935

Supplementary Table 3.3: *list of modulated proteins in SARS-CoV-2/CP vs SARS-CoV-2*

Protein Name	P-value	Fold Change
COX6C_HUMAN	0,00015	2,435401674
GRAA_HUMAN	0,00688	1,658566627
DCTN2_HUMAN	0,01043	1,894606152
RHOG_HUMAN	0,01052	0,290692187
K2C73_HUMAN	0,01055	1,594499206
S10A4_HUMAN	0,01481	0,2736431
1433E_HUMAN	0,01602	1,598506229
CBX3_HUMAN	0,02163	0,397119987
ARL8B_HUMAN	0,0314	2,331087125
SNF5_HUMAN	0,0341	2,650942551
UTRO_HUMAN	0,03523	1,524168087
H15_HUMAN	0,03653	0,540303543
VDAC3_HUMAN	0,0371	2,816672981
RL27_HUMAN	0,03968	2,046211294
ZN195_HUMAN	0,04112	1,908297563
RASA3_HUMAN	0,04155	1,801245009
GLOD4_HUMAN	0,04263	0,468490396
F13A_HUMAN	0,04712	2,015220337
GNAI2_HUMAN	0,04739	22,62881957
H2A1_HUMAN	0,04928	0,276434847

4 VIRAL INFECTION

4.1 FUNCTIONS AND ROLES OF EXOSOMES IN PATHOGEN INFECTIONS

Exosomes are extracellular vesicles derived from cell endocytosis and released by all kinds of mammalian cells [130]. Vesicle contains a variety of proteins, lipids, mRNAs and miRNAs [131], which are specific to the origin of the exosomes and contribute to cell-cell communication [132]. Consequently, they can reflect the physiological or pathological conditions of tissues and organs. Emerging evidence demonstrates that proteomic analysis of exosomes is of great significance in studying and evaluating the development, diagnosis, treatment, and prognosis of diseases. [133–135] Respect the traditional circulating markers, such as hormones and cytokines, exosomes can remain stable in body fluids for several months at -80 °C without repeated freezing and thawing. Due to the advantages of easy sampling and less trauma, the analysis of exosomes in body fluid specimens is more acceptable than biopsy and histopathology examination [136]. For this reason, there are many potential applications for exosomes to be used as disease-specific biomarkers and targeted therapeutic approaches in clinical studies [137]. The interest in exosomes is consistently growing, with an increasing number of studies focusing on the function and application of exosomes in pathogen infections. In particular, exosomes play a crucial role in pathogen infections accelerating or inhibiting the process of infection [138]. In both cases, exosomes make possible connections between host cells or between pathogens and host cells. As carriers of proteins and RNAs derived from pathogens, exosomes can promote infections by transmitting pathogen-related molecules, participating in the immune escape of pathogens, and inhibiting immune responses by favoring immune cell apoptosis [138]. Although exosomes play an important role in the process of infection by pathogens, they may also participate in the fight against infections by inhibiting pathogen proliferation and transmission and stimulating host immune response.

4.2 PROTEOMICS ANALYSIS OF CIRCULATING EXOSOMES REVEALED THEIR INVOLVEMENT IN SARS-COV-2 INFECTION

4.2.1 Background and Rationale

The novel coronavirus disease (COVID-19), caused by the severe acute respiratory syndrome coronavirus 2 (SARS-CoV-2), was firstly reported in Wuhan, China, in December 2019, and is now responsible for over 6 million deaths worldwide (18TH December 2022) [139]. The clinical presentation of COVID-19 is very heterogeneous [140], ranging from asymptomatic patients to severe respiratory distress syndromes (ARDS), requiring invasive mechanical ventilation [141,142]. Advanced age and presence of certain disorders, including hypertension, diabetes mellitus, chronic obstructive pulmonary disease, cardiovascular diseases, and chronic kidney disease, can be considered as risk factors for the development of severe COVID-19 and poor prognosis [141,143,144]. Even though respiratory failure is the most common clinical presentation, it is also known that COVID-19 patients can rapidly progress to a multiple organ dysfunction syndrome (MODS) [145]. The involvement of different organs and systems, such as liver, kidney, heart, and gastrointestinal, hematological, and nervous system, in severe patients results in lengthening the hospitalization duration and increasing the mortality rate [146].

In spite of the COVID-19 vaccine development success, the SARS-CoV-2 pandemic is still challenging due to slow vaccination globally and fast-evolving mutant strains [147–149]. Furthermore, there is always the risk of future emerging coronaviruses infecting human. Consequently, it is urgent to develop novel therapeutic tool that can broadly target distinct strains of evolving SARS-CoV-2 and future coronaviruses. Although a wide range of distinct therapeutic protocols have been investigated, adequate therapeutic options, together with optimal prevention and early diagnosis, are still needed. Extracellular vesicles (EVs) could represent a useful tool for COVID-19 management. Extracellular vesicles (EVs) are microparticles, including large microvesicles (200–1000 μm), small exosomes (50–200 μm), and newly identified exomeres (<50 μm) [150–152], released from several types of activated cells. EVs, as a carrier for cell-to-cell transfer of biomolecules such as mRNA, microRNA, proteins, receptors, lipids and metabolites play a crucial role in the mechanisms of cell-to-cell communication [153]. They can reprogram the target cells in fate, function, and morphology, resulting in physiological or pathological effects [154,155]. EVs can be transported or accumulate in a variety of biological fluids, such as blood, saliva, urine, pleural fluid, bronchoalveolar lavage fluid (BAL), peritoneal fluid, cerebrospinal fluid, breast milk, amniotic fluid, and so on [156,157].

Exosomes are amongst the best characterized small EVs that likely participate in a variety of physiological and pathobiological functions such as cancer progression [158], transmitting viral infection and immune response activation [159]. It was found that EVs can function as vectors of viral infection by transferring viral components, for example, virus-derived miRNAs and viral proteins from virus-infected cells to healthy cells [160,161]. Studies have shown that during SARS-CoV-2 infection the number of EVs secreted from infected cells increased significantly highlighting an important role of EVs in the pathogenesis of diseases [162]. Proteomics technology has been widely used to characterize and study EVs. [163]. Characterization of exosomal cargo is of significant interest because it can provide information on exosome biogenesis, targeting, and cellular effects and may be a source of novel biomarkers and therapeutic targets.

It was reported that EVs promoted the pathogenesis of diseases such as cancer, neurodegenerative, inflammatory and infectious diseases [164,165]. The interesting interaction between EVs and the virus provides a new perspective on the treatment of COVID-19 [166]. Viral infection may affect the exosomal-loading mechanisms of the host cells, resulting in changes in protein and nucleic acid content. Recent improvements of EVs isolation and characterization protocols [167], offered new opportunities to study their roles both as biomarkers and as mediators of several human diseases. [168]. Here, we investigated —via proteomic analysis— how SARS-CoV-2 infection modulates exosome content, exosomes' involvement in disease progression, and the potential use of plasma exosomes as biomarkers of disease severity.

4.2.2 Materials and Methods

4.2.2.1 Patients

Plasma samples from 17 subjects, admitted to Novara University Hospital for pneumonia and/or respiratory failure from March to April 2020 were collected at the Emergency Department or at COVID-19 wards including the Intensive Care Unit. All the patients had a confirmed diagnosis of SARS-CoV-2 infection by reverse-transcriptase polymerase chain reaction (RT-PCR). We considered critical patients those with respiratory failure admitted to the intensive care unit requiring mechanical ventilation, while non-critical patients all other patients with mild to severe respiratory failure requiring oxygen supplementation but neither invasive nor noninvasive mechanical ventilation. Out of the 17 COVID-19 patients enrolled, 7 were critical and 10 non-critical. Healthy

individuals (n=7) were enrolled as controls. For the validation phase 36 COVID-19 patients, including non-critical (23) and critical (13) subjects, and on 39 non-COVID-19 patients, including 6 critical patients, 8 non-critical patients, 7 healthy subjects and 7 healed COVID-19 subjects were used. The Institutional Review Board (Comitato Etico Interaziendale Novara) approved this study. Clinical characteristics of the patients involved in the study are reported in **table 4.1**, **4.2**.

Table 4.1: *characteristics of the patients included in the discovery study*

Variable	Non-COVID-19 patients	COVID-19 patients		
	Healthy Control (N=7)	Total (N=17)	Non-critical (N=10)	Critical (N=7)
Sex (no.)				
Male	2	8	5	3
Female	5	9	5	4
Age (year)				
Mean ± SD	51.4 ± 4.8	64.3 ± 16.5	68.3 ± 19.7	58.7 ± 8.8
Range	43.0 - 56.0	37.0 - 97.0	37.0 - 97.0	47.0 - 70.0
Time from onset to admission (days)				
Mean ± SD		5.2 ± 5.0	6.2 ± 5.8	3.6 ± 3.5
Range		1.0 - 18	1.0 - 18.0	1.0 - 9.0
Time from admission to severe (days)				
Mean ± SD				3.8 ± 2.9
Range				1.0 - 8.0
Symptoms (n°)				
Fever		8	4	4
Cough		6	5	2
Headache		0	0	0
Fatigue		1	1	0
Dyspnea		3	2	1
Diarrhea		2	1	1
Chest pain		1	1	0
Abdominal pain		1	0	1
Vomiting		1	1	0
Comorbidity (n°)				
Hypertension		4	1	3
Diabetes		6	2	4
Respiratory system		9	6	3
Cardiovascular system		6	3	3
Other endocrine system		2	0	2
Chronic kidney		3	0	3
Digestive system		4	1	3
Oxygen saturation index (%)				
Mean ± SD		93.4 ± 7.1	94.3 ± 4.4	92.1 ± 10.5
Range		71.0 - 99.0	86.0 - 99.0	71.0 - 98.0

Table 4.2: characteristics of the patients included in the validation study

Variables	COVID-19			Non-COVID-19				
	Total (N=36)	Non-Critical (N=23)	Critical (N=13)	Total (N=29)	Non-Critical (N=8)	Critical (N=6)	Healthy Control (N=8)	Healed(N=7)
Sex - no.								
Male	21	13	8	12	5	3	2	2
Female	15	10	5	17	3	3	6	5
Age-year								
Mean ±SD	65.6 ± 17.6	66.5 ± 20.6	53.8 ± 10.7	60.4 ± 17.0	76 ± 12.9	68.6 ± 8.9	50.4 ± 5.4	46.8 ±17.6
Range	35.0 - 101.0	35.0 - 101.0	49.0 - 84.0	30.0 - 96.0	59.0 - 96.0	56.0 - 82.0	43.0 - 56.0	30.0 - 72.0
Time from Onset to Admission, Days								
Mean ±SD	4.3 ± 4.5	4.5 ± 5.0	4 ± 3.6	4.8 ± 6.1	5.7 ± 7.0	1.0 ± 0.0		
Range	1.0 - 19.0	1.0 - 19.0	1.0 - 10.0	1.0-21.0	1.0-21.0	1.0-1.0		
Time from Admission to Severe, Days								
Mean ±SD			3.1 ± 2.8			3.0 ± 4.9		
Range			1.0 - 8.0			1.0 - 13.0		
No covid score - no.								
Mean ±SD	3.0 ± 1.9	3.5 ± 2.0	4 ± 1.4					
Range	1.0 - 6.0	1.0 - 6.0	1.0 - 4.0					
Symptoms - no.								
Fever	18	11	7	3	1	2		
Cough	16	11	5	3	0	3		
Headache	0	0	0	2	0	2		
fatigue	3	2	1	3	0	3		
Dyspnea	8	6	2	5	1	4		
Diarrhea	4	2	2	0	0	0		
Chest pain	1	1	0	2	0	2		
Abdomial Pain	2	1	1	0	0	0		
vomit	1	1	0	1	1	0		
Comorbility - no.								
Hypertension	10	5	5	6	4	2		
Diabetes	8	4	4	1	0	1		
Respiratory system	4	2	2	1	1	0		
Cardiovascolar system	16	8	8	1	0	1		
Other Endocrine system	1	0	1	8	8	0		
Chronic Kidney	3	1	2	1	1	0		
Oxygen saturation index - %								
Mean ±SD	91.3 ± 7.4	93.3 ± 5.2	97.4 ± 9.6	92.1 ± 5.6	94.0 ± 4.1	85.5 ± 6.4		
Range	71.0 - 99.0	81.0 - 99.0	71.0 - 98.0	81.0 - 99.0	87.0 - 99.0	81.0 - 90.0		

4.2.2.2 *Isolation of plasma exosomes*

Exosomes were isolated using Exo-Spin exosome purification kit for plasma (Cell Guidance Systems, UK). In brief, 250 µL of plasma samples were centrifuged first at 300g and then at 16 000g for 10 and 30 minutes, respectively, to remove platelets and larger vesicles. Half the volume of Exo-Spin buffer was added to the plasma samples, which were then mixed by inverting and incubated at 4 °C for 1 h before centrifugation at 16 000g for 60 min. Exosome pellets were resuspended in 100 µL phosphate-buffered saline (PBS) and purified using the Exo-Spin column. Finally, exosome were eluted in 200 µL PBS.

4.2.2.3 *Nanoparticle Tracking Analysis (NanoSight NS300)*

Particle size and concentration of plasma-derived exosomes were analyzed by NTA using the NanoSight Technology NS300. In brief, exosomes were diluted in sterile saline buffer solution (1:100) and analyzed by the Nanoparticle Analyses System using the NTA 1.4 Analytical Software.

4.2.2.4 *Western blotting*

Analysis of exosomes by immunoblotting was performed using standard protocols: proteins were denatured, separated on 4–12% polyacrylamide gels, transferred onto a nitrocellulose membrane and probed with antibodies against tetraspanins CD9 (Santa Cruz Biotechnology) and CD63 (Santa Cruz Biotechnology). The immunocomplexes were visualized by chemiluminescence using the Chemidoc MP imaging system (Bio-Rad Laboratories). Signal intensity of the bands was measured by using Image Lab software (Bio-Rad Laboratories).

4.2.2.5 *One-Step Reverse Transcription-Droplet digital Polymerase Chain Reaction (RT-ddPCR)*

Total RNA was extracted from 50 µL of plasma-derived exosomes using NucleoZOL (Macherey-Nagel) following manufacturer's instruction. SARS-CoV-2 RNA was quantified by means of the QX200TM Droplet Digital TM PCR System (ddPCR, Biorad) using the Bio-Rad SARS-CoV-2 ddPCR Kit and following manufacturer's instruction. Data were analyzed using the QuantaSoftTM 1.7.4 Software (Bio-Rad) and SARS-CoV-2 quantification was expressed in number copies/10 µl of exosomes.

4.2.2.6 Immunodepletion of high-abundant plasma proteins and digestion

Exosomes were lysed using 200 µL of RIPA buffer (50mM Tris HCl pH 7.2, 0.05%SDS) and sonication. Proteins were then precipitated overnight using cold acetone at -20°C. The pellet was then resuspended using urea buffer and ammonium bicarbonate. In order to improve the identification and quantification of exosomal proteins we depleted high-abundance proteins using the Seppro IgY14 spin column kit (Sigma-Aldrich Inc., St. Louis, MO, USA) according to the manufacturer's procedure. The samples were then prepared as reported in paragraph 3.3.2.3.

4.2.2.7 Proteomics analysis and data processing

The digested peptides were analyzed with an EASY nano-LC 1200 system (Thermo Scientific, Milano, Italy) coupled to a 5600+ TripleTOF system (AB Sciex, Concord, Canada). The liquid chromatography parameters were as follows: analytical column Acclaim PepMap C18 2µm 75µm x 150mm and injection volume 2 µL. The flow rate was 300 nL/min, phase A was 0.1% formic acid/water and phase B was 80% acetonitrile/0.1% formic acid/20% water. A two-hour gradient was used (3-45%). For identification purposes the mass spectrometer analysis was performed using a mass range of 100–1600 Da (TOF scan with an accumulation time of 0.25 s), followed by a MS/MS product ion scan from 400 to 1250 Da (accumulation time of 5.0 ms) with the abundance threshold set at 30 cps (40 candidate ions can be monitored during every cycle). The ion source parameters in electrospray positive mode were set as follows: curtain gas (N2) at 30 psig, nebulizer gas GAS1 at 25 psig, ionspray floating voltage (ISFV) at 2700 V, source temperature at 90 °C and declustering potential at 85V.

For label-free quantification, samples were then subjected to cyclic data independent analysis (DIA) of the mass spectra, using a 25-Da window. A 50-ms survey scan (TOF-MS) was performed, followed by MS/MS experiments on all precursors. These MS/MS experiments were performed in a cyclic manner using an accumulation time of 40 ms per 25-Da swath (36 swaths in total) for a total cycle time of 1.5408 s. The ions were fragmented for each MS/MS experiment in the collision cell using the rolling collision energy. The MS data were acquired with Analyst TF 1.7 (SCIEX, Concord, Canada).

The mass spectrometry files were searched using Protein Pilot (AB SCIEX, Concord, Canada) and Mascot (Matrix Science Inc., Boston, USA). Samples were input in the Protein Pilot software v. 4.2 (AB SCIEX, Concord, Canada), with the following parameters: cysteine alkylation, digestion by trypsin, no special factors and False Discovery Rate at 1%. The UniProt Swiss-Prot reviewed database containing human proteins (version 01/02/2018, containing 42271 sequence entries) and SARS-

CoV-2 (version 28/04/2020, containing 13175 sequence entries) were used. The Mascot search was performed on Mascot v. 2.4, the digestion enzyme selected was trypsin, with 2 missed cleavages and a search tolerance of 50 ppm was specified for the peptide mass tolerance, and 0.1 Da for the MS/MS tolerance. The charges of the peptides to search for were set to 2 +, 3 + and 4 +, and the search was set on monoisotopic mass. The instrument was set to ESI-QUAD-TOF and the following modifications were specified for the search: carbamidomethyl cysteines as fixed modification and oxidized methionine as variable modification [53,54].

The quantification was performed by integrating the extracted ion chromatogram of all the unique ions for a given peptide. The quantification was carried out with PeakView 2.2 and MarkerView 1.2. (Sciex, Concord, ON, Canada). Six peptides per protein and six transitions per peptide were extracted from the SWATH files. Shared peptides were excluded as well as peptides with modifications. Peptides with FDR lower than 1.0% were exported in MarkerView for the t-test.

Statistical analysis and related graphical representations were done using GraphPad Prism v. 8 and MetaboAnalyst software (www.metaboanalyst.org). Ingenuity Pathways Analysis (IPA) software (Qiagen, Redwood City, CA, USA) and FunRich (http://www.funrich.org) were used for bioinformatics analysis.

4.2.3 Results

4.2.3.1 Exosomes incorporate SARS-CoV-2 RNA

The presence of viral RNA in the exosome cargo was investigated using reverse transcription-droplet digital polymerase chain reaction (RT-ddPCR). RT-ddPCR enables a significant gain in dynamic range while decreasing the cost of analysis. In addition, it is more sensitive than qPCR, and it provides more accurate data—especially at low target copy numbers [169]. Analysis of exosome content purified from critical and non-critical patients revealed the presence of SARS-CoV-2 RNA in the exosomal cargo. We found viral material that ranges from 15 to 88 copies/10 μL with no significant differences between the two groups. No viral material was detected in healthy subjects.

4.2.3.2 Proteomic analysis of plasma-derived exosomes from COVID-19 patients

Untargeted proteomic analysis was performed on plasma-derived exosomes from 17 SARS-CoV-2 positive patients and seven healthy controls. The patients enrolled in this study resided in Northern Italy, which was the COVID-19 pandemic's Italian epicenter.

We divided our patient group in two cohorts: critical (patients with respiratory failure who were admitted to intensive care units, requiring mechanical ventilation), and non-critical (all other patients, with mild to severe respiratory failure, requiring oxygen supplementation but neither invasive nor noninvasive mechanical ventilation). Out of 17 patients, seven patients were in critical condition, and 10 were in non-critical condition. Critical COVID-19 patients' blood levels of white blood cells (WBCs) and eosinophil were significantly higher than non-critical patients'. On the contrary, we found a slight increase in red blood cells and lymphocyte counts among non-critical COVID-19 patients (**Supplementary Table 4.1**).

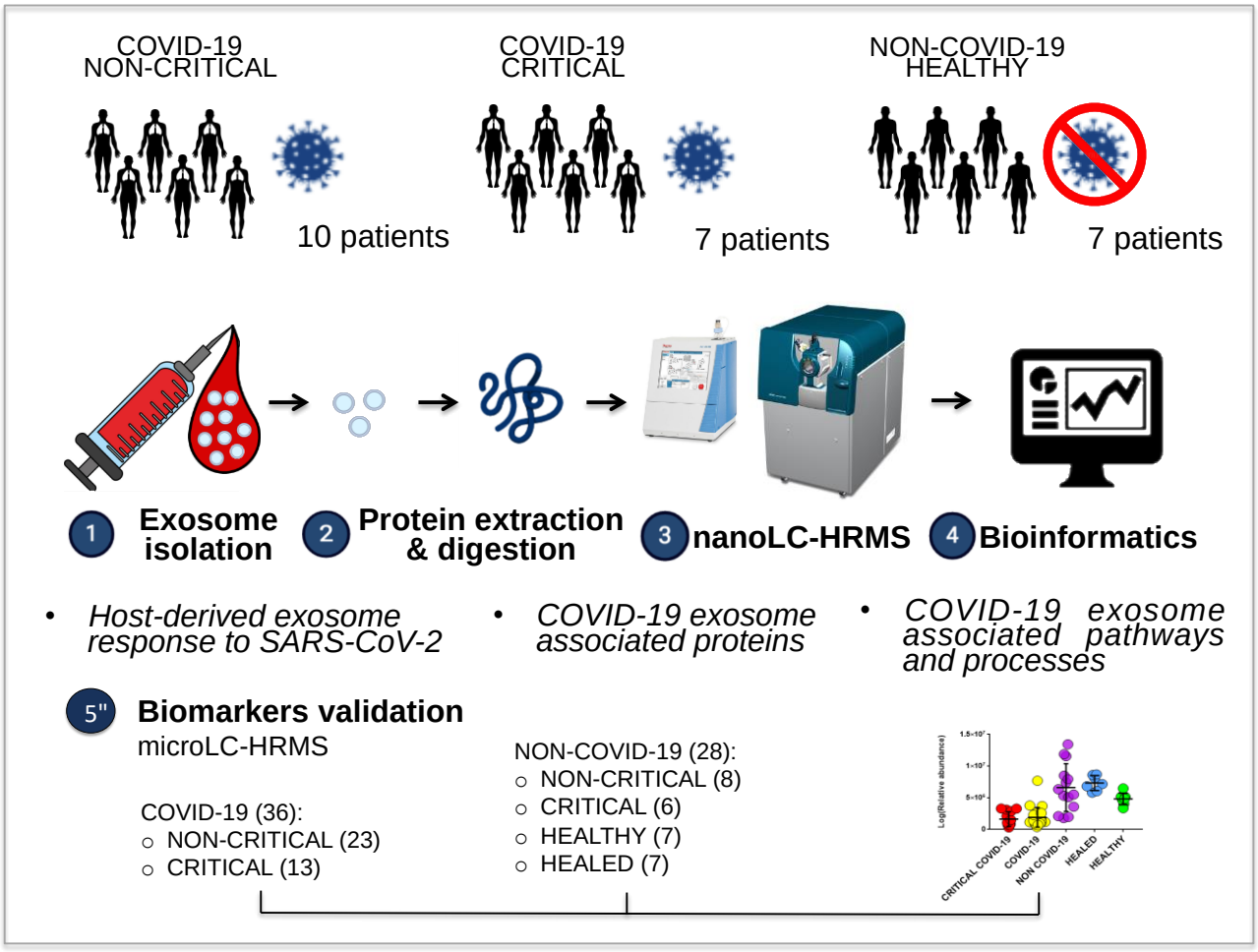

Figure 4.1: *overview of this study's experimental design: plasma exosomes from 10 non-critical COVID-19 patients, seven critical COVID-19 patients, and seven healthy subjects were isolated using a commercial kit. The exosomes' protein content was analyzed using proteomics analysis (nanoLC-HRMS), and the identified and modulated proteins were elaborated with bioinformatics in order to identify the host-derived exosome response to SARS-CoV-2 and its associated pathways. The analysis suggested the presence of new biomarkers. The validation of potential exosomal biomarkers was performed on an external cohort of patients using a proteomics approach on a microLC-HRMS. 36 COVID-19 patients, including non-critical (23) and critical (13) subjects, and on 28 non-COVID-19 patients, including 6 critical patients, 8 non-critical patients, 7 healthy subjects and 7 healed COVID-19 subjects were analyzed.*

Figure 4.1 provides an overview of this study's experimental design. A brief description follows here. Exosomes were isolated from plasma. The purification of the exosomes was subjected to several control analyses. Nanosight and Western blotting were employed to characterize the quality of the method of purification; these analyses, which were performed only on healthy subjects for safety reasons, confirmed the isolation protocol of exosomes with a size ranging from 30 to 100 nm (peak 37.70 ± 3 nm) and a concentration of $3x10^{11}$ particles/mL (**Supplementary Figure 4.1**). In addition, the typical exosomal markers CD9 and CD63 were detected, confirming these vesicles as exosomes.

Exosomal proteins were then extracted, digested, and analyzed using a nano-liquid chromatography/tandem mass spectrometry (nanoLC-MS/MS). The results were elaborated using bioinformatics tools to highlight the main functions and pathways associated with the host response to SARS-CoV-2 infection.

The validation of potential biomarkers was then performed using a microLC-MS/MS on 36 COVID-19 patients, including non-critical (23) and critical (13) subjects, and on 39 non-COVID-19 patients, including 6 critical patients, 8 non-critical patients, 7 healthy subjects and 7 healed COVID-19 subjects.

4.2.3.3 Circulating exosomes in COVID-19 patients have a specific proteomic signature

To identify the proteins potentially involved in the development of SARS-CoV-2 infection and in any immunomodulatory functions mediated by circulating exosomes, plasma exosomes from COVID-19 patients with varying disease severity were analyzed using shotgun proteomic analysis.

A total of 913 different proteins were identified in plasma exosomes; among them, 281 were found in critical, non-critical, and healthy subjects, as **Figure 4.2** shows. Interestingly, non-critical patients are characterized by the presence of a higher number of proteins (706), while a similar number of proteins were identified in critical patients (478) and healthy subjects (454).

By analyzing exosomal cargo, we found that it was mainly characterized by the presence of extracellular, exosomal, lysosome, and cytoskeleton proteins (**Fig. 4.2B**). Moreover, these proteins are involved in transport activity, complement activity, protease inhibitor activity, extracellular matrix structural constituents, and defense/immunity activity (**Fig. 4.2C**). Interestingly, some proteins are associated with immune response and coagulation (complement activity, immune response, regulation of complement activation, Fc-gamma receptor signaling pathway, immunoglobulin production, and antimicrobial humoral response), as **Figure 4.2D** shows.

The samples were also classified using a supervised partial least square discriminant analysis (PLS-DA), which was exploited to achieve maximum separation between the two patient groups (**Fig. 4.4A**).

To assess overall differences between exosomes from COVID-19 patients and healthy subjects, protein abundances were analyzed using multivariate statistical analysis. Principal component analysis (PCA)—in particular, the first and second principal components—clearly separated the samples according to the groups.

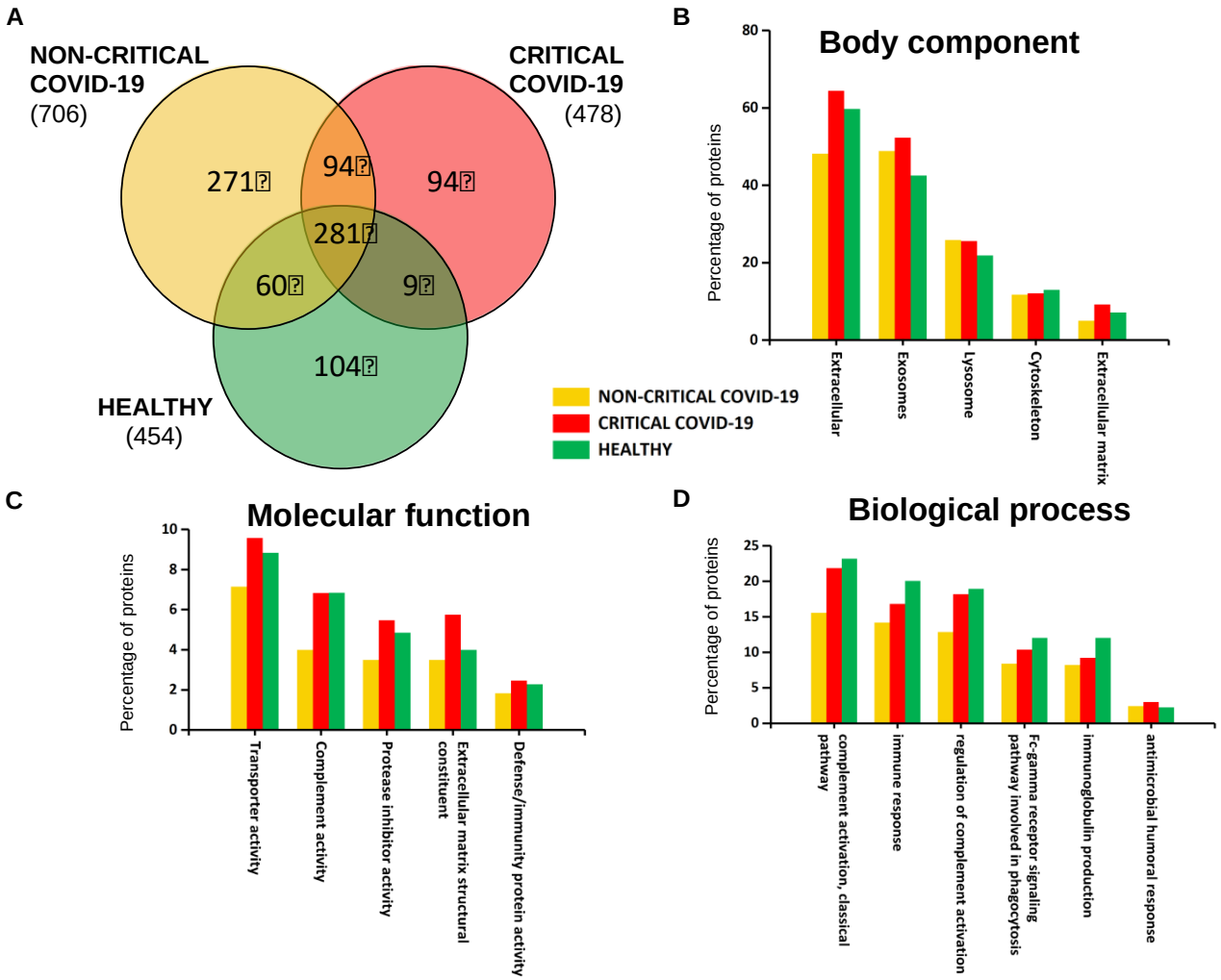

Figure 4.2: *plasma-exosomes protein content. A Venn diagram (A) of identified proteins in critical and non-critical COVID-19 patients and in healthy subjects. A gene ontology classification of identified proteins based on body component (B), molecular function (C), and biological process (D).*

The first component explained the differences between COVID-19 samples (red and yellow dots) and non-COVID-19 samples (green dots), while the second component mainly explained the differences between in disease severity (**Fig. 4.3A**). **Figure 4.3B** reports a bi-plot of the scores and

individual proteins' loading information. The plot reports the proteins that are "driving the separation" between the patient groups. For example, interestingly, CRP protein (CRP_HUMAN) was able to discriminate positive patients from non-positive patients but also critical patients from non-critical patients.

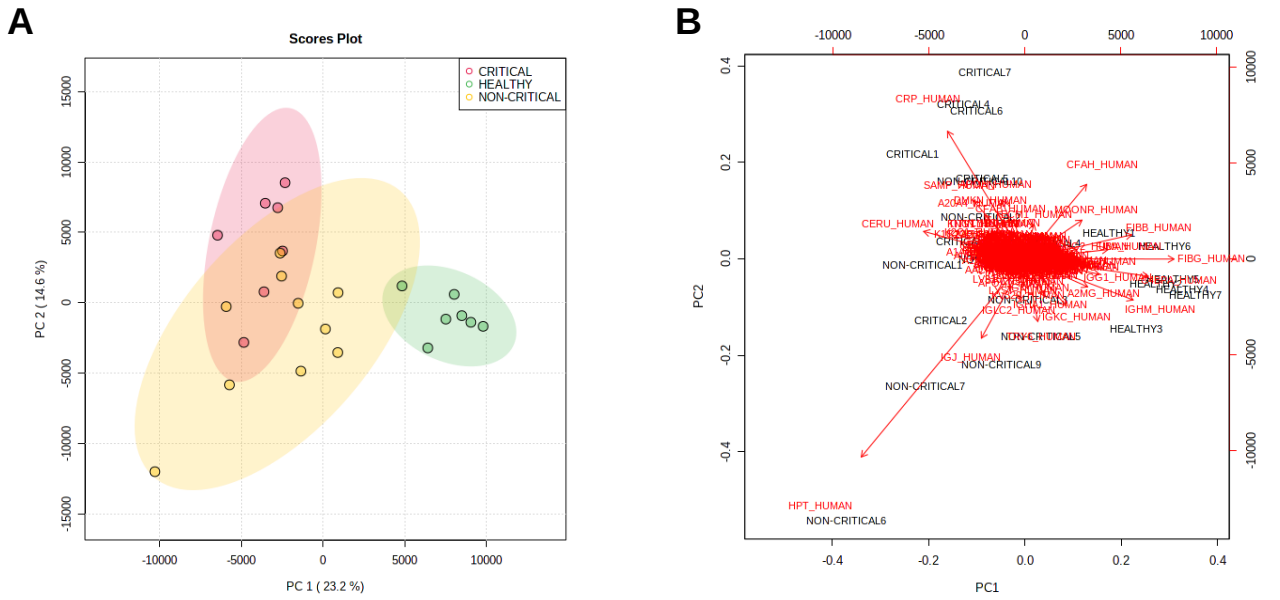

Figure 4.3: *principal component analysis. The score plot (A) of PC1 and PC2 shows a clear separation of healthy subjects (green dots) from critical COVID-19 patients (red dots) and non-critical (yellow dots) COVID-19 patients. (B) The bi-plot of the scores (black) and loading (red) of PC1 and PC2.*

The most predictive or discriminative features that are potentially useful in helping sample classification were also determined through the VIP (variable of importance in projection) score. The VIP score summarized the most prominent proteins contributing to the observed phenotypic variations in the COVID-19 plasma exosomes (**Fig. 4.4B**). Proteomics differences between the three groups of samples were mostly due to haptoglobin (HPT_HUMAN), C-reactive protein (CRP_HUMAN), Beta-2-glycoprotein 1 (APOH_HUMAN) and Complement factor H (CFAH_HUMAN). The dendrogram of hierarchical clustering of protein abundance in exosomes from critical patients (red), non-critical patients (yellow), and healthy subjects (green) confirmed that exosomal proteins correlated with the SARS-CoV-2 infection and with the disease's severity (**Fig. 4.4C**).

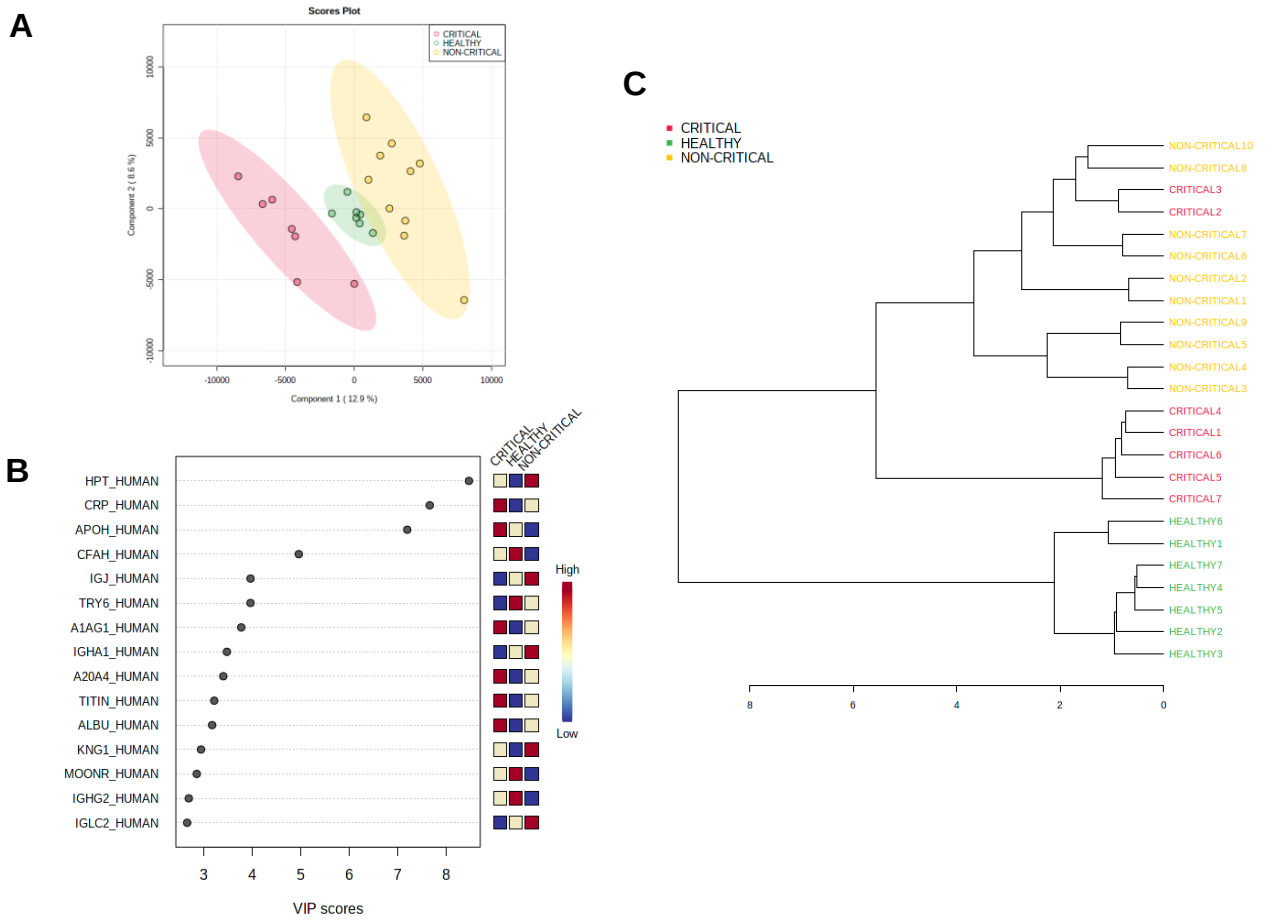

Figure 4.4: *partial least square discriminant analysis (PLS-DA) of critical patients (red dots), non-critical patients (yellow dots), and healthy subjects (green dots). The three groups are well separated (A). Important features identified by PLS-DA (B): colored boxes indicate the most predictive or discriminative features in each group (red, high; blue, low; white, middle). A dendrogram from the hierarchical clustering (C) of protein abundance in the exosomes from critical patients (red), non-critical patients (yellow), and healthy subjects (green).*

4.2.3.4 Exosomal proteins are strongly involved in the host response to SARS-CoV-2

Next, we performed a univariate analysis of quantified proteins using the relative abundance of 518 proteins quantified in all samples. A total of 157 proteins were modulated in exosomes from critical COVID-19 patients compared to healthy subjects, while 97 proteins were regulated in non-critical patients (p-value < 0.05, fold change > 1.3). Volcano plots (**Fig. 4.5A and Fig. 4.5B**) showed the most significant differences among proteins and the positive or negative fold-changes in exosomes from critical and non-critical COVID-19 patients compared to the healthy group. To summarize the univariate results, we used a heat map (**Fig. 4.5C**) to display the fold changes of the top modulated proteins. This heat map allowed visualization of the three clusters of samples and different protein levels. The complete list of modulated proteins is reported in **supplementary tables 4.2 and 4.3**.

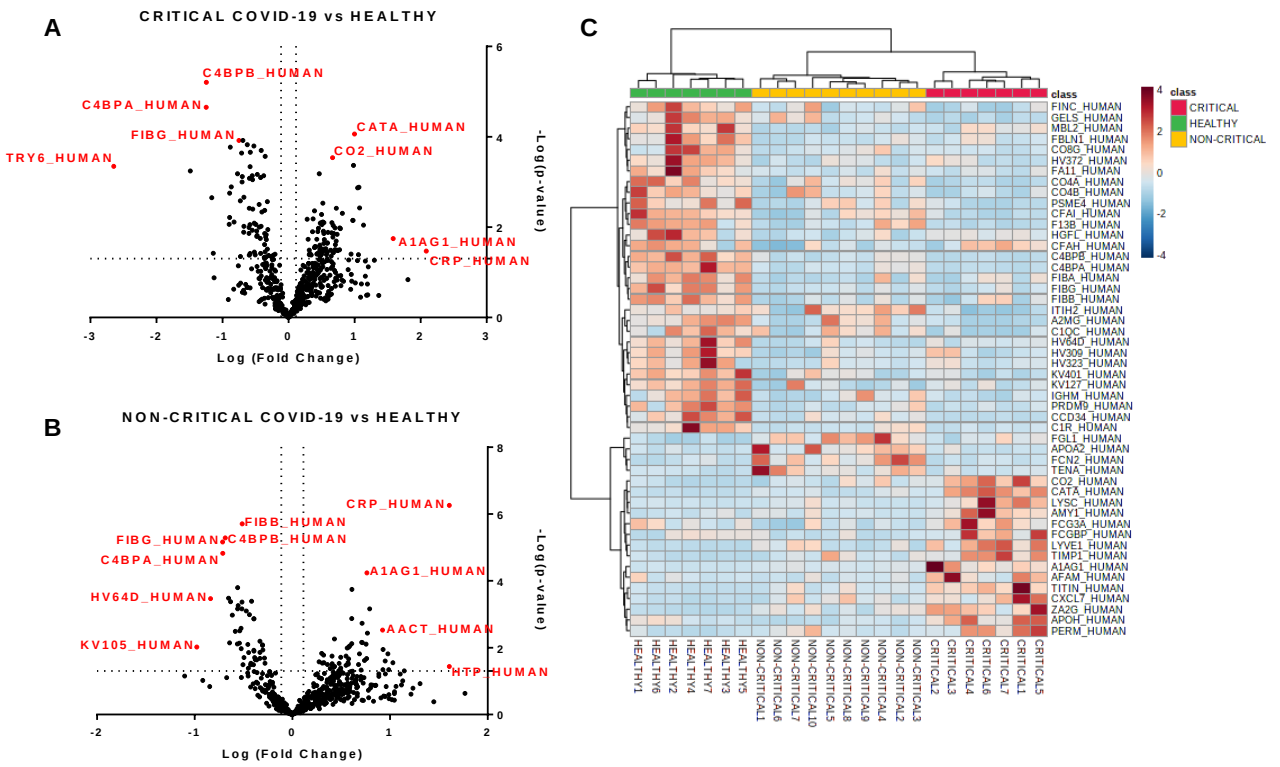

Figure 4.5: *modulated exosomal proteins in SARS-CoV-2 infection. Volcano plots of quantified proteins (A and B). A total of 157 and 97 proteins were modulated in critical (A) and non-critical (B) COVID-19 patients, respectively (p-value < 0.05 and fold change > 1.3). Hierarchical heat maps of quantified proteins (C) highlighting the three clusters of samples, with critical COVID-19 patients in red, non-critical COVID-19 patients in yellow, and healthy subjects in green.*

The top regulated proteins in both critical and non-critical patients, compared to healthy subjects, mainly included inflammatory, immune-response, and coagulation proteins. In critical patients, C-reactive protein (122-fold), alpha-1-acid glycoprotein 1 (38-fold), lysozyme C (13-fold), titin (12-fold), and zinc-alpha-2-glycoprotein (12-fold) were up-regulated while putative trypsin-6 (31-fold), coiled-coil domain-containing protein 34 (18-fold), C4b-binding protein alpha chain (18-fold), C4b-binding protein beta chain (15-fold), and pre-mRNA-processing factor 19 (14-fold) were down-regulated. Among non-critical COVID-19 patients, the top five up-regulated proteins were haptoglobin (41-fold), C-reactive protein (40-fold), trypsin-3 (14-fold), adenomatous polyposis coli protein (11-fold), and hyaluronan-binding protein 2 (10-fold) while immunoglobulin kappa variables 1–5 (10-fold), immunoglobulin heavy variables 3–64D (7-fold), fibrinogen gamma chain (5-fold), C4b-binding protein alpha chain (5-fold), and C4b-binding protein beta chain (5-fold) were under-expressed.

4.2.3.5 *Circulating exosomes in COVID-19 patients may modulate immune response, inflammation, and coagulation pathways*

To obtain a global overview of the exosome proteomic response in COVID-19, modulated proteins were analyzed with bioinformatics tools. Ingenuity pathway analysis (IPA) was employed to identify the main pathways, biological processes, molecular functions, and cellular component associated with SARS-CoV-2 infection. The canonical pathways involved in the host response mainly related to immune response, inflammation, and coagulation. The chord diagrams in **figures 4.6A and 4.6B** report the top 10 pathways and their relative proteins involved in critical (**4.6A**) and non-critical (**4.6B**) patients. The main pathways involved in non-critical and critical patients were the complement system pathway, acute-phase response signaling, the coagulation system, the LXR/RXR activation pathway, the extrinsic and intrinsic prothrombin activation pathway, the FXR/RXR activation pathway, IL-12 signaling and production in macrophages, the production of nitric oxide and reactive oxygen species in macrophages, and clathrin-mediated endocytosis signaling. As **Figure 4.6C** shows, some pathways were more altered in non-critical patients—specifically, acute phase response signaling, LXR/RXR, and FXR/RXR activation. Meanwhile, other pathways—such as the complement system, the coagulation system, and the extrinsic and intrinsic prothrombin activation pathway—were more altered in critical patients.

Diseases and disorders analysis highlighted the involvement of the inflammatory response and immunological disease, while physiological system development and function elaboration showed that the protein cargo is associated with a humoral immune response and immune cell trafficking (**Fig. 4.6D and Fig. 4.6E**).

4.2.3.6 *Upstream analysis highlighted the relation between inflammation and protein cargo*

To predict the upstream molecules (transcription factor, microRNA, etc.) that could play a role in the observed proteome modulation and, thus, in the host response to SARS-CoV-2 infection, we performed upstream regulator analysis through IPA software. IPA analysis suggested that interleukin IL-6 (IL-6) and transforming growth factor (TGF)-beta1 (TGFB1) are the most significant upstream regulators (**fig. 4.7A and fig. 4.7C**). Among other upstream regulators, IL-1 was marked as a significantly activated regulator (z score=2.6) while IRF2 was predicted as an inhibited regulator (z score=-2.0), as **figures 4.7B** and 4.**7D** show.

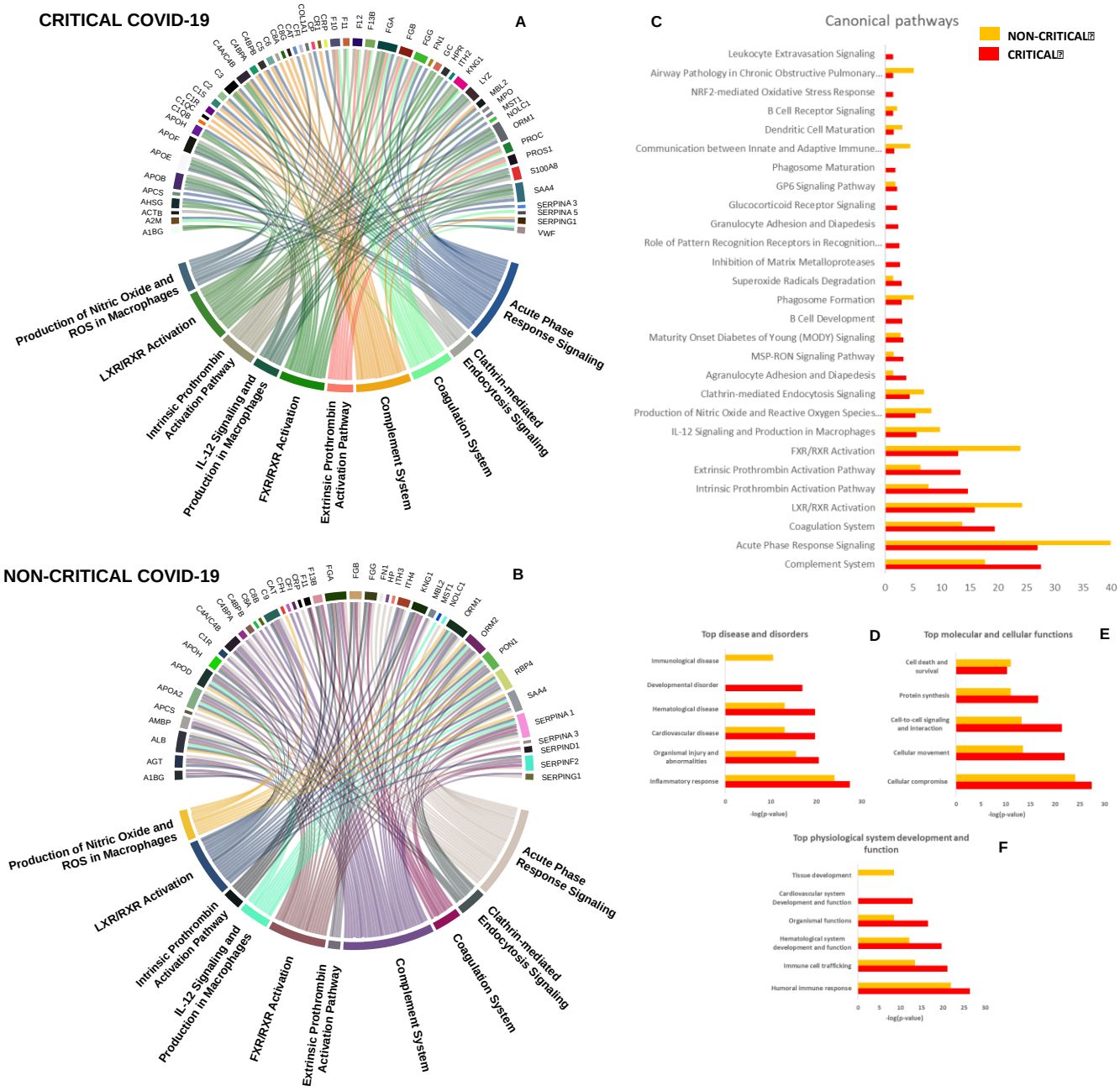

Figure 4.6: *canonical pathway analysis. A Chord diagram presenting a pathway analysis of significantly altered proteins in response to SARS-CoV-2 infection in critical (A) and non-critical (B) patients. Each pathway's width is determined by the number of proteins associated with each pathway. Canonical pathways' significance (-log[p-value]) was also compared (C): this analysis showed similar exosome responses in critical and non-critical patients. The diseases and disorders analysis (D), molecular and cellular functions (E), and physiological system development and function elaboration (F) are also shown.*

The dysregulation of IL-6–targeted genes (FGA, FGB, FGG, FGL1, HSPA5, IGHM, LRG1, PPBP, S100A9, SAA4, SERPINA3, SGK1, SPP1, TIMP1, VCAM1, A2M, AGT, APCS, and CP) and of TGFB1-targeted genes (VCAM1, TIMP1, SPP1, SGK1, SERPINA3, PSEM4, LYVE1, KNG1, IGHM, HSPG2, HSPA5, GSN, FN1, FGG, FGB, FGA, FCGR3A/FCGR3B, CP, CFH, C4BPB, C4BPA, C1R, and ADAMTS2) may contribute

to SARS-CoV-2–related dysfunctions. As mentioned above, most of these regulated genes are involved in inflammation, immune response, and coagulation.

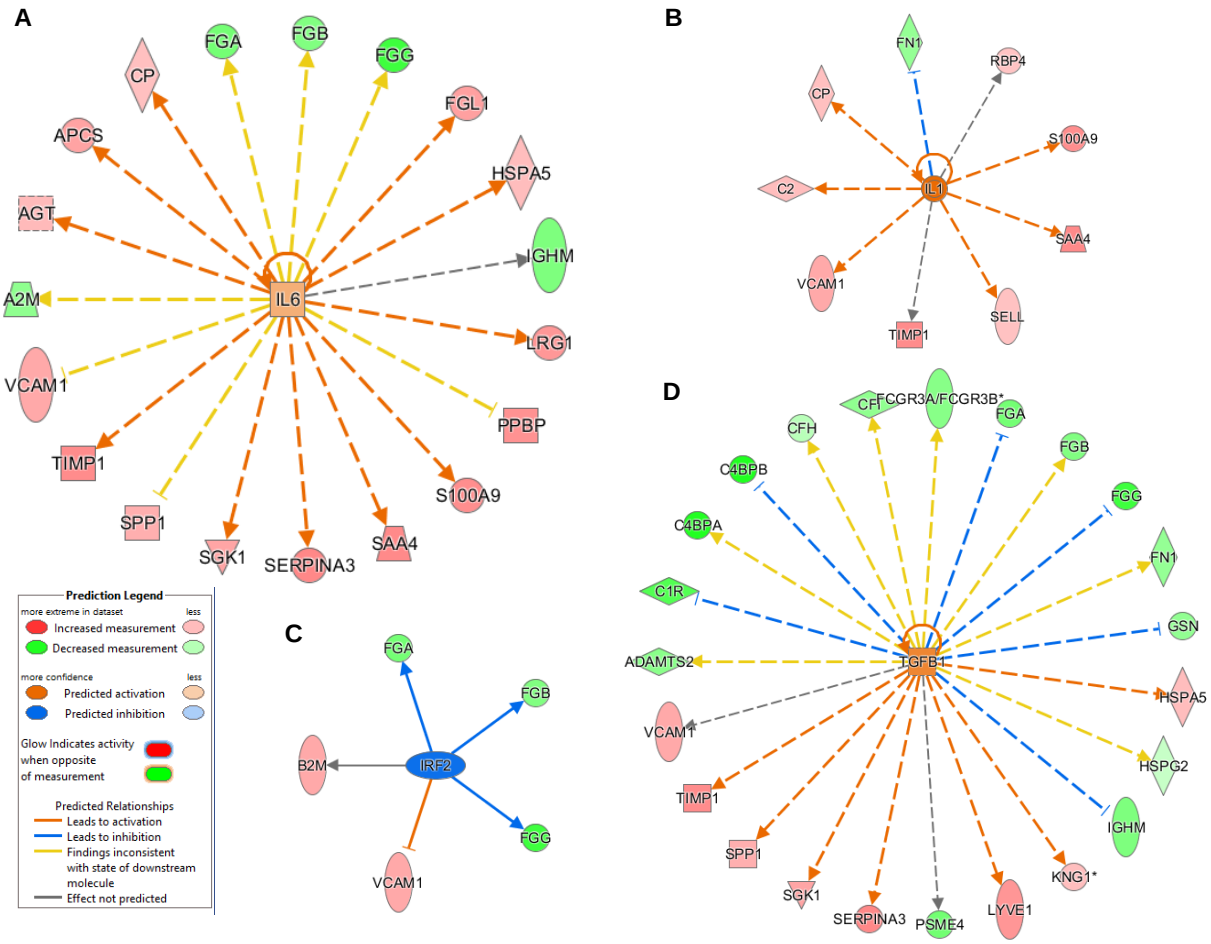

Figure 4.7: *upstream gene regulator analysis. IL-6 (A) and transforming growth factor (TGF)-beta1 (B) are the most significant upstream regulators. IL-1 resulted significantly activated (z score=2.6) while interferon regulatory factor 2 was predicted as an inhibited regulator (z score=-2.0).*

4.2.3.7 Association of exosome cargo with pathologically relevant clinical indices

We then evaluated whether exosomal protein cargo in COVID-19 patients significantly correlated with CRP and d-dimer levels, platelets, neutrophil, and monocytes counts. Spearman correlations were performed, and only correlations with $p<0.05$ were considered and shown in **supplementary tables 4.4–4.8**. We found that circulating CRP levels positively correlated with CRP, IBP2, CHI3L1, FGB, FHR5, IGHV3-73, FGG, PRSS2, CFP, CFH, CD163, FCGBP, and CAT exosomal proteins, which are linked to inflammation, complement activation, and pulmonary fibrosis [170]. Fibronectin, alpha-2-HS-glycoprotein, and alpha-1-acid glycoprotein 1 protein positively correlated with d-dimer levels,

and platelet counts positively correlated with TIMP1, COL6A3, SPINK1, IGFBP4, IGHV1-8, NCAM1, COL18A1, APOA2, CFB, and MYH7 exosomal proteins, which are involved in platelets' aggregation, adhesion, or activation and complement activation [171].

Regarding neutrophil count, we found an increase in neutrophil among critical COVID-19 patients, and our analysis of exosomal cargo revealed a positive correlation with FGA protein, which is implicated in neutrophil activation [172], but also with TPI1 protein, which has already been found in exosome cargo [173], and with other inflammatory proteins (i.e., SAA1, coagulation factor XI, etc.). Monocyte counts positively correlated with IGFALS, CFP, CLU, and SERPINC1 exosomal proteins, which are involved in the migration and chemotaxis of human monocytes [174].

4.2.3.8 Circulating exosomes are potential biomarkers of COVID-19

Potential biomarkers were explored by carefully analyzing modulated proteins' distribution and by using ROC curves. We firstly evaluated modulated proteins obtained from the discovery phase. Interestingly, we found that the abundance of several proteins directly correlated with the disease's severity. In particular, critical patients displayed higher levels of CRP, A1AG1, A1AG2, CXCL7, SAMP, and ZA2G and lower levels of CCD34, C4BPA, and GELS than non-critical patients (**Fig. 4.8A–I**). In addition, this analysis reported the presence of several proteins that are able to discriminate between COVID-19 patients and healthy subjects.

Biomarkers were validated on a new cohort of patients that included not only COVID-19 critical (n=13) and non-critical (n=26) patients and healthy subjects (n=7), but also critical (n=6) and non-critical (n=8) patients admitted for pneumonia and/or respiratory failure with negative nucleic acid test results (NON-COVID-19) and COVID-19 healed patients (n=7). Interestingly, fibrinogen proteins fibrinogen alpha chain (FIBA_HUMAN), fibrinogen beta chain (FIBB_HUMAN) and fibrinogen gamma chain (FIBG_HUMAN) showed an AUC value of 0.94 (sensitivity (SE): 86%; specificity (SP): 97%), 0.90 (sensitivity (SE): 92%; specificity (SP): 86%) and 0.93 (sensitivity (SE): 83%; specificity (SP): 91%), respectively. In addition, fibronectin (FINC_HUMAN), Complement C1r subcomponent (C1R_HUMAN) and Serum amyloid P-component (SAMP_HUMAN) showed an AUC value of 0.92 (sensitivity (SE): 94%; specificity (SP): 82%), 0.93 (sensitivity (SE): 89%; specificity (SP): 82%) and 0.91 (sensitivity (SE): 89%; specificity (SP): 82%), respectively (**Fig. 4.8J–O**).

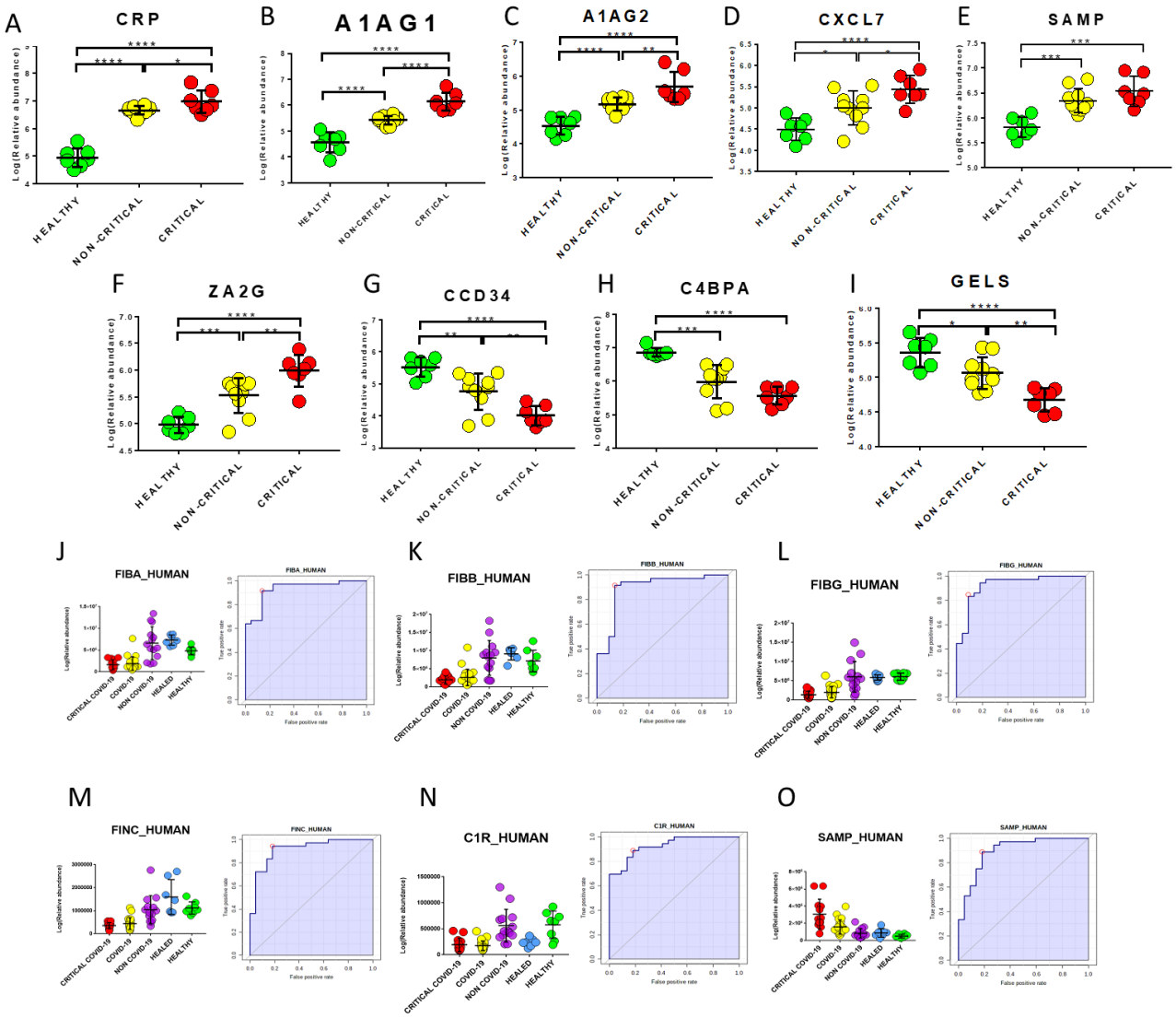

Figure 4.8: *box-plots and ROC curves for the best potential biomarkers identified using proteomic analysis of the exosome cargo. For (A–I), box-plots of proteins that are well correlated with the disease's severity are reported. Red dots indicate critical COVID-19 patients while yellow dots indicate non-critical COVID-19 patients. Fibrinogen alpha chain (J), fibrinogen beta chain (K), fibrinogen gamma chain (L) fibronectin (M), Complement C1r subcomponent (N) and Serum amyloid P-component (O) were confirmed as good biomarkers in the validation. Purple dots indicate NON-COVID-19 patients while green and blue dots and indicate healthy and healed subjects, respectively.*

We also compared modulated exosomal proteins with regulated serum proteins in COVID-19 patients reported in the literature ([175–177].**Table 4.2** reports the list of common differentially expressed proteins. Interestingly, more than 50% of proteins (27 out of 50) presented the same direction of modulation identified in previous research on serum circulating proteins—even if the fold-change levels in plasma-exosome were higher than in serum.

Table 4.2: *comparison of modulated exosomal proteins with regulated serum proteins in COVID-19 patients reported in literature. Protein modulation (Up or Down) is indicated*

Gene	Plasma-exosome		Serum (22)	Serum (23)	Serum (24)
	Non-critical	Critical			
A1BG	Up	Up	–	–	Up
ACTB	–	Up	–	–	Up
AHSG	–	Up	Down	–	–
ALB	Up	–	Down	–	–
APO2	Up	–	–	Down	–
APOD	Up	–	–	Up	–
APOF	–	Up	Up	–	–
APOH	Down	Up	–	Down	–
C1R	Down	Down	–	–	Up
C1S	–	Down	–	–	Up
C4BPA	Down	Down	–	Up	–
C9	Up	–	Up	–	–
CLEC3B	–	Down	Down	–	–
CRP	Up	Up	Up	–	Up
CST3	–	Up	Up	–	–
F13B	Down	Down	Down	–	–
FCN2	Up	–	Down	Down	–
FGA	Down	Down	-	–	Up
FGB	Down	Down	-	–	Up
FGG	Down	Down	-	–	Up
FN1	Down	Down	-	–	–
GSN	Down	Down	Down	–	Down
HP	Up	–	–	–	Up
IGHV1-2	Down	–	Up	–	–
IGHV3-15	–	Down	Up	–	–
IGHV3–23	Down	Down	Up	–	–
IGHV3–9	Down	Down	Up	–	–
IGHV4–28	–	Down	Up	–	–
IGHV4–38–2	Down	–	Up	–	–
IGKV1–5	Down	–	Up	–	–
IGKV4–1	Down	–	Up	–	–
ITIH1	–	Down	Down	–	–
ITIH2	–	Down	Down	–	–
ITIH3	Up	–	Down	Up	Up
ITIH4	Up	–	Down	Up	Up
LRG1	Up	Up	Up	–	–
LYZ	–	Up	Up	–	–
ORM1	Up	Up	Up	Up	–
PGLYRP2	Down	–	Down	–	–
PON1	Up	–	Down	–	–
PPBP	Up	Up	Down	–	–
S100A8	–	Up	Up	–	–
S100A9	–	Up	Up	–	–
SAA4	Up	Up	–	Up	–
SERPINA3	Up	Up	Up	Up	–
SERPINA6	–	Up	Down	–	–
SERPING1	Up	Up	Up	–	–
TIMP1	Up	Up	Up	–	–
VCAM1	Up	Up	–	Up	–
VWF	–	Down	Up	–	–

4.2.4 Discussion

This study provides the first proteomic characterization of plasma-derived exosomes from COVID-19 patients and healthy controls. Participating patients were enrolled from a hospital located in Northern Italy, the first western epicenter of the COVID-19 pandemic. WBC, neutrophil, and eosinophil counts were increased in critical COVID-19 patients while the number of red blood cells, as well as lymphocytes, were significantly decreased [178].

Exosomes and EVs play significant roles in various biological functions and, particularly, in both physiological and pathological processes [151]. Indeed, they are associated with immune responses, viral pathogenicity, pregnancy, cardiovascular diseases, central nervous system–related diseases, and cancer progression [179]. Several examples of scientific evidence have shown that viruses might use EVs to enter uninfected cells [180]. During the course of infections, EVs can convey pathogen molecules that serve as antigens or agonists of innate immune receptors to induce host defense and immunity or serve as regulators of host defense and mediators of immune evasion [181,182]. Our data reports, for the first time, the presence of viral material in COVID-19 patients' host exosomal cargo. This finding suggests that SARS-CoV-2 may use the endocytosis route to spread infection throughout the host. We did not identify viral proteins via the purification of exosomes; thus, we can conclude that viral particles were not purified together with exosomes, suggesting that the RNA material was originally present in the cargo. A very recent study showed that exosomal microRNAs may drive thrombosis in COVID-19 patients [183] while Song and colleagues found that GM3-enriched exosomes positively correlated with disease severity, suggesting that they may participate in the pathological processes associated with COVID-19 progression (Song et al., 2020). Moreover, exosome-based strategies were also proposed to treat COVID-19 [184] or prevent SARS-CoV-2 infection [185].

Our findings show that circulating exosomes are strongly involved in the processes associated with SARS-CoV-2 infection. Interestingly, our proteomic analysis of plasma-derived exosomes from COVID-19 patients revealed a specific proteomic signature. This signature was particularly evident using multivariate statistical analysis (PCA and PLS-DA), which highlighted the presence of proteomic features that are able to clearly discriminate between the samples, according to the diagnosis. Bioinformatics analysis revealed the presence of proteins related to the coagulation process, transport activity, complement activity, protease inhibitor activity, and defense/immunity protein activity.

Interestingly, exosomal proteins' relative abundance in COVID-19 patients significantly differed from healthy subjects. Indeed, 157 and 97 proteins were significantly modulated in critical and non-critical COVID-19 patients, respectively. Our canonical pathway analysis performed on modulated proteins revealed the involvement of pathways associated with immune response, coagulation, and inflammation, as in **Figure 4.9** summarizes.

The complement pathway is a double-edged sword for our immune system: it may offer protection by favoring viral clearance, but unrestrained activation may also result in pathological acute and chronic inflammations, tissue injury, and activation of the coagulation pathway [186]. Complement activation has been linked to the pathophysiology of ARDS caused by various underlying diseases, and it has also been associated with COVID-19 [187]. Chahar et al. demonstrated that exosomes derived from respiratory syncytial virus–infected cells were able to activate an innate immune response by inducing cytokine and chemokine release from human monocytes and airway epithelial cells [188]. As **figures 4.6A and 4.6B** show, we found a dysregulation of 17 proteins (C1QB, C1QC, C1R, C1S, C2, C3, C4A/C4B, C4BPA, C4BPB, C5, C6, C8A, C8G, CFI, CR1, MBL2, SERPING1) in critical patients associated with the complement system pathway while, in non-critical patients, 11 proteins were modulated (C1R, C4A/C4B, C4BPA, C4BPB, C8A, C8G, C9, CFH, CFI, MBL2, SERPING1). In addition, the complement system pathway appeared more altered in critical patients (-log [p-value] =27.6) than non-critical patients (-log [p-value] =17.7). Among complement-related proteins, CFH and C4BPA had already been identified as transcriptional markers associated with severe SARS-CoV-2 infection: these molecules play central roles in complement activation and innate immunity [189]. Moreover, we found a 2.5-fold increase of C9 in non-critical patients and a down-regulation of CFH; these findings suggest that, in critical COVID-19 patients, the C9 complement component might be impaired due to SARS-CoV-2 infection, as has already been shown for the hepatitis C virus [190]. Interestingly, a global down-regulation of proteins coding for antibodies such as IGHV1-2, IGHV3-15, IGHV3-23, IGHV3-9, IGHV4-28, IGHV4-38-2, IGKV1-5, and IGKV4-1 was especially found in critical COVID-19 patients, suggesting the involvement of the humoral immune response, as Rolla et al. (2020) have already shown in reporting a significantly lower count of antibody-synthesizing lymphocyte among critical COVID-19 patients. Our results provide the first evidence of circulating exosomes' potential immunomodulatory contribution in response to SARS-CoV-2 infection.

Furthermore, our analysis highlighted the implication of proteins in the acute-phase response pathway. The human immune system plays a key role in the defense against pathogens [191]. The acute-phase response is an innate body defense activated during acute illnesses, and it involves increased production of acute-phase proteins such as CRP and cytokines. In the case of an infection, the inflammatory response stimulates the liver to synthesize and release anti-inflammatory proteins that suppress inflammation and regulate immunity in the body [192]. As already reported, SARS-CoV-2 infected patients show high levels of pro-inflammatory cytokines and chemokines associated with pulmonary inflammation and extensive lung involvement; such inflammation has also been

observed in SARS and MERS patients [193]. Other studies have reported an elevation in acute-phase reactants among patients with COVID-19, including ESR, C-reactive protein (CRP), serum amyloid A, and ferritin—suggesting a rapid activation of the innate immune response [194]. Moreover, serum changes in acute-phase response proteins were used as indicators to identify the degree and progression of COVID-19. A significant increase in CRP and SAA content and a decrease C3 and C4 content have been associated with the disease's severity [195]. In our study, among acute-phase proteins, exosomal CRP resulted in 122-fold and 40-fold up-regulation in critical and non-critical patients, respectively. A preliminary analysis of hematological and inflammatory parameters was associated with elevated CRP, IL-6, and NLR values and with worse outcomes as well as a lack of response to treatment [196,197]. High C-reactive protein independently predicted the risk of mortality in a cohort of 183 COVID-19 patients [198]. Another study identified increased CRP levels in a limited number (31.0%) of COVID-19 patients [199]. While high CRP levels were already reported during inflammation processes, our results indicate that CRP can be transported to other cells through EVs, thus driving the infection's inflammatory effect. Alpha-1-acid glycoprotein protein (AGP), which is one of the major acute-phase proteins in humans, was up-regulated in both critical and non-critical patients. During the acute-phase response, the serum concentration of AGP increases as a liver hepatocytes response to the cytokines that are released by monocytes and other cells in the early phase of inflammation or infection [200]. Alpha 1-antichymotrypsin (AACT_HUMAN) is another acute-phase protein that was found to be overexpressed in critical COVID-19 patients.

IL-12 signaling and production in macrophages pathways were significantly altered in both critical and non-critical patients, although we did not identify IL-12 protein directly in exosome cargo. Experimental evidence has shown that IL-12 rapidly activates both innate and specific immune responses, promoting host cellular responses, the clearance of the virus, and host recovery from infection [201].

Interestingly, we found a significant modulation of the MSP-RON signaling pathway. This pathway contributes to the macrophage-induced immune response in order to assist the host in viral recognition via the macrophage stimulating protein (MSP) and the transmembrane receptor kinase RON Protein Tyrosine Kinase/Receptor d.

Coagulation's involvement in SARS-CoV-2 infection has been extensively reported in COVID-19 [202,203]. Proteins involved in platelet degranulation were down-regulated in SARS-CoV-2–infected

patients [204], together with the low platelet count associated with severe COVID-19 and mortality [176,205]. Our bioinformatics analysis demonstrated that exosomal proteins are associated with the coagulation system pathway and with the intrinsic and extrinsic prothrombin activation pathways. Complement factors are able to increase tissue factor activity, form activated thrombin from prothrombin, increase platelet activity and aggregation, increase prothrombinase activity, and release platelet-derived procoagulant granules [206].

Among the effects of the viral ACE2 used by SARS-CoV-2 for cell entry, the connection between ACE2 and the Kallikrein/Kinin system—which regulates coagulation, fibrinolysis, and complement cascade—has resulted in great interest [207] Indeed, ACE2 physiologically binds and cleaves Lys-des-Arg9-Bradykinin and Des-Arg9 Bradykinin, which are potent ligands of Bradykinin Receptor 1 in the lungs [208]. When the virus blocks ACE2, the degradation of bradykinin cannot be performed, causing the accumulation of bradykinin itself; consequently, bradykinin—a product of high-molecular-weight kininogen—binds to its receptor (bradikynin-1receptor), triggering acute inflammation in the lungs due to the release of pro-inflammatory chemokines and cytokines such as the well-known IL-6 [207]. Moreover, the kallikrein/kinin and renin-angiotensin systems also play a thrombo-regulatory role [209]. Our data showed a two-fold up-regulation of Kininogen-1 in the exosomes of COVID-19 patients. Kininogen-1 itself has a relationship with the coagulation cascade, and it is considered an anti-thrombotic target. Indeed, its gene deletion has been associated with a reduced risk of induced thrombosis in mice [209]. Hemostatic and thrombotic manifestations are common in critical COVID-19 patients, and they are among the leading causes of death [203], while a high number of venous thromboembolism (VTE) events among severely ill patients with COVID-19 pneumonia has been observed worldwide [210]. Relying on the role of Kininogen-1 and our findings, we speculate that exosomes may serve as a reserve and carrier of Kininogen-1.

Bioinformatic analysis has also pointed out the IL-6 and TGFβ1 cytokines' involvement as upstream regulators of modulated protein. IL-6 is recognized as the main mediator of the inflammatory and immune response initiated by SARS-CoV-2 infection [211]. As an upstream regulator of the exosomal proteins in COVID-19 patients, we speculate that IL-6 may also affect protein secretion from cells through EVs. TGFβ1 is a pleiotropic cytokine with regulatory capabilities, and it is involved in the resolution of the inflammatory response [212]. The host response to infection could be regulated by TGFβ1 with the help of a cytokine storm and the presence of TNF, IL-1β, and IL-6 [213]. Lung fibrosis is among the clinical hallmarks of COVID-19 infection. It was identified as a leading cause of

pulmonary damage, as reported by Polak et al. (2020), who showed that 22% of patients presented a fibrotic pattern of lung injury characterized by interstitial fibrosis. Our data also suggest a correlation between TGFβ1, glucose, and exosomes. Interestingly, a correlation between a high concentration of glucose and worsening COVID-19 has been reported; for example, diabetic patients with uncontrolled glucose levels are evidently more prone to manifesting COVID-19 complications and consequent increased mortality—though the molecular mechanism currently remains undetermined [214]. Prolonged and uncontrolled hyperglycemia was also described as a prognostic factor [215]. Most importantly, exosomes' key role was already reported in the pathogenesis of diabetes nephropathy: high glucose leads to increased excretion of exosomes from macrophages through the TGF-β1 mRNA, which acts as a bridge between macrophages and mesangial cells [216]. A similar connection might also be applied to COVID-19, between macrophages and lung cells, even if other research is needed to investigate this hypothesis.

We also investigated exosomal proteins' potential role as diagnostic biomarkers for COVID-19 infection and disease severity. Several exosomal proteins—such as C-reactive protein, fibrinogen gamma chain, C4b-binding protein alpha chain, and alpha-1-acid glycoprotein 1—presented very good biomarker candidates, reporting an AUC of 1.

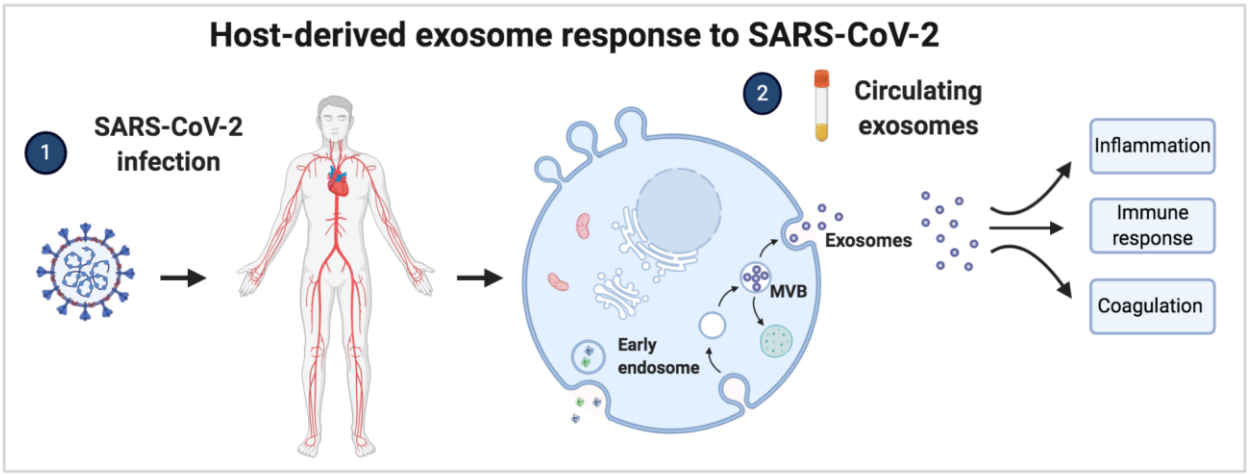

Figure 4.9: *host-derived exosome response to SARS-CoV-2 infection. Circulating exosomes are characterized by proteins and pathways involved in inflammation, immune response, and coagulation.*

Interestingly, the abundance of CRP, A1AG1, A1AG2, CXCL7, SAMP, and ZA2G proteins directly correlated with the disease's severity, as their increase among critical patients showed, by suggesting a potential use of these proteins not only for diagnosis but also for monitoring the disease's outcome and, potentially, any response to therapies. In line with our hypothesis, the

exosomal proteome was already investigated to monitor sepsis progression[217] and HIV patients subjected to antiretroviral therapy [218]. Huan et al. found that COVID-19 patients had significantly increased SAA and CRP levels, suggesting that SAA could serve as a biomarker to monitor the respiratory diseases' progression [219]. CRP levels positively correlated with the diameter of lung lesions and severe presentation [220,221], but also with an increased risk of organ failure and death [222]. Another interesting protein that we found to be up-regulated in critical patients is Fetuin-A. Exosomal Fetuin-A was already identified as a novel urinary biomarker for detecting acute kidney injury. We speculate that its up-regulation in critical COVID-19 patients can explain kidney injury, which is often reported in severe patients [223].

Further, among the exosomal proteins modulated in SARS-CoV-2 infection we found LYVE1, TIMP1 and CXCL7 (**fig. 4.5C**). This expression profile supports to some extent the role of macrophage activation syndrome (MAS) as the main driver of hyperinflammatory response in COVID-19 patients [224]. Indeed, while LYVE-1-expressing macrophages control arterial stiffness through modulation of the metalloproteinase-dependent proteolysis of the MMP-9 matrix [225], the expression of the MMPs inhibitor TIMP1 is related to the frequency of pulmonary macrophages and is involved in influenza-induced lung injury [226] and CXCL7 is a known attractant of macrophages in lung inflammation [227].

In addition, our data revealed the presence of several exosomal proteins that present the same expression pattern as proteins detected in the serum of COVID-19 patients. Serum proteomics is usually performed on circulating serum proteins, with a bias not to discriminate between proteins contained in the exosome cargo used for cell-to-cell communication, and it may represent a picture of the mechanisms involved in COVID-19. Exosomes' role may be particularly relevant in COVID-19 because SARS-CoV-2 infection is associated with tissue damage and multiple organ dysfunctions and circulating exosomes can potentially reach several distant target cells and organs.

Taken together, our study's findings provide the first evidence that circulating exosomes are strongly modulated during COVID-19 infection and might be involved in pathogenesis. The presence of viral material in the exosomal cargo showed that SARS-CoV-2 could use the cell-to-cell communication system to spread infection in the host. Proteomic analysis of plasma exosomes identified several molecules involved in immune response, inflammation, and the activation of coagulation and complement pathways, suggesting a significant role for exosomes in the mechanisms associated with tissue damage and multiple organ dysfunctions typical of COVID-19.

Another remarkable result emerging from these data is the presence of several potential biomarkers that are well correlated with the disease's severity. Although, to date, ours is the first study that characterizes the circulating exosomal proteins and pathways from SARS-CoV-2 infected patients, future studies are needed to determine the number and size of EVs in COVID-19. Moreover, monitoring exosomal content during infection may contribute to a better understanding of whether exosomes support viral spreading or induce immunological protection.

The present research has been carried out at the beginning of the pandemic. Several studies on vesicles were published after that. Pesce et al. showed that exosomes recovered from the plasma of COVID-19 Patients efficiently display SARS-CoV-2 Spike-derived fragments and can be used as a source of antigen presentation to enhance immune responses and through promote T-cell activation [228]. Interestingly, circulating EVs contribute to the production of antibodies and protective immunity [229,230]. Antibodies were found in circulating EVs 14 days after the second immunization and their levels were 12-fold higher compared to 14 days after the first vaccination [231]. In addition, clinical trials have shown some positive results in the therapeutical use of EVs indicating that EVs can help patients recover from COVID-19 [232]. Their findings showed that treatment with stem cell-derived EVs could play an important role in anti-SARS-CoV-2 and COVID-19-related inflammatory responses. Even though inactivated or attenuated viruses, single peptides, or viral vectors are currently being used for vaccine development [233], they failed to provide long-term immunity. EVs, as carriers for pathogenic vaccines, have been proposed as a new path for the development of effective novel COVID-19 pneumonia vaccines [234,235].

4.2.5 Supplementary data

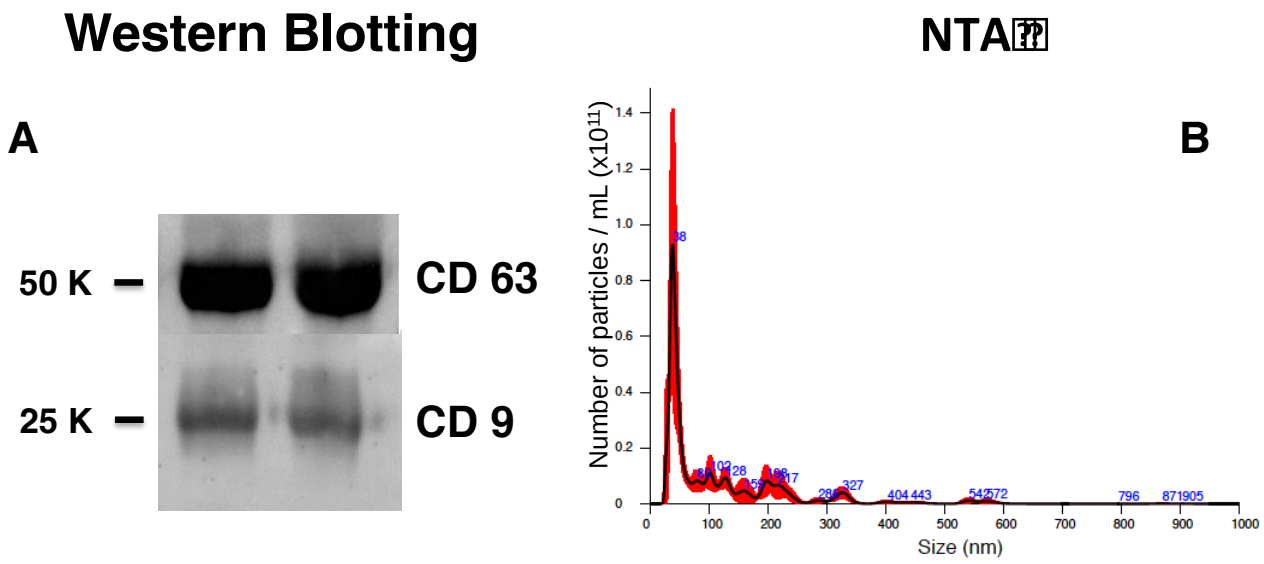

Supplementary figure 4.1: *characterization of exosomes isolated from the plasma of healthy patients. (A) Western blot analysis of the expression of proteins enriched in exosomes, including CD63 and CD9. (B) Nanoparticle tracking analysis to quantify the size and concentration of exosomes.*

Supplementary Table 4.1: *clinical indices of critical and non-critical COVID-19 patients.*

	Critical (n=7)	**Non-critical (n=10)**	***p-value***
D-dimer ng/mL	1927.40(1137-3030)	1127.37(298-2799)	0.12
Circulating CRP mg/L	14.22(2.84-32.21)	5.96(0.38-15.82)	0.073
PLTs (*10^3/µl)	305.57(45-514)	207.40(33-350)	0.13
RBCs (*10^3/µl)	**3.18(2.79-3.99)**	**4.53(2.67-6.07)**	**0.0071**
WBC (*10^3/µl)	**13.52(6.48-23.05)**	**6.80(1.75-14.11)**	**0.017**
Neutrophils (*10^2/µl)	81.88(65.6-93.1)	69.51(47.7-89.8)	0.063
Lymphocytes (*10^2/µl)	**11.04(3.9-19.4)**	**23.18(6.7-46)**	**0.034**
Monocytes (*10^2/µl)	5.14(2.2-11)	6.59(2.6-9.8)	0.32
Eosinophils (*10^2/µl)	**1.55(0-4.6)**	**0.28(0-1.2)**	**0.027**
Basophils (*10^2/µl)	0.37(0.1-1.1)	0.44(0-1.7)	0.75

Supplementary Table 4.2: *list of modulated proteins in critical COVID-19 patients compared to healthy subjects (Fold change > 1,3 and p-value < 0,05)*

Protein name	**p-value**	**Fold Change**
C4BPB_HUMAN	6,2342E-06	0,057068043
C4BPA_HUMAN	0,000022124	0,056619354
CATA_HUMAN	0,000086701	9,986360014
FIBG_HUMAN	0,00012	0,177521543
F13B_HUMAN	0,00012	0,203419412
C1S_HUMAN	0,00015	0,237813833
KV401_HUMAN	0,00016	0,29879762
A2MG_HUMAN	0,00017	0,130823636
ITIH2_HUMAN	0,0002	0,386749369
CFAI_HUMAN	0,00022	0,263697741
CO4A_HUMAN	0,00023	0,195003252
KV127_HUMAN	0,00027	0,441843837
CO2_HUMAN	0,00029	4,650412509
LYVE1_HUMAN	0,00043	9,661245093
TRY6_HUMAN	0,00045	0,002252562
FINC_HUMAN	0,00046	0,262336941
CCD34_HUMAN	0,00057	0,032457006
LYAM1_HUMAN	0,00066	2,919229176
PRDM9_HUMAN	0,00066	0,168694524
FIBA_HUMAN	0,00068	0,3358245
CO5_HUMAN	0,00073	0,420694062
HV226_HUMAN	0,00073	0,281968213

GELS_HUMAN	0,00076	0,199232169
FIBB_HUMAN	0,0008	0,376638163
PROS_HUMAN	0,00083	0,256666978
CO4B_HUMAN	0,00089	0,285894083
C2CD3_HUMAN	0,001	0,197743042
PSME4_HUMAN	0,00128	0,1354769
ZA2G_HUMAN	0,00131	11,64577619
TIMP1_HUMAN	0,00135	11,14554671
EXD1_HUMAN	0,00176	0,128289368
TRY1_HUMAN	0,00191	0
IGHM_HUMAN	0,00218	0,210444517
PRP19_HUMAN	0,00223	0,068783288
C1QC_HUMAN	0,00262	0,186194923
APOE_HUMAN	0,00274	0,47584927
H33_HUMAN	0,00295	3,309966072
NOLC1_HUMAN	0,00314	0,357875978
TITIN_HUMAN	0,00376	11,92626787
HV64D_HUMAN	0,0038	0,254752775
PERM_HUMAN	0,0038	5,290529099
HV601_HUMAN	0,00398	0,286883525
ITIH1_HUMAN	0,00427	0,434659046
SEMG2_HUMAN	0,00435	2,470272462
FA12_HUMAN	0,00463	0,395176878
SHRM3_HUMAN	0,00495	6,527870333
SAA4_HUMAN	0,00525	3,159165246
FCN3_HUMAN	0,00609	0,128247693
ANXA2_HUMAN	0,00657	2,346901685
HGFA_HUMAN	0,00667	1,917309949
CXCL7_HUMAN	0,0071	9,392765707
S10A9_HUMAN	0,0071	9,422251773
C1R_HUMAN	0,00771	0,14933392
ILDR2_HUMAN	0,00773	3,302530646
APOH_HUMAN	0,00781	3,318007921
IC1_HUMAN	0,00795	3,427063096
K2C78_HUMAN	0,00799	4,527978891
1B51_HUMAN	0,00804	3,111992864
CO1A1_HUMAN	0,00816	3,018184279
CO6_HUMAN	0,00817	0,301476058
AT1A1_HUMAN	0,00864	0,12594374
C1QB_HUMAN	0,00875	0,32003548
VTDB_HUMAN	0,00878	3,201480222
APOB_HUMAN	0,0088	0,26104253
LYSC_HUMAN	0,00903	13,65084913

CAH1_HUMAN	0,0092	4,747490261
FBLN1_HUMAN	0,00957	0,383056767
CD5L_HUMAN	0,00957	0,210198015
HV372_HUMAN	0,00998	0,360344636
CO3_HUMAN	0,01013	0,251835626
SAMP_HUMAN	0,01037	5,959375175
S10A8_HUMAN	0,0104	5,050026135
CHIT1_HUMAN	0,01058	2,840403577
AMY1_HUMAN	0,01079	6,094253621
KV106_HUMAN	0,01129	0,486089866
FA11_HUMAN	0,01169	0,282835232
VWF_HUMAN	0,01216	0,329685708
CERU_HUMAN	0,01227	3,376122098
FGL1_HUMAN	0,01254	2,769790781
PI16_HUMAN	0,01259	2,307028384
CO8G_HUMAN	0,0129	0,209817223
SRCRL_HUMAN	0,01309	3,94947218
VCAM1_HUMAN	0,0134	4,493661069
TETN_HUMAN	0,01378	0,251628074
SGK1_HUMAN	0,01381	4,8289747
FCG2C_HUMAN	0,01381	3,428590231
HV428_HUMAN	0,01386	0,434828534
MNS1_HUMAN	0,01443	5,435953758
HV315_HUMAN	0,01472	0,457275916
KV224_HUMAN	0,01529	0,334545421
IGJ_HUMAN	0,01607	0,330227766
LYST_HUMAN	0,01643	0,451086431
HBB_HUMAN	0,01664	4,691635447
IGL1_HUMAN	0,01781	0,372168417
A1AG1_HUMAN	0,01795	38,43218244
FA10_HUMAN	0,01852	2,682969182
KNG1_HUMAN	0,01859	1,984182793
HV551_HUMAN	0,01889	0,461950379
DMKN_HUMAN	0,0189	3,482605646
OSTP_HUMAN	0,02028	5,272393106
IPSP_HUMAN	0,02226	3,875684488
DCD_HUMAN	0,02273	3,849522843
H4_HUMAN	0,02282	3,434246449
HV309_HUMAN	0,02427	0,432314978
HNRH2_HUMAN	0,02454	5,113294387
IFFO2_HUMAN	0,02509	2,980791689
PC_Human	0,02671	2,512048554
PTPRC_HUMAN	0,02728	2,608309747

BST1_HUMAN	0,02837	2,470849689
SNED1_HUMAN	0,02922	3,054256726
CATS_HUMAN	0,03021	3,668176032
MBL2_HUMAN	0,0306	0,475917868
CYTA_HUMAN	0,03073	3,451870845
A20A4_HUMAN	0,03155	5,051623717
JHD2C_HUMAN	0,03163	5,920581658
A2GL_HUMAN	0,03209	5,393946144
APOF_HUMAN	0,03219	2,063805162
TPM4_HUMAN	0,0325	4,347605515
THIO_HUMAN	0,03257	2,971901497
AACT_HUMAN	0,03296	5,575361494
FHR3_HUMAN	0,03304	3,309404011
SODE_HUMAN	0,0335	3,527582679
CRP_HUMAN	0,034	122,0134602
LV949_HUMAN	0,03522	0,439982297
CR1_HUMAN	0,03548	3,857242056
HV323_HUMAN	0,03562	0,304537476
A1BG_HUMAN	0,03644	3,038527378
ACTB_HUMAN	0,03672	4,784631774
SRRM1_HUMAN	0,03784	0,072398658
QSOX1_HUMAN	0,03803	2,109645278
HPTR_HUMAN	0,03817	0,377157268
TIMP2_HUMAN	0,03821	3,043441212
HBA_HUMAN	0,03827	3,043410786
FETUA_HUMAN	0,0384	2,747753339
PROC_HUMAN	0,03848	0,261749402
CBG_HUMAN	0,03854	2,966059111
CYTC_HUMAN	0,0393	8,83023845
TBA1A_HUMAN	0,03954	2,678010139
IGG1_HUMAN	0,0396	0,623000452
H2B1J_HUMAN	0,03962	3,177320683
TNPO1_HUMAN	0,04043	3,746682361
AFAM_HUMAN	0,04066	3,054642422
TKT_HUMAN	0,04077	2,058223139
CCL14_HUMAN	0,04084	11,40462505
PAP1L_HUMAN	0,04122	0,311776305
BGH3_HUMAN	0,04135	2,204790137
LV657_HUMAN	0,04161	0,585207638
CO8A_HUMAN	0,0419	0,254931084
AXDN1_HUMAN	0,04235	2,975056289
CBPB2_HUMAN	0,04243	0,500084574
SRGN_HUMAN	0,04367	4,437883439

K2C1B_HUMAN	0,04379	3,024623582
FBLN1_HUMAN	0,04449	0,187130142
HV118_HUMAN	0,04516	0,546925874
HGFL_HUMAN	0,04549	0,462200139
FBLN3_HUMAN	0,04642	0,427911564
IGHG3_HUMAN	0,04957	0,434122795

Supplementary Table 4.3: *list of modulated proteins in non-critical COVID-19 patients compared to healthy subjects (Fold change > 1,3 and p-value < 0,05).*

Protein name	p-value	Fold Change
CRP_HUMAN	5,5248E-07	40,4018464
FIBB_HUMAN	1,9737E-06	0,30600139
C4BPB_HUMAN	5,1798E-06	0,20579365
FIBG_HUMAN	0,000006867	0,1931
C4BPA_HUMAN	0,00001503	0,194354342
A1AG1_HUMAN	0,000057988	5,799444828
FIBA_HUMAN	0,00016	0,275962221
A1AG2_HUMAN	0,00018	4,069317641
MBL2_HUMAN	0,00033	0,222591309
HV64D_HUMAN	0,00034	0,145197669
KV401_HUMAN	0,00041	0,382486948
PRDM9_HUMAN	0,00042	0,233036509
KVD30_HUMAN	0,00043	0,305092188
HV309_HUMAN	0,00055	0,278452627
FBLN1_HUMAN	0,00069	0,304220987
HV372_HUMAN	0,00069	0,275015185
FGL1_HUMAN	0,00069	6,184636789
PGRP2_HUMAN	0,0008	0,336908232
CFAH_HUMAN	0,00103	0,363171483
CCD34_HUMAN	0,00106	0,24274253
ZA2G_HUMAN	0,00135	4,053021644
KV127_HUMAN	0,00136	0,403975815
MOONR_HUMAN	0,00138	0,403644554
ALBU_HUMAN	0,00187	5,166482861
ATS2_HUMAN	0,00263	0,298665866
AACT_HUMAN	0,00296	8,398893959
FA11_HUMAN	0,00316	0,28986986
HGFL_HUMAN	0,00324	0,260521693
FCN2_HUMAN	0,00369	5,858964805
PKP1_HUMAN	0,00548	2,692385236
CFAI_HUMAN	0,00644	0,465444934

B2MG_HUMAN	0,00694	5,134931064
HEP2_HUMAN	0,00707	5,220725291
HV323_HUMAN	0,00715	0,227460187
HVD82_HUMAN	0,00732	0,287649455
JHD2C_HUMAN	0,00755	4,057396809
C1R_HUMAN	0,00775	0,273841296
A2GL_HUMAN	0,00787	5,68147206
HV364_HUMAN	0,00803	0,34998924
IGHG2_HUMAN	0,00833	0,496151782
FINC_HUMAN	0,00849	0,495880541
VCAM1_HUMAN	0,00888	3,870749324
A1AT_HUMAN	0,00954	3,79142094
KV105_HUMAN	0,00959	0,104961724
SAMP_HUMAN	0,01029	3,646505404
CO8G_HUMAN	0,01068	0,300000335
APOA2_HUMAN	0,01139	8,504293381
CO4A_HUMAN	0,01174	0,498299509
HV551_HUMAN	0,01196	0,403565587
PSME4_HUMAN	0,01265	0,404291151
F13B_HUMAN	0,01384	0,465788971
APOH_HUMAN	0,01394	0,356661201
CATA_HUMAN	0,01489	1,994838608
SAA4_HUMAN	0,01537	9,534034159
TENA_HUMAN	0,01539	4,867651292
NCAM1_HUMAN	0,01676	2,092365207
CO9_HUMAN	0,01782	2,552254852
IC1_HUMAN	0,01789	3,551246946
AMBP_HUMAN	0,01946	3,127272694
IGHM_HUMAN	0,01976	0,410331102
FCG3B_HUMAN	0,0199	0,319699988
GELS_HUMAN	0,02037	0,519283985
HV102_HUMAN	0,02105	0,465136952
APOD_HUMAN	0,02108	5,761049855
ANGT_HUMAN	0,02177	3,770039234
IGHG3_HUMAN	0,02297	0,41724942
KV224_HUMAN	0,02317	0,432151711
A1BG_HUMAN	0,02432	5,468056453
ITIH3_HUMAN	0,02491	8,915050778
ITIH4_HUMAN	0,02656	1,880666769
GGH_HUMAN	0,02816	2,102032915
CXCL7_HUMAN	0,02817	3,719329452
APC_HUMAN	0,02845	10,69922885
ILDR2_HUMAN	0,02897	2,029607667

CO4B_HUMAN	0,0294	0,523361586
IGLL1_HUMAN	0,02941	0,376986418
TITIN_HUMAN	0,02962	3,017172332
A2AP_HUMAN	0,03029	2,552497644
PSA5_HUMAN	0,03139	3,738470765
SRCRL_HUMAN	0,03185	4,763554475
IGA2_HUMAN	0,03204	2,286289975
NOLC1_HUMAN	0,03231	0,40015027
HV349_HUMAN	0,03236	0,373924209
CO8A_HUMAN	0,03244	0,312816789
TPM4_HUMAN	0,03351	2,571856485
KNG1_HUMAN	0,03393	3,552948208
LG3BP_HUMAN	0,03664	2,712516234
HPT_HUMAN	0,03667	40,5088796
PON1_HUMAN	0,03925	2,638056721
TPM1_HUMAN	0,04091	3,131972523
IGHG4_HUMAN	0,04133	0,353915401
RET4_HUMAN	0,04222	2,447074625
PIT1_HUMAN	0,0455	8,455563275
HABP2_HUMAN	0,04575	9,690248441
KNG1_HUMAN	0,04671	5,04949148
LYVE1_HUMAN	0,04866	2,984066259
TRY3_HUMAN	0,04919	13,9783535

Supplementary Table 4.4: *correlation analysis between proteins abundance and platelets count. The p-value, R square and r are reported for the most correlated proteins.*

accession name	Protein name	gene	P (two-tailed)	R squared	r
TIMP2_HUMAN	Metalloproteinase inhibitor 2	TIMP2	0,0108	0,3608	0,6007
K2C6A_HUMAN	Keratin, type II cytoskeletal 6A	KRT6A **K6A,** *KRT6D*	0,0116	0,3547	-0,5956
ANXA6_HUMAN	Annexin A6	ANXA6 **ANX6**	0,0146	0,3368	0,5804
CO6A3_HUMAN	Collagen alpha-3(VI) chain	COL6A3	0,0147	0,3362	0,5799
ISK1_HUMAN	Serine protease inhibitor Kazal-typ**…**	SPINK1 **PSTI**	0,0165	0,327	0,5718
IBP4_HUMAN	Insulin-like growth factor-binding **…**	IGFBP4 **IBP4**	0,0209	0,3074	0,5544
IBP2_HUMAN	Insulin-like growth factor-binding **…**	IGFBP2 **BP2,** *IBP2*	0,0222	0,3025	0,55
HV108_HUMAN	Immunoglobulin heavy variable 1-8	IGHV1-8	0,0223	0,3019	0,5495
VSIG4_HUMAN	V-set and immunoglobulin domain-con**…**	VSIG4 **CRIg**, *Z39IG, UNQ317/PRO362*	0,0258	0,2899	0,5384
NCAM1_HUMAN	Neural cell adhesion molecule 1	NCAM1 **NCAM**	0,0278	0,2833	-0,5323
COIA1_HUMAN	Collagen alpha-1(XVIII) chain	COL18A1	0,0326	0,2697	0,5193
APOA2_HUMAN	Apolipoprotein A-II	APOA2	0,0334	0,2678	-0,5175
APOC2_HUMAN	Apolipoprotein C-II	APOC2 *APC2*	0,0343	0,2655	-0,5153
CFAB_HUMAN	Complement factor B	CFB BF**,** *BFD*	0,0351	0,2636	0,5134
MYH7_HUMAN	Myosin-7	MYH7 *MYHCB*	0,0399	0,2523	0,5023

K2C75_HUMAN	Keratin, type II cytoskeletal 75	KRT75 **K6HF,** *KB18*	0,043	0,2457	-0,4957
CH3L1_HUMAN	Chitinase-3-like protein 1	CHI3L1	0,0487	0,2348	0,4846

Supplementary Table 4.5: *correlation analysis between proteins abundance and circulating CRP levels. The p-value, R square and r are reported for the most correlated proteins.*

accession name	Protein name	gene	P (two-tailed)	R squared	r
CRP_HUMAN	C-reactive protein	CRP *PTX1*	0,0002	0,6994	0,8363
IBP2_HUMAN	Insulin-like growth factor-binding ...	IGFBP2 **BP2,** *IBP2*	0,0003	0,6762	0,8223
CH3L1_HUMAN	Chitinase-3-like protein 1	CHI3L1	0,0005	0,6534	0,8083
MOONR_HUMAN	Protein moonraker	KIAA0753 **MNR**, *OFIP*	0,0007	0,6324	0,7952
ISK1_HUMAN	Serine protease inhibitor Kazal-typ...	SPINK1 **PSTI**	0,0011	0,6049	0,7778
IBP4_HUMAN	Insulin-like growth factor-binding ...	IGFBP4 **IBP4**	0,0023	0,5521	0,743
FIBB_HUMAN	Fibrinogen beta chain	FGB	0,0028	0,5392	0,7343
FHR5_HUMAN	Complement factor H-related protein...	CFHR5 **CFHL5,** *FHR5*	0,0028	0,5378	0,7333
HV373_HUMAN	Immunoglobulin heavy variable 3-73	IGHV3-73	0,0082	0,4542	0,674
FIBG_HUMAN	Fibrinogen gamma chain	FGG **PRO2061**	0,009	0,4469	0,6685
TRY2_HUMAN	Trypsin-2	PRSS2 **TRY2,** *TRYP2*	0,0145	0,4045	0,636
LYVE1_HUMAN	Lymphatic vessel endothelial hyalur...	LYVE1 **CRSBP1,** *HAR, XLKD1, UNQ230/PRO263*	0,0161	0,3949	0,6284
PROP_HUMAN	Properdin	CFP **PFC**	0,0164	0,3931	0,627
FIBA_HUMAN	Fibrinogen alpha chain	FGA	0,0195	0,3772	0,6142
APC_HUMAN	Adenomatous polyposis coli protein	APC *DP2.5*	0,0316	0,3303	-0,5747
CFAH_HUMAN	Complement factor H	CFH **HF**, *HF1, HF2*	0,0332	0,3254	0,5705
C163A_HUMAN	Scavenger receptor cysteine-rich ty...	CD163 **M130**	0,0352	0,3193	0,565
FCGBP_HUMAN	IgGFc-binding protein	FCGBP	0,0366	0,3155	0,5617
CATA_HUMAN	Catalase	CAT	0,0426	0,3001	0,5478

Supplementary Table 4.6: *correlation analysis between proteins abundance and D-dimer levels. The p-value, R square and r are reported for the most correlated proteins.*

accession name	Protein name	gene	P (two-tailed)	R squared	r
FETUA_HUMAN	Alpha-2-HS-glycoprotein	AHSG *FETUA, PRO2743*	0,0053	0,5219	0,7224
KPYM_HUMAN	Pyruvate kinase PKM	PKM *OIP3, PK2, PK3, PKM2*	0,007	0,498	0,7057
FINC_HUMAN	Fibronectin	FN1 *FN*	0,0143	0,4342	-0,6589
A1AG1_HUMAN	Alpha-1-acid glycoprotein 1	ORM1 *AGP1*	0,0228	0,3887	0,6235
VSIG4_HUMAN	V-set and immunoglobulin domain-con...	VSIG4 **CRIg**, *Z39IG, UNQ317/PRO362*	0,0256	0,5329	-0,73
TRY6_HUMAN	Putative trypsin-6	PRSS3P2 **T6,** *TRY6*	0,0416	0,4697	-0,6853
SAMP_HUMAN	Serum amyloid P-component	APCS **PTX2**	0,0418	0,3253	-0,5703
MOONR_HUMAN	Protein moonraker	KIAA0753 **MNR**, *OFIP*	0,0446	0,4601	-0,6783
CO4B_HUMAN	Complement C4-B	C4B **CO4,** *CPAMD3*	0,0448	0,3178	-0,5637

Supplementary Table 4.7: *correlation analysis between proteins abundance and neutrophils counts. The p-value, R square and r are reported for the most correlated proteins.*

Accession name	Protein name	Gene	P (two-tailed)	R squared	r
FIBA_HUMAN	Fibrinogen alpha chain	FGA	0.0051	0.41	0.64
TPIS_HUMAN	Triosephosphate isomerase	TPI1	0.010	0.36	-0.60
IGLC7_HUMAN	Immunoglobulin lambda constant 7	IGLC7	0.010	0.36	-0.6
CLUS_HUMAN	Clusterin	CLU	0.012	0.34	0.58
SAA1_HUMAN	Serum amyloid A-1 protein	SAA1	0.013	0.34	0.58
APC_HUMAN	Adenomatous polyposis coli protein	APC	0.016	0.32	-0.57
FA11_HUMAN	Coagulation factor XI	F11	0.017	0.32	0.56
SAA2_HUMAN	Serum amyloid A-2 proteincur	SAA2	0.018	0.31	0.56
QSOX1_HUMAN	Sulfhydryl oxidase 1	QSOX1	0.027	0.28	0.53
ANT3_HUMAN	Antithrombin-III	SERPI	0.027	0.28	0.53
PLAK_HUMAN	Junction plakoglobin	JUP	0.030	0.27	-0.52
EMSY_HUMAN	BRCA2-interacting transcriptional	EMSY	0.032	0.26	-0.51
NUCL_HUMAN	Nucleolin	NCL	0.036	0.26	0.51
TRY3_HUMAN	Trypsin-3	PRSS3	0.039	0.25	-0.50
ANXA6_HUMAN	Annexin A6	ANXA6	0.040	0.25	0.50
IGHG4_HUMAN	Immunoglobulin heavy constant gamma	IGHG4	0.040	0.25	0.50
ZA2G_HUMAN	Zinc-alpha-2-glycoprotein	AZGP1	0.041	0.24	0.49
TRY6_HUMAN	Putative trypsin-6	PRSS3P2	0.042	0.24	-0.49
CO8A_HUMAN	Complement component C8 alpha chain	C8A	0.046	0.23	0.48

Supplementary Table 4.8: *correlation analysis between proteins abundance and monocytes counts. The p-value, R square and r are reported for the most correlated proteins.*

Accession name	Protein name	Gene	P (two-tailed)	R squared	r
ALS_HUMAN	Insulin-like growth factor-binding	IGFALS	0.0032	0.45	-0.67
PROP_HUMAN	Properdin	CFP	0.0049	0.41	0.64
CLUS_HUMAN	Clusterin	CLU	0.0071	0.39	-0.62
ZA2G_HUMAN	Zinc-alpha-2-glycoprotein	AZGP1	0.011	0.35	-0.59
ANT3_HUMAN	Antithrombin-III	SERPINC1	0.013	0.34	-0.58
FA11_HUMAN	Coagulation factor XI	F11	0.018	0.31	-0.56
QSOX1_HUMAN	Sulfhydryl oxidase 1	QSOX1	0.027	0.28	-0.53
HV373_HUMAN	Immunoglobulin heavy variable 3-73	IGHV3-73	0.028	0.28	0.52
GPX3_HUMAN	Glutathione peroxidase 3	GPX3	0.034	0.26	-0.51
TPM4_HUMAN	Tropomyosin alpha-4 chain	TPM4	0.037	0.25	-0.50
A2GL_HUMAN	Leucine-rich alpha-2-glycoprotein	LRG1	0.042	0.24	-0.49
APOC3_HUMAN	Apolipoprotein C-III	APOC3	0.044	0.24	-0.49
AACT_HUMAN	Alpha-1-antichymotrypsin	SERPINA3	0.044	0.24	-0.49
SEPP1_HUMAN	Selenoprotein P	SELENOP	0.047	0.23	-0.48
IFFO2_HUMAN	Intermediate filament family orphan	IFFO2	0.048	0.23	0.48

5 METABOLIC DISEASE

5.1 METAPROTEOMICS AND METABOLOMICS FOR CHARACTERIZING THE TAXONOMY AND FUNCTIONALITY OF THE GUT MICROBIOTA

The term *gut microbiome* describes the vast collection of symbiotic microorganisms in the human gastrointestinal system that have co-evolved with our species and are essential for human health [236]. The gut microbiome performs numerous important biochemical functions for the host, and disorders of the microbiome are associated with many and diverse human disease processes [237]. Many factors, such as environment, aging, diet, and the immune system, can disturb the intestinal microbiota composition, known as dysbiosis. Changes in the bacterial composition of the gut microbiota have been associated not only with the dysfunction of the digestive system, such as inflammatory bowel diseases (IBDs) [238] and obesity [239], but also with the etiopathogenesis of circulatory disease [240], autism [241] and cancer [242]. Whereas the next-generation sequencing can be readily used to determine the composition of the microbiota, metaproteomics and metabolomics enables the functional study of proteins and metabolites as they are expressed and produced by microbial communities [243]. Considering that the gut microbiome may be directly modulated for the benefit of the host organism, it represents a fertile ground for the development of the next generation of therapeutic drug targets [244]. Quantitative metaproteomics and metabolomics emerged as powerful approaches to characterize microbial function in diseases pathogenesis [245].

5.2 METAPROTEOMICS AND METABOLOMICS INVESTIGATION OF MICROBIOME ALTERATIONS IN PEDIATRIC OBESE PATIENTS SUBJECTED TO A DIETARY INTERVENTION WITH MEDITERRANEAN DIET

5.2.1 Background and Rationale

In 1997, the W.H.O. (World Health Organization) recognized obesity in childhood as a global phenomenon with epidemic character and important health implications (World Health Organization, 1997). From 1980 to 2013, the worldwide prevalence of overweight and obesity in children and adolescents increased by 47.1%, with alarming data especially in developing countries [164]. Several studies reported a close association between pediatric obesity and co-morbidities

such as cardiovascular diseases and diabetes [246]. In addition, obese children and adolescents are likely to maintain excess weight in adulthood [247], and although acute cardiovascular events are rare in children, problems related to hypertension, dyslipidemia, insulin resistance and endothelial dysfunctions are often diagnosed in young obese subjects [248,249].

However, the progression of obesity-associated co-morbidities can be delayed or even prevented in pediatric age if appropriate lifestyle modifications, such as diet and physical activity, are implemented. Indeed, among adults, a Mediterranean lifestyle has been inversely associated with mortality and development of chronic disorders, such as cardiovascular disease, obesity, metabolic syndrome, type 2 diabetes mellitus, and neoplasms, but also an improved cognitive status, longevity, and overall health well-being [250]. The MD is characterized by a high intake of vegetables, legumes, fruits, nuts, and grains, with a moderate-to-high intake of fish and unsaturated fats (in particular, olive oil), and a low-to-moderate intake of dairy products and meats, which are low in saturated fat [251]. Despite the enthusiasm derived from the results on the Mediterranean lifestyle, few but alarming data suggest its poor adherence in pediatric age, who usually prefer unhealthy food [164].

Although the great efforts in public health and policy to reverse childhood obesity, limited interventional studies with effective long-term maintenance of weight loss in children are available. However, a growing interest on the use of educational training and gamification to influence lifestyle and to improve well-being is emerging.

Recently, several evidence linked obesity to the gut microbiota [252]. Human gut microbiota is the set of microorganisms that colonize the human intestine establishing a symbiosis that in a physiological situation brings multiple benefits to the host (eubiosis). Both genetic and environmental factors can cause dysbiosis of the gut microbiota, thus contributing to pathological states such as obesity. The state of intestinal dysbiosis can be improved through the modulation of several factors, including lifestyle and diet, with the latter being one of the main determinants. To date, several studies investigated the relationships between nutrition, microbiota and obesity[252], and a future goal will be the modulation of the gut microbiota through nutrition to improve the pathological condition of obesity and other diseases.

Although the study of intestinal microbiota is still challenging, today, thanks to recent developments of omics techniques such as metagenomics, metaproteomics and metabolomics, the gut microbiota characterization is possible. Metagenomics has been widely applied to investigate bacteria alterations [253], while metaproteomics and metabolomics involves non-targeted mass

spectrometry to assess the diversity and abundance of microbial proteins and the impact of microbiota on small molecules production, respectively [254].

In the present research we aimed to assess the impact of a MD intervention on the gut microbiota of pediatric obese patients. The dietary intervention was based on educational training using gamification, while untargeted metaproteomics and metabolomics were employed to study alterations of the gut microbiota and plasma after six and twelve months of diet.

5.2.2 Material and methods

5.2.2.1 Experimental design

The study involved 15 pediatric obese subjects (9 male and 6 female) aged between 10 and 15 years (**Table 5.1**). The obesity condition was defined according to the International Obesity Task Force (IOTF) criteria [255]. The inclusion criteria were: waist circumference ≥ 90th percentile, BMI z-score > 25 and no previous adherence to any diet. The exclusion criteria were: secondary obesity associated to endocrine or genetic causes, type 1 diabetes and previous kidney diseases.

The enrolled patients received a standard diet, based on the Mediterranean pyramid, according to *Good Clinical Practice*[1]. The diet expected the consumption of 55-60% of carbohydrates (45-50% complex and no more than 10% refined and processed sugars), 25-30% lipids and 15% proteins. The dietary plan at the individual level was calculated in accordance with the Italian Reference Dietary Intakes (LARN) guidelines for age and gender [256]. The dietary intakes of macronutrients before, at 6 and 12 months of MD are shown in **table 4.1.** Before starting the diet, patients followed a MD educational training with explanation of MD Pyramid and gamification of the dietary plan through "The Mediterranean Goose". The game has been proposed in an educational project known as "Mediterranean diet and enhancement of traditional foodstuff - MedDiet", founded by European Union in the framework of the ENPI CBC Mediterranean Sea Basin Program [257]. In addition, all subjects received general recommendations about performing physical activity. Patients were subjected to biochemical and ultrasound evaluations at the time of enrollment and during the first 2 weeks after study started. During the year of diet intervention, patients were also evaluated after 6 and 12 months through the collection of stool and blood samples.

[1] Good Clinical Practice: the protocol will be conducted in accordance with the declaration of Helsinki. Informed consent will be obtained from all parents prior to the evaluations and after careful explanations to each patient.

Table 45.1: *demographic characteristics and macronutrient intake of the subjects enrolled in the study.*

Variable	Obese subjects					
	0 months		6 months		12 months	
	Mean	*Range*	*Mean*	*Range*	*Mean*	*Range*
Gender (n°)	15					
Male	9					
Female	6					
Age Mean (years)	12	10.0 - 15.0				
BMI for age (percentile)	97	95 - 99	94	82 - 99	96	92 - 99
Carbohydrate intake	254	177 - 354	237	192 - 344	248	191 - 323
Protein intake (g)	74	50 - 93	79	60 - 93	72	59 - 84
Fiber intake (g)	17	7.6 - 30.2	19	10.7 - 27.1	18	7.8 - 25.2
Fat intake (g)	89	57 - 139	77	56 - 96	74	57 - 93

5.2.2.2 Metaproteomics analysis

Each stool sample underwent microbial cell and protein extractions. Following protein purification, proteins were subjected to tryptic proteolytic digestion and desalting to obtain purified peptides. Peptides were separated, analyzed, and quantified by nano liquid chromatography coupled to mass spectrometry (nanoLC-MS/MS). Through metaproteomics analysis of the identified peptides, phylogenetic and functional analyses were performed to assign the identified peptides to bacterial taxa, biological processes, molecular functions, and enzymes. An appropriate statistical analysis was conducted aimed at understanding and discussing the statistically significant results.

5.2.2.3 Sample preparation and proteins extraction

Fecal samples were collected from patients and immediately stored at −80 °C. 100 mg of stool sample was weighted under a biological hood and deposited in a screw top tube with 1.4mm ceramic beads, 0.1mm silica beads and 4mm glass beads. 1ml of PBS was added and vortexed. Samples were then lysed using a Tissue Lyser FastPrep-24 5G (MP Biomedical, LCC) for 40 seconds at 6 m/s. The samples were then subjected to 300 x g of centrifugation for 5 minutes at 4 °C. The supernatant was transferred to new centrifuge tube and stored at 4 °C. The pellet was subjected to an additional 3 cycles of Tissue Lyser with the addition of 1 mL of PBS each time. Next, for each sample, the resulting supernatants were combined and subjected to centrifugation at 14.000 x g for 20 minutes at 4 °C. The supernatants were then discarded, the pellets resuspended with 1 mL PBS and centrifuged at 14.000 x g for 20 min at 4 °C. Next, the supernatant was discarded, and the pellet resuspended in 200 µL of NH_4HCO_3 100 mM. Then, 200 µL of lysis buffer (4% SDS, 6M Urea, 50 mM

Tris HCl pH8) were added and mixed thoroughly by vortexing. Samples were sonicated for 2 minutes at 27% amplitude (10 second pulse + 10 second rest for 6 times). Successively, samples were subjected to protein precipitation: 1.5 mL of acetone:ethanol (1:1) acidified with HCl (pH 2) were added and mixed well. Samples were left over night (approximately 18 hours) at -20 °C.

Subsequently, samples were centrifuged at 5.000 x g of centrifugation for 30 min at 4 °C. The supernatant was discarded and the pellet containing bacterial proteins was resuspended with 1.5 mL of acidified (pH 2) acetone:ethanol (1:1) and centrifuged at 20.000 x g for 10 minutes at 4°C. Finally, the supernatant was removed and the pellet containing only bacterial proteins was resuspended in 200 µl of urea buffer (8M urea, 10 mM tris HCl pH 8) and stored at 4°C. Protein quantification was performed using Bradford assay.

5.2.2.4 Protein digestion and peptides purification

For each sample, 80 µg of total protein was then subjected to reduction with DTT 200 mM, alkylation with IAM 200 mM, and to complete enzymatic digestion with trypsin 0.2 ug/uL at a 1:25 protein ratio (Sigma-Aldrich Inc., St. Louis, MO, USA).

Peptides were desalted on the Discovery® DSC-18 solid phase extraction (SPE) 96-well plate (25 mg/well) (Sigma-Aldrich Inc., St. Louis, MO, United States) as described previously (**paragraph. 2.3.2.3**). After the desalting process, the samples were vacuum-evaporated and reconstituted in mobile phase (0.1 % formic acid in water) for successive analysis.

5.2.2.5 NanoLC-MS/MS analysis

NanoLC-MS/MS analysis was performed with an Easy nano-LC 1200 system (Thermo Scientific, Milan), on a 200-cm PharmaFluidics µPACTM C18 column. The injection volume for each analysis was 2.0 µL. The mobile phases consisted of 0.1% formic acid in water (solvent A) and 0.1% formic acid in 80:20 acetonitrile:water (solvent B), the column flow rate was 300 nL min-1. The solvent gradient used for the chromatographic run was 210 min: 2 to 30% solvent B for 147 min, 56% solvent B for 56 min, and 99% solvent B for 7 min. The LC system was interfaced with a TripleTOF 5600+ (Sciex, Concord, Canada) equipped with a DuoSpray ion source. The mass spectrometry analysis was performed in a mass range of 100 to 1600 Da (TOF scan with an accumulation time of 0.25 s), followed by an MS/MS scan of product ions from 400 to 1250 Da (accumulation time 5.0 ms) with an abundance threshold set at 30 cps (40 candidate ions could be monitored per cycle). The MS data were acquired with Analyst TF 1.7 (AB SCIEX, Concord, Canada). Peptides (and proteins) were identified using DDA followed by database search.

5.2.2.6 *Proteins and peptides identification*

Protein identification was performed by building a database using the adapted MetaProIQ approach [258]. The mass spectrometry files were searched using Mascot v. 2.4 (Matrix Science Inc., Boston, USA). The digestion enzyme selected was trypsin with 2 missed cleavages and the following modifications: carbamidomethyl cysteines as fixed modification and oxidized methionine as variable modification. The peptide mass tolerance was set to 50 ppm, while 0.1 Da were used for the MS/MS tolerance. The charges of the peptides to search for were set to 2 +, 3 + and 4 +, the search was put on monoisotopic mass, and the instrument was set to ESI-QUAD-TOF. Each sample was searched against a reduced database generated by merging two existing databases: UniProt-KB Swiss-Prot Bacteria (331.559 sequences) [259] and Integrated Gene Catalog (IGC) [260]. IGC is a database of bacterial protein sequences built by combining data from 249 sequenced samples of the Metagenomics of the Human Intestinal Tract (MetaHit) project with 1018 samples previously sequenced in other works. IGC contains 9879896 genes related to most human intestinal bacteria.
The MetaProIQ approach consists of an initial search against the entire database and the creation of a reduced database generated with the proteins identified by the first search without filtering for FDR and converted in FASTA sequences. This was done for each sample. Each sample was finally analyzed against the corresponding reduced database and the proteins identified at this stage were filtered with FDR 1%.

5.2.2.7 *Metaproteomics data analysis and statistical analysis*

Metaproteomics analysis of the data was performed by evaluating the peptides identified by mass spectrometry analysis. The identified peptides were processed on Unipept version 4.0 [261] in order to analyze phylogenetical and functional variations of the microbiota of obese pediatric patients at time 0 and following the six-month and twelve-months of MD intervention.
Unipept analysis provides graphical representations of the microbiota composition (Kingdom, Phylum, Class, Order, Family, Genus and Species) and simultaneously allows the download of results related to the number of peptides assigned to each component of each taxonomic level. Through the use of Unipept, the proteomic analysis of the previously identified peptides was carried out not only for a phylogenetic framework (phylum, order, genus and species levels were analyzed in the present work) but also for the evaluation of the functions of the intestinal microbiota in order to assess differences in metabolic activities of taxa present within the microbiota community following six and twelve months of treatment with MD. To this end, Unipept, through its accurate database

search, allows to assign the identified unique peptides to EC number (Enzyme Commission number) and to GO term (Gene ontology term). It must be pointed out that an EC number does not indicate a specific enzyme but rather a specific reaction. If different enzymes catalyze the same reaction (e.g., of different organisms) they receive the same EC number.

All graphs of biometric analysis, heat maps and statistical analysis were performed using Metaboanalyst 5.0 [262], while box-plots were made using GraphPad v. 8.0.

5.2.2.8 Extraction of short chain fatty acids from feces

SCFAs were extracted from 30 mg of fecal sample. Briefly, 300 µL of water and 16 µL of the internal standard propanoic acid d2 (20,5 ppm) and 5 µL of tridecanoic acid (500 ppm) were added. The sample was then homogenized with FastPrep-24 5G (MP Biomedicals, USA) for 40 s at 6.0 m/s and vortexed at 1000 rpm at 4°C for 30 minutes. The sample centrifuged at 21.1 x g for 30 minutes at 4°C. 100 µL of supernatant were placed in a new tube, bringing the pH to 2 using 6 M HCl. For the extraction of SCFAs, 140 µL of MTBE were added and the tube was placed on a rotator for 15 minutes at 40 rpm, followed by a centrifugation for 10 minutes at 4°C at 21.1 x g. Then, 100 µL of the organic phase, that contains the SCFAs, were analyzed with bi-dimensional gas chromatography coupled to mass spectrometry (GCxGC-TOFMS). Calibration curve for the absolute quantification of the main SCFAs were also built.

5.2.2.9 Extraction of short chain fatty acids from plasma

Plasma SCFAs were extracted using a liquid–liquid extraction with methyl tert-butyl ether (MTBE). Briefly, 50 uL of plasma was placed in a tube, then 2,5 µL of the internal standard propanoic acid d2 and acetic acid d4 (20.4 ppm) were added, and the sample was vortexed for 20 s, followed by a spin centrifugation for 15 s. The sample was then brought to pH 2 using 6 M HCl. 140 µL of MTBE was added, and the tube was placed on a rotator for 15 min, followed by centrifugation for 10 min at 4 °C and 21.1×g. Then, 100 µL of the organic phase containing the SCFAs was analyzed with GCxGC-TOFMS.

5.2.2.10 GCxGC-TOFMS analysis

For the analysis, a LECO Pegasus BT 4D GCxGC-TOFMS instrument (Leco Corp., St. Josef, MI, USA) equipped with a LECO dual stage quad jet thermal modulator was used. The GC part of the instrument was an Agilent 7890 gas chromatograph (Agilent Technologies, Palo Alto, CA), equipped with a split/splitless injector. The first dimension column was a 30 m Rxi-5Sil (Restek Corp.,

Bellefonte, PA) MS capillary column with an internal diameter of 0.25 mm and a stationary phase film thickness of 0.25 µm for metabolite from aqueous solution, while for SCFAs analysis the column was a 30 m DB-FATWAX-UI (Agilent Technologies, Santa Clara, CA) with a diameter of 0.25 mm and a film thickness of 0.25 µm, and the second dimension chromatographic columns was a 2 m Rxi-17Sil MS (Restek Corp., Bellefonte, PA) with a diameter of 0.25 mm and a film thickness of 0.25 µm. High-purity helium (99,9999%) was used as the carrier gas with a flow rate of 1.4 mL/min. 1 µL of sample was injected in splitless mode at 250°C. The temperature program for metabolites analysis was as follows: the initial temperature was set at 70°C for 2 minutes, then ramped 6°C/min up to 160°C, 10°C/min up to 240°C, 20°C/min to 300 and then held at this value for 6 minutes. The secondary column was maintained at +5°C relative to the GC oven temperature of the first column. The temperature program for SCFAs was as follows: the initial temperature was 40°C for 2 minutes, then ramped 7°C/min up to 165°C, 25°C/min up to 240°C, maintained for 5 minutes. The secondary column was maintained at +5°C relative to the GC oven temperature of the first column. Electron impact ionization was applied (70 eV). The ion source temperature was set at 250°C, the mass range was 40 to 300 m/z with an extraction frequency of 32 kHz, for the SCFAs analysis, while for the metabolites the mass range was 25 to 550 m/z. The acquisition rates were 200 spectra/s. The modulation periods for both programs were 4s for the entire run. The modulator temperature offset was set at +15°C relative to the secondary oven temperature, while the transfer line was set at 280°C.

5.2.2.11 Data analysis

The chromatograms were acquired in TIC (total ion current) mode. Peaks with signal to- noise (S/N) value lower than 500.0 were rejected. ChromaTOF version 5.31 was used for raw data processing. Mass spectral assignment was performed by matching with NIST MS Search 2.3 libraries adding Fiehn Library. Commercial mix standard of free fatty acids composed by acetic acid, propanoic acid, propanoic acid 2-methyl, butanoic acid, butanoic acid 3-methyl and pentanoic acid was run individually and EI spectra were matched against the NIST library. The calibration curves of the SCFAs were obtained using excels, while the analytical results were processed and compared with the opensource software MetaboAnalyst 5.0 [262].

5.2.3 Results

5.2.3.1 BMI Z-score decreased after MD intervention

A total of 15 pediatric obese patients, diet naïve or with failure to a previous weight loss program were recruited and involved in the present study. All the subjects were characterized by a measure of relative weight adjusted for child age and sex (BMI z-score) higher than 25. Patients followed an educational training to MD with gamification aimed at the improvement of their dietary regime and lifestyle. Clinical and auxological data were collected before the beginning of the study, after 6 and 12 months. Stools and plasma samples were also collected and then used to investigate the impact of MD on microbiota and plasma using untargeted proteomics and metabolomics (**Figure 5.1**). The MD intervention for six and twelve months caused a significant reduction of the BMI z-score (**Figure 5.2A**). This result supports the use of educational training to MD performed with gamification for the development of public health strategies to reduce the impact of obesity in children.

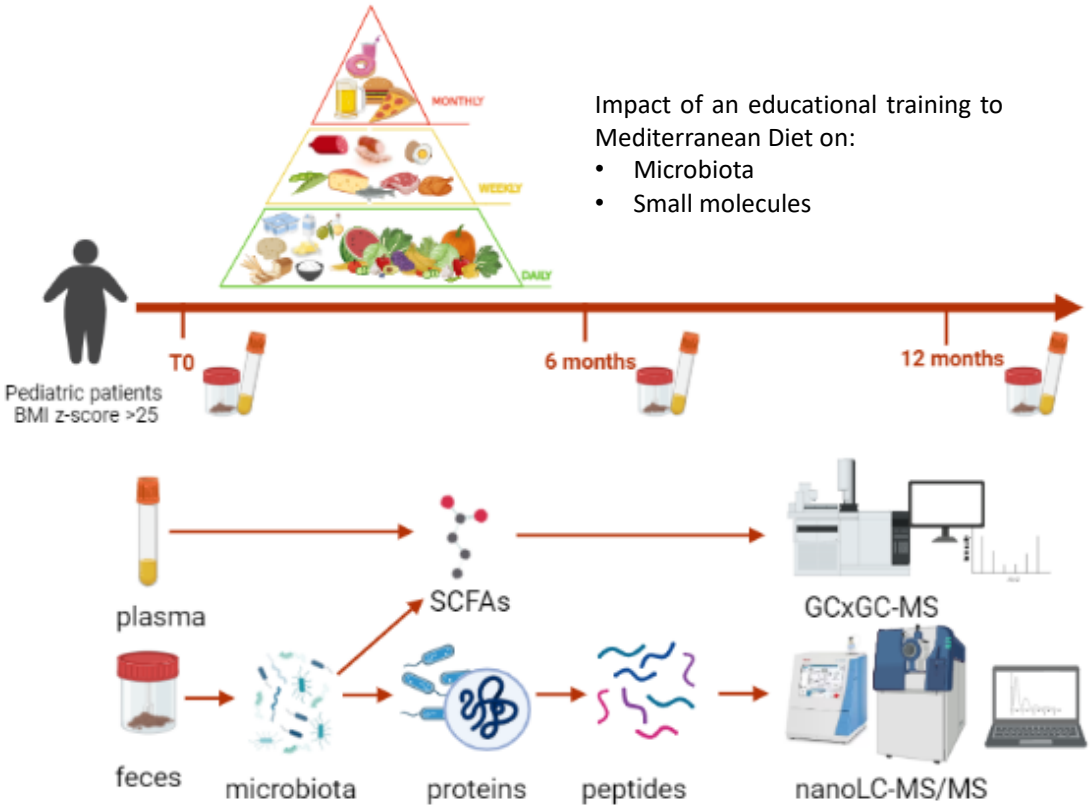

Figure 5.1: *design of the study: pediatric obese patients followed an educational training to MD and were then monitored for 12 months through metaproteomic and metabolomics analysis performed on fecal and serum samples before the dietary intervention and after 6 and 12 months*.

5.2.3.2 *Metaproteomics revealed strong taxonomic gut microbiota changes after MD*

Stool samples were then used to study the impact of MD on microbiota. A metaproteomic approach was employed to extract bacterial proteins from fecal samples and to identify their proteins. A total of 254583 peptides were identified, 68121 of which were unique while 13200 were in common with all the three experimental times (**Figure 5.2B**). The analysis allowed the identification of 70116 total proteins, 32367 of which were unique (**Figure 5.2C**). Identified peptides were then used to perform phylogenetic and functional analysis of the gut microbiota.

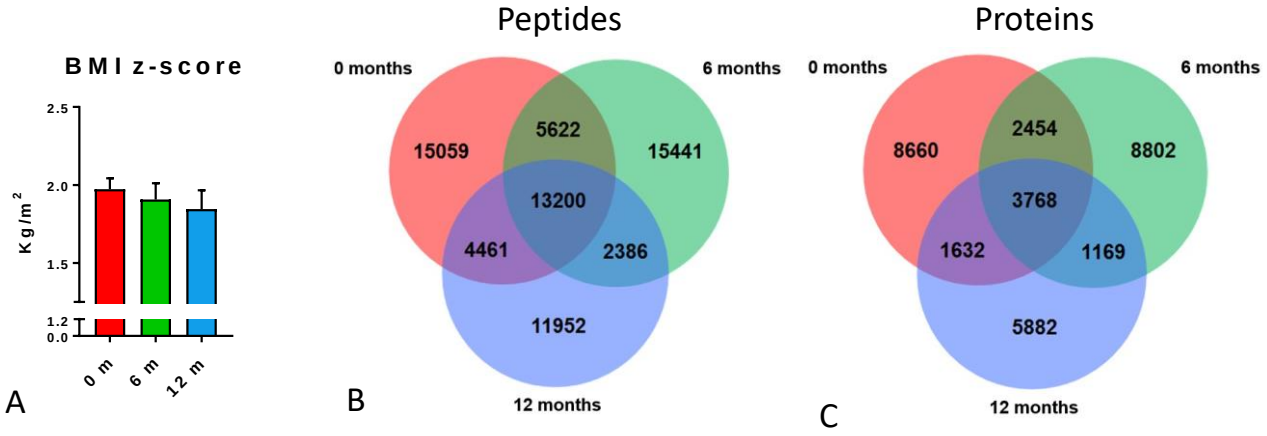

Figure 5.2: *impact of MD on BMI, on peptides and proteins identified in fecal samples. Changes in the BMI z-score after 6 (green) and 12 months (blue) of MD intervention (A); identified peptides (B) and proteins (C) in the fecal samples before (red), after 6 (green) and 12 months (blue) of MD intervention.*

Phylogenetic analysis allowed the identification of 43 unique phyla (29 of which were identified at 0 months, 33 at 6 months and 33 at 12 months) and 24 phyla in common between the three time points of the experimental design (**Figure 5.3A**). The distribution of the major phyla at each time (**Figure 5.3B**) and for each subject (**Figure 5.3C**) showed that the most abundant bacterial species belong to Proteobacteria, Actinobacteria, Bacteroidetes and Firmicutes (**Supplementary table 5.1**). Although statistical analysis did not reveal a significant variation, an overall change in Firmicutes and Bacteroidetes abundances can be appreciated (**Figure 5.3D-E**). These changes led to an overall increase of the ratio Bacteroidetes/Firmicutes after 12 months (**Figure 5.3F**). In addition, the hierarchical clustering heatmap showed the presence of a phyla distribution clearly associated to the effect of the diet (**Figure 5.3G**).

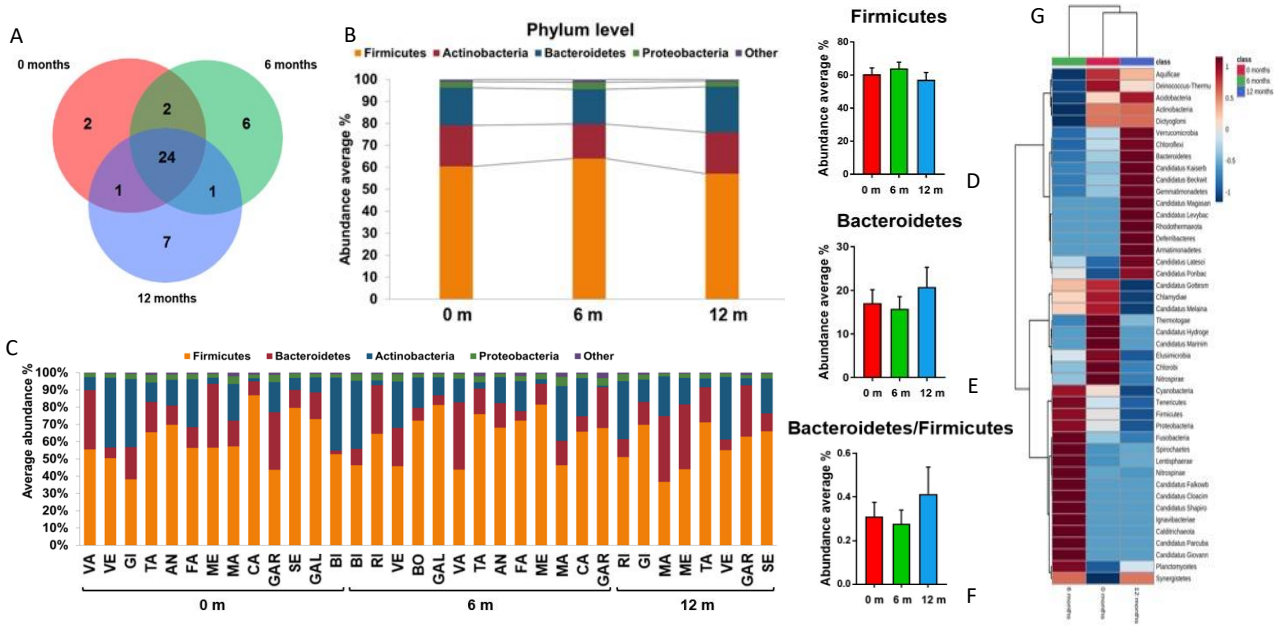

Figure 5.3: *impact of MD on microbiota at the phyla level. Venn diagram of identified phyla before (red) and after (green and blue) MD (A); bar graphs reporting the distribution of the most abundant phyla in the three groups (B) and in each subject (C); box-plots of Firmicutes (D), Bacteroidetes (E) and their ratio (F); hierarchical clustering heatmap of the most relevant phyla within each time point.*

Metaproteomics analysis also allowed the classification of bacteria based on orders: a total of 121 unique orders were detected, 107 of which were identified in the samples before the intervention, 103 in the samples after 6 months and 105 after 12 months. Of these, 92 orders were found in all the conditions (**Figure 5.4A**). The analysis performed at this taxonomic level showed that the most abundant orders found within the fecal samples were Clostridiales, Bacteroidales, Bifidobacteriales, Coriobacteriales, Veillonellales, Lactobacillales, Enterobacteriales and Bacillales, as reported in the bar graph in **figure 5.4B**. Among all orders, only Nitrosomonadales showed a statistically significant modulation during the MD intervention (**Figure 5.4C**). In addition, other orders were impacted by MD, some increased their abundances (Bacteroidales, Bifidobacteriales) while other decreased (Clostridiales, Coriobacteriales, Bacillales, and Pasteurellales) (**Supplementary table 5.2**). Multivariate analysis also highlighted the presence of an order-level signature between the three groups, as reported by PLS-DA and the heatmap (**Figure 5.4D-E**).

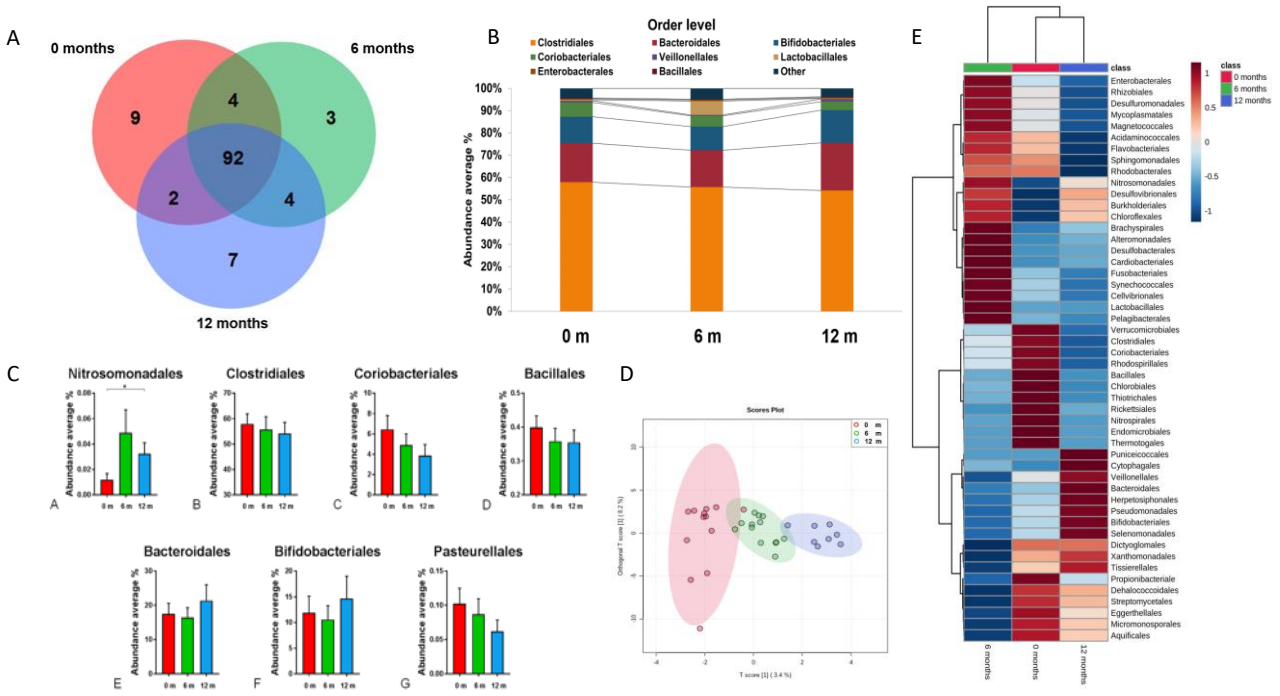

Figure 5.4: *impact of MD on microbiota at the order level. Venn diagram of identified orders before (red) and after MD (green and blue) (A); bar graphs reporting the distribution of the most abundant orders in the three groups (B); box-plots of Nitrosomonadales, Clostridiales, Coriobacteriales, Bacillales, Bacteroidales, Bifidobacteriales and Pasteurellales (C); score plot of PLS-DA reporting the three clusters of patients before (red) and after 6 (green) and 12 (blue) months of MD; hierarchical clustering heatmap of the most relevant orders within each time point (E).*

At the genus level, 529 unique genera were identified among all samples (**Supplementary figure 5.1**). *Bifidobacterium*, *Bacteroides*, *Faecalibacterium*, *Ruminococcus*, *Prevotella* and *Collinsella* were among the most abundant genera identified (**Supplementary table 5.3**). *Coprobacillus* and *Alkaliphilus* significantly changed their abundances in gut microbiota after twelve months of MD (**Figure 5.5A-B**), while other genera such as *Oscillibacter, Parabacteroides, bacillus, eubacterium, Coprococcus, Alistipes, clostridium, Collinsella, Bacteroides and Bifidobacterium* reported increased or decreased trends over the time (**Figure 5.5C to L**).

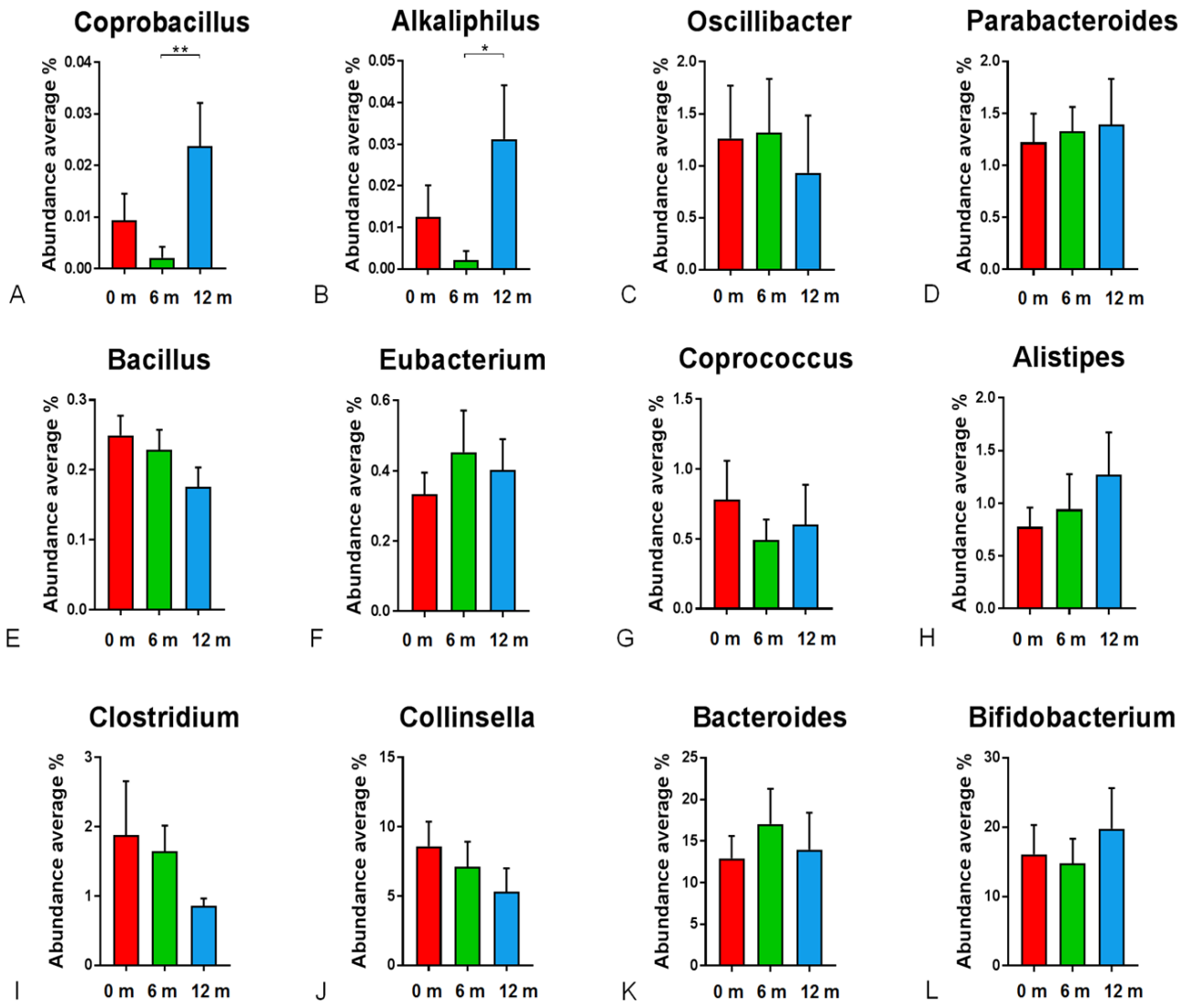

Figure 5.5: *impact of MD on bacteria at the genera level. Box plots of Coprobacillus, Alkaliphilus, Oscillibacter, Parabacteroides, bacillus, eubacterium, Coprococcus, Alistipes, clostridium, Collinsella, Bacteroides and Bifidobacterium before (red) and after 6 (green) and 12 months (blue).*

Finally, the taxonomic analysis performed at the species level showed the identification of 873 total unique species distributed among the three groups (**Supplementary figure 5.2**). **Table 5.2** reports the distribution of the most abundant species: among them there are *Faecalibacterium prausnitzii, Ruminococcus bromiii, Collinsella aerofaciens, Prevotella copri, Ruminococcaceae bacterium, Roseburia faecis and Bacteroides uniformis.* The statistical analysis reported a significant modulation of *Eubacterium ventrosium and Bifidobacterium animalis*, both increased after 6 months, with higher levels of the latter increased also after 12 months. In addition, *Bifidobacterium adolescentis, Collinsella aerofasciens, Bacteroides stercoris, Akkermansia muciniphila, Acidaminococcus*

fermentas, Eubacterium rectale, Roseburia inulinivorans e Lactobacillus reuteri also reported different changes over the MD treatment (**Figure 5.6**).

Table 5.2: *distribution of bacterial species before the MD intervention, after 6 and 12 months.*

Taxon	0 months		6 months		12 months	
Species	*Average %*	*St. Dev.*	*Average %*	*St. Dev.*	*Average %*	*St. Dev.*
Faecalibacterium prausnitzii	17.35	7.49	19.30	8.13	16.22	7.58
Ruminococcus bromii	13.55	14.07	9.12	6.68	14.52	10.18
Collinsella aerofaciens	12.10	9.64	9.51	7.96	6.85	6.36
Prevotella copri	11.11	20.37	6.67	16.77	15.78	22.07
Ruminococcaceae bacterium	9.77	9.62	9.54	8.21	11.11	8.73
Roseburia faecis	4.46	5.01	7.19	6.79	3.97	2.97
Bacteroides uniformis	3.90	5.45	2.73	3.91	3.62	4.18
Ruminococcus bicirculans	1.77	1.96	1.59	2.00	0.66	0.82
Bifidobacterium adolescentis	1.72	2.80	1.80	2.36	2.40	2.79
Parabacteroides merdae	1.21	0.93	0.84	0.98	1.29	1.17
Bifidobacterium bifidum	1.03	1.06	1.23	2.34	1.02	1.32
Bifidobacterium longum	0.92	0.91	0.55	0.63	1.08	1.72
Clostridiales bacterium	0.85	0.75	1.04	0.68	1.94	2.21
Evtepia gabavorous	0.74	1.14	0.44	0.65	0.41	0.32
Lachnospiraceae bacterium	0.65	0.71	1.03	0.91	0.63	0.46
Coprococcus eutactus	0.64	0.83	0.31	0.62	0.39	1.00
Bacteroides dorei	0.59	0.79	0.87	2.49	0.55	0.75
Gemmiger formicilis	0.56	0.52	0.46	0.54	0.36	0.37
Acidaminococcus intestini	0.49	1.06	0.78	1.68	0.10	0.26
Dialister invisus	0.49	0.62	0.34	0.34	0.48	0.52
Alistipes putredinis	0.44	0.52	0.86	1.40	0.45	0.61
Clostridiaceae bacterium	0.43	1.49	0.13	0.28	0.00	0.01
Clostridium cellulovorans	0.41	1.49	0.00	0.00	0.00	0.00
Coprococcus catus	0.38	0.69	0.36	0.27	0.47	0.36
Pseudomonas extremaustralis	0.38	0.23	0.36	0.29	0.25	0.16
Dialister succinatiphilus	0.30	0.54	0.18	0.17	0.68	1.65
Sutterella wadsworthensis	0.29	0.50	0.22	0.39	0.36	0.64
Subdoligranulum variabile	0.27	0.24	0.30	0.35	0.42	0.46
Blautia obeum	0.25	0.24	0.24	0.21	0.15	0.16
Bacteroides stercoris	0.25	0.66	0.48	1.01	0.90	2.10
Ruminococcus callidus	0.25	0.32	0.73	1.41	0.42	0.50

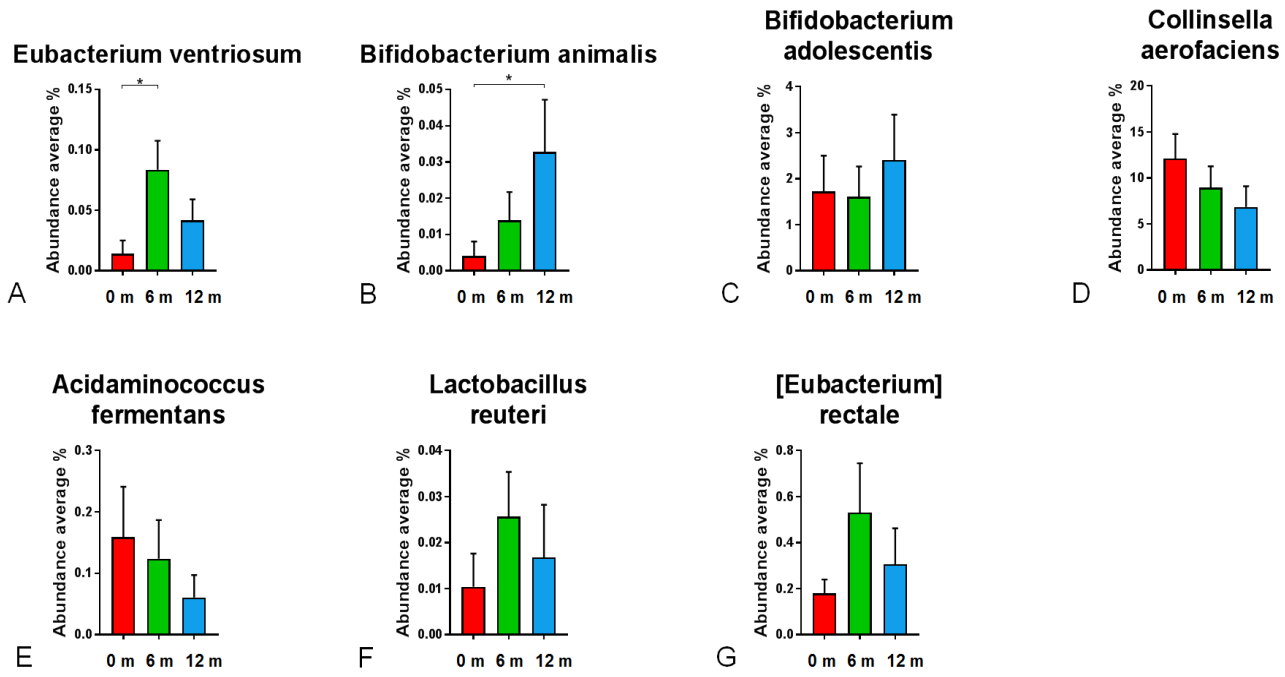

Figure 5.6: *impact of MD on bacteria at the species level. Box plots of Eubacterium ventriosum, Bifidobacterium animalis, Bifidobacterium adolescentis, Collinsella aerofaciens, Acidaminococcus fermentas, Lactobacillus reuteri and Eubacterium rectale before (red) and after 6 (green) and 12 months (blue).*

5.2.3.3 *Gut microbiota functions are altered after MD*

Intestinal microbiota functions were also evaluated to investigate metabolic activities alterations within the microbiota community after twelve months of MD intervention. The distribution of peptides/proteins associated to molecular functions, biological processes and chemical reactions catalyzed by enzymes (EC enzymes) was then calculated and compared between the three time points of the intervention **(Supplementary figure 5.3).**

Among modulated molecular functions, an increase of proteins related to acyl-CoA hydrolase activity, long-chain fatty acyl-CoA binding, glycerol-3-phospate dehydrogenase [NAD+] activity, and glycerol kinase activity was found after 12 months of MD. In addition, an increase of biological processes related to cellular amino acid catabolic processes, glycerol-3-phosphate metabolic and catabolic processes, glycerol catabolic processes, acyl-CoA metabolic processes and lipid catabolic processes were detected at the same time point. Finally, a significant increase of glycerol kinase was identified after 12 months of MD (**Figure 5.7**).

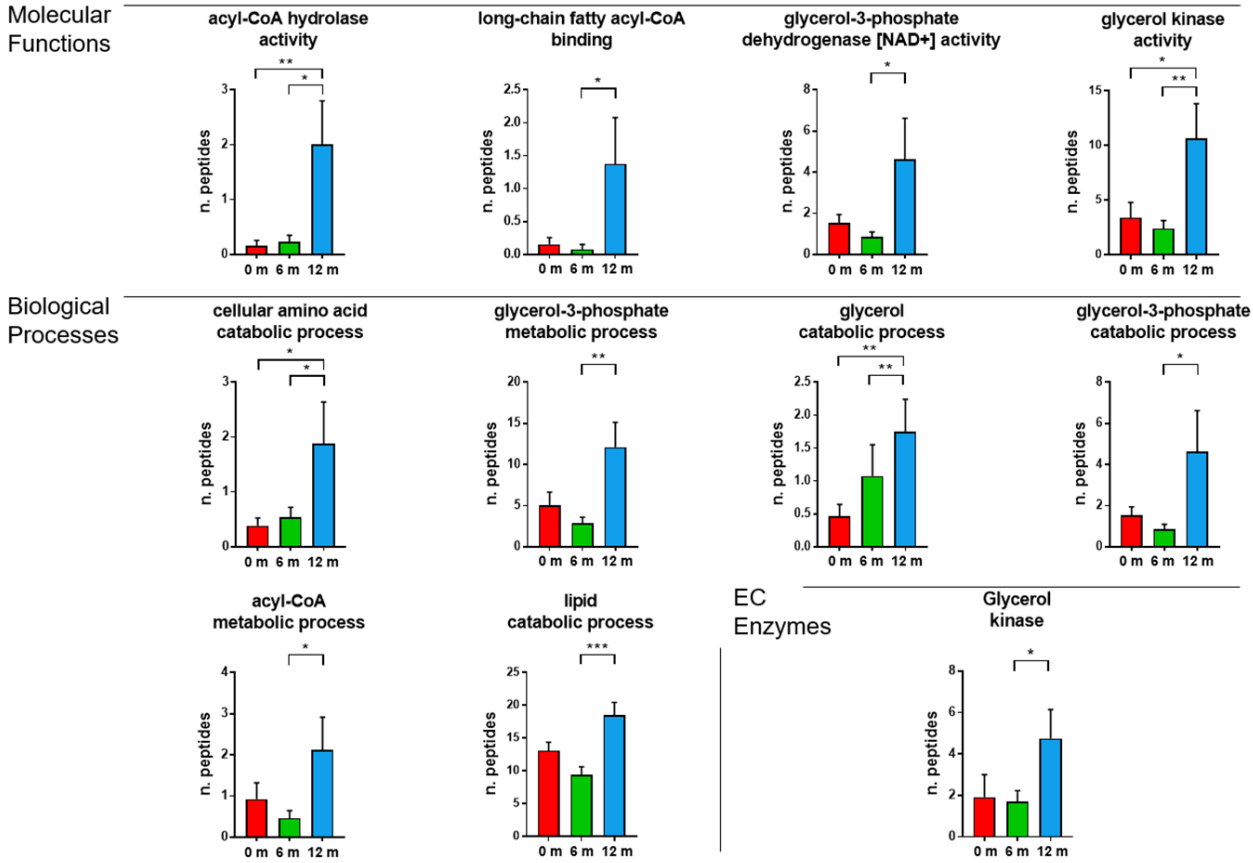

Figure 5.7: *molecular functions, biological processes and enzymes changes before (red) and after 6 (green) and 12 months (blue) of MD intervention.*

5.2.3.4 *MD caused a decrease of gut and serum SCFA levels*

Fecal and serum concentration of SCFAs were quantified before and after the MD intervention (**Figure 5.8).** The metabolomic analysis revealed a significant decrease of the fecal acetic acid (FC = 0.63), butanoic acid (FC = 0.46), and propanoic acid (FC = 0.56) after twelve months of MD. Similarly, a significant down regulation of serum acetic acid (FC = 0.63), butanoic acid (FC = 0.72), and propanoic acid (FC = 0.59) was detected, as well as serum butanoic acid 3-methyl (FC = 0.56), pentanoic acid (FC = 0.41), and propanoic acid 2-methyl (FC = 0.69), suggesting an important effect of MD on the obese gut microbiota and microbial metabolite production.

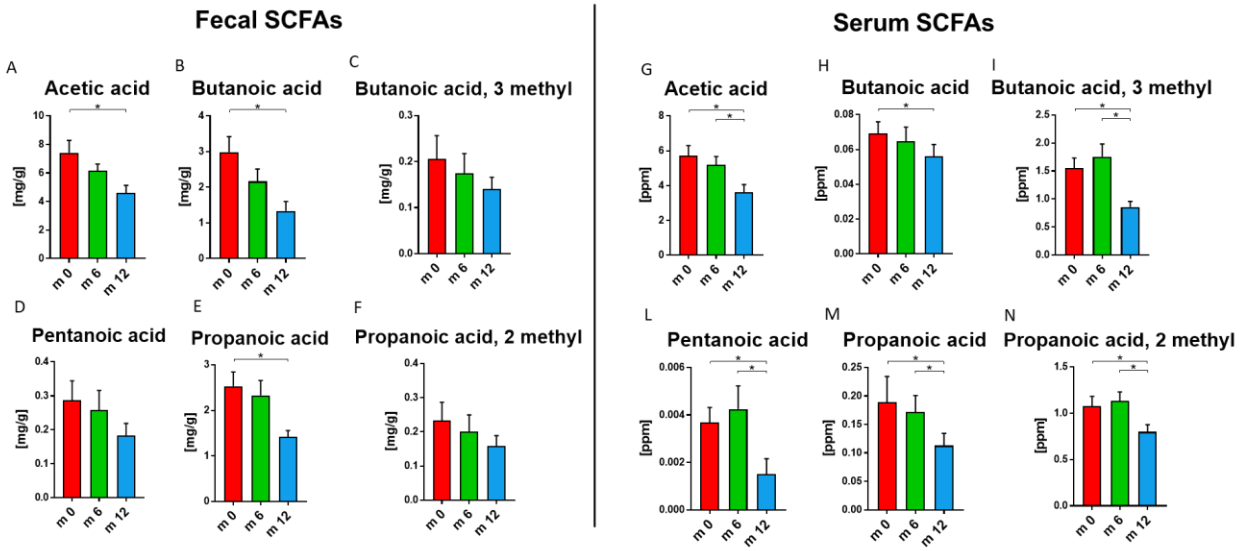

Figure 5.8: *alteration of fecal and serum short chain fatty acids (SCFAs) after MD. A global decrease of SCFAs was observed.*

5.2.4 Discussion

The MD intervention performed through educational training on 15 pediatric obese patients caused a significant reduction of the BMI z-score after 6 and 12 months. Metaproteomics and metabolomics analyses were able to identify the main gut microbiota and plasma changes, demonstrating the impact of MD on gut and on circulating molecules, especially SCFAs. Although no dietary restrictions were used, but only a qualitative improvement in nutritional intake through education, both taxonomic and functional modifications were detected in the gut ecosystems.

At the phylum level, after twelve months of MD, the Bacteroidetes/Firmicutes ratio was slightly increased: this behavior it has been widely associated with a BMI decrease [263–266]. Firmicutes are more efficient in energy extraction from food than Bacteroidetes, thus promoting a better intestinal absorption of nutrient (and calories), resulting in weight gain [267]. The orders Bacillales and Clostridiales, which are both Firmicutes, decreased after six and twelve months of MD. An opposite behavior has been associated with high-fat dietary interventions [268,269]. At the same time, an increase of Bacteroidales, which are an order of the Bacteroidetes, was detected after twelve months of MD. Bacteroidales were already used to alleviate intestinal dysbiosis and metabolic syndrome induced by high-fat diets. Some Bacteroidales have been also shown to decrease fat accumulation and inflammation [270].

At the order-level, the MD intervention caused a significant increase of Nitrosomonadales. The abundance of Nitrosomonadales was linked to a healthy condition and its decrease has been observed in alcoholic fatty liver disease [271]. Of particular interest is also the decrease of Coriobacteriales and Pasteurellales. An increase of Coriobacteriales has been observed during consumption of high-fat diet [272], while Pasteurellales were classified among the pro-inflammatory strains inversely associated with well-balanced diets [273].

Statistical analysis at the genus-level showed that Coprobacillus and Alkaliphilus both increased their abundance after twelve months of MD. An enrichment of Coprobacillus was observed in gut microbiota of healthy children compared to obese children [274], while an enrichment of Alkaliphilus, was negatively correlated with BMI [275]. Our results are in agreement with an overall health improvement of subjects after MD.

Improved nutritional intake for twelve months also determined a decrease of Oscillibacter, Coprococcus, Clostridium and Collinsella, while Parabacteroides, Eubacterium, Alistipes and Bifidobacterium increased their abundances. These changes are in agreement with previous studies that demonstrated the presence of a correlation between their levels and improved health conditions. In fact, low levels of Collinsella were linked to anti-inflammatory dysbiosis in type 2 diabetes, high consumption of fibers, improvement of nonalcoholic steatohepatitis and metabolic endotaxemia conditions [276,277]. Low abundances of Oscillibacer was associated to normal and healthy gut microbiota compared to gut microbiota from high fat diet interventions [278,279], while Coprococcus and Clostridium were lowest in lean subjects than overweight/obese patients and researchers proposed that they may contribute to the improvement of gut dysbiosis conditions [280,281]. Finally, the increase of Eubacterium spp., Alistipes and Bifidobacterium may have a beneficial role in the modulation of inflammation [282–284].

Interestingly, at the species-level, the statistical analysis revealed significantly changes in *Bifidobacterium animalis* and *Eubacterium ventriosum*: they were enriched after twelve and six months of MD, respectively. Researchers already associated high levels of *B. Animalis* to normal weight, and they suggested a potential role of the specie in controlling weight gain. In addition, there are much evidence that *B. Animalis* may improve the epithelial integrity by rebalancing a dysbiotic state induced by obesogenic and high fat diets [196,285,286]. Regarding *E. Ventriosum*, it was already associated to healthy conditions when compared to inflammatory conditions in colorectal adenoma [283].

In addition, MD intervention determined an overall taxonomic change, including the modulation of several bacterial species that were already linked to a general improvement of obesity conditions and gut symbiosis. For example, the increase of *B. adolescentis* was associated to an improvement of high fat diet-induced obesity [287], while the decreasing of *C. aerofaciens*, which is classified as a pro-inflammatory species of gut microbiota, was linked to an improvement of inflammation in T2D [288]. Other studies suggested the presence of an inverse correlation between *E. rectale* and dysbiosis in ulcerative colitis and Crohn disease [289,290]. Finally, a study demonstrated that a treatment with *L. reuteri* could alleviate mucosal inflammation by microbe-host interactions that protect intestinal epithelial cells from injury [291].

Functional analysis performed on modulated peptides/proteins suggested an alteration of bacterial metabolism caused by MD. A global reduction of glucidic metabolism and an increase of non-glucidic metabolism was observed. In fact, after twelve months of MD a significant increase of Acyl-CoA metabolism, of its hydrolase activity and of long-chain fatty Acyl-CoA binding was detected. Acyl-CoA is a group of coenzymes that metabolize fatty acids. At the same time, a decrease of glucose metabolism and carbohydrate derivative metabolism after six and twelve months of MD was observed.

In addition, through EC enzyme analysis, changes of some specific glycolytic enzymes emerged. Some enzymes such as Glyceraldehyde-3-P dehydrogenase, Phosphopyruvate hydratase and Piruvate kinase, increased, bringing to pyruvate production. Piruvate synthase is also increased resulting in the decarboxylation of pyruvate with the formation of Acetyl-CoA which then enters the citric acid cycle.

A statistically significant increase of glycerol metabolism was also detected. Metabolic and catabolic processes of glycerol and glycerol 3-P were increased together with glycerol kinase and glycerol 3-P dehydrogenase activities. Glycerol kinase catalyzes the production of glycerol 3-phosphate. Glycerol 3-P dehydrogenase converts glycerol 3-phosphate to dihydroxyacetone phosphate (DHAP). The main consequence is an increased production of dihydroxyacetone phosphate (DHAP) that may be used in glycolysis or gluconeogenesis pathways.

A significant increase of cellular amino acid and lipid catabolic processes after twelve months of MD was also observed, suggesting their use for the synthesis of glucose.

MD also impacted the production and use of SCFAs which are organic fatty acids with one to six carbon atoms and are the major molecules produced by microbial fermentation of undigested carbohydrates. Butyrate, propionate, and acetate account for 90% to 95% of the SCFAs present in the human colon.

One of the main mechanisms by which the gut microbiota contributes to obesity is through an improved energy extraction from diet by the conversion of dietary fibers to SCFAs [292].

Bacterial SCFAs affect host energy metabolism and contribute to the development of diet-induced obesity through increasing de novo hepatic lipogenesis and lipid accumulation in the host. In addition, the production of bacterial SCFAs also depends on the taxonomic composition of the gut microbiota, even if this relationship in humans has not yet been clarified [293].

In our study, a statistically significant decrease of some SCFAs (acetic acid, butanoic acid, butanoic acid-3-methyl, pentanoic acid, propanoic acid and propanoic acid-2-methyl) in response to 12-month intervention with MD was detected. SCFAs, mainly butyrate, propionate and acetate are a key energy source for the intestinal epithelium and liver [294], and participate in a variety of metabolic and physiologic processes, including hepatic gluconeogenesis and lipogenesis [295,296], gut motility [297], gut barrier function [298,299], and immune responses [300,301]. Fecal and serum concentration of SCFAs depends on the balance between their production, absorption and excretion [302]. Alterations in diet can lead to rapid and significant changes in gut bacterial composition and metabolite production including SCFAs [303]. While plant-based diets, rich in complex carbohydrates, are associated with increased abundance of SCFA-producing bacteria [304–306], greater intake of simple sugars, animal products and saturated fats are associated with a decrease in SCFA-producing bacteria [307,308]. Consequently, subjects that follow a Mediterranean-type diet, characterized by a high content of plant-based food, showed a higher percentage of SCFAs and of fiber-degrading bacteria in the feces compared with subjects with poor adherence to the MD [309]. However, diet alone is not a consistent predictor of SCFA production or abundance. The amount of SCFAs depends also on various host, environmental, and gut microbiota factors. There is growing evidence from both animal and human studies that suggests an important role of gut microbiota and its metabolites, particularly SCFAs, in obesity [310–312]. These studies reported that micronutrients and SCFAs produced by intestinal microbiota can alter host energy metabolism in the development of diet-induced obesity, increasing lipid accumulation and de novo lipogenesis in the liver. It has been observed that the gut microbiota of obese children has a higher ability to ferment carbohydrates when compared to lean volunteers [313] leading to a higher concentration

of fecal SCFAs. However, in human studies, contrasting results regarding SCFAs-obesity relationship were reported. For example, some studies have reported a positive correlation between fecal SCFAs levels and obesity [314–316], while other studies have reported a negative relationship between SCFAs concentrations and obesity. [317]. SCFAs may indirectly contribute to obesity through the modulation of intestinal and systemic inflammation, promoting or exacerbating metabolic dysfunction [318]. Thus, in the setting of inflammation and obesity, obese individuals could have an impaired utilization of SCFA that translates into a higher lipogenic effect and contribute to lipid accumulation in adipocytes, leading to energy harvest compared to lean individuals who might better take advantage of the anti-inflammatory role.

5.2.5 Conclusions

Since diet is one of the main determinants of gut microbiota dysbiosis contributing to pathological states such as obesity [222], modulation of the gut microbiota through nutrition may improve the pathological condition of obesity and other diseases. In our study, twelve months of MD intervention determined overall taxonomic and functional changes on the gut microbiota of pediatric obese patients, including the modulation of several bacterial species that were already linked to a general improvement of high fat-induced obesity conditions, gut symbiosis and inflammation. MD also impacted the production and use of gut and circulating SCFAs, suggesting an indirect contribution of bacteria-produced SCFAs to obesity.

5.2.6 Supplementary Data

Supplementary Table 5.1: *distribution of bacterial phyla before the MD intervention, after 6 and 12 months.*

Time	0 months		6 months		12 months	
Phyla	*Average %*	*St. Dev.*	*Average %*	*St. Dev.*	*Average %*	*St. Dev.*
Firmicutes	60.42	13.96	63.98	13.78	57.10	12.52
Actinobacteria	18.70	14.42	15.69	11.97	18.80	11.93
Bacteroidetes	17.04	11.19	15.79	9.93	20.76	12.80
Proteobacteria	2.86	0.96	3.25	1.08	2.54	0.78

Supplementary Table 5.2: *distribution of bacterial orders before the MD intervention, after 6 and 12 months.*

Taxon	0 months		6 months		12 months	
Orders	*Average %*	*St. Dev.*	*Average %*	*St. Dev.*	*Average %*	*St. Dev.*
Clostridiales	57.92	14.34	55.74	18.11	54.14	12.47
Bacteroidales	17.49	11.26	16.50	10.17	21.42	13.09
Bifidobacteriales	11.88	11.72	10.58	9.77	14.65	12.41
Coriobacteriales	6.45	4.90	4.89	4.01	3.87	3.08
Veillonellales	0.72	0.69	0.34	0.21	1.13	1.58
Lactobacillales	0.43	0.29	6.23	17.41	0.29	0.11
Enterobacterales	0.40	0.20	0.48	0.27	0.35	0.10
Bacillales	0.40	0.12	0.36	0.14	0.36	0.10

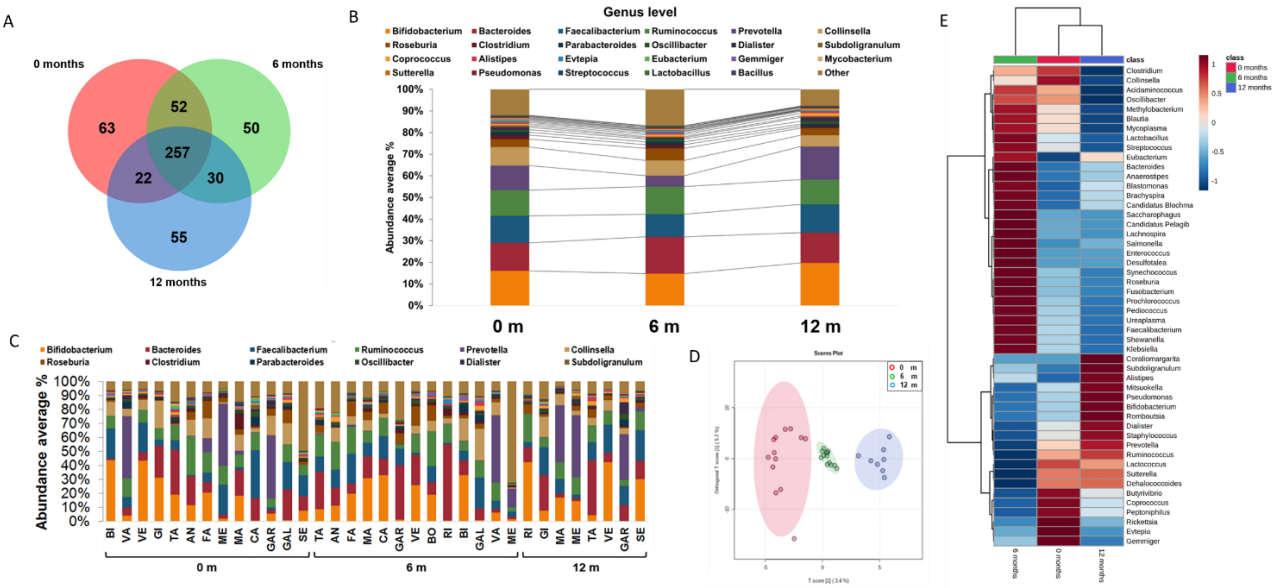

Supplementary Figure 5.1: *impact of MD on microbiota at the genus level. Venn diagram of identified genera before (red) and after (green and blue) MD (A); bar graphs reporting the distribution of the most abundant genera in the three groups (B) and in each subject (C); score plot of O-PLS-DA reporting the three clusters of patients before (red), after 6 (green) and 12 (blue) months of MD; hierarchical clustering heatmap of the most relevant genera within each time point (E).*

Supplementary table 5.3: *distribution of bacterial Genera before the MD intervention, after 6 and 12 months.*

Taxon	0 months		6 months		12 months	
Genera	*Average %*	*St. Dev.*	*Average %*	*St. Dev.*	*Average %*	*St. Dev.*
Bifidobacterium	16.07	15.20	14.79	12.77	19.77	16.51
Bacteroides	12.91	9.73	17.04	15.26	13.96	12.56
Faecalibacterium	12.53	10.43	10.44	6.71	13.12	7.39
Ruminococcus	11.85	5.51	12.78	6.48	11.44	4.77
Prevotella	11.38	19.06	5.02	13.47	15.24	20.19
Collinsella	8.60	6.39	7.12	6.49	5.31	4.78
Roseburia	3.66	3.81	5.59	4.40	3.24	2.24
Clostridium	1.88	2.81	1.64	1.34	0.86	0.30
Parabacteroides	1.26	1.83	1.32	1.86	0.93	1.56
Oscillibacter	1.22	1.00	1.33	0.84	1.39	1.24
Dialister	1.14	1.09	0.60	0.41	1.80	2.68
Subdoligranulum	0.78	1.00	0.49	0.53	0.60	0.81
Coprococcus	0.77	0.66	0.94	1.20	1.27	1.14
Alistipes	0.66	0.58	0.72	0.94	0.91	0.87
Evtepia	0.52	0.44	0.67	0.79	0.32	0.17
Eubacterium	0.49	0.79	0.29	0.40	0.27	0.21
Gemmiger	0.44	0.63	0.54	0.92	0.11	0.20
Mycobacterium	0.37	0.38	0.27	0.29	0.25	0.24
Sutterella	0.35	0.14	0.32	0.15	0.43	0.26
Pseudomonas	0.33	0.22	0.45	0.43	0.40	0.25
Streptococcus	0.29	0.38	0.20	0.27	0.29	0.50
Lactobacillus	0.28	0.17	0.46	0.39	0.16	0.10
Bacillus	0.27	0.52	0.23	0.22	0.26	0.28

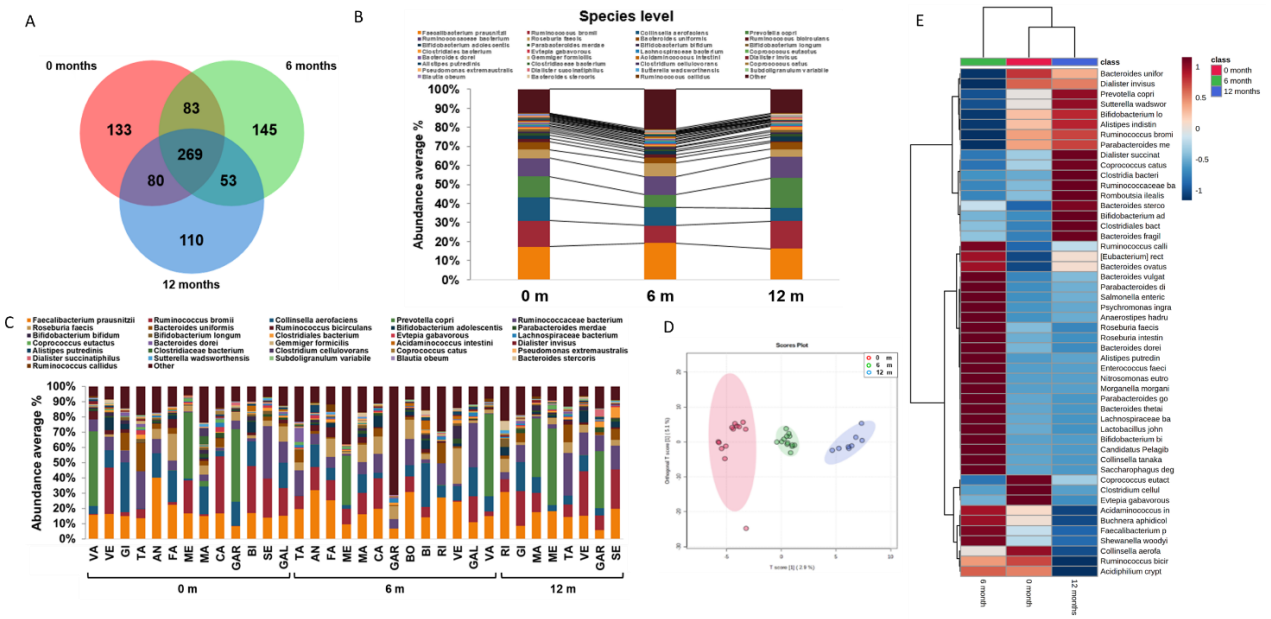

Supplementary Figure 5.2: *impact of MD on microbiota at the specie level. Venn diagram of identified species before (red) and after (green and blue) MD (A); bar graphs reporting the distribution of the most abundant genera in the three groups (B) and in each subject (C); score plot of O-PLS-DA reporting the three clusters of patients before (red), after 6 (green) and 12 (blue) months of MD; hierarchical clustering heatmap of the most relevant species within each time point (E).*

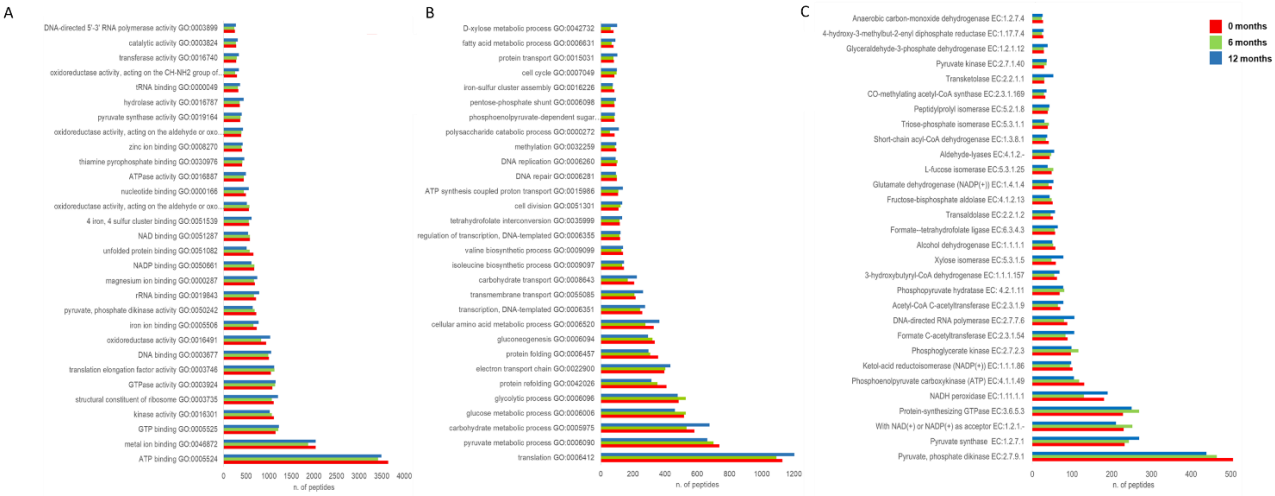

Supplementary Figure 5.3: *GO term and EC Enzyme analysis of the identified microbial peptides/proteins. Distribution of peptides/proteins associated to molecular functions (A), biological processes (B) and chemical reactions catalyzed by enzymes (C) was compared between the three time points of MD intervention: before (red), after 6 (green) and 12 (blue) months.*

6 CONCLUSIONS AND FUTURE PERSPECTIVES

In the present thesis, proteomic, peptidomic and metabolomic analysis were performed to investigate various biological aspects of cancer, viral infection, and metabolic diseases. All the studies were carried out through using untargeted approach using a high-resolution mass spectrometry coupled with liquid or gas chromatography.

The first part of the thesis focused on MS-based cancer proteomics. Currently, cancer proteomics is playing a crucial role in understanding mechanisms of disease pathogenesis, metastasis and chemoresistance [319], and in identifying novel biomarkers [320] or therapeutic targets [321] for diagnosis, prognosis, and treatment of patients.

Proteins and peptides have been proposed as active targets of most cancer therapeutics including the growing field of immunotherapies. The first study focused on cancer vaccine-based immunotherapies. Our findings demonstrated that salmonella infection of STSs/bone sarcoma primary human cells induces the release of immunogenic peptides in the extracellular medium. The peptides resulted not patient specific but are shared among several patients. They have been selected for their overrepresentation in Salmonella treated cell secretomes and for their HLA-binding ability. In vitro results showed their immunogenic activities. These preliminary results suggested that these 12 peptides can be considered as a ‘‘signature’’ of antigens that could be used as a universal sarcoma vaccine treatment. Future studies will purify the candidate peptides and will validate their immunogenic capabilities through in vivo experiments. If successful, the use of universal peptides will have tremendous translational relevance because providing immediate benefit to metastatic sarcoma patients.

The ability to effectively cure and treat cancer is directly dependent on the ability to detect cancers at their earliest stages. MS-based proteomic analysis is a key method for the rapid identification of cancer-specific biomarkers, which may contribute to the detection of early-stage cancer. Currently, invasive procedures are required for definitive histological and bio-molecular diagnosis of MPM [37]. Consequently, there is a critical need for a specific non-invasive biomarker-based screening test to potentially diagnose mesothelioma at an early stage and thus to improve the overall survival of patients. In the second study of the present thesis, we employed an untargeted proteomic discovery approach to identify potential MPM biomarkers in serum and pleural effusion that were

then validated on a bigger cohort of patients including lung adenocarcinoma patients, healthy subjects, and patients with lung hyperplasia. Two candidate biomarkers were confirmed by ELISA: Gelsolin for serum and Lumican for pleural effusion. Their levels were also higher in patients with sarcomatous, and biphasic subtypes compared to the epithelioid one, suggesting their potential use for the detection of the histological subtype. Moreover, high Lumican and Gelsolin levels were significantly associated with shorter survival times, confirming them as markers for poor MPM prognosis. Finally, the bioinformatic analysis highlighted the overall involvement of proteins related to the inflammatory and immune response in the disease. Our data reported new and high-specific biomarkers for the diagnosis and treatment of MPM in an early stage to have better outcome and overall survival of patients. The diagnostic accuracy of our proteomic signature was comparable with standard biomarker assays already optimized for clinical use. Its increased sensitivity and sensibility for the detection of MPM may complement current diagnostic approaches for monitoring people at risk for the cancer. Its prognostic ability may support patient's stratification and treatment selection. We believe that the results reported in this exploratory study represent an additional diagnostic approach for informing clinical decisions for patients at risk for MPM using MS-based proteomics in plasma and pleural effusions. Future research should focus on combinations into biomarker panels and a combination of biomarker matrices, as well as new markers.

The third study of the thesis mainly focused on cancer patients affected by COVID-19 disease. Cancer patients, as elderly and immunosuppressed subjects, are particularly at risk of SARS-CoV2 infection and may present a more serious form of COVID-19 disease [129]. The mechanisms that drive their predisposition towards severe forms of COVID-19 have not been deciphered yet. Since metabolic disorders are associated with homeostatic frailty, that predispose to the onset of infection and cancer [91,92]. In the third part of the thesis we have carried out a proteomic analysis to identify immuno-metabolic pathways that intersect Sars-Cov-2 infection and cancer. The emerging proteomic profile of Sars-Cov-2 and cancer patients showed alterations in the modulation of pathways and proteins associated with immunodeficiency, susceptibility to viral infection and inflammatory modulation. These results suggest that the concomitant presence of cancer condition and viral infection may increase the inflammatory state of patients, contributing to extra pulmonary inflammatory complications and fragility in cancer patients. Another remarkable result emerging from these data is the presence of several potential biomarkers correlated with the immunometabolic status of CA-COVID-19 patients. This is the first study that characterizes the

proteomic content of PBMCs from CA-COVID-19 patients. This proteome-profiling study, together with additional data obtained from metabolomic, lipidomic and flow cytometric analysis, could offer a great opportunity to explore the interference mechanisms elicited by viral infections and tumors coexistence providing not only an overview of the balance of benefits and risks when planning normally routine cancer treatments, but also new therapeutic targets for the treatment of patients with cancer affected by COVID-19. Future studies will validate in vitro the molecular mechanism and pathways altered in CA-COVID-19 patients.

The fourth study discussed in the present thesis focused on the investigation – via proteomic approach - of the host circulating exosome's response to Sars-CoV-2 infection. Our findings showed that circulating exosomes are strongly involved in the processes associated with SARS-CoV-2 infection. The proteomic analysis of plasma exosomes identified several molecules involved in immune response, inflammation, activation of coagulation and complement pathways, suggesting a significant role of the exosomes in the mechanisms associated to tissue damage and multiple organ dysfunctions, which are typical of COVID-19 disease. Another remarkable result emerging from these data is the presence of several potential biomarkers that are well correlated with the severity of the disease.

At the beginning of the pandemic, ours was the first study that characterizes the circulating exosomal proteins and pathways from SARS-CoV-2 infected patients. Monitoring exosomal content during infection may contribute to a better understanding of whether exosomes support viral spreading or induce immunological protection, not only for COVID-19 but also for other diseases. Following studies on vesicles showed that circulating EVs contribute to the production of antibodies and protective immunity [229,230]. In addition, clinical trials have shown some positive results in the therapeutical use of EVs indicating that EVs can help patients recover from COVID-19 [232]. EVs, as carriers for pathogenic vaccines, have been proposed as a new path for the development of effective novel COVID-19 pneumonia vaccines [234,235].

The last part of the thesis reports a metaproteomics and metabolomics analysis of the gut microbiota in pediatric obese children before and after six and twelve months of MD intervention. Gut microbiome is important in multiple aspects of physiological processes related to health and diseases [236,237]. Several factors, including nutrition, have been shown to affect the composition of gut microbiota [220]. Our results showed that MD induces in pediatric obese patients an

increasing of the Bacteroidetes/Firmicutes ratio and the modulation of several bacterial species that were already linked to a general improvement of intestinal dysbiosis, inflammation and metabolic syndrome induced by high-fat diets. In addition, MD also impacted the production and use of gut and circulating SCFAs, suggesting an indirect contribution of bacteria-produced SCFAs to obesity. Although the modification of the gut microbiota composition by diet has been reported before, there are remarkably few studies investigating, via metaproteomic and metabolomic approaches, their influence on the microbiota activity and functionality. In this scenario, mass spectrometry can play a central role in the study of the interaction of the gut microbiome with the human health state. The combination of more than one omics science looks to be a promising strategy for studying the complex relations between the host, the gut microbiota, and diet.

7 REFERENCES

1. Aebersold, R.; Mann, M. Mass Spectrometry-Based Proteomics. *Nature* **2003**, *422*, 198–207, doi:10.1038/nature01511.
2. Sabidó, E.; Selevsek, N.; Aebersold, R. Mass Spectrometry-Based Proteomics for Systems Biology. *Current Opinion in Biotechnology* **2012**, *23*, 591–597, doi:10.1016/j.copbio.2011.11.014.
3. Aretz, I.; Meierhofer, D. Advantages and Pitfalls of Mass Spectrometry Based Metabolome Profiling in Systems Biology. *International Journal of Molecular Sciences* **2016**, *17*, 632, doi:10.3390/ijms17050632.
4. Angel, T.E.; Aryal, U.K.; Hengel, S.M.; Baker, E.S.; Kelly, R.T.; Robinson, E.W.; Smith, R.D. Mass Spectrometry Based Proteomics: Existing Capabilities and Future Directions. *Chem Soc Rev* **2012**, *41*, 3912–3928, doi:10.1039/c2cs15331a.
5. Baker, E.S.; Liu, T.; Petyuk, V.A.; Burnum-Johnson, K.E.; Ibrahim, Y.M.; Anderson, G.A.; Smith, R.D. Mass Spectrometry for Translational Proteomics: Progress and Clinical Implications. *Genome Medicine* **2012**, *4*, 63, doi:10.1186/gm364.
6. Foreman, R.E.; George, A.L.; Reimann, F.; Gribble, F.M.; Kay, R.G. Peptidomics: A Review of Clinical Applications and Methodologies. *J Proteome Res* **2021**, *20*, 3782–3797, doi:10.1021/acs.jproteome.1c00295.
7. Dallas, D.C.; Guerrero, A.; Parker, E.A.; Robinson, R.C.; Gan, J.; German, J.B.; Barile, D.; Lebrilla, C.B. Current Peptidomics: Applications, Purification, Identification, Quantification, and Functional Analysis. *PROTEOMICS* **2015**, *15*, 1026–1038, doi:10.1002/pmic.201400310.
8. Macklin, A.; Khan, S.; Kislinger, T. Recent Advances in Mass Spectrometry Based Clinical Proteomics: Applications to Cancer Research. *Clinical Proteomics* **2020**, *17*, 17, doi:10.1186/s12014-020-09283-w.
9. Wulfkuhle, J.D.; Liotta, L.A.; Petricoin, E.F. Proteomic Applications for the Early Detection of Cancer. *Nat Rev Cancer* **2003**, *3*, 267–275, doi:10.1038/nrc1043.
10. Etzioni, R.; Urban, N.; Ramsey, S.; McIntosh, M.; Schwartz, S.; Reid, B.; Radich, J.; Anderson, G.; Hartwell, L. The Case for Early Detection. *Nat Rev Cancer* **2003**, *3*, 243–252, doi:10.1038/nrc1041.
11. Autier, P.; Boniol, M. Mammography Screening: A Major Issue in Medicine. *Eur J Cancer* **2018**, *90*, 34–62, doi:10.1016/j.ejca.2017.11.002.
12. French, W.W.; Wallen, E.M. Advances in the Diagnostic Options for Prostate Cancer. *Postgraduate Medicine* **2020**, *132*, 52–62, doi:10.1080/00325481.2020.1822067.
13. Ganesh, K.; Massagué, J. Targeting Metastatic Cancer. *Nat Med* **2021**, *27*, 34–44, doi:10.1038/s41591-020-01195-4.
14. McDonald, W.H.; Yates, J.R. Shotgun Proteomics and Biomarker Discovery. *Dis Markers* **2002**, *18*, 99–105, doi:10.1155/2002/505397.

15. Johann, D.J.; McGuigan, M.D.; Patel, A.R.; Tomov, S.; Ross, S.; Conrads, T.P.; Veenstra, T.D.; Fishman, D.A.; Whiteley, G.R.; Petricoin, E.F.; et al. Clinical Proteomics and Biomarker Discovery. *Ann N Y Acad Sci* **2004**, *1022*, 295–305, doi:10.1196/annals.1318.045.
16. Cho, W.C. Mass Spectrometry-Based Proteomics in Cancer Research. *Expert Rev Proteomics* **2017**, *14*, 725–727, doi:10.1080/14789450.2017.1365604.
17. Kwon, Y.W.; Jo, H.-S.; Bae, S.; Seo, Y.; Song, P.; Song, M.; Yoon, J.H. Application of Proteomics in Cancer: Recent Trends and Approaches for Biomarkers Discovery. *Front Med (Lausanne)* **2021**, *8*, 747333, doi:10.3389/fmed.2021.747333.
18. Schumacher, T.N.; Schreiber, R.D. Neoantigens in Cancer Immunotherapy. *Science* **2015**, *348*, 69–74, doi:10.1126/science.aaa4971.
19. van der Burg, S.H.; Arens, R.; Ossendorp, F.; van Hall, T.; Melief, C.J.M. Vaccines for Established Cancer: Overcoming the Challenges Posed by Immune Evasion. *Nat Rev Cancer* **2016**, *16*, 219–233, doi:10.1038/nrc.2016.16.
20. Bassani-Sternberg, M. Mass Spectrometry Based Immunopeptidomics for the Discovery of Cancer Neoantigens. *Methods Mol Biol* **2018**, *1719*, 209–221, doi:10.1007/978-1-4939-7537-2_14.
21. Bassani-Sternberg, M.; Bräunlein, E.; Klar, R.; Engleitner, T.; Sinitcyn, P.; Audehm, S.; Straub, M.; Weber, J.; Slotta-Huspenina, J.; Specht, K.; et al. Direct Identification of Clinically Relevant Neoepitopes Presented on Native Human Melanoma Tissue by Mass Spectrometry. *Nat Commun* **2016**, *7*, 13404, doi:10.1038/ncomms13404.
22. Jo, V.Y.; Fletcher, C.D.M. WHO Classification of Soft Tissue Tumours: An Update Based on the 2013 (4th) Edition. *Pathology* **2014**, *46*, 95–104, doi:10.1097/PAT.0000000000000050.
23. Grünewald, T.G.; Alonso, M.; Avnet, S.; Banito, A.; Burdach, S.; Cidre-Aranaz, F.; Di Pompo, G.; Distel, M.; Dorado-Garcia, H.; Garcia-Castro, J.; et al. Sarcoma Treatment in the Era of Molecular Medicine. *EMBO Mol Med* **2020**, *12*, e11131, doi:10.15252/emmm.201911131.
24. King, T.J.; Bertram, J.S. Connexins as Targets for Cancer Chemoprevention and Chemotherapy. *Biochimica et Biophysica Acta (BBA) - Biomembranes* **2005**, *1719*, 146–160, doi:10.1016/j.bbamem.2005.08.012.
25. Mesnil, M.; Crespin, S.; Avanzo, J.-L.; Zaidan-Dagli, M.-L. Defective Gap Junctional Intercellular Communication in the Carcinogenic Process. *Biochim Biophys Acta* **2005**, *1719*, 125–145, doi:10.1016/j.bbamem.2005.11.004.
26. Melacarne, A.; Ferrari, V.; Tiraboschi, L.; Mishto, M.; Liepe, J.; Aralla, M.; Marconato, L.; Lizier, M.; Pozzi, C.; Zeira, O.; et al. Identification of a Class of Non-Conventional ER-Stress-Response-Derived Immunogenic Peptides. *Cell Rep* **2021**, *36*, 109312, doi:10.1016/j.celrep.2021.109312.

27. Saccheri, F.; Pozzi, C.; Avogadri, F.; Barozzi, S.; Faretta, M.; Fusi, P.; Rescigno, M. Bacteria-Induced Gap Junctions in Tumors Favor Antigen Cross-Presentation and Antitumor Immunity. *Sci Transl Med* **2010**, *2*, 44ra57, doi:10.1126/scitranslmed.3000739.
28. Marconato, L.; Melacarne, A.; Aralla, M.; Sabattini, S.; Tiraboschi, L.; Ferrari, V.; Zeira, O.; Balboni, A.; Faroni, E.; Guerra, D.; et al. A Target Animal Effectiveness Study on Adjuvant Peptide-Based Vaccination in Dogs with Non-Metastatic Appendicular Osteosarcoma Undergoing Amputation and Chemotherapy. *Cancers (Basel)* **2022**, *14*, 1347, doi:10.3390/cancers14051347.
29. Reynisson, B.; Alvarez, B.; Paul, S.; Peters, B.; Nielsen, M. NetMHCpan-4.1 and NetMHCIIpan-4.0: Improved Predictions of MHC Antigen Presentation by Concurrent Motif Deconvolution and Integration of MS MHC Eluted Ligand Data. *Nucleic Acids Res* **2020**, *48*, W449–W454, doi:10.1093/nar/gkaa379.
30. Robinson, B.M. Malignant Pleural Mesothelioma: An Epidemiological Perspective. *Ann Cardiothorac Surg* **2012**, *1*, 491–496, doi:10.3978/j.issn.2225-319X.2012.11.04.
31. Gilham, C.; Rake, C.; Burdett, G.; Nicholson, A.G.; Davison, L.; Franchini, A.; Carpenter, J.; Hodgson, J.; Darnton, A.; Peto, J. Pleural Mesothelioma and Lung Cancer Risks in Relation to Occupational History and Asbestos Lung Burden. *Occup Environ Med* **2016**, *73*, 290–299, doi:10.1136/oemed-2015-103074.
32. Røe, O.D.; Stella, G.M. Malignant Pleural Mesothelioma: History, Controversy and Future of a Manmade Epidemic. *Eur Respir Rev* **2015**, *24*, 115–131, doi:10.1183/09059180.00007014.
33. Brcic, L.; Kern, I. Clinical Significance of Histologic Subtyping of Malignant Pleural Mesothelioma. *Transl Lung Cancer Res* **2020**, *9*, 924–933, doi:10.21037/tlcr.2020.03.38.
34. Tomek, S.; Emri, S.; Krejcy, K.; Manegold, C. Chemotherapy for Malignant Pleural Mesothelioma: Past Results and Recent Developments. *Br J Cancer* **2003**, *88*, 167–174, doi:10.1038/sj.bjc.6600673.
35. Nowak, A.K. Chemotherapy for Malignant Pleural Mesothelioma: A Review of Current Management and a Look to the Future. *Ann Cardiothorac Surg* **2012**, *1*, 508–515, doi:10.3978/j.issn.2225-319X.2012.10.05.
36. Gray, S.G.; Mutti, L. Immunotherapy for Mesothelioma: A Critical Review of Current Clinical Trials and Future Perspectives. *Transl Lung Cancer Res* **2020**, *9*, S100–S119, doi:10.21037/tlcr.2019.11.23.
37. Greillier, L.; Astoul, P. Mesothelioma and Asbestos-Related Pleural Diseases. *Respiration* **2008**, *76*, 1–15, doi:10.1159/000127577.
38. Ahmadzada, T.; Reid, G.; Kao, S. Biomarkers in Malignant Pleural Mesothelioma: Current Status and Future Directions. *J Thorac Dis* **2018**, *10*, S1003–S1007, doi:10.21037/jtd.2018.04.31.
39. Viscardi, G.; Di Natale, D.; Fasano, M.; Brambilla, M.; Lobefaro, R.; De Toma, A.; Galli, G. Circulating Biomarkers in Malignant Pleural Mesothelioma. *Explor Target Antitumor Ther* **2020**, *1*, 434–451, doi:10.37349/etat.2020.00028.

40. Cristaudo, A.; Bonotti, A.; Simonini, S.; Vivaldi, A.; Guglielmi, G.; Ambrosino, N.; Chella, A.; Lucchi, M.; Mussi, A.; Foddis, R. Combined Serum Mesothelin and Plasma Osteopontin Measurements in Malignant Pleural Mesothelioma. *J Thorac Oncol* **2011**, *6*, 1587–1593, doi:10.1097/JTO.0b013e31821e1c08.
41. Hirayama, N.; Tabata, C.; Tabata, R.; Maeda, R.; Yasumitsu, A.; Yamada, S.; Kuribayashi, K.; Fukuoka, K.; Nakano, T. Pleural Effusion VEGF Levels as a Prognostic Factor of Malignant Pleural Mesothelioma. *Respir Med* **2011**, *105*, 137–142, doi:10.1016/j.rmed.2010.10.010.
42. Pass, H.I.; Levin, S.M.; Harbut, M.R.; Melamed, J.; Chiriboga, L.; Donington, J.; Huflejt, M.; Carbone, M.; Chia, D.; Goodglick, L.; et al. Fibulin-3 as a Blood and Effusion Biomarker for Pleural Mesothelioma. *N Engl J Med* **2012**, *367*, 1417–1427, doi:10.1056/NEJMoa1115050.
43. Tabata, C.; Shibata, E.; Tabata, R.; Kanemura, S.; Mikami, K.; Nogi, Y.; Masachika, E.; Nishizaki, T.; Nakano, T. Serum HMGB1 as a Prognostic Marker for Malignant Pleural Mesothelioma. *BMC Cancer* **2013**, *13*, 205, doi:10.1186/1471-2407-13-205.
44. Mundt, F.; Heidari-Hamedani, G.; Nilsonne, G.; Metintas, M.; Hjerpe, A.; Dobra, K. Diagnostic and Prognostic Value of Soluble Syndecan-1 in Pleural Malignancies. *Biomed Res Int* **2014**, *2014*, 419853, doi:10.1155/2014/419853.
45. Hollevoet, K.; Reitsma, J.B.; Creaney, J.; Grigoriu, B.D.; Robinson, B.W.; Scherpereel, A.; Cristaudo, A.; Pass, H.I.; Nackaerts, K.; Rodríguez Portal, J.A.; et al. Serum Mesothelin for Diagnosing Malignant Pleural Mesothelioma: An Individual Patient Data Meta-Analysis. *J Clin Oncol* **2012**, *30*, 1541–1549, doi:10.1200/JCO.2011.39.6671.
46. Creaney, J.; Segal, A.; Olsen, N.; Dick, I.M.; Musk, A.W.B.; Skates, S.J.; Robinson, B.W. Pleural Fluid Mesothelin as an Adjunct to the Diagnosis of Pleural Malignant Mesothelioma. *Dis Markers* **2014**, *2014*, 413946, doi:10.1155/2014/413946.
47. Robinson, B.W.S.; Creaney, J.; Lake, R.; Nowak, A.; Musk, A.W.; de Klerk, N.; Winzell, P.; Hellstrom, K.E.; Hellstrom, I. Mesothelin-Family Proteins and Diagnosis of Mesothelioma. *Lancet* **2003**, *362*, 1612–1616, doi:10.1016/S0140-6736(03)14794-0.
48. Scherpereel, A.; Grigoriu, B.; Conti, M.; Gey, T.; Grégoire, M.; Copin, M.-C.; Devos, P.; Chahine, B.; Porte, H.; Lassalle, P. Soluble Mesothelin-Related Peptides in the Diagnosis of Malignant Pleural Mesothelioma. *Am J Respir Crit Care Med* **2006**, *173*, 1155–1160, doi:10.1164/rccm.200511-1789OC.
49. Schneider, J.; Hoffmann, H.; Dienemann, H.; Herth, F.J.F.; Meister, M.; Muley, T. Diagnostic and Prognostic Value of Soluble Mesothelin-Related Proteins in Patients with Malignant Pleural Mesothelioma in Comparison with Benign Asbestosis and Lung Cancer. *J Thorac Oncol* **2008**, *3*, 1317–1324, doi:10.1097/JTO.0b013e318187491c.
50. Creaney, J.; Dick, I.M.; Meniawy, T.M.; Leong, S.L.; Leon, J.S.; Demelker, Y.; Segal, A.; Musk, A.W.B.; Lee, Y.C.G.; Skates, S.J.; et al. Comparison of Fibulin-3 and Mesothelin as Markers in Malignant Mesothelioma. *Thorax* **2014**, *69*, 895–902, doi:10.1136/thoraxjnl-2014-205205.

51. Ostroff, R.M.; Mehan, M.R.; Stewart, A.; Ayers, D.; Brody, E.N.; Williams, S.A.; Levin, S.; Black, B.; Harbut, M.; Carbone, M.; et al. Early Detection of Malignant Pleural Mesothelioma in Asbestos-Exposed Individuals with a Noninvasive Proteomics-Based Surveillance Tool. *PLoS One* **2012**, *7*, e46091, doi:10.1371/journal.pone.0046091.

52. Cerciello, F.; Choi, M.; Sinicropi-Yao, S.L.; Lomeo, K.; Amann, J.M.; Felley-Bosco, E.; Stahel, R.A.; Robinson, B.W.S.; Creaney, J.; Pass, H.I.; et al. Verification of a Blood-Based Targeted Proteomics Signature for Malignant Pleural Mesothelioma. *Cancer Epidemiol Biomarkers Prev* **2020**, *29*, 1973–1982, doi:10.1158/1055-9965.EPI-20-0543.

53. Dalla Pozza, E.; Manfredi, M.; Brandi, J.; Buzzi, A.; Conte, E.; Pacchiana, R.; Cecconi, D.; Marengo, E.; Donadelli, M. Trichostatin A Alters Cytoskeleton and Energy Metabolism of Pancreatic Adenocarcinoma Cells: An in Depth Proteomic Study. *J Cell Biochem* **2018**, *119*, 2696–2707, doi:10.1002/jcb.26436.

54. Dalle Carbonare, L.; Manfredi, M.; Caviglia, G.; Conte, E.; Robotti, E.; Marengo, E.; Cheri, S.; Zamboni, F.; Gabbiani, D.; Deiana, M.; et al. Can Half-Marathon Affect Overall Health? The Yin-Yang of Sport. *Journal of Proteomics* **2018**, *170*, 80–87, doi:10.1016/j.jprot.2017.09.004.

55. Silacci, P.; Mazzolai, L.; Gauci, C.; Stergiopulos, N.; Yin, H.L.; Hayoz, D. Gelsolin Superfamily Proteins: Key Regulators of Cellular Functions. *Cell Mol Life Sci* **2004**, *61*, 2614–2623, doi:10.1007/s00018-004-4225-6.

56. Piktel, E.; Levental, I.; Durnaś, B.; Janmey, P.A.; Bucki, R. Plasma Gelsolin: Indicator of Inflammation and Its Potential as a Diagnostic Tool and Therapeutic Target. *Int J Mol Sci* **2018**, *19*, 2516, doi:10.3390/ijms19092516.

57. Napoli, F.; Listì, A.; Zambelli, V.; Witel, G.; Bironzo, P.; Papotti, M.; Volante, M.; Scagliotti, G.; Righi, L. Pathological Characterization of Tumor Immune Microenvironment (TIME) in Malignant Pleural Mesothelioma. *Cancers (Basel)* **2021**, *13*, 2564, doi:10.3390/cancers13112564.

58. Oikonomou, N.; Thanasopoulou, A.; Tzouvelekis, A.; Harokopos, V.; Paparountas, T.; Nikitopoulou, I.; Witke, W.; Karameris, A.; Kotanidou, A.; Bouros, D.; et al. Gelsolin Expression Is Necessary for the Development of Modelled Pulmonary Inflammation and Fibrosis. *Thorax* **2009**, *64*, 467–475, doi:10.1136/thx.2008.107946.

59. Tanaka, M.; Müllauer, L.; Ogiso, Y.; Fujita, H.; Moriya, S.; Furuuchi, K.; Harabayashi, T.; Shinohara, N.; Koyanagi, T.; Kuzumaki, N. Gelsolin: A Candidate for Suppressor of Human Bladder Cancer. *Cancer Res* **1995**, *55*, 3228–3232.

60. Dosaka-Akita, H.; Hommura, F.; Fujita, H.; Kinoshita, I.; Nishi, M.; Morikawa, T.; Katoh, H.; Kawakami, Y.; Kuzumaki, N. Frequent Loss of Gelsolin Expression in Non-Small Cell Lung Cancers of Heavy Smokers. *Cancer Res* **1998**, *58*, 322–327.

61. Miyauchi, E.; Furuta, T.; Ohtsuki, S.; Tachikawa, M.; Uchida, Y.; Sabit, H.; Obuchi, W.; Baba, T.; Watanabe, M.; Terasaki, T.; et al. Identification of Blood Biomarkers in Glioblastoma by SWATH Mass

Spectrometry and Quantitative Targeted Absolute Proteomics. *PLOS ONE* **2018**, *13*, e0193799, doi:10.1371/journal.pone.0193799.

62. Wu, Y.; Zheng, J.; Yan, Y.; Liu, J.; Zhou, Y. Gelsolin Can Be a Prognostic Biomarker and Correlated with Immune Infiltrates in Gastric Cancer. *Int J Gen Med* **2022**, *15*, 927–936, doi:10.2147/IJGM.S339940.
63. Li, W.-X.; Yang, M.-X.; Hong, X.-Q.; Dong, T.-G.; Yi, T.; Lin, S.-L.; Qin, X.-Y.; Niu, W.-X. Overexpression of Gelsolin Reduces the Proliferation and Invasion of Colon Carcinoma Cells. *Mol Med Rep* **2016**, *14*, 3059–3065, doi:10.3892/mmr.2016.5652.
64. Liao, C.-J.; Wu, T.-I.; Huang, Y.-H.; Chang, T.-C.; Wang, C.-S.; Tsai, M.-M.; Hsu, C.-Y.; Tsai, M.-H.; Lai, C.-H.; Lin, K.-H. Overexpression of Gelsolin in Human Cervical Carcinoma and Its Clinicopathological Significance. *Gynecologic Oncology* **2011**, *120*, 135–144, doi:10.1016/j.ygyno.2010.10.005.
65. Chen, C.-C.; Chiou, S.-H.; Yang, C.-L.; Chow, K.-C.; Lin, T.-Y.; Chang, H.-W.; You, W.-C.; Huang, H.-W.; Chen, C.-M.; Chen, N.-C.; et al. Secreted Gelsolin Desensitizes and Induces Apoptosis of Infiltrated Lymphocytes in Prostate Cancer. *Oncotarget* **2017**, *8*, 77152–77167, doi:10.18632/oncotarget.20414.
66. Asare-Werehene, M.; Tsuyoshi, H.; Zhang, H.; Salehi, R.; Chang, C.-Y.; Carmona, E.; Librach, C.L.; Mes-Masson, A.-M.; Chang, C.-C.; Burger, D.; et al. Plasma Gelsolin Confers Chemoresistance in Ovarian Cancer by Resetting the Relative Abundance and Function of Macrophage Subtypes. *Cancers* **2022**, *14*, 1039, doi:10.3390/cancers14041039.
67. Zhang, Y.; Luo, X.; Lin, J.; Fu, S.; Feng, P.; Su, H.; He, X.; Liang, X.; Liu, K.; Deng, W. Gelsolin Promotes Cancer Progression by Regulating Epithelial-Mesenchymal Transition in Hepatocellular Carcinoma and Correlates with a Poor Prognosis. *J Oncol* **2020**, *2020*, 1980368, doi:10.1155/2020/1980368.
68. Shieh, D.B.; Godleski, J.; Herndon, J.E.; Azuma, T.; Mercer, H.; Sugarbaker, D.J.; Kwiatkowski, D.J. Cell Motility as a Prognostic Factor in Stage I Nonsmall Cell Lung Carcinoma: The Role of Gelsolin Expression. *Cancer* **1999**, *85*, 47–57, doi:10.1002/(sici)1097-0142(19990101)85:1<47::aid-cncr7>3.0.co;2-l.
69. Appunni, S.; Rubens, M.; Ramamoorthy, V.; Anand, V.; Khandelwal, M.; Saxena, A.; McGranaghan, P.; Odia, Y.; Kotecha, R.; Sharma, A. Lumican, pro-Tumorigenic or Anti-Tumorigenic: A Conundrum. *Clin Chim Acta* **2021**, *514*, 1–7, doi:10.1016/j.cca.2020.12.011.
70. Wang, X.; Zhou, Q.; Yu, Z.; Wu, X.; Chen, X.; Li, J.; Li, C.; Yan, M.; Zhu, Z.; Liu, B.; et al. Cancer-Associated Fibroblast-Derived Lumican Promotes Gastric Cancer Progression via the Integrin B1-FAK Signaling Pathway. *Int J Cancer* **2017**, *141*, 998–1010, doi:10.1002/ijc.30801.
71. Mu, Q.-M.; He, W.; Hou, G.-M.; Liang, Y.; Wang, G.; Li, C.-L.; Liao, B.; Liu, X.; Ye, Z.; Lu, J.-L.; et al. [Interference of Lumican Regulates the Invasion and Migration of Liver Cancer Cells]. *Sichuan Da Xue Xue Bao Yi Xue Ban* **2018**, *49*, 358–363.
72. Mao, W.; Luo, M.; Huang, X.; Wang, Q.; Fan, J.; Gao, L.; Zhang, Y.; Geng, J. Knockdown of Lumican Inhibits Proliferation and Migration of Bladder Cancer. *Transl Oncol* **2019**, *12*, 1072–1078, doi:10.1016/j.tranon.2019.05.014.

73. Pietraszek, K.; Brézillon, S.; Perreau, C.; Malicka-Błaszkiewicz, M.; Maquart, F.-X.; Wegrowski, Y. Lumican – Derived Peptides Inhibit Melanoma Cell Growth and Migration. *PLoS One* **2013**, *8*, e76232, doi:10.1371/journal.pone.0076232.

74. Li, X.; Truty, M.A.; Kang, Y.; Chopin-Laly, X.; Zhang, R.; Roife, D.; Chatterjee, D.; Lin, E.; Thomas, R.M.; Wang, H.; et al. Extracellular Lumican Inhibits Pancreatic Cancer Cell Growth and Is Associated with Prolonged Survival after Surgery. *Clinical Cancer Research* **2014**, *20*, 6529–6540, doi:10.1158/1078-0432.CCR-14-0970.

75. Yang, C.-T.; Li, J.-M.; Chu, W.-K.; Chow, S.-E. Downregulation of Lumican Accelerates Lung Cancer Cell Invasion through P120 Catenin. *Cell Death Dis* **2018**, *9*, 1–16, doi:10.1038/s41419-017-0212-3.

76. Karamanou, K.; Franchi, M.; Onisto, M.; Passi, A.; Vynios, D.H.; Brézillon, S. Evaluation of Lumican Effects on Morphology of Invading Breast Cancer Cells, Expression of Integrins and Downstream Signaling. *FEBS J* **2020**, *287*, 4862–4880, doi:10.1111/febs.15289.

77. Cappellesso, R.; Millioni, R.; Arrigoni, G.; Simonato, F.; Caroccia, B.; Iori, E.; Guzzardo, V.; Ventura, L.; Tessari, P.; Fassina, A. Lumican Is Overexpressed in Lung Adenocarcinoma Pleural Effusions. *PLOS ONE* **2015**, *10*, e0126458, doi:10.1371/journal.pone.0126458.

78. Cray, C.; Zaias, J.; Altman, N.H. Acute Phase Response in Animals: A Review. *Comp Med* **2009**, *59*, 517–526.

79. Lakota, K.; Frank, M.; Buzan, O.; Tomsic, M.; Rozman, B.; Sodin-Semrl, S.; Lakota, K.; Frank, M.; Buzan, O.; Tomsic, M.; et al. *Acute Phase Proteins in Prototype Rheumatic Inflammatory Diseases*; IntechOpen, 2011; ISBN 978-953-307-252-4.

80. Tanrikulu, A.C.; Abakay, A.; Kaplan, M.A.; Küçüköner, M.; Palanci, Y.; Evliyaoglu, O.; Sezgi, C.; Sen, H.; Carkanat, A.İ.; Kirbas, G. A Clinical, Radiographic and Laboratory Evaluation of Prognostic Factors in 363 Patients with Malignant Pleural Mesothelioma. *Respiration* **2010**, *80*, 480–487, doi:10.1159/000321370.

81. Nojiri, S.; Gemba, K.; Aoe, K.; Kato, K.; Yamaguchi, T.; Sato, T.; Kubota, K.; Kishimoto, T. Survival and Prognostic Factors in Malignant Pleural Mesothelioma: A Retrospective Study of 314 Patients in the West Part of Japan. *Japanese Journal of Clinical Oncology* **2011**, *41*, 32–39, doi:10.1093/jjco/hyq159.

82. Vogl, M.; Rosenmayr, A.; Bohanes, T.; Scheed, A.; Brndiar, M.; Stubenberger, E.; Ghanim, B. Biomarkers for Malignant Pleural Mesothelioma-A Novel View on Inflammation. *Cancers (Basel)* **2021**, *13*, 658, doi:10.3390/cancers13040658.

83. Shannahan, J.H.; Alzate, O.; Winnik, W.M.; Andrews, D.; Schladweiler, M.C.; Ghio, A.J.; Gavett, S.H.; Kodavanti, U.P. Acute Phase Response, Inflammation and Metabolic Syndrome Biomarkers of Libby Asbestos Exposure. *Toxicol Appl Pharmacol* **2012**, *260*, 105–114, doi:10.1016/j.taap.2012.02.006.

84. Falanga, A.; Marchetti, M.; Vignoli, A. Coagulation and Cancer: Biological and Clinical Aspects. *J Thromb Haemost* **2013**, *11*, 223–233, doi:10.1111/jth.12075.

85. Falanga, A.; Russo, L.; Milesi, V. The Coagulopathy of Cancer. *Curr Opin Hematol* **2014**, *21*, 423–429, doi:10.1097/MOH.0000000000000072.
86. Nguyen, D.; Lee, S.-J.; Libby, E.; Verschraegen, C. Rate of Thromboembolic Events in Mesothelioma. *Ann Thorac Surg* **2008**, *85*, 1032–1038, doi:10.1016/j.athoracsur.2007.11.064.
87. Revel, M.; Daugan, M.V.; Sautés-Fridman, C.; Fridman, W.H.; Roumenina, L.T. Complement System: Promoter or Suppressor of Cancer Progression? *Antibodies* **2020**, *9*, 57, doi:10.3390/antib9040057.
88. Davalieva, K.; Kiprijanovska, S.; Maleva Kostovska, I.; Stavridis, S.; Stankov, O.; Komina, S.; Petrusevska, G.; Polenakovic, M. Comparative Proteomics Analysis of Urine Reveals Down-Regulation of Acute Phase Response Signaling and LXR/RXR Activation Pathways in Prostate Cancer. *Proteomes* **2017**, *6*, 1, doi:10.3390/proteomes6010001.
89. Tang, H.; Mirshahidi, S.; Senthil, M.; Kazanjian, K.; Chen, C.-S.; Zhang, K. Down-Regulation of LXR/RXR Activation and Negative Acute Phase Response Pathways in Colon Adenocarcinoma Revealed by Proteomics and Bioinformatics Analysis. *Cancer Biomarkers* **2014**, *14*, 313–324, doi:10.3233/CBM-140409.
90. Benedetti, S.; Nuvoli, B.; Catalani, S.; Galati, R. Reactive Oxygen Species a Double-Edged Sword for Mesothelioma. *Oncotarget* **2015**, *6*, 16848–16865, doi:10.18632/oncotarget.4253.
91. Rahman, M.; Nirala, N.K.; Singh, A.; Zhu, L.J.; Taguchi, K.; Bamba, T.; Fukusaki, E.; Shaw, L.M.; Lambright, D.G.; Acharya, J.K.; et al. Drosophila Sirt2/Mammalian SIRT3 Deacetylates ATP Synthase β and Regulates Complex V Activity. *The Journal of Cell Biology* **2014**, *206*, 289, doi:10.1083/jcb.201404118.
92. Handforth, C.; Clegg, A.; Young, C.; Simpkins, S.; Seymour, M.T.; Selby, P.J.; Young, J. The Prevalence and Outcomes of Frailty in Older Cancer Patients: A Systematic Review. *Ann Oncol* **2015**, *26*, 1091–1101, doi:10.1093/annonc/mdu540.
93. Franceschi, C.; Garagnani, P.; Parini, P.; Giuliani, C.; Santoro, A. Inflammaging: A New Immune-Metabolic Viewpoint for Age-Related Diseases. *Nat Rev Endocrinol* **2018**, *14*, 576–590, doi:10.1038/s41574-018-0059-4.
94. Rosas, I.O.; Bräu, N.; Waters, M.; Go, R.C.; Malhotra, A.; Hunter, B.D.; Bhagani, S.; Skiest, D.; Savic, S.; Douglas, I.S.; et al. Tocilizumab in Patients Hospitalised with COVID-19 Pneumonia: Efficacy, Safety, Viral Clearance, and Antibody Response from a Randomised Controlled Trial (COVACTA). *EClinicalMedicine* **2022**, *47*, 101409, doi:10.1016/j.eclinm.2022.101409.
95. Fajgenbaum, D.C.; June, C.H. Cytokine Storm. *N Engl J Med* **2020**, *383*, 2255–2273, doi:10.1056/NEJMra2026131.
96. Sica, A.; Colombo, M.P.; Trama, A.; Horn, L.; Garassino, M.C.; Torri, V. Immunometabolic Status of COVID-19 Cancer Patients. *Physiol Rev* **2020**, *100*, 1839–1850, doi:10.1152/physrev.00018.2020.
97. Sica, A.; Mantovani, A. Macrophage Plasticity and Polarization: In Vivo Veritas. *J Clin Invest* **2012**, *122*, 787–795, doi:10.1172/JCI59643.

98. Mantovani, A.; Marchesi, F.; Malesci, A.; Laghi, L.; Allavena, P. Tumour-Associated Macrophages as Treatment Targets in Oncology. *Nat Rev Clin Oncol* **2017**, *14*, 399–416, doi:10.1038/nrclinonc.2016.217.
99. Pavel, A.B.; Glickman, J.W.; Michels, J.R.; Kim-Schulze, S.; Miller, R.L.; Guttman-Yassky, E. Th2/Th1 Cytokine Imbalance Is Associated With Higher COVID-19 Risk Mortality. *Frontiers in Genetics* **2021**, *12*.
100. Blagih, J.; Jones, R.G. Polarizing Macrophages through Reprogramming of Glucose Metabolism. *Cell Metab* **2012**, *15*, 793–795, doi:10.1016/j.cmet.2012.05.008.
101. Trus, I.; Udenze, D.; Berube, N.; Wheler, C.; Martel, M.-J.; Gerdts, V.; Karniychuk, U. CpG-Recoding in Zika Virus Genome Causes Host-Age-Dependent Attenuation of Infection With Protection Against Lethal Heterologous Challenge in Mice. *Frontiers in Immunology* **2020**, *10*.
102. Fung, T.S.; Liao, Y.; Liu, D.X. Regulation of Stress Responses and Translational Control by Coronavirus. *Viruses* **2016**, *8*, 184, doi:10.3390/v8070184.
103. de Breyne, S.; Vindry, C.; Guillin, O.; Condé, L.; Mure, F.; Gruffat, H.; Chavatte, L.; Ohlmann, T. Translational Control of Coronaviruses. *Nucleic Acids Res* **2020**, *48*, 12502–12522, doi:10.1093/nar/gkaa1116.
104. Baltzis, D.; Pluquet, O.; Papadakis, A.I.; Kazemi, S.; Qu, L.-K.; Koromilas, A.E. The EIF2alpha Kinases PERK and PKR Activate Glycogen Synthase Kinase 3 to Promote the Proteasomal Degradation of P53. *J Biol Chem* **2007**, *282*, 31675–31687, doi:10.1074/jbc.M704491200.
105. Krähling, V.; Stein, D.A.; Spiegel, M.; Weber, F.; Mühlberger, E. Severe Acute Respiratory Syndrome Coronavirus Triggers Apoptosis via Protein Kinase R but Is Resistant to Its Antiviral Activity. *J Virol* **2009**, *83*, 2298–2309, doi:10.1128/JVI.01245-08.
106. Scaturro, P.; Stukalov, A.; Haas, D.A.; Cortese, M.; Draganova, K.; Płaszczyca, A.; Bartenschlager, R.; Götz, M.; Pichlmair, A. An Orthogonal Proteomic Survey Uncovers Novel Zika Virus Host Factors. *Nature* **2018**, *561*, 253–257, doi:10.1038/s41586-018-0484-5.
107. Chen, Z.; Wang, C.; Feng, X.; Nie, L.; Tang, M.; Zhang, H.; Xiong, Y.; Swisher, S.K.; Srivastava, M.; Chen, J. *Comprehensive Analysis of the Host-Virus Interactome of SARS-CoV-2*; Molecular Biology, 2021;
108. Aydemir, M.N.; Aydemir, H.B.; Korkmaz, E.M.; Budak, M.; Cekin, N.; Pinarbasi, E. Computationally Predicted SARS-COV-2 Encoded MicroRNAs Target NFKB, JAK/STAT and TGFB Signaling Pathways. *Gene Rep* **2021**, *22*, 101012, doi:10.1016/j.genrep.2020.101012.
109. Zarbock, A.; Kempf, T.; Wollert, K.C.; Vestweber, D. Leukocyte Integrin Activation and Deactivation: Novel Mechanisms of Balancing Inflammation. *J Mol Med (Berl)* **2012**, *90*, 353–359, doi:10.1007/s00109-011-0835-2.
110. Kourtzelis, I.; Mitroulis, I.; von Renesse, J.; Hajishengallis, G.; Chavakis, T. From Leukocyte Recruitment to Resolution of Inflammation: The Cardinal Role of Integrins. *J Leukoc Biol* **2017**, *102*, 677–683, doi:10.1189/jlb.3MR0117-024R.

111. Alon, R.; Sportiello, M.; Kozlovski, S.; Kumar, A.; Reilly, E.C.; Zarbock, A.; Garbi, N.; Topham, D.J. Leukocyte Trafficking to the Lungs and beyond: Lessons from Influenza for COVID-19. *Nat Rev Immunol* **2021**, *21*, 49–64, doi:10.1038/s41577-020-00470-2.
112. Bunnell, T.M.; Burbach, B.J.; Shimizu, Y.; Ervasti, J.M. β-Actin Specifically Controls Cell Growth, Migration, and the G-Actin Pool. *MBoC* **2011**, *22*, 4047–4058, doi:10.1091/mbc.e11-06-0582.
113. Sharapova, S.O.; Haapaniemi, E.; Sakovich, I.S.; Kostyuchenko, L.V.; Donkó, A.; Dulau-Florea, A.; Malko, O.; Bondarenko, A.V.; Stegantseva, M.V.; Leto, T.L.; et al. Heterozygous Activating Mutation in RAC2 Causes Infantile-Onset Combined Immunodeficiency with Susceptibility to Viral Infections. *Clin Immunol* **2019**, *205*, 1–5, doi:10.1016/j.clim.2019.05.003.
114. Guo, F.; Cancelas, J.A.; Hildeman, D.; Williams, D.A.; Zheng, Y. Rac GTPase Isoforms Rac1 and Rac2 Play a Redundant and Crucial Role in T-Cell Development. *Blood* **2008**, *112*, 1767–1775, doi:10.1182/blood-2008-01-132068.
115. Li, J.; Guo, M.; Tian, X.; Wang, X.; Yang, X.; Wu, P.; Liu, C.; Xiao, Z.; Qu, Y.; Yin, Y.; et al. Virus-Host Interactome and Proteomic Survey Reveal Potential Virulence Factors Influencing SARS-CoV-2 Pathogenesis. *Med (N Y)* **2021**, *2*, 99-112.e7, doi:10.1016/j.medj.2020.07.002.
116. Casalou, C.; Ferreira, A.; Barral, D.C. The Role of ARF Family Proteins and Their Regulators and Effectors in Cancer Progression: A Therapeutic Perspective. *Frontiers in Cell and Developmental Biology* **2020**, *8*.
117. Menzel, S.; Koudelka, T.; Rissiek, B.; Haag, F.; Meyer-Schwesinger, C.; Tholey, A.; Koch-Nolte, F. ADP-Ribosylation Regulates the Signaling Function of IFN-γ. *Frontiers in Immunology* **2021**, *12*.
118. Rosado, M.M.; Pioli, C. ADP-Ribosylation in Evasion, Promotion and Exacerbation of Immune Responses. *Immunology* **2021**, *164*, 15–30, doi:10.1111/imm.13332.
119. Rahman, S.; Islam, R. Mammalian Sirt1: Insights on Its Biological Functions. *Cell Commun Signal* **2011**, *9*, 11, doi:10.1186/1478-811X-9-11.
120. Liu, T.F.; McCall, C.E. Deacetylation by SIRT1 Reprograms Inflammation and Cancer. *Genes Cancer* **2013**, *4*, 135–147, doi:10.1177/1947601913476948.
121. Ghosh, H.S.; Reizis, B.; Robbins, P.D. SIRT1 Associates with EIF2-Alpha and Regulates the Cellular Stress Response. *Sci Rep* **2011**, *1*, 150, doi:10.1038/srep00150.
122. Allegretti, M.; Cesta, M.C.; Zippoli, M.; Beccari, A.; Talarico, C.; Mantelli, F.; Bucci, E.M.; Scorzolini, L.; Nicastri, E. Repurposing the Estrogen Receptor Modulator Raloxifene to Treat SARS-CoV-2 Infection. *Cell Death Differ* **2022**, *29*, 156–166, doi:10.1038/s41418-021-00844-6.
123. Li, Y.; Jerkic, M.; Slutsky, A.S.; Zhang, H. Molecular Mechanisms of Sex Bias Differences in COVID-19 Mortality. *Critical Care* **2020**, *24*, 405, doi:10.1186/s13054-020-03118-8.
124. Hu, S.; Yin, F.; Nie, L.; Wang, Y.; Qin, J.; Chen, J. Estrogen and Estrogen Receptor Modulators: Potential Therapeutic Strategies for COVID-19 and Breast Cancer. *Frontiers in Endocrinology* **2022**, *13*.

125. Channappanavar, R.; Fett, C.; Mack, M.; Ten Eyck, P.P.; Meyerholz, D.K.; Perlman, S. Sex-Based Differences in Susceptibility to Severe Acute Respiratory Syndrome Coronavirus Infection. *J Immunol* **2017**, *198*, 4046–4053, doi:10.4049/jimmunol.1601896.
126. Pelzl, L.; Singh, A.; Funk, J.; Witzemann, A.; Marini, I.; Zlamal, J.; Weich, K.; Abou-Khalel, W.; Hammer, S.; Uzun, G.; et al. Antibody-Mediated Procoagulant Platelet Formation in COVID-19 Is AKT Dependent. *J Thromb Haemost* **2022**, *20*, 387–398, doi:10.1111/jth.15587.
127. Tao, S.-L.; Wang, X.; Feng, Y.; Kang, P.; Li, Q.; Sun, T.; Tan, Q.; Deng, B. Is the Presence of Lung Injury in COVID-19 an Independent Risk Factor for Secondary Lung Cancer? *Med Hypotheses* **2020**, *143*, 110074, doi:10.1016/j.mehy.2020.110074.
128. Moreno Roig, E.; Groot, A.J.; Yaromina, A.; Hendrickx, T.C.; Barbeau, L.M.O.; Giuranno, L.; Dams, G.; Ient, J.; Olivo Pimentel, V.; van Gisbergen, M.W.; et al. HIF-1α and HIF-2α Differently Regulate the Radiation Sensitivity of NSCLC Cells. *Cells* **2019**, *8*, 45, doi:10.3390/cells8010045.
129. Dai, M.; Liu, D.; Liu, M.; Zhou, F.; Li, G.; Chen, Z.; Zhang, Z.; You, H.; Wu, M.; Zheng, Q.; et al. Patients with Cancer Appear More Vulnerable to SARS-CoV-2: A Multicenter Study during the COVID-19 Outbreak. *Cancer Discov* **2020**, *10*, 783–791, doi:10.1158/2159-8290.CD-20-0422.
130. Klumperman, J.; Raposo, G. The Complex Ultrastructure of the Endolysosomal System. *Cold Spring Harb Perspect Biol* **2014**, *6*, a016857, doi:10.1101/cshperspect.a016857.
131. Théry, C.; Zitvogel, L.; Amigorena, S. Exosomes: Composition, Biogenesis and Function. *Nat Rev Immunol* **2002**, *2*, 569–579, doi:10.1038/nri855.
132. Guay, C.; Regazzi, R. Exosomes as New Players in Metabolic Organ Cross-Talk. *Diabetes Obes Metab* **2017**, *19 Suppl 1*, 137–146, doi:10.1111/dom.13027.
133. Huang, T.; Deng, C.-X. Current Progresses of Exosomes as Cancer Diagnostic and Prognostic Biomarkers. *Int J Biol Sci* **2019**, *15*, 1–11, doi:10.7150/ijbs.27796.
134. Miao, M.; Miao, Y.; Zhu, Y.; Wang, J.; Zhou, H. Advances in Exosomes as Diagnostic and Therapeutic Biomarkers for Gynaecological Malignancies. *Cancers* **2022**, *14*, 4743, doi:10.3390/cancers14194743.
135. Han, L.; Zhao, Z.; Yang, K.; Xin, M.; Zhou, L.; Chen, S.; Zhou, S.; Tang, Z.; Ji, H.; Dai, R. Application of Exosomes in the Diagnosis and Treatment of Pancreatic Diseases. *Stem Cell Research & Therapy* **2022**, *13*, 153, doi:10.1186/s13287-022-02826-y.
136. Hou, R.; Li, Y.; Sui, Z.; Yuan, H.; Yang, K.; Liang, Z.; Zhang, L.; Zhang, Y. Advances in Exosome Isolation Methods and Their Applications in Proteomic Analysis of Biological Samples. *Anal Bioanal Chem* **2019**, *411*, 5351–5361, doi:10.1007/s00216-019-01982-0.
137. Jablonska, J.; Pietrowska, M.; Ludwig, S.; Lang, S.; Thakur, B.K. Challenges in the Isolation and Proteomic Analysis of Cancer Exosomes—Implications for Translational Research. *Proteomes* **2019**, *7*, 22, doi:10.3390/proteomes7020022.

138. Zhang, W.; Jiang, X.; Bao, J.; Wang, Y.; Liu, H.; Tang, L. Exosomes in Pathogen Infections: A Bridge to Deliver Molecules and Link Functions. *Front Immunol* **2018**, *9*, 90, doi:10.3389/fimmu.2018.00090.
139. WHO Coronavirus (COVID-19) Dashboard Available online: https://covid19.who.int (accessed on 7 December 2022).
140. Williamson, E.J.; Walker, A.J.; Bhaskaran, K.; Bacon, S.; Bates, C.; Morton, C.E.; Curtis, H.J.; Mehrkar, A.; Evans, D.; Inglesby, P.; et al. Factors Associated with COVID-19-Related Death Using OpenSAFELY. *Nature* **2020**, *584*, 430–436, doi:10.1038/s41586-020-2521-4.
141. Guan, W.-J.; Ni, Z.-Y.; Hu, Y.; Liang, W.-H.; Ou, C.-Q.; He, J.-X.; Liu, L.; Shan, H.; Lei, C.-L.; Hui, D.S.C.; et al. Clinical Characteristics of Coronavirus Disease 2019 in China. *N Engl J Med* **2020**, *382*, 1708–1720, doi:10.1056/NEJMoa2002032.
142. Huang, C.; Wang, Y.; Li, X.; Ren, L.; Zhao, J.; Hu, Y.; Zhang, L.; Fan, G.; Xu, J.; Gu, X.; et al. Clinical Features of Patients Infected with 2019 Novel Coronavirus in Wuhan, China. *Lancet* **2020**, *395*, 497–506, doi:10.1016/S0140-6736(20)30183-5.
143. Zhou, F.; Yu, T.; Du, R.; Fan, G.; Liu, Y.; Liu, Z.; Xiang, J.; Wang, Y.; Song, B.; Gu, X.; et al. Clinical Course and Risk Factors for Mortality of Adult Inpatients with COVID-19 in Wuhan, China: A Retrospective Cohort Study. *The Lancet* **2020**, *395*, 1054–1062, doi:10.1016/S0140-6736(20)30566-3.
144. Liu, W.; Tao, Z.-W.; Wang, L.; Yuan, M.-L.; Liu, K.; Zhou, L.; Wei, S.; Deng, Y.; Liu, J.; Liu, H.-G.; et al. Analysis of Factors Associated with Disease Outcomes in Hospitalized Patients with 2019 Novel Coronavirus Disease. *Chin Med J (Engl)* **2020**, *133*, 1032–1038, doi:10.1097/CM9.0000000000000775.
145. Wu, D.; Lu, J.; Liu, Y.; Zhang, Z.; Luo, L. Positive Effects of COVID-19 Control Measures on Influenza Prevention. *Int J Infect Dis* **2020**, *95*, 345–346, doi:10.1016/j.ijid.2020.04.009.
146. Gupta, A.; Madhavan, M.V.; Sehgal, K.; Nair, N.; Mahajan, S.; Sehrawat, T.S.; Bikdeli, B.; Ahluwalia, N.; Ausiello, J.C.; Wan, E.Y.; et al. Extrapulmonary Manifestations of COVID-19. *Nat Med* **2020**, *26*, 1017–1032, doi:10.1038/s41591-020-0968-3.
147. Zhou, P.; Yang, X.-L.; Wang, X.-G.; Hu, B.; Zhang, L.; Zhang, W.; Si, H.-R.; Zhu, Y.; Li, B.; Huang, C.-L.; et al. A Pneumonia Outbreak Associated with a New Coronavirus of Probable Bat Origin. *Nature* **2020**, *579*, 270–273, doi:10.1038/s41586-020-2012-7.
148. Zhu, N.; Zhang, D.; Wang, W.; Li, X.; Yang, B.; Song, J.; Zhao, X.; Huang, B.; Shi, W.; Lu, R.; et al. A Novel Coronavirus from Patients with Pneumonia in China, 2019. *N Engl J Med* **2020**, *382*, 727–733, doi:10.1056/NEJMoa2001017.
149. Rothan, H.A.; Byrareddy, S.N. The Epidemiology and Pathogenesis of Coronavirus Disease (COVID-19) Outbreak. *J Autoimmun* **2020**, *109*, 102433, doi:10.1016/j.jaut.2020.102433.
150. Raposo, G.; Stoorvogel, W. Extracellular Vesicles: Exosomes, Microvesicles, and Friends. *Journal of Cell Biology* **2013**, *200*, 373–383, doi:10.1083/jcb.201211138.

151. Zhang, Q.; Higginbotham, J.N.; Jeppesen, D.K.; Yang, Y.-P.; Li, W.; McKinley, E.T.; Graves-Deal, R.; Ping, J.; Britain, C.M.; Dorsett, K.A.; et al. Transfer of Functional Cargo in Exomeres. *Cell Rep* **2019**, *27*, 940-954.e6, doi:10.1016/j.celrep.2019.01.009.
152. S, A.; M, S.; S, M. Exomeres: A New Member of Extracellular Vesicles Family. *Sub-cellular biochemistry* **2021**, *97*, doi:10.1007/978-3-030-67171-6_5.
153. Huang, W.; Yan, Y.; Liu, Y.; Lin, M.; Ma, J.; Zhang, W.; Dai, J.; Li, J.; Guo, Q.; Chen, H.; et al. Exosomes with Low MiR-34c-3p Expression Promote Invasion and Migration of Non-Small Cell Lung Cancer by Upregulating Integrin A2β1. *Signal Transduct Target Ther* **2020**, *5*, 39, doi:10.1038/s41392-020-0133-y.
154. Kowal, J.; Tkach, M.; Théry, C. Biogenesis and Secretion of Exosomes. *Curr Opin Cell Biol* **2014**, *29*, 116–125, doi:10.1016/j.ceb.2014.05.004.
155. Maas, S.L.N.; Breakefield, X.O.; Weaver, A.M. Extracellular Vesicles: Unique Intercellular Delivery Vehicles. *Trends Cell Biol* **2017**, *27*, 172–188, doi:10.1016/j.tcb.2016.11.003.
156. Camussi, G.; Deregibus, M.C.; Bruno, S.; Cantaluppi, V.; Biancone, L. Exosomes/Microvesicles as a Mechanism of Cell-to-Cell Communication. *Kidney Int* **2010**, *78*, 838–848, doi:10.1038/ki.2010.278.
157. PULLIERO, A.; PERGOLI, L.; LA MAESTRA, S.; MICALE, R.T.; CAMOIRANO, A.; BOLLATI, V.; IZZOTTI, A.; DE FLORA, S. Extracellular Vesicles in Biological Fluids. A Biomarker of Exposure to Cigarette Smoke and Treatment with Chemopreventive Drugs. *J Prev Med Hyg* **2019**, *60*, E327–E336, doi:10.15167/2421-4248/jpmh2019.60.4.1284.
158. Paskeh, M.D.A.; Entezari, M.; Mirzaei, S.; Zabolian, A.; Saleki, H.; Naghdi, M.J.; Sabet, S.; Khoshbakht, M.A.; Hashemi, M.; Hushmandi, K.; et al. Emerging Role of Exosomes in Cancer Progression and Tumor Microenvironment Remodeling. *Journal of Hematology & Oncology* **2022**, *15*, 83, doi:10.1186/s13045-022-01305-4.
159. Owczarek, K.; Szczepanski, A.; Milewska, A.; Baster, Z.; Rajfur, Z.; Sarna, M.; Pyrc, K. Early Events during Human Coronavirus OC43 Entry to the Cell. *Sci Rep* **2018**, *8*, 7124, doi:10.1038/s41598-018-25640-0.
160. Ali, S.A.; Huang, M.-B.; Campbell, P.E.; Roth, W.W.; Campbell, T.; Khan, M.; Newman, G.; Villinger, F.; Powell, M.D.; Bond, V.C. Genetic Characterization of HIV Type 1 Nef-Induced Vesicle Secretion. *AIDS Res Hum Retroviruses* **2010**, *26*, 173–192, doi:10.1089/aid.2009.0068.
161. Arenaccio, C.; Anticoli, S.; Manfredi, F.; Chiozzini, C.; Olivetta, E.; Federico, M. Latent HIV-1 Is Activated by Exosomes from Cells Infected with Either Replication-Competent or Defective HIV-1. *Retrovirology* **2015**, *12*, 87, doi:10.1186/s12977-015-0216-y.
162. Yoshikawa, F.S.Y.; Teixeira, F.M.E.; Sato, M.N.; Oliveira, L.M. da S. Delivery of MicroRNAs by Extracellular Vesicles in Viral Infections: Could the News Be Packaged? *Cells* **2019**, *8*, 611, doi:10.3390/cells8060611.
163. Simpson, R.J.; Lim, J.W.; Moritz, R.L.; Mathivanan, S. Exosomes: Proteomic Insights and Diagnostic Potential. *Expert Rev Proteomics* **2009**, *6*, 267–283, doi:10.1586/epr.09.17.

164. Fleming, A.; Sampey, G.; Chung, M.C.; Bailey, C.; van Hoek, M.L.; Kashanchi, F.; Hakami, R.M. The Carrying Pigeons of the Cell: Exosomes and Their Role in Infectious Diseases Caused by Human Pathogens. *Pathogens and Disease* **2014**, *71*, 109–120, doi:10.1111/2049-632X.12135.
165. Han, L.; Lam, E.W.-F.; Sun, Y. Extracellular Vesicles in the Tumor Microenvironment: Old Stories, but New Tales. *Mol Cancer* **2019**, *18*, 59, doi:10.1186/s12943-019-0980-8.
166. Dogrammatzis, C.; Waisner, H.; Kalamvoki, M. Cloaked Viruses and Viral Factors in Cutting Edge Exosome-Based Therapies. *Frontiers in Cell and Developmental Biology* **2020**, *8*.
167. Théry, C.; Witwer, K.W.; Aikawa, E.; Alcaraz, M.J.; Anderson, J.D.; Andriantsitohaina, R.; Antoniou, A.; Arab, T.; Archer, F.; Atkin-Smith, G.K.; et al. Minimal Information for Studies of Extracellular Vesicles 2018 (MISEV2018): A Position Statement of the International Society for Extracellular Vesicles and Update of the MISEV2014 Guidelines. *J Extracell Vesicles* **2018**, *7*, 1535750, doi:10.1080/20013078.2018.1535750.
168. Maione, F.; Cappellano, G.; Bellan, M.; Raineri, D.; Chiocchetti, A. Chicken-or-egg Question: Which Came First, Extracellular Vesicles or Autoimmune Diseases? *J Leukoc Biol* **2020**, *108*, 601–616, doi:10.1002/JLB.3MR0120-232R.
169. Rački, N.; Morisset, D.; Gutierrez-Aguirre, I.; Ravnikar, M. One-Step RT-Droplet Digital PCR: A Breakthrough in the Quantification of Waterborne RNA Viruses. *Anal Bioanal Chem* **2014**, *406*, 661–667, doi:10.1007/s00216-013-7476-y.
170. Lu, F.; Lamontagne, J.; Sun, A.; Pinkerton, M.; Block, T.; Lu, X. Role of the Inflammatory Protein Serine Protease Inhibitor Kazal in Preventing Cytolytic Granule Granzyme A-Mediated Apoptosis. *Immunology* **2011**, *134*, 398–408, doi:10.1111/j.1365-2567.2011.03498.x.
171. Stecher, V.J.; Kaplan, J.E.; Connolly, K.; Mielens, Z.; Saelens, J.K. Fibronectin in Acute and Chronic Inflammation. *Arthritis Rheum* **1986**, *29*, 394–399, doi:10.1002/art.1780290313.
172. Rubel, C.; Fernández, G.C.; Dran, G.; Bompadre, M.B.; Isturiz, M.A.; Palermo, M.S. Fibrinogen Promotes Neutrophil Activation and Delays Apoptosis. *J Immunol* **2001**, *166*, 2002–2010, doi:10.4049/jimmunol.166.3.2002.
173. Vargas, A.; Roux-Dalvai, F.; Droit, A.; Lavoie, J.-P. Neutrophil-Derived Exosomes: A New Mechanism Contributing to Airway Smooth Muscle Remodeling. *Am J Respir Cell Mol Biol* **2016**, *55*, 450–461, doi:10.1165/rcmb.2016-0033OC.
174. Peix, L.; Evans, I.C.; Pearce, D.R.; Simpson, J.K.; Maher, T.M.; McAnulty, R.J. Diverse Functions of Clusterin Promote and Protect against the Development of Pulmonary Fibrosis. *Sci Rep* **2018**, *8*, 1906, doi:10.1038/s41598-018-20316-1.
175. D'Alessandro, A.; Thomas, T.; Dzieciatkowska, M.; Hill, R.C.; Francis, R.O.; Hudson, K.E.; Zimring, J.C.; Hod, E.A.; Spitalnik, S.L.; Hansen, K.C. Serum Proteomics in COVID-19 Patients: Altered Coagulation and

Complement Status as a Function of IL-6 Level. *J Proteome Res* **2020**, *19*, 4417–4427, doi:10.1021/acs.jproteome.0c00365.

176. Shen, B.; Yi, X.; Sun, Y.; Bi, X.; Du, J.; Zhang, C.; Quan, S.; Zhang, F.; Sun, R.; Qian, L.; et al. Proteomic and Metabolomic Characterization of COVID-19 Patient Sera. *Cell* **2020**, *182*, 59-72.e15, doi:10.1016/j.cell.2020.05.032.
177. Messner, C.B.; Demichev, V.; Wendisch, D.; Michalick, L.; White, M.; Freiwald, A.; Textoris-Taube, K.; Vernardis, S.I.; Egger, A.-S.; Kreidl, M.; et al. Ultra-High-Throughput Clinical Proteomics Reveals Classifiers of COVID-19 Infection. *Cell Syst* **2020**, *11*, 11-24.e4, doi:10.1016/j.cels.2020.05.012.
178. Terpos, E.; Ntanasis-Stathopoulos, I.; Elalamy, I.; Kastritis, E.; Sergentanis, T.N.; Politou, M.; Psaltopoulou, T.; Gerotziafas, G.; Dimopoulos, M.A. Hematological Findings and Complications of COVID-19. *Am J Hematol* **2020**, *95*, 834–847, doi:10.1002/ajh.25829.
179. Kalluri, R.; LeBleu, V.S. The Biology, Function, and Biomedical Applications of Exosomes. *Science* **2020**, *367*, eaau6977, doi:10.1126/science.aau6977.
180. Urbanelli, L.; Buratta, S.; Tancini, B.; Sagini, K.; Delo, F.; Porcellati, S.; Emiliani, C. The Role of Extracellular Vesicles in Viral Infection and Transmission. *Vaccines (Basel)* **2019**, *7*, 102, doi:10.3390/vaccines7030102.
181. Kadiu, I.; Narayanasamy, P.; Dash, P.K.; Zhang, W.; Gendelman, H.E. Biochemical and Biologic Characterization of Exosomes and Microvesicles as Facilitators of HIV-1 Infection in Macrophages. *J Immunol* **2012**, *189*, 744–754, doi:10.4049/jimmunol.1102244.
182. Schorey, J.S.; Harding, C.V. Extracellular Vesicles and Infectious Diseases: New Complexity to an Old Story. *J Clin Invest* **2016**, *126*, 1181–1189, doi:10.1172/JCI81132.
183. Gambardella, J.; Sardu, C.; Morelli, M.B.; Messina, V.; Castellanos, V.; Marfella, R.; Maggi, P.; Paolisso, G.; Wang, X.; Santulli, G. Exosomal MicroRNAs Drive Thrombosis in COVID-19 2020, 2020.06.16.20133256.
184. Hassanpour, M.; Rezaie, J.; Nouri, M.; Panahi, Y. The Role of Extracellular Vesicles in COVID-19 Virus Infection. *Infect Genet Evol* **2020**, *85*, 104422, doi:10.1016/j.meegid.2020.104422.
185. Cocozza, F.; Névo, N.; Piovesana, E.; Lahaye, X.; Buchrieser, J.; Schwartz, O.; Manel, N.; Tkach, M.; Théry, C.; Martin-Jaular, L. Extracellular Vesicles Containing ACE2 Efficiently Prevent Infection by SARS-CoV-2 Spike Protein-containing Virus. *J Extracell Vesicles* **2020**, *10*, e12050, doi:10.1002/jev2.12050.
186. Noris, M.; Benigni, A.; Remuzzi, G. The Case of Complement Activation in COVID-19 Multiorgan Impact. *Kidney Int* **2020**, *98*, 314–322, doi:10.1016/j.kint.2020.05.013.
187. Risitano, A.M.; Mastellos, D.C.; Huber-Lang, M.; Yancopoulou, D.; Garlanda, C.; Ciceri, F.; Lambris, J.D. Complement as a Target in COVID-19? *Nat Rev Immunol* **2020**, *20*, 343–344, doi:10.1038/s41577-020-0320-7.

188. Chahar, H.S.; Corsello, T.; Kudlicki, A.S.; Komaravelli, N.; Casola, A. Respiratory Syncytial Virus Infection Changes Cargo Composition of Exosome Released from Airway Epithelial Cells. *Sci Rep* **2018**, *8*, 387, doi:10.1038/s41598-017-18672-5.
189. Ramlall, V.; Thangaraj, P.M.; Meydan, C.; Foox, J.; Butler, D.; Kim, J.; May, B.; De Freitas, J.K.; Glicksberg, B.S.; Mason, C.E.; et al. Immune Complement and Coagulation Dysfunction in Adverse Outcomes of SARS-CoV-2 Infection. *Nat Med* **2020**, *26*, 1609–1615, doi:10.1038/s41591-020-1021-2.
190. Kim, H.; Meyer, K.; Di Bisceglie, A.M.; Ray, R. Hepatitis C Virus Suppresses C9 Complement Synthesis and Impairs Membrane Attack Complex Function. *J Virol* **2013**, *87*, 5858–5867, doi:10.1128/JVI.00174-13.
191. Li, G.; Fan, Y.; Lai, Y.; Han, T.; Li, Z.; Zhou, P.; Pan, P.; Wang, W.; Hu, D.; Liu, X.; et al. Coronavirus Infections and Immune Responses. *J Med Virol* **2020**, *92*, 424–432, doi:10.1002/jmv.25685.
192. Gelain, M.E.; Bonsembiante, F. Acute Phase Proteins in Marine Mammals: State of Art, Perspectives and Challenges. *Frontiers in Immunology* **2019**, *10*.
193. Coperchini, F.; Chiovato, L.; Croce, L.; Magri, F.; Rotondi, M. The Cytokine Storm in COVID-19: An Overview of the Involvement of the Chemokine/Chemokine-Receptor System. *Cytokine Growth Factor Rev* **2020**, *53*, 25–32, doi:10.1016/j.cytogfr.2020.05.003.
194. Jamilloux, Y.; Henry, T.; Belot, A.; Viel, S.; Fauter, M.; El Jammal, T.; Walzer, T.; François, B.; Sève, P. Should We Stimulate or Suppress Immune Responses in COVID-19? Cytokine and Anti-Cytokine Interventions. *Autoimmun Rev* **2020**, *19*, 102567, doi:10.1016/j.autrev.2020.102567.
195. Li, L.; Chen, C. Contribution of Acute-Phase Reaction Proteins to the Diagnosis and Treatment of 2019 Novel Coronavirus Disease (COVID-19). *Epidemiology and Infection* **2020**, *148*, doi:10.1017/S095026882000165X.
196. Montesarchio, V.; Parrella, R.; Iommelli, C.; Bianco, A.; Manzillo, E.; Fraganza, F.; Palumbo, C.; Rea, G.; Murino, P.; De Rosa, R.; et al. Outcomes and Biomarker Analyses among Patients with COVID-19 Treated with Interleukin 6 (IL-6) Receptor Antagonist Sarilumab at a Single Institution in Italy. *J Immunother Cancer* **2020**, *8*, e001089, doi:10.1136/jitc-2020-001089.
197. Khinda, J.; Janjua, N.Z.; Cheng, S.; van den Heuvel, E.R.; Bhatti, P.; Darvishian, M. Association between Markers of Immune Response at Hospital Admission and COVID-19 Disease Severity and Mortality: A Meta-Analysis and Meta-Regression. *J Med Virol* **2021**, *93*, 1078–1098, doi:10.1002/jmv.26411.
198. Rolla, R.; Vidali, M.; Puricelli, C.; Scotta, A.M.; Pedrinelli, A.; Pergolini, P.; Pirisi, M.; Dianzani, U.; Rigamonti, C. Reduced Activity of B Lymphocytes, Recognised by Sysmex XN-2000™ Haematology Analyser, Predicts Mortality in Patients with Coronavirus Disease 2019. *International Journal of Laboratory Hematology* **2021**, *43*, e5–e8, doi:10.1111/ijlh.13331.

199. Ren, H.-W.; Wu, Y.; Dong, J.-H.; An, W.-M.; Yan, T.; Liu, Y.; Liu, C.-C. Analysis of Clinical Features and Imaging Signs of COVID-19 with the Assistance of Artificial Intelligence. *Eur Rev Med Pharmacol Sci* **2020**, *24*, 8210–8218, doi:10.26355/eurrev_202008_22510.
200. van Dijk, W.; Pos, O.; van der Stelt, M.E.; Moshage, H.J.; Yap, S.H.; Dente, L.; Baumann, P.; Eap, C.B. Inflammation-Induced Changes in Expression and Glycosylation of Genetic Variants of Alpha 1-Acid Glycoprotein. Studies with Human Sera, Primary Cultures of Human Hepatocytes and Transgenic Mice. *Biochem J* **1991**, *276 (Pt 2)*, 343–347, doi:10.1042/bj2760343.
201. Komastu, T.; Ireland, D.D.; Reiss, C.S. IL-12 and Viral Infections. *Cytokine Growth Factor Rev* **1998**, *9*, 277–285, doi:10.1016/s1359-6101(98)00017-3.
202. Palumbo, D.; Guazzarotti, G.; De Cobelli, F. Spontaneous Major Hemorrhage in COVID-19 Patients: Another Brick in the Wall of SARS-CoV-2-Associated Coagulation Disorders? *J Vasc Interv Radiol* **2020**, *31*, 1494–1496, doi:10.1016/j.jvir.2020.06.010.
203. Al-Samkari, H.; Karp Leaf, R.S.; Dzik, W.H.; Carlson, J.C.T.; Fogerty, A.E.; Waheed, A.; Goodarzi, K.; Bendapudi, P.K.; Bornikova, L.; Gupta, S.; et al. COVID-19 and Coagulation: Bleeding and Thrombotic Manifestations of SARS-CoV-2 Infection. *Blood* **2020**, *136*, 489–500, doi:10.1182/blood.2020006520.
204. Zheng, Y.; Zhang, Y.; Chi, H.; Chen, S.; Peng, M.; Luo, L.; Chen, L.; Li, J.; Shen, B.; Wang, D. The Hemocyte Counts as a Potential Biomarker for Predicting Disease Progression in COVID-19: A Retrospective Study. *Clin Chem Lab Med* **2020**, *58*, 1106–1115, doi:10.1515/cclm-2020-0377.
205. Lippi, G.; Plebani, M.; Henry, B.M. Thrombocytopenia Is Associated with Severe Coronavirus Disease 2019 (COVID-19) Infections: A Meta-Analysis. *Clin Chim Acta* **2020**, *506*, 145–148, doi:10.1016/j.cca.2020.03.022.
206. Fletcher-Sandersjöö, A.; Bellander, B.-M. Is COVID-19 Associated Thrombosis Caused by Overactivation of the Complement Cascade? A Literature Review. *Thromb Res* **2020**, *194*, 36–41, doi:10.1016/j.thromres.2020.06.027.
207. Colarusso, C.; Terlizzi, M.; Pinto, A.; Sorrentino, R. A Lesson from a Saboteur: High-MW Kininogen Impact in Coronavirus-induced Disease 2019. *Br J Pharmacol* **2020**, *177*, 4866–4872, doi:10.1111/bph.15154.
208. van de Veerdonk, F.L.; Netea, M.G.; van Deuren, M.; van der Meer, J.W.; de Mast, Q.; Brüggemann, R.J.; van der Hoeven, H. Kallikrein-Kinin Blockade in Patients with COVID-19 to Prevent Acute Respiratory Distress Syndrome. *Elife* **2020**, *9*, e57555, doi:10.7554/eLife.57555.
209. Fang, C.; Schmaier, A.H. Novel Anti-Thrombotic Mechanisms Mediated by Mas Receptor as Result of Balanced Activities between the Kallikrein/Kinin and the Renin-Angiotensin Systems. *Pharmacol Res* **2020**, *160*, 105096, doi:10.1016/j.phrs.2020.105096.

210. Fontana, P.; Casini, A.; Robert-Ebadi, H.; Glauser, F.; Righini, M.; Blondon, M. Venous Thromboembolism in COVID-19: Systematic Review of Reported Risks and Current Guidelines. *Swiss Med Wkly* **2020**, *150*, w20301, doi:10.4414/smw.2020.20301.
211. Grifoni, E.; Valoriani, A.; Cei, F.; Lamanna, R.; Gelli, A.M.G.; Ciambotti, B.; Vannucchi, V.; Moroni, F.; Pelagatti, L.; Tarquini, R.; et al. Interleukin-6 as Prognosticator in Patients with COVID-19. *J Infect* **2020**, *81*, 452–482, doi:10.1016/j.jinf.2020.06.008.
212. Sanjabi, S.; Zenewicz, L.A.; Kamanaka, M.; Flavell, R.A. Anti- and Pro-Inflammatory Roles of TGF-β, IL-10, and IL-22 In Immunity and Autoimmunity. *Curr Opin Pharmacol* **2009**, *9*, 447–453, doi:10.1016/j.coph.2009.04.008.
213. Chen, W. A Potential Treatment of COVID-19 with TGF-β Blockade. *Int J Biol Sci* **2020**, *16*, 1954–1955, doi:10.7150/ijbs.46891.
214. Zhu, L.; She, Z.-G.; Cheng, X.; Qin, J.-J.; Zhang, X.-J.; Cai, J.; Lei, F.; Wang, H.; Xie, J.; Wang, W.; et al. Association of Blood Glucose Control and Outcomes in Patients with COVID-19 and Pre-Existing Type 2 Diabetes. *Cell Metab* **2020**, *31*, 1068-1077.e3, doi:10.1016/j.cmet.2020.04.021.
215. Brufsky, A. Hyperglycemia, Hydroxychloroquine, and the COVID-19 Pandemic. *J Med Virol* **2020**, *92*, 770–775, doi:10.1002/jmv.25887.
216. Zhu, Q.-J.; Zhu, M.; Xu, X.-X.; Meng, X.-M.; Wu, Y.-G. Exosomes from High Glucose-Treated Macrophages Activate Glomerular Mesangial Cells *via* TGF-B1/Smad3 Pathway *in Vivo* and *in Vitro*. *FASEB J* **2019**, *33*, 9279–9290, doi:10.1096/fj.201802427rrr.
217. Xu, L.; Gimple, R.C.; Lau, W.B.; Lau, B.; Fei, F.; Shen, Q.; Liao, X.; Li, Y.; Wang, W.; He, Y.; et al. THE PRESENT AND FUTURE OF THE MASS SPECTROMETRY-BASED INVESTIGATION OF THE EXOSOME LANDSCAPE. *Mass spectrometry reviews* **2020**, *39*, 745–762, doi:10.1002/mas.21635.
218. Chettimada, S.; Lorenz, D.R.; Misra, V.; Dillon, S.T.; Reeves, R.K.; Manickam, C.; Morgello, S.; Kirk, G.D.; Mehta, S.H.; Gabuzda, D. Exosome Markers Associated with Immune Activation and Oxidative Stress in HIV Patients on Antiretroviral Therapy. *Sci Rep* **2018**, *8*, 7227, doi:10.1038/s41598-018-25515-4.
219. Li, H.; Xiang, X.; Ren, H.; Xu, L.; Zhao, L.; Chen, X.; Long, H.; Wang, Q.; Wu, Q. Serum Amyloid A Is a Biomarker of Severe Coronavirus Disease and Poor Prognosis. *J Infect* **2020**, *80*, 646–655, doi:10.1016/j.jinf.2020.03.035.
220. Matsumoto, H.; Kasai, T.; Sato, A.; Ishiwata, S.; Yatsu, S.; Shitara, J.; Murata, A.; Kato, T.; Suda, S.; Matsue, Y.; et al. Association between C-Reactive Protein Levels at Hospital Admission and Long-Term Mortality in Patients with Acute Decompensated Heart Failure. *Heart Vessels* **2019**, *34*, 1961–1968, doi:10.1007/s00380-019-01435-9.
221. Wang, L. C-Reactive Protein Levels in the Early Stage of COVID-19. *Med Mal Infect* **2020**, *50*, 332–334, doi:10.1016/j.medmal.2020.03.007.
222. Pierrakos, C.; Vincent, J.-L. Sepsis Biomarkers: A Review. *Crit Care* **2010**, *14*, R15, doi:10.1186/cc8872.

223. Zhou, H.; Pisitkun, T.; Aponte, A.; Yuen, P.S.T.; Hoffert, J.D.; Yasuda, H.; Hu, X.; Chawla, L.; Shen, R.-F.; Knepper, M.A.; et al. Exosomal Fetuin-A Identified by Proteomics: A Novel Urinary Biomarker for Detecting Acute Kidney Injury. *Kidney Int* **2006**, *70*, 1847–1857, doi:10.1038/sj.ki.5001874.
224. Schulert, G.S.; Grom, A.A. Pathogenesis of Macrophage Activation Syndrome and Potential for Cytokine- Directed Therapies. *Annu Rev Med* **2015**, *66*, 145–159, doi:10.1146/annurev-med-061813-012806.
225. Lim, H.Y.; Lim, S.Y.; Tan, C.K.; Thiam, C.H.; Goh, C.C.; Carbajo, D.; Chew, S.H.S.; See, P.; Chakarov, S.; Wang, X.N.; et al. Hyaluronan Receptor LYVE-1-Expressing Macrophages Maintain Arterial Tone through Hyaluronan-Mediated Regulation of Smooth Muscle Cell Collagen. *Immunity* **2018**, *49*, 326-341.e7, doi:10.1016/j.immuni.2018.06.008.
226. Allen, J.R.; Ge, L.; Huang, Y.; Brauer, R.; Parimon, T.; Cassel, S.; Sutterwala, F.; Peter, C. TIMP-1 Promotes the Immune Response in Influenza Induced Acute Lung Injury. *Lung* **2018**, *196*, 737–743, doi:10.1007/s00408-018-0154-2.
227. Unver, N.; Esendagli, G.; Yilmaz, G.; Guc, D. CXCL7-Induced Macrophage Infiltration in Lung Tumor Is Independent of CXCR2 Expression: CXCL7-Induced Macrophage Chemotaxis in LLC Tumors. *Cytokine* **2015**, *75*, 330–337, doi:10.1016/j.cyto.2015.07.018.
228. Pesce, E.; Manfrini, N.; Cordiglieri, C.; Santi, S.; Bandera, A.; Gobbini, A.; Gruarin, P.; Favalli, A.; Bombaci, M.; Cuomo, A.; et al. Exosomes Recovered From the Plasma of COVID-19 Patients Expose SARS-CoV-2 Spike-Derived Fragments and Contribute to the Adaptive Immune Response. *Front Immunol* **2021**, *12*, 785941, doi:10.3389/fimmu.2021.785941.
229. Tsai, S.J.; Atai, N.A.; Cacciottolo, M.; Nice, J.; Salehi, A.; Guo, C.; Sedgwick, A.; Kanagavelu, S.; Gould, S.J. Exosome-Mediated MRNA Delivery in Vivo Is Safe and Can Be Used to Induce SARS-CoV-2 Immunity. *J Biol Chem* **2021**, *297*, 101266, doi:10.1016/j.jbc.2021.101266.
230. Miyashita, Y.; Yoshida, T.; Takagi, Y.; Tsukamoto, H.; Takashima, K.; Kouwaki, T.; Makino, K.; Fukushima, S.; Nakamura, K.; Oshiumi, H. Circulating Extracellular Vesicle MicroRNAs Associated with Adverse Reactions, Proinflammatory Cytokine, and Antibody Production after COVID-19 Vaccination. *NPJ Vaccines* **2022**, *7*, 16, doi:10.1038/s41541-022-00439-3.
231. Bansal, S.; Perincheri, S.; Fleming, T.; Poulson, C.; Tiffany, B.; Bremner, R.M.; Mohanakumar, T. Cutting Edge: Circulating Exosomes with COVID Spike Protein Are Induced by BNT162b2 (Pfizer–BioNTech) Vaccination Prior to Development of Antibodies: A Novel Mechanism for Immune Activation by MRNA Vaccines. *The Journal of Immunology* **2021**, *207*, 2405–2410, doi:10.4049/jimmunol.2100637.
232. Zhu, Y.-G.; Shi, M.-M.; Monsel, A.; Dai, C.-X.; Dong, X.; Shen, H.; Li, S.-K.; Chang, J.; Xu, C.-L.; Li, P.; et al. Nebulized Exosomes Derived from Allogenic Adipose Tissue Mesenchymal Stromal Cells in Patients with Severe COVID-19: A Pilot Study. *Stem Cell Res Ther* **2022**, *13*, 220, doi:10.1186/s13287-022-02900-5.

233. van Riel, D.; de Wit, E. Next-Generation Vaccine Platforms for COVID-19. *Nat Mater* **2020**, *19*, 810–812, doi:10.1038/s41563-020-0746-0.
234. Sabanovic, B.; Piva, F.; Cecati, M.; Giulietti, M. Promising Extracellular Vesicle-Based Vaccines against Viruses, Including SARS-CoV-2. *Biology (Basel)* **2021**, *10*, 94, doi:10.3390/biology10020094.
235. Jiang, L.; Driedonks, T.A.P.; Jong, W.S.P.; Dhakal, S.; Bart van den Berg van Saparoea, H.; Sitaras, I.; Zhou, R.; Caputo, C.; Littlefield, K.; Lowman, M.; et al. A Bacterial Extracellular Vesicle-Based Intranasal Vaccine against SARS-CoV-2 Protects against Disease and Elicits Neutralizing Antibodies to Wild-Type and Delta Variants. *J Extracell Vesicles* **2022**, *11*, e12192, doi:10.1002/jev2.12192.
236. Gill, S.R.; Pop, M.; DeBoy, R.T.; Eckburg, P.B.; Turnbaugh, P.J.; Samuel, B.S.; Gordon, J.I.; Relman, D.A.; Fraser-Liggett, C.M.; Nelson, K.E. Metagenomic Analysis of the Human Distal Gut Microbiome. *Science* **2006**, *312*, 1355–1359, doi:10.1126/science.1124234.
237. Issa Isaac, N.; Philippe, D.; Nicholas, A.; Raoult, D.; Eric, C. Metaproteomics of the Human Gut Microbiota: Challenges and Contributions to Other OMICS. *Clinical Mass Spectrometry* **2019**, *14*, 18–30, doi:10.1016/j.clinms.2019.06.001.
238. Marchesi, J.R.; Holmes, E.; Khan, F.; Kochhar, S.; Scanlan, P.; Shanahan, F.; Wilson, I.D.; Wang, Y. Rapid and Noninvasive Metabonomic Characterization of Inflammatory Bowel Disease. *J Proteome Res* **2007**, *6*, 546–551, doi:10.1021/pr060470d.
239. Turnbaugh, P.J.; Ley, R.E.; Mahowald, M.A.; Magrini, V.; Mardis, E.R.; Gordon, J.I. An Obesity-Associated Gut Microbiome with Increased Capacity for Energy Harvest. *Nature* **2006**, *444*, 1027–1031, doi:10.1038/nature05414.
240. Holmes, E.; Loo, R.L.; Stamler, J.; Bictash, M.; Yap, I.K.S.; Chan, Q.; Ebbels, T.; De Iorio, M.; Brown, I.J.; Veselkov, K.A.; et al. Human Metabolic Phenotype Diversity and Its Association with Diet and Blood Pressure. *Nature* **2008**, *453*, 396–400, doi:10.1038/nature06882.
241. Finegold, S.M. Therapy and Epidemiology of Autism--Clostridial Spores as Key Elements. *Med Hypotheses* **2008**, *70*, 508–511, doi:10.1016/j.mehy.2007.07.019.
242. Gagnière, J.; Raisch, J.; Veziant, J.; Barnich, N.; Bonnet, R.; Buc, E.; Bringer, M.-A.; Pezet, D.; Bonnet, M. Gut Microbiota Imbalance and Colorectal Cancer. *World J Gastroenterol* **2016**, *22*, 501–518, doi:10.3748/wjg.v22.i2.501.
243. Muller, E.; Algavi, Y.M.; Borenstein, E. A Meta-Analysis Study of the Robustness and Universality of Gut Microbiome-Metabolome Associations. *Microbiome* **2021**, *9*, 203, doi:10.1186/s40168-021-01149-z.
244. Kinross, J.M.; Darzi, A.W.; Nicholson, J.K. Gut Microbiome-Host Interactions in Health and Disease. *Genome Medicine* **2011**, *3*, 14, doi:10.1186/gm228.
245. Nicholson, J.K.; Holmes, E.; Wilson, I.D. Gut Microorganisms, Mammalian Metabolism and Personalized Health Care. *Nat Rev Microbiol* **2005**, *3*, 431–438, doi:10.1038/nrmicro1152.

246. Ebbeling, C.B.; Pawlak, D.B.; Ludwig, D.S. Childhood Obesity: Public-Health Crisis, Common Sense Cure. *Lancet* **2002**, *360*, 473–482, doi:10.1016/S0140-6736(02)09678-2.
247. Freedman, D.S.; Khan, L.K.; Dietz, W.H.; Srinivasan, S.R.; Berenson, G.S. Relationship of Childhood Obesity to Coronary Heart Disease Risk Factors in Adulthood: The Bogalusa Heart Study. *Pediatrics* **2001**, *108*, 712–718, doi:10.1542/peds.108.3.712.
248. Tirosh, A.; Shai, I.; Afek, A.; Dubnov-Raz, G.; Ayalon, N.; Gordon, B.; Derazne, E.; Tzur, D.; Shamis, A.; Vinker, S.; et al. Adolescent BMI Trajectory and Risk of Diabetes versus Coronary Disease. *N Engl J Med* **2011**, *364*, 1315–1325, doi:10.1056/NEJMoa1006992.
249. Young-Hyman, D.; Schlundt, D.G.; Herman, L.; De Luca, F.; Counts, D. Evaluation of the Insulin Resistance Syndrome in 5- to 10-Year-Old Overweight/Obese African-American Children. *Diabetes Care* **2001**, *24*, 1359–1364, doi:10.2337/diacare.24.8.1359.
250. Naska, A.; Trichopoulou, A. Back to the Future: The Mediterranean Diet Paradigm. *Nutr Metab Cardiovasc Dis* **2014**, *24*, 216–219, doi:10.1016/j.numecd.2013.11.007.
251. Bach-Faig, A.; Berry, E.M.; Lairon, D.; Reguant, J.; Trichopoulou, A.; Dernini, S.; Medina, F.X.; Battino, M.; Belahsen, R.; Miranda, G.; et al. Mediterranean Diet Pyramid Today. Science and Cultural Updates. *Public Health Nutr* **2011**, *14*, 2274–2284, doi:10.1017/S1368980011002515.
252. Liu, B.-N.; Liu, X.-T.; Liang, Z.-H.; Wang, J.-H. Gut Microbiota in Obesity. *World Journal of Gastroenterology* **2021**, *27*, 3837–3850, doi:10.3748/wjg.v27.i25.3837.
253. Wang, W.-L.; Xu, S.-Y.; Ren, Z.-G.; Tao, L.; Jiang, J.-W.; Zheng, S.-S. Application of Metagenomics in the Human Gut Microbiome. *World J Gastroenterol* **2015**, *21*, 803–814, doi:10.3748/wjg.v21.i3.803.
254. Peters, D.L.; Wang, W.; Zhang, X.; Ning, Z.; Mayne, J.; Figeys, D. Metaproteomic and Metabolomic Approaches for Characterizing the Gut Microbiome. *Proteomics* **2019**, *19*, e1800363, doi:10.1002/pmic.201800363.
255. Cole, T.J.; Lobstein, T. Extended International (IOTF) Body Mass Index Cut-Offs for Thinness, Overweight and Obesity. *Pediatr Obes* **2012**, *7*, 284–294, doi:10.1111/j.2047-6310.2012.00064.x.
256. Iacoviello, L.; Bonaccio, M.; Cairella, G.; Catani, M.V.; Costanzo, S.; D'Elia, L.; Giacco, R.; Rendina, D.; Sabino, P.; Savini, I.; et al. Diet and Primary Prevention of Stroke: Systematic Review and Dietary Recommendations by the Ad Hoc Working Group of the Italian Society of Human Nutrition. *Nutrition, Metabolism and Cardiovascular Diseases* **2018**, *28*, 309–334, doi:10.1016/j.numecd.2017.12.010.
257. .:: .:: MedDiet - Mediterranean Diet ::. Available online: https://www.med-diet.eu/ (accessed on 13 December 2022).
258. Zhang, X.; Ning, Z.; Mayne, J.; Moore, J.I.; Li, J.; Butcher, J.; Deeke, S.A.; Chen, R.; Chiang, C.-K.; Wen, M.; et al. MetaPro-IQ: A Universal Metaproteomic Approach to Studying Human and Mouse Gut Microbiota. *Microbiome* **2016**, *4*, 31, doi:10.1186/s40168-016-0176-z.

259. UniProt Consortium UniProt: A Worldwide Hub of Protein Knowledge. *Nucleic Acids Res* **2019**, *47*, D506–D515, doi:10.1093/nar/gky1049.
260. Li, J.; Jia, H.; Cai, X.; Zhong, H.; Feng, Q.; Sunagawa, S.; Arumugam, M.; Kultima, J.R.; Prifti, E.; Nielsen, T.; et al. An Integrated Catalog of Reference Genes in the Human Gut Microbiome. *Nat Biotechnol* **2014**, *32*, 834–841, doi:10.1038/nbt.2942.
261. Gurdeep Singh, R.; Tanca, A.; Palomba, A.; Van der Jeugt, F.; Verschaffelt, P.; Uzzau, S.; Martens, L.; Dawyndt, P.; Mesuere, B. Unipept 4.0: Functional Analysis of Metaproteome Data. *J Proteome Res* **2019**, *18*, 606–615, doi:10.1021/acs.jproteome.8b00716.
262. Pang, Z.; Zhou, G.; Ewald, J.; Chang, L.; Hacariz, O.; Basu, N.; Xia, J. Using MetaboAnalyst 5.0 for LC–HRMS Spectra Processing, Multi-Omics Integration and Covariate Adjustment of Global Metabolomics Data. *Nat Protoc* **2022**, *17*, 1735–1761, doi:10.1038/s41596-022-00710-w.
263. Duncan, S.H.; Lobley, G.E.; Holtrop, G.; Ince, J.; Johnstone, A.M.; Louis, P.; Flint, H.J. Human Colonic Microbiota Associated with Diet, Obesity and Weight Loss. *Int J Obes (Lond)* **2008**, *32*, 1720–1724, doi:10.1038/ijo.2008.155.
264. Jumpertz, R.; Le, D.S.; Turnbaugh, P.J.; Trinidad, C.; Bogardus, C.; Gordon, J.I.; Krakoff, J. Energy-Balance Studies Reveal Associations between Gut Microbes, Caloric Load, and Nutrient Absorption in Humans. *Am J Clin Nutr* **2011**, *94*, 58–65, doi:10.3945/ajcn.110.010132.
265. Xu, P.; Li, M.; Zhang, J.; Zhang, T. Correlation of Intestinal Microbiota with Overweight and Obesity in Kazakh School Children. *BMC Microbiology* **2012**, *12*, 283, doi:10.1186/1471-2180-12-283.
266. Indiani, C.M.D.S.P.; Rizzardi, K.F.; Castelo, P.M.; Ferraz, L.F.C.; Darrieux, M.; Parisotto, T.M. Childhood Obesity and Firmicutes/Bacteroidetes Ratio in the Gut Microbiota: A Systematic Review. *Child Obes* **2018**, *14*, 501–509, doi:10.1089/chi.2018.0040.
267. Krajmalnik-Brown, R.; Ilhan, Z.-E.; Kang, D.-W.; DiBaise, J.K. Effects of Gut Microbes on Nutrient Absorption and Energy Regulation. *Nutr Clin Pract* **2012**, *27*, 201–214, doi:10.1177/0884533611436116.
268. de La Serre, C.B.; Ellis, C.L.; Lee, J.; Hartman, A.L.; Rutledge, J.C.; Raybould, H.E. Propensity to High-Fat Diet-Induced Obesity in Rats Is Associated with Changes in the Gut Microbiota and Gut Inflammation. *Am J Physiol Gastrointest Liver Physiol* **2010**, *299*, G440-448, doi:10.1152/ajpgi.00098.2010.
269. An, Y.; Li, Y.; Wang, X.; Chen, Z.; Xu, H.; Wu, L.; Li, S.; Wang, C.; Luan, W.; Wang, X.; et al. Cordycepin Reduces Weight through Regulating Gut Microbiota in High-Fat Diet-Induced Obese Rats. *Lipids in Health and Disease* **2018**, *17*, 276, doi:10.1186/s12944-018-0910-6.
270. Xu, Y.; Ai, C.; Jiang, P.; Sun, X.; Liu, Y.; Jiang, G.; Song, S. Oligosaccharides from Gracilaria Lemaneiformis Better Attenuated High Fat Diet-Induced Metabolic Syndrome by Promoting the Bacteroidales Proliferation. *Food Funct* **2020**, *11*, 1049–1062, doi:10.1039/c9fo01996k.

271. Zhao, L.; Zhang, Q.; Ma, W.; Tian, F.; Shen, H.; Zhou, M. A Combination of Quercetin and Resveratrol Reduces Obesity in High-Fat Diet-Fed Rats by Modulation of Gut Microbiota. *Food Funct* **2017**, *8*, 4644–4656, doi:10.1039/c7fo01383c.
272. Picchianti-Diamanti, A.; Panebianco, C.; Salemi, S.; Sorgi, M.L.; Di Rosa, R.; Tropea, A.; Sgrulletti, M.; Salerno, G.; Terracciano, F.; D'Amelio, R.; et al. Analysis of Gut Microbiota in Rheumatoid Arthritis Patients: Disease-Related Dysbiosis and Modifications Induced by Etanercept. *Int J Mol Sci* **2018**, *19*, 2938, doi:10.3390/ijms19102938.
273. Wang, H.; Yan, Y.; Yi, X.; Duan, Y.; Wang, J.; Li, S.; Luo, L.; Huang, T.; Inglis, B.; Li, X.; et al. Histopathological Features and Composition of Gut Microbiota in Rhesus Monkey of Alcoholic Liver Disease. *Frontiers in Microbiology* **2019**, *10*.
274. Hou, Y.-P.; He, Q.-Q.; Ouyang, H.-M.; Peng, H.-S.; Wang, Q.; Li, J.; Lv, X.-F.; Zheng, Y.-N.; Li, S.-C.; Liu, H.-L.; et al. Human Gut Microbiota Associated with Obesity in Chinese Children and Adolescents. *Biomed Res Int* **2017**, *2017*, 7585989, doi:10.1155/2017/7585989.
275. Quiroga, R.; Nistal, E.; Estébanez, B.; Porras, D.; Juárez-Fernández, M.; Martínez-Flórez, S.; García-Mediavilla, M.V.; de Paz, J.A.; González-Gallego, J.; Sánchez-Campos, S.; et al. Exercise Training Modulates the Gut Microbiota Profile and Impairs Inflammatory Signaling Pathways in Obese Children. *Exp Mol Med* **2020**, *52*, 1048–1061, doi:10.1038/s12276-020-0459-0.
276. Gomez-Arango, L.F.; Barrett, H.L.; Wilkinson, S.A.; Callaway, L.K.; McIntyre, H.D.; Morrison, M.; Dekker Nitert, M. Low Dietary Fiber Intake Increases Collinsella Abundance in the Gut Microbiota of Overweight and Obese Pregnant Women. *Gut Microbes* **2018**, *9*, 189–201, doi:10.1080/19490976.2017.1406584.
277. Astbury, S.; Atallah, E.; Vijay, A.; Aithal, G.P.; Grove, J.I.; Valdes, A.M. Lower Gut Microbiome Diversity and Higher Abundance of Proinflammatory Genus Collinsella Are Associated with Biopsy-Proven Nonalcoholic Steatohepatitis. *Gut Microbes* **2020**, *11*, 569–580, doi:10.1080/19490976.2019.1681861.
278. Lam, Y.Y.; Ha, C.W.Y.; Campbell, C.R.; Mitchell, A.J.; Dinudom, A.; Oscarsson, J.; Cook, D.I.; Hunt, N.H.; Caterson, I.D.; Holmes, A.J.; et al. Increased Gut Permeability and Microbiota Change Associate with Mesenteric Fat Inflammation and Metabolic Dysfunction in Diet-Induced Obese Mice. *PLOS ONE* **2012**, *7*, e34233, doi:10.1371/journal.pone.0034233.
279. Jung, M.-J.; Lee, J.; Shin, N.-R.; Kim, M.-S.; Hyun, D.-W.; Yun, J.-H.; Kim, P.S.; Whon, T.W.; Bae, J.-W. Chronic Repression of MTOR Complex 2 Induces Changes in the Gut Microbiota of Diet-Induced Obese Mice. *Sci Rep* **2016**, *6*, 30887, doi:10.1038/srep30887.
280. Castaner, O.; Goday, A.; Park, Y.-M.; Lee, S.-H.; Magkos, F.; Shiow, S.-A.T.E.; Schröder, H. The Gut Microbiome Profile in Obesity: A Systematic Review. *Int J Endocrinol* **2018**, *2018*, 4095789, doi:10.1155/2018/4095789.
281. Gomes, A.C.; Hoffmann, C.; Mota, J.F. The Human Gut Microbiota: Metabolism and Perspective in Obesity. *Gut Microbes* **2018**, *9*, 308–325, doi:10.1080/19490976.2018.1465157.

282. O'Neill, I.; Schofield, Z.; Hall, L.J. Exploring the Role of the Microbiota Member Bifidobacterium in Modulating Immune-Linked Diseases. *Emerg Top Life Sci* **2017**, *1*, 333–349, doi:10.1042/ETLS20170058.
283. Mukherjee, A.; Lordan, C.; Ross, R.P.; Cotter, P.D. Gut Microbes from the Phylogenetically Diverse Genus Eubacterium and Their Various Contributions to Gut Health. *Gut Microbes* **2020**, *12*, 1802866, doi:10.1080/19490976.2020.1802866.
284. Parker, B.J.; Wearsch, P.A.; Veloo, A.C.M.; Rodriguez-Palacios, A. The Genus Alistipes: Gut Bacteria With Emerging Implications to Inflammation, Cancer, and Mental Health. *Front Immunol* **2020**, *11*, 906, doi:10.3389/fimmu.2020.00906.
285. Uusitupa, H.-M.; Rasinkangas, P.; Lehtinen, M.J.; Mäkelä, S.M.; Airaksinen, K.; Anglenius, H.; Ouwehand, A.C.; Maukonen, J. Bifidobacterium Animalis Subsp. Lactis 420 for Metabolic Health: Review of the Research. *Nutrients* **2020**, *12*, 892, doi:10.3390/nu12040892.
286. Mao, K.; Gao, J.; Wang, X.; Li, X.; Geng, S.; Zhang, T.; Sadiq, F.A.; Sang, Y. Bifidobacterium Animalis Subsp. Lactis BB-12 Has Effect Against Obesity by Regulating Gut Microbiota in Two Phases in Human Microbiota-Associated Rats. *Front Nutr* **2022**, *8*, 811619, doi:10.3389/fnut.2021.811619.
287. Wang, B.; Kong, Q.; Cui, S.; Li, X.; Gu, Z.; Zhao, J.; Zhang, H.; Chen, W.; Wang, G. Bifidobacterium Adolescentis Isolated from Different Hosts Modifies the Intestinal Microbiota and Displays Differential Metabolic and Immunomodulatory Properties in Mice Fed a High-Fat Diet. *Nutrients* **2021**, *13*, 1017, doi:10.3390/nu13031017.
288. Kulkarni, P.; Devkumar, P.; Chattopadhyay, I. Could Dysbiosis of Inflammatory and Anti-Inflammatory Gut Bacteria Have an Implications in the Development of Type 2 Diabetes? A Pilot Investigation. *BMC Research Notes* **2021**, *14*, 52, doi:10.1186/s13104-021-05466-2.
289. Knoll, R.L.; Forslund, K.; Kultima, J.R.; Meyer, C.U.; Kullmer, U.; Sunagawa, S.; Bork, P.; Gehring, S. Gut Microbiota Differs between Children with Inflammatory Bowel Disease and Healthy Siblings in Taxonomic and Functional Composition: A Metagenomic Analysis. *Am J Physiol Gastrointest Liver Physiol* **2017**, *312*, G327–G339, doi:10.1152/ajpgi.00293.2016.
290. Pittayanon, R.; Lau, J.T.; Leontiadis, G.I.; Tse, F.; Yuan, Y.; Surette, M.; Moayyedi, P. Differences in Gut Microbiota in Patients With vs Without Inflammatory Bowel Diseases: A Systematic Review. *Gastroenterology* **2020**, *158*, 930-946.e1, doi:10.1053/j.gastro.2019.11.294.
291. Wang, G.; Huang, S.; Cai, S.; Yu, H.; Wang, Y.; Zeng, X.; Qiao, S. Lactobacillus Reuteri Ameliorates Intestinal Inflammation and Modulates Gut Microbiota and Metabolic Disorders in Dextran Sulfate Sodium-Induced Colitis in Mice. *Nutrients* **2020**, *12*, 2298, doi:10.3390/nu12082298.
292. Blaut, M. Gut Microbiota and Energy Balance: Role in Obesity. *Proc Nutr Soc* **2015**, *74*, 227–234, doi:10.1017/S0029665114001700.
293. Kim, K.N.; Yao, Y.; Ju, S.Y. Short Chain Fatty Acids and Fecal Microbiota Abundance in Humans with Obesity: A Systematic Review and Meta-Analysis. *Nutrients* **2019**, *11*, 2512, doi:10.3390/nu11102512.

294. Bouchard-Mercier, A.; Rudkowska, I.; Lemieux, S.; Couture, P.; Vohl, M.-C. The Metabolic Signature Associated with the Western Dietary Pattern: A Cross-Sectional Study. *Nutr J* **2013**, *12*, 158, doi:10.1186/1475-2891-12-158.
295. Tremaroli, V.; Bäckhed, F. Functional Interactions between the Gut Microbiota and Host Metabolism. *Nature* **2012**, *489*, 242–249, doi:10.1038/nature11552.
296. Petriz, B.A.; Castro, A.P.; Almeida, J.A.; Gomes, C.P.; Fernandes, G.R.; Kruger, R.H.; Pereira, R.W.; Franco, O.L. Exercise Induction of Gut Microbiota Modifications in Obese, Non-Obese and Hypertensive Rats. *BMC Genomics* **2014**, *15*, 511, doi:10.1186/1471-2164-15-511.
297. de Oliveira, E.P.; Burini, R.C. The Impact of Physical Exercise on the Gastrointestinal Tract. *Curr Opin Clin Nutr Metab Care* **2009**, *12*, 533–538, doi:10.1097/MCO.0b013e32832e6776.
298. Matsumoto, M.; Inoue, R.; Tsukahara, T.; Ushida, K.; Chiji, H.; Matsubara, N.; Hara, H. Voluntary Running Exercise Alters Microbiota Composition and Increases N-Butyrate Concentration in the Rat Cecum. *Biosci Biotechnol Biochem* **2008**, *72*, 572–576, doi:10.1271/bbb.70474.
299. Queipo-Ortuño, M.I.; Seoane, L.M.; Murri, M.; Pardo, M.; Gomez-Zumaquero, J.M.; Cardona, F.; Casanueva, F.; Tinahones, F.J. Gut Microbiota Composition in Male Rat Models under Different Nutritional Status and Physical Activity and Its Association with Serum Leptin and Ghrelin Levels. *PLoS One* **2013**, *8*, e65465, doi:10.1371/journal.pone.0065465.
300. De Filippo, C.; Cavalieri, D.; Di Paola, M.; Ramazzotti, M.; Poullet, J.B.; Massart, S.; Collini, S.; Pieraccini, G.; Lionetti, P. Impact of Diet in Shaping Gut Microbiota Revealed by a Comparative Study in Children from Europe and Rural Africa. *Proc Natl Acad Sci U S A* **2010**, *107*, 14691–14696, doi:10.1073/pnas.1005963107.
301. Cardoso, I.; Bovet, P.; Viswanathan, B.; Luke, A.; Marques-Vidal, P. Nutrition Transition in a Middle-Income Country: 22-Year Trends in the Seychelles. *Eur J Clin Nutr* **2013**, *67*, 135–140, doi:10.1038/ejcn.2012.199.
302. Overby, H.B.; Ferguson, J.F. Gut Microbiota-Derived Short-Chain Fatty Acids Facilitate Microbiota:Host Cross Talk and Modulate Obesity and Hypertension. *Curr Hypertens Rep* **2021**, *23*, 8, doi:10.1007/s11906-020-01125-2.
303. David, L.A.; Maurice, C.F.; Carmody, R.N.; Gootenberg, D.B.; Button, J.E.; Wolfe, B.E.; Ling, A.V.; Devlin, A.S.; Varma, Y.; Fischbach, M.A.; et al. Diet Rapidly and Reproducibly Alters the Human Gut Microbiome. *Nature* **2014**, *505*, 559–563, doi:10.1038/nature12820.
304. Sonnenburg, E.D.; Smits, S.A.; Tikhonov, M.; Higginbottom, S.K.; Wingreen, N.S.; Sonnenburg, J.L. Diet-Induced Extinctions in the Gut Microbiota Compound over Generations. *Nature* **2016**, *529*, 212–215, doi:10.1038/nature16504.
305. Mayengbam, S.; Lambert, J.E.; Parnell, J.A.; Tunnicliffe, J.M.; Nicolucci, A.C.; Han, J.; Sturzenegger, T.; Shearer, J.; Mickiewicz, B.; Vogel, H.J.; et al. Impact of Dietary Fiber Supplementation on Modulating

Microbiota-Host-Metabolic Axes in Obesity. *J Nutr Biochem* **2019**, *64*, 228–236, doi:10.1016/j.jnutbio.2018.11.003.

306. Reimer, R.A.; Soto-Vaca, A.; Nicolucci, A.C.; Mayengbam, S.; Park, H.; Madsen, K.L.; Menon, R.; Vaughan, E.E. Effect of Chicory Inulin-Type Fructan-Containing Snack Bars on the Human Gut Microbiota in Low Dietary Fiber Consumers in a Randomized Crossover Trial. *Am J Clin Nutr* **2020**, *111*, 1286–1296, doi:10.1093/ajcn/nqaa074.
307. Fava, F.; Gitau, R.; Griffin, B.A.; Gibson, G.R.; Tuohy, K.M.; Lovegrove, J.A. The Type and Quantity of Dietary Fat and Carbohydrate Alter Faecal Microbiome and Short-Chain Fatty Acid Excretion in a Metabolic Syndrome "at-Risk" Population. *Int J Obes (Lond)* **2013**, *37*, 216–223, doi:10.1038/ijo.2012.33.
308. Wan, Y.; Tong, W.; Zhou, R.; Li, J.; Yuan, J.; Wang, F.; Li, D. Habitual Animal Fat Consumption in Shaping Gut Microbiota and Microbial Metabolites. *Food Funct.* **2019**, *10*, 7973–7982, doi:10.1039/C9FO01490J.
309. De Filippis, F.; Pellegrini, N.; Vannini, L.; Jeffery, I.B.; La Storia, A.; Laghi, L.; Serrazanetti, D.I.; Di Cagno, R.; Ferrocino, I.; Lazzi, C.; et al. High-Level Adherence to a Mediterranean Diet Beneficially Impacts the Gut Microbiota and Associated Metabolome. *Gut* **2016**, *65*, 1812–1821, doi:10.1136/gutjnl-2015-309957.
310. den Besten, G.; Lange, K.; Havinga, R.; van Dijk, T.H.; Gerding, A.; van Eunen, K.; Müller, M.; Groen, A.K.; Hooiveld, G.J.; Bakker, B.M.; et al. Gut-Derived Short-Chain Fatty Acids Are Vividly Assimilated into Host Carbohydrates and Lipids. *Am J Physiol Gastrointest Liver Physiol* **2013**, *305*, G900-910, doi:10.1152/ajpgi.00265.2013.
311. Liou, A.P.; Paziuk, M.; Luevano, J.-M.; Machineni, S.; Turnbaugh, P.J.; Kaplan, L.M. Conserved Shifts in the Gut Microbiota Due to Gastric Bypass Reduce Host Weight and Adiposity. *Sci Transl Med* **2013**, *5*, 178ra41, doi:10.1126/scitranslmed.3005687.
312. Perry, R.J.; Peng, L.; Barry, N.A.; Cline, G.W.; Zhang, D.; Cardone, R.L.; Petersen, K.F.; Kibbey, R.G.; Goodman, A.L.; Shulman, G.I. Acetate Mediates a Microbiome-Brain-β-Cell Axis to Promote Metabolic Syndrome. *Nature* **2016**, *534*, 213–217, doi:10.1038/nature18309.
313. Goffredo, M.; Mass, K.; Parks, E.J.; Wagner, D.A.; McClure, E.A.; Graf, J.; Savoye, M.; Pierpont, B.; Cline, G.; Santoro, N. Role of Gut Microbiota and Short Chain Fatty Acids in Modulating Energy Harvest and Fat Partitioning in Youth. *J Clin Endocrinol Metab* **2016**, *101*, 4367–4376, doi:10.1210/jc.2016-1797.
314. Fernandes, J.; Su, W.; Rahat-Rozenbloom, S.; Wolever, T.M.S.; Comelli, E.M. Adiposity, Gut Microbiota and Faecal Short Chain Fatty Acids Are Linked in Adult Humans. *Nutr Diabetes* **2014**, *4*, e121, doi:10.1038/nutd.2014.23.

315. Rahat-Rozenbloom, S.; Fernandes, J.; Gloor, G.B.; Wolever, T.M.S. Evidence for Greater Production of Colonic Short-Chain Fatty Acids in Overweight than Lean Humans. *Int J Obes (Lond)* **2014**, *38*, 1525–1531, doi:10.1038/ijo.2014.46.
316. Riva, A.; Borgo, F.; Lassandro, C.; Verduci, E.; Morace, G.; Borghi, E.; Berry, D. Pediatric Obesity Is Associated with an Altered Gut Microbiota and Discordant Shifts in Firmicutes Populations. *Environ Microbiol* **2017**, *19*, 95–105, doi:10.1111/1462-2920.13463.
317. Barczyńska, R.; Litwin, M.; Sliżewska, K.; Szalecki, M.; Berdowska, A.; Bandurska, K.; Libudzisz, Z.; Kapuśniak, J. Bacterial Microbiota and Fatty Acids in the Faeces of Overweight and Obese Children. *Polish Journal of Microbiology* **2018**, *67*, 339–345, doi:10.21307/pjm-2018-041.
318. Meijnikman, A.S.; Gerdes, V.E.; Nieuwdorp, M.; Herrema, H. Evaluating Causality of Gut Microbiota in Obesity and Diabetes in Humans. *Endocr Rev* **2018**, *39*, 133–153, doi:10.1210/er.2017-00192.
319. Righetti, P.G.; Castagna, A.; Antonioli, P.; Cecconi, D.; Campostrini, N.; Righetti, S.C. Proteomic Approaches for Studying Chemoresistance in Cancer. *Expert Rev Proteomics* **2005**, *2*, 215–228, doi:10.1586/14789450.2.2.215.
320. Hristova, V.A.; Chan, D.W. Cancer Biomarker Discovery and Translation: Proteomics and Beyond. *Expert Rev Proteomics* **2019**, *16*, 93–103, doi:10.1080/14789450.2019.1559062.
321. Yeat, N.C.; Lin, C.; Sager, M.; Lin, J. Cancer Proteomics: Developments in Technology, Clinical Use and Commercialization. *Expert Review of Proteomics* **2015**, *12*, 391–405, doi:10.1586/14789450.2015.1051969.

Published paper related to the thesis:

Barberis E, Vanella VV, Falasca M, Caneparo V, Cappellano G, Raineri D, Ghirimoldi M, De Giorgis V, Puricelli C, Vaschetto R, Sainaghi PP, Bruno S, Sica A, Dianzani U, Rolla R, Chiocchetti A, Cantaluppi V, Baldanzi G, Marengo E, Manfredi M. Circulating Exosomes Are Strongly Involved in SARS-CoV-2 Infection. *Front Mol Biosci* **2021**, 8:632290. doi: 10.3389/fmolb.2021.632290.